EFFECT OF DIFFERENT SHAPED TRANSVERSE GROOVES ON A ZERO PRESSURE GRADIENT TURBULENT BOUNDARY LAYER

SUTARDI

NOTE TO USERS

Page(s) not included in the original manuscript and are unavailable from the author or university. The manuscript was scanned as received.

89

This reproduction is the best copy available.

UMI®

Your file Votre référence
ISBN: 0-612-89702-8
Our file Notre référence
ISBN: 0-612-89702-8

EFFECT OF DIFFERENT SHAPED TRANSVERSE GROOVES ON A ZERO PRESSURE GRADIENT TURBULENT BOUNDARY LAYER

By

©Sutardi

A thesis submitted to the School of Graduate
Studies in partial fulfillment of the
requirements for the degree of
Doctor of Philosophy

Faculty of Engineering and Applied Science
Memorial University of Newfoundland
December, 2002

St. John's Newfoundland Canada

Abstract

An experimental study has been performed to investigate the response of a turbulent boundary layer to different shaped transverse grooves. Square, semicircular and triangular grooves with widths of 5, 10 and 20mm and depth to width (d/w) ratio of unity were investigated. The ratios of the groove depth to the oncoming boundary layer thickness (d/δ_0) are 0.067, 0.133 and 0.267, respectively, for d = 5, 10 and 20mm. The experiments were performed at two freestream velocities (U_0) of 2.0 and 5.5m/s, corresponding to Reynolds number (R_θ) based on the momentum thickness just upstream of the groove of 1000 and 3000, respectively. The turbulence parameters were measured using hot-wire anemometry, and measurements were performed at several locations downstream of the groove. The development of the wall shear stress and the internal layer downstream of the groove was also investigated. The ejection and sweep events and the bursting frequency were estimated based on the quadrant decomposition method.

The development of the turbulent boundary layer downstream of the grooves was compared with results from the corresponding smooth-wall case. For all groove shapes, the 20mm groove has the most pronounced effect on all turbulence parameters. In general, the effect of the square groove on the turbulent characteristics is more pronounced than the effects of the semicircular and triangular grooves. The wall shear stress (τ_w) was estimated from the slope of mean velocity at the wall. An increase in τ_w just downstream of the groove for all groove shapes and sizes was observed. The increase in τ_w is followed by a small decrease in τ_w below the smooth-wall value before it relaxes back to the corresponding smooth-wall value at approximately x/δ_0 = 3. The increase in τ_w is more pronounced at R_θ = 3000 than that at R_θ = 1000. At R_θ = 1000, the spectrum of

wall-normal turbulence intensity (v') downstream of the groove shows a significant increase at the higher wave number (k_1), while the increase in the spectrum of streamwise turbulence intensity (u') is not discernible at the same k_1 range. There is an increase in the bursting frequency (f_B^+) on the grooved-wall compared to the smooth-wall case. The variation of f_B^+ downstream of the groove is somewhat similar to the variation of τ_w.

Acknowledgements

My deep gratitude goes to my supervisor Dr. Chan Ching for his guidance with this thesis. The frequent discussions with Dr. Ching have helped me with my experimental work and completing the thesis writing. His helpful hand and honesty have been invaluable and unforgettable.

I would also like to thank my supervisory committee members, Dr. Neil A. Hookey and Dr. Bruce L. Parsons, for their time and valuable suggestions, which were very useful in my research.

I would like to thank the Indonesian Government for supporting my graduate study at Memorial University of Newfoundland. The financial support from May 1998 to April 2002 is gratefully acknowledged. The financial support from the Mechanical Engineering Department, ITS, Surabaya, Indonesia, and from the Natural Science and Engineering Research Council (NSERC) Canada for the completion of my research are also gratefully acknowledged.

My thanks to Aung N. Oo for providing enthusiastic help with the wind tunnel work. Furthermore, I would like to express my thanks to Darrell Sparkes and Tom Pike for their help and kind assistance with the preparation of the test plate in the wind tunnel test section.

Finally, I am indebted to my wife Heny and my son Farhan for their continuous support, encouragement, patience and understanding.

Table of Contents

List of Figures

List of Tables

List of Symbols

General:

B y-intercept (Eq. 3.4) [non-dimensional]

C_f skin friction coefficient, ($C_f \equiv 2\tau_w / (\rho(U_0)^2)$) [non-dimensional]

$C_{f,0}$ skin friction coefficient on the smooth-wall [non-dimensional]

C_u correction factor for the mean velocity (Eq. 3.9) [non-dimensional]

d groove depth, or the outside tube diameter in the Preston tube measurements, or detection function in turbulent burst analysis [m] (for the groove depth and the outside tube diameter), [non-dimensional] (for the detection function)

d^+ du_τ/ν [non-dimensional]

d_i internal layer thickness [m]

D empirical constant (Eq. 3.10) [non-dimensional]

D_h diameter of the idealized primary eddy inside the groove [m] (Fig. 6.3.1)

$D_{h,s}$ diameter of the idealized secondary eddies inside the groove [m] (Fig. 6.3.1)

E turbulent energy spectrum, or y-intercept for the velocity defect-law (Eq. 4.3) [m^3/s^2] (for the turbulent energy spectrum), [non-dimensional] (for the y-intercept]

f frequency [rad/s]

f_B bursting frequency [burst/s]

f_B^+ normalized bursting frequency ($f_B^+ \equiv \nu f_B / (u_\tau)^2$) [non-dimensional]

f_s sampling frequency [sample/s]

h channel height [m] (Table 4.5)

H threshold level (Eq. 3.14) [non-dimensional]

h_f height of idealized ejected fluid from a groove [m] (Fig. 5.4.1)

k wave number ($2\pi f/U$) [/m]

L tunnel span [m]

l_e effective length of the wire (for hot-wire) [m]

l_f length of idealized ejected fluid from a groove [m] (Fig. 5.4.1)

N_b number of bursts

Δp differential pressure between the total and static pressures at the wall [N/m^2] (Eq. 3.11)

Δp^+ normalized Δp ($\Delta p^+ \equiv \Delta p d^2/(\rho\nu^2)$) [non-dimensional] (Eq. 3.13)

q_i^+ quadrant decomposition contributing to the total Reynolds stress $\langle -uv \rangle$. ($q_i^+ \equiv \langle -uv \rangle_i/(u_\tau)^2$, i = 1, 2, 3, 4) [non-dimensional]

R_δ Reynolds number based on δ ($R_\delta \equiv U_0\delta/\nu$) [non-dimensional]

$R_{e,d}$ Reynolds number based on Preston tube outside diameter, d ($R_{e,d} \equiv U_0 d/\nu$) [non-dimensional] (Eq. 4.2)

Re_h Reynolds number based on h and U_m ($Re_h \equiv U_m h/\nu$) [non-dimensional] (Table 4.5)

R_θ Reynolds number based on θ ($R_\theta \equiv U_0\theta/\nu$) [non-dimensional]

$\vec{S}(t)$ instantaneous velocity vector [m/s]

s groove or riblet spacing [m]

s^+ normalized s by inner variables ($s^+ \equiv su_\tau/\nu$) [non-dimensional]

T temperature (C)

$\overline{T_B}$ average time between bursts [s]

$\overline{T_B}^+$ normalized average time between bursts ($\overline{T_B}^+ \equiv \overline{T_B}u_\tau^2/\nu$) [non-dimensional]

T_e time between two consecutive detected ejections [s]

$T_{e,m}$ average of T_e [s]

T_o average of the duration of detected ejections [s]

T_s sampling time [s]

t time [s]

t^+ normalized t by inner variables ($t^+ \equiv u_\tau^2 t/\nu$) [non-dimensional] (Fig. 2.9)

U mean velocity in the x-direction [m/s]

U_c correct local mean velocity [m/s]

U_m average mass velocity in the channel flow [m/s]

U_{meas} measured local mean velocity [m/s]

U_0 free stream velocity [m/s]

U^+ normalized mean velocity in the x-direction by inner variable ($U^+ \equiv U/u_\tau$) [non-dimensional]

$\tilde{u}(t)$ instantaneous velocity in the x-direction ($\tilde{u}(t) = U + u(t)$) [m/s]

$u(t)$ instantaneous fluctuation velocity in the x-direction [m/s]

u' rms of fluctuation of velocity in the x-direction [m/s]

u'^+ normalized u' by inner variable ($u'^+ \equiv u'/u_\tau$) [non-dimensional]

u_τ friction velocity ($u_\tau \equiv (\tau_w/\rho)^{0.5}$) [m/s]

$\langle uv \rangle$ Reynolds stress [m^2/s^2]

$\tilde{v}(t)$ instantaneous velocity in the y-direction ($\tilde{v}(t) = V + v(t)$) [m/s]

$v(t)$ instantaneous fluctuation velocity in the y-direction [m/s]

v' rms of fluctuation of velocity in the y-direction [m/s]

w groove width in the streamwise direction [m]

x streamwise coordinate measured from the groove trailing edge [m]

x^* normalized pressure (Eq. 3.12) [non-dimensional]

y wall-normal coordinate [m]

y^+ normalized y by inner variables ($y^+ \equiv yu_\tau/\nu$) [non-dimensional]

y^* normalized wall shear stress (Eq. 3.12) [non-dimensional]

Greek symbols:

α constant in the power-law equation (Eq. 3.6) [non-dimensional]

β instantaneous velocity angle (Eqs. A.2 and A.3), or a constant in the hot-wire calibration (Eq. C.3) [degree] (for the instantaneous velocity angle), [non-dimensional] (for the constant in the hot-wire calibration)

δ local boundary layer thickness [m]

δ_0 boundary layer thickness just upstream of the groove, unless otherwise stated [m]

ε turbulent kinetic energy dissipation rate [m2/s3]

ϕ wire diameter [m]

η Kolmogorov length scale ($\eta \equiv \nu^{3/4}/\varepsilon^{1/4}$) [m]

κ von Kármán constant [non-dimensional]

ν kinematic viscosity [m^2/s]

θ momentum thickness [m]

ρ fluid density [kg/m^3]

τ_{max} maximum value of T_e [s]

τ_w wall shear stress [N/m^2]

τ^+ normalized wall shear stress (Eq. 3.13) [non-dimensional]

υ Kolmogorov velocity scale ($\upsilon \equiv (\nu\varepsilon)^{1/4}$) [m/s]

Miscellaneous:

$\langle ..... \rangle$ and $\overline{.....}$ are used interchangably to denote the time averaged quantities

Abbreviations:

A/D	analog to digital
DNS	direct numerical simulation
HWA	hot-wire anemometry
LDA	laser Doppler anemometry
LDV	laser Doppler velocimetry
LEBU	large eddy break-up
LES	large eddy simulation
MEMS	micro-electro-mechanical-system
PIV	particle image velocimetry
PTV	particle tracking velocimetry
VITA	variable-time interval-averaging

List of Appendices

Chapter 1

Introduction

Despite being studied for many years, turbulent boundary layers, particularly over rough surfaces, still remain poorly understood. A complete picture of the interaction of the near-wall structures in turbulent boundary layers with the surface has not been uncovered. A significant effort is still devoted to the study of the turbulent boundary layer because of its importance in many practical applications. The interaction of the near-wall structures with the surface is primarily responsible for the high skin friction on the surface. A turbulent boundary layer responds differently to different surface geometries. For example, it has been shown that longitudinal riblets (Fig. 1.2) can reduce the friction drag, while transversal riblets tend to increase the friction drag.

The inner most region of the layer is particularly interesting, because of the possibility of manipulating the turbulent structures in this region to obtain some desired benefits. The inner region constitutes approximately 20 percent of the total boundary layer thickness (δ), but the most dominant turbulent activities take place within this

region. For example, approximately 85 percent of the total turbulent kinetic energy dissipation takes place in this region (Klebanoff, 1955). Experimental and numerical results show that the turbulent quantities, such as turbulence intensities, turbulence energy spectra, and Reynolds stresses, change very rapidly in this region as the solid boundary is approached. Also, turbulent bursts, recognized as one of the most important stress-producing events in a turbulent boundary layer, originate in this inner region. A study of the structure of turbulent boundary layers, especially in the innermost region, is important to enhance our understanding of the near-wall characteristics of the layer.

Skin friction, which is dissipative in nature, plays an important role in the system performance for both external and internal flows. For example, the skin friction drag determines the overall efficiency of aircraft, high-speed vehicles, marine vessels, piping, and ducting systems. In transportation applications, overall fuel efficiency can be improved by reducing the total drag force. The required thrust is directly proportional to drag force, and for a typical civil transport aircraft, skin friction drag can contribute up to 50 percent of the total drag at cruising speed (Coustol and Savill, 1991). In internal flows, such as in pipelines and ducting systems, almost 100 percent of the drag is due to skin friction. A large number of investigations of skin friction drag reduction have been performed over the last five decades, because of the economic benefits. For example, for a typical long range transport aircraft, a reduction in skin friction drag of less than 5 percent can produce a considerable savings on direct operating costs. The drag reduction is directly related to the reduction in fuel consumption, and the fuel consumption contributes up to approximately 22 percent of the total direct operating cost (Marec, 2000).

1.1 Background of Study

A tremendous amount of literature on methods of manipulating a turbulent boundary layer to achieve a skin friction drag reduction is already available. It is well known that the coherent structures such as quasi-streamwise vortices and low-speed streaks embedded in the near-wall region of the turbulent boundary layer can be manipulated for possible skin friction drag reduction. However, a clear understanding of the near-wall structures of a turbulent boundary layer and how they interact with a surface is necessary to implement any drag reduction scheme. Despite being studied for many years, probably since the study of Nikuradse (1933), the effect of different surface modifications on a turbulent boundary layer is still not fully understood.

Several drag reduction schemes have been investigated, which can basically be classified into two different categories: active and passive control. For active control, external energy is required, while no auxiliary energy is necessary for passive control. Some active control techniques are: (1) laminar flow control; (2) suction and blowing; (3) micro bubble technique; (4) moving surface; (5) electromagnetic forces; and (6) reactive control. With laminar flow control, transition of the boundary layer to turbulence can be delayed. Suction in a turbulent boundary layer can be used for re-laminarization and attenuation of turbulent activity in the near-wall region. A reduction in skin friction drag due to suction has been reported (Antonia et al., 1995; Park and Choi, 1999). Injection of light gases or micro-bubbles into a turbulent boundary layer can reduce skin friction drag (Latorre and Babenko, 1998; Kodama et al., 2000). Using this technique, an overall skin friction drag reduction up to 30 percent has been reported (Latorre and Babenko, 1998).

A moving surface either in the streamwise direction (Modi, 1997), or oscillating motion in the spanwise direction (Choi and Clayton, 1998; Choi, 2002) can be used to reduce drag. Choi and Clayton (1998) and Choi (2002) reported that a reduction in skin friction drag up to 45 percent can be achieved using an oscillating surface in the spanwise direction. Electromagnetic forces can be used for controlling turbulent boundary layers in conductive fluids such as seawater (Kim, 1998; Lee and Kim, 2002). A drag reduction up to 50 percent using this control scheme was reported (Kim, 1998). A recent development of turbulent boundary layer control is through reactive control. In general, reactive control is more complex and its construction and implementation are more difficult than the previous methods (Gad-el-Hak, 1996). Although skin friction drag reduction of up to 50 percent can be achieved using active control, the overall energy efficiency of this control technique is poor (Kim, 1998). Through passive turbulence control techniques, the skin friction drag could potentially be reduced without any extra auxiliary energy. Two of the most well known passive control techniques for turbulent skin friction drag reduction are the use of external manipulators such as large eddy break-up devices (LEBUs) embedded in the outer part of a turbulent boundary layer (Fig. 1.1), or internal devices that involve an alteration of the wall geometry such as longitudinal grooves (riblets) on the surface (Fig. 1.2). Sowdon (1998) noted an average local skin friction drag reduction of approximately 3 percent downstream of LEBUs. The LEBU support drag and the structural complexity necessary for their installation, however, tend to negate any benefits of drag reduction. Bechert et al. (1997) showed that when the geometry of the riblets is properly optimized, a drag reduction of approximately 10 percent can be achieved. The maintenance of longitudinal micro grooves on a surface has

posed several difficulties, however. While passive control techniques will not yield as much drag reduction as active control, they are simpler to implement.

Perturbing elements can be used on a flat plate to enhance momentum and heat transfer associated with boundary layers. The enhancement of the momentum and heat transfer is a result of an increase in turbulent transport due to higher turbulence intensity levels in the near-wall region. In the studies using a transverse square groove (Choi and Fujisawa, 1993; Elavarasan et al., 1996; Pearson et al., 1997) and a V-shaped groove (Tantirige et al., 1994), an increase in the turbulence intensity was reported. There have been several studies of the response of a turbulent boundary layer to a short perturbation; see, for example, Andreopoulus and Wood (1982), Webster et al. (1995) and Pearson et al., (1997, 1998). In these studies, it was shown that skin friction coefficient (C_f) and Reynolds stresses, including u', v', and $\langle -uv \rangle$, are significantly shifted from the original smooth-wall values. There is a local increase and decrease in C_f downstream of the perturbation, and the Reynolds stresses are increased considerably downstream of the perturbing element. Pearson et al. (1998) noted that the C_f distribution downstream of the perturbation is an indicator of the response of the turbulent boundary layer to the perturbation. While the response of turbulent boundary layers to a short perturbation with a single sized perturbing element is well documented, there have been relatively few studies of the effect of different sized and shaped short perturbations. There is a need for more studies to investigate the response of turbulent boundary layers to different sized and shaped short perturbations.

1.2 Purpose and Significance of Study

A study of the response of a turbulent boundary layer to short perturbations will provide a better insight and understanding into the interaction between the surface and the boundary layer, especially in the near-wall region. Although there have been several studies on turbulent boundary layers perturbed by a single transverse square or V-groove, the effect of the size of the groove has not been investigated. There have been no systematic studies on the relaxation of a turbulent boundary layer downstream of different shaped transverse grooves. The possibility of drag reduction using a *d*-type roughness has been proposed (Choi and Fujisawa, 1993). A small local skin friction reduction downstream of a transverse square groove was observed (Choi and Fujisawa, 1993; Elavarasan et al., 1996; Pearson et al., 1997). The total skin friction drag due to the presence of the groove, however, is higher than the corresponding smooth-wall value (Elavarasan et al., 1996). Ching and Parsons (1999) suggested a possibility to reduce the total skin friction drag by using transverse square grooves in series in the main flow direction.

The main purpose of the present study is to investigate the response of a turbulent boundary layer to different shaped transverse grooves. Three different groove shapes: square (SQ), semicircular base (SC) and triangular (TR) were investigated. For each shape, three different sized grooves were used in this study: 5, 10 and 20mm (Fig. 1.3). The depth to width ratio (d/w) of each groove was set to unity. The response of the turbulent boundary layer to the groove is investigated from $x/\delta_0 = 0$ up to $x/\delta_0 \approx 2.0$. Experiments were performed at two Reynolds numbers, $R_\theta = 1000$ and 3000. Hot-wire

anemometry using single-normal and X-wires was used to measure the turbulence characteristics downstream of the groove.

The present study attempts to clarify the differences of the turbulent boundary layer characteristics over different transverse grooves from the corresponding smooth-wall case. First, different techniques of wall shear stress (τ_w) measurements for smooth-wall turbulent boundary layers are evaluated. The most appropriate τ_w measurement techniques using indirect methods applied to a boundary layer developing downstream of a short perturbation are then examined. Next, the τ_w distribution in turbulent boundary layers downstream of the different sized and shaped grooves is studied. This provides some insight into the possibility of drag reduction in turbulent boundary layers using different sized and shaped grooves. The changes in turbulent characteristics (u', v', $\langle -uv \rangle$, $E(k_1)$, sweep and ejection events, and the bursting frequency) and their relaxation downstream of the grooves are studied. Also, the effects of the oncoming boundary layer thickness (δ_0) on the turbulent characteristics are evaluated.

1.3 Outline of Thesis

A literature review relevant to this research is presented in chapter 2, which consists of four sections. In the first section, coherent structures in a turbulent boundary layer are reviewed, while the structure of a turbulent boundary layer under zero pressure gradient on smooth and non-smooth walls is reviewed in the second and third sections, respectively. Simulations and experimental techniques used to study turbulent boundary layers are reviewed in the fourth section.

In chapter 3, descriptions of the experimental facility, instrumentation and data reduction procedures are presented. Firstly, the wind tunnel is described with details of the tunnel geometry, dimensions, capabilities and limitations. A brief description of hot-wire anemometry is presented next, followed by a description of the Preston tube arrangement and data acquisition system. The data reduction procedures for the Reynolds stress, wall shear stress, internal layer growth, sweep and ejection events, and bursting frequency are presented in this chapter. The last part of this chapter presents the experimental uncertainties.

In chapter 4, the experimental results for the baseline smooth-wall turbulent boundary layer are presented and discussed. The results and discussion include wall shear stress (τ_w), mean velocity (U), Reynolds stresses and turbulent energy spectra. Sweep and ejection events and bursting frequency are also discussed. Wall shear stress measurements using a Preston tube are also presented in this chapter.

In chapter 5, the experimental results of the grooved-wall experiments are presented and discussed, which includes the experimental results from the square (SQ), semicircular base (SC) and triangular (TR) grooves. The main emphasis of the discussion in this chapter is to examine the effect of the groove size on flow parameters close to the groove such as wall shear stress (τ_w), mean velocity (U) and internal layer (d_i) growth downstream of the groove. The turbulence measurements, sweep and ejection events, and bursting frequency are presented and discussed in separate sub-sections.

In chapter 6, the effects of the different shapes of the grooves on the turbulent boundary layer are discussed. Conclusions and recommendations are given in chapter 7, and the contributions of the present study to the literature are also highlighted.

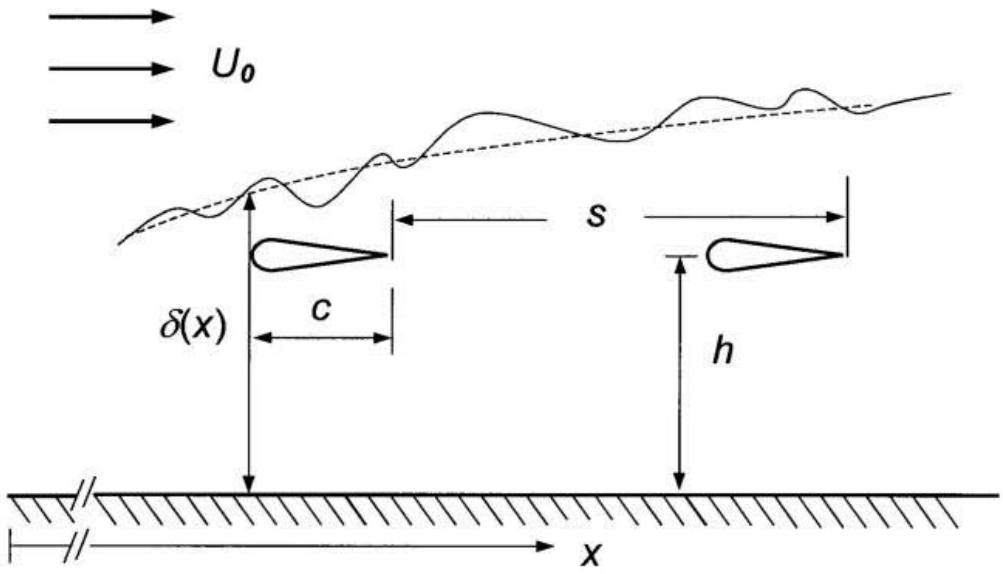

Fig. 1.1 Outer manipulator using large-eddy break-up (LEBU)

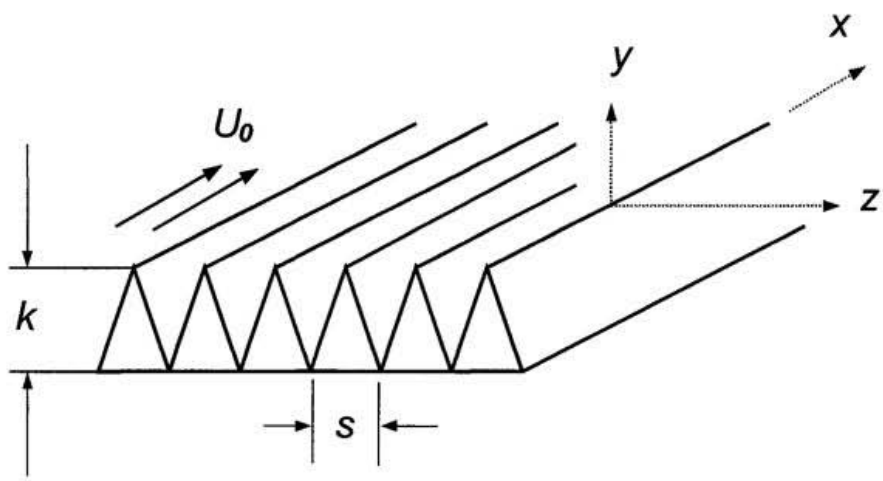

Fig. 1.2 Surface with longitudinal riblets

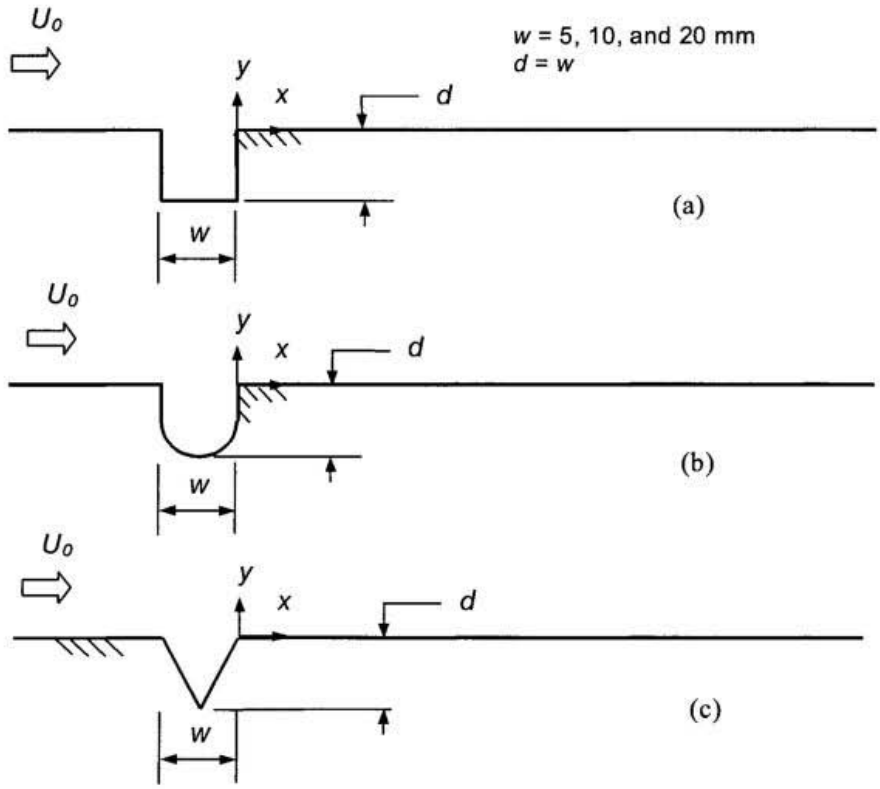

Fig. 1.3 Groove shapes on the test surface: (a) Square (SQ); (b) semicircular base (SC); (c) triangular (TR).

Chapter 2

Literature Review

Boundary layers play an important role in the momentum and heat transfer at the wall. Typically, boundary layers can be classified into three different regimes: laminar, transitional, and turbulent (Fig. 2.1). In laminar boundary layers, the momentum transfer is essentially by molecular diffusion, whereas in turbulent boundary layers the momentum transfer by the fluctuating velocity plays a significant role. In transitional boundary layers, momentum transfer due to velocity fluctuations can take place, however, the momentum transfer is not as intense as in turbulent boundary layers. There has been a large amount of research on turbulent boundary layers, both experimentally and numerically, because of its importance in many practical applications. Although the transport mechanisms in turbulent boundary layers have been studied for many decades, the dynamics of turbulent boundary layers are still not fully understood. With advances in modern instrumentation along with the recent advances in direct numerical simulation (DNS), however, some of the key dynamics in turbulent boundary layers have been

uncovered, especially the role of the quasi-coherent structures, or coherent motions. In this chapter, previous studies on turbulent boundary layers are reviewed briefly. The review consists of four sections: (i) coherent structures in turbulent boundary layers; (ii) turbulent boundary layers on smooth-walls; (iii) turbulent boundary layers on non-smooth-walls; and (iv) simulations and experimental techniques in turbulent boundary layer studies. This short review should provide a better understanding of the effect of different surface geometries on the structure and characteristics of a turbulent boundary layer.

2.1 Coherent Structures in a Turbulent Boundary Layer

In the last decade or so, a significant amount of effort has been devoted to the study of quasi-coherent structures, or coherent motions, in a turbulent boundary layer. A substantial amount of information has been collected on these structures through detailed probe measurements, flow visualization, whole flow field measurements, particle image velocimetry (PIV), and from direct numerical simulation (DNS) (e.g. Head and Bandyopadhyay, 1981; Robinson, 1991; Moin and Mahesh, 1998; Na et al., 2001). While there is no precise definition for quasi-coherent structures, Robinson (1991) provides a definition for a coherent structure as "*a three-dimensional region of the flow over which at least one fundamental flow variable* (*velocity component, density, temperature, etc.*) *exhibits significant correlation with itself, or with another variable, over a range of space and/or time that is significantly larger than the smallest local scales of the flow*". The coherent structures in a turbulent flow field occur randomly in time and space, and they are characterized by a very wide range of length and time scales (Carpenter, 1997). The

most dynamically dominant coherent structures in the near-wall region of a turbulent boundary layer are the quasi-streamwise vortices (Head and Bandyopadhyay, 1981; Cantwell, 1981; Smith and Schwartz, 1983). Jeong et al. (1997) showed that the coherent structures in the near-wall region are mostly highly elongated quasi-streamwise vortices, and these vortices are well organized. Low-speed streaks are formed between two adjacent quasi-streamwise vortices. Figure 2.2 depicts a schematic diagram of a low-speed streak surrounded by quasi-streamwise vortices (reproduced from Blackwelder and Eckelmann, 1979), and Fig. 2.3 shows the near-wall streak structure at $y^+ = 2.7$ (reproduced from Kline et al., 1967). As the vortices develop, they become longer, reduce in diameter, and lift up away from the wall. When the 'head' of the vortex lifts up, the leading edge of the low-speed streak moves together with the vortex away from the wall (Smith and Walker, 1997). In the final step of their cycle, they break up ('bursting'). Figure 2.4 shows a schematic diagram of burst formation in the near-wall region (reproduced from Hinze, 1975). It is believed that the bursting proccess initiates a new generation of vortical structures, and then the cycle is repeated (Carpenter, 1997). In addition to the streamwise vortices, transverse (lateral) and wall-normal vortices may be present, with the latter ones occurring less frequently. These vortices, except the wall-normal vortices, could 'pump-out' mass and momentum from the wall (Robinson, 1991). It is conjectured that there is a strong correlation between skin friction and the quasi-streamwise vortices in the near-wall region. If these vortices can be moved away from the near-wall region, a reduction in skin friction may be possible (Pollard, 1996). Also, if the coherent structures can be stabilized, then the skin friction drag would be reduced (Sirovich and Karlsson, 1997).

Flow visualization was used extensively in many early studies (e.g. Kline et al., 1967; Kim et al., 1971; Falco, 1980a, b, 1991; Head and Bandyopadhyay, 1981) to educe the structure of turbulent boundary layers. Kline et al. showed that there were well organized motions in the inner region of the layer. Streak patterns in the layer were shown at several different distances from the wall, from very close to the wall ($y^+ = 2.7$) up to the wake region ($y^+ = 507$). The streak patterns across the layer were shown to be different from one location to another as the streak moves away from the wall. In the innermost region, the orientation of the streaks is well defined and is in the streamwise direction. Farther away from the wall, the orientation of the streaks is less defined. Falco (1980a) showed that large-scale three-dimensional bulges are present in the outer region of the turbulent boundary layer.

The near-wall turbulent dynamics are continuous and self-regenerating activities (Choi, 1996). Ejections and sweeps play an important role in the dynamics of turbulent Reynolds stresses, turbulence production, and turbulent kinetic energy dissipation (Coustols and Savill, 1991). The ejections are associated with negative streamwise ($-u$) and positive wall-normal ($+v$) velocity fluctuations, while the sweeps are associated with positive streamwise ($+u$) and negative wall-normal ($-v$) velocity fluctuations (Wallace et al., 1972). In the uv quadrant-splitting description (Wallace et al., 1972; Willmarth and Lu, 1972), ejections and sweeps are defined as $(uv)_2$ and $(uv)_4$, respectively, where subscripts 2 and 4 represent the second and fourth quadrant, respectively (Fig. 2.5). Wallace et al. (1972) identified that the major turbulent events in the wall region are ejections of low-speed fluid outward from the wall and sweeps of high-speed fluid inward toward the wall. The ejections and sweeps are believed to play a key role in

maintaining the turbulence activities in the near-wall region, and these two activities produce the major part of the Reynolds stresses (Schetz, 1993).

In the outer region of a turbulent boundary layer, large scale eddies seem to be more dominant. Robinson (1991) found eddies on the scale of the boundary layer thickness (δ) in this region. Falco (1980a, b) observed a clear demarcation line between the turbulent and non-turbulent region. It is believed that there is a strong interaction between the outer large-scale structures and the quasi-streamwise coherent structures in the inner region. Several studies have shown that breaking the outer large-scale structures, using LEBUs or micro-electro-mechanical-systems (MEMS) for example, can result in a skin friction reduction (Moin and Bewley, 1994; Ho and Tai, 1998; Sowdon, 1998). The definite relationship between the outer large-scale structures and inner region coherent structures, however, has not been clearly resolved. Despite the vast amount of information available on these coherent motions, the interaction of these motions with different surface geometries has not been resolved. For example, there is still no consensus on how different surface roughnesses interact with the near-wall low-speed streaks and quasi-streamwise vortices. Additionally, although several mechanisms for reduction in skin friction drag by manipulating the near-wall coherent structures have been proposed, the exact mechanism of this is not clearly understood. So far, there has been no systematic study of the influence of wall-roughness on the turbulent bursting frequency. Although flow visualization showed the structure of the turbulent boundary layer on non-smooth surfaces does not differ significantly from that on a smooth surface (Grass, 1971; Ching et al., 1995b), the roughness geometry can affect the bursting frequency. In the following section, previous studies on the effects of different surface

geometries on the near-wall turbulent structures and turbulent parameters are described briefly.

2.2 Turbulent Boundary Layers on Smooth-Walls

A significant number of experimental and numerical studies of turbulent boundary layers over both smooth- and non-smooth-walls have been performed. The characteristics of smooth-wall turbulent boundary layers are briefly reviewed first to provide a better understanding of how the characteristics of turbulent boundary layers over non-smooth-walls differ. There are two main regions in a turbulent boundary layer designated as the inner and the outer regions (Fig. 2.6). The inner region occupies approximately 20 percent of the boundary layer thickness (δ) and consists of three sub-regions: the laminar sub-layer (up to $y^+ = 5$), buffer region ($5 \leq y^+ \leq 40$), and an overlap region. In the laminar sub-layer the viscous shear dominates, while in the overlap region both viscous and turbulent shear stresses are non-negligible. The inner limit of the overlap region is approximately at $y^+ = 40$, but the outer limit of this region depends on the flow Reynolds number. For example, at a Reynolds number about 1000 (based on the momentum thickness and freestream velocity), this outer limit is approximately $y^+ = 200$, but this limit increases up to approximately at $y^+ = 750$ at $R_\theta = 13000$. In the figure, the outer limit of the overlap region refers to the data at the lower R_θ. The outer region consists of two sub-regions: the overlap region and a wake region. The outer region is much larger than the inner region, and occupies up to approximately 80 percent of the boundary layer thickness. Unlike in the inner region, the turbulent shear stress is much more important than the viscous shear stress in the outer region.

Up to date, there has been a vast amount of reviews and studies on smooth-wall turbulent boundary layers. Several issues, such as the effect of Reynolds number (e.g. Gad-el-Hak and Bandyopadhyay, 1994; Ching et al., 1995a; Mochizuki and Nieuwstadt, 1996), scaling laws (Clauser, 1956; George and Castillo, 1997; DeGraff and Eaton, 2000), and universal log-law in the overlap region (Österlund et al., 2000) have been investigated.

The structures of turbulent boundary layers depend strongly on Reynolds numbers. It is well known that at higher Reynolds numbers, there exists an overlap region of mean velocity when normalized using wall variables (u_τ and ν). The extent of the overlap region widens as the Reynolds number increases. At low Reynolds numbers, however, the overlap region is very narrow, and its existence is questionable (Ching et al., 1995a). The latter authors also showed that the locations of peak values of Reynolds stresses (v'^+, w'^+, and $\langle -u^+v^+ \rangle$) increase with R_θ, although the location of the peak value of u'^+ is nearly unchanged. In the study of Antonia and Kim (1994), it was shown that the low Reynolds number effect can be identified using two important characteristics. First, there is an intensification of the quasi-streamwise vortices, but the average location and diameter of the vortices, in terms of u_τ and ν, were approximately unchanged. Second, the use of u_τ and ν as the normalizing parameters for most turbulence quantities in the near-wall region were less appropriate than the use of Kolmogorov velocity (υ) and length (η) scales. The Reynolds number effects are found to penetrate deeper into the boundary layer in the case of streamwise turbulence intensity (u') than that of the mean velocity (U) (Gad-el-Hak and Bandyopadhyay, 1994). A strong dependence of u' on the Reynolds number is also evident from the studies of Fernholz and Finley (1996).

Mochizuki and Nieuwstadt (1996) showed the peak value of u' is nearly independent of the Reynolds number, while Metzger and Klewicki (2001) found that the peak value of u' is dependent on R_θ. The Reynolds number effect on wall-normal turbulence intensity (v') and Reynolds stress ($\langle -uv \rangle$) have also been reported (Fernholz and Finley, 1996; Ching et al., 1995a). In general, self similarities in v'^+ and $\langle -u^+v^+ \rangle$ are confined to the region very close to the wall (say $y^+ \leq 10$).

Scaling issues in turbulent boundary layers are still being investigated. For instance, while the scaling parameter for mean velocity is well established, scaling parameters for normal stresses are still in debate. For example, Purtell et al. (1981) argued that streamwise turbulence intensity scales favorably with outer parameters (U_0 and δ), whereas DeGraff and Eaton (2000) proposed that mixed-parameters are more appropriate. Moreover, the correct scaling parameters for the turbulent burst are still not clearly understood. For example, Blackwelder and Haritonidis (1983), Kim and Spalart (1987), and Luchik and Tiederman (1987) argued that the inner variables (u_τ and ν) are the best scaling parameters for the average bursting period. On the contrary, Rao et al. (1971) and Kim et al. (1971) found that outer variables (δ and U_0) were more appropriate. While the inner scaling parameters may be the most appropriate for the turbulent burst period at low Reynolds numbers, scaling using mixed variables (outer and inner variables) seems to be more appropriate at higher Reynolds numbers ($R_\theta \geq 6000$) (Shah and Antonia, 1989).

The studies of Klebanoff and Diehl (1952) and Klebanoff (1955) were the earliest comprehensive experimental studies on smooth-wall turbulent boundary layers. They found that the turbulent energy production and dissipation reach a maximum value in the

region close to the wall ($y^+ < 30$). They also suggested that the concept of local isotropy was not appropriate to estimate the rate of turbulent energy dissipation. The flow visualization studies of Kline et al. (1967) and Head and Bandyopadhyay (1981) provided some insight into the near-wall turbulent structures, including low- and high-speed streaks. More recently, direct numerical simulations (DNS) (see, for example, Spalart, 1988) have provided considerable insight into turbulent boundary layers and provided a benchmark database for laboratory experimental data.

2.3 Turbulent Boundary Layers on Non-Smooth-Walls

The discovery of coherent structures, including quasi-streamwise vortices and streak structures in wall-bounded turbulent flows, led to the possibility of developing flow control schemes for turbulent boundary layers. The control schemes can be classified as active methods or passive methods using surface modifications. Only the passive methods using surface modifications are discussed in this thesis. The surface modifications include surface roughness or the use of short perturbations.

Using flow visualization, Grass (1971) and Grass et al. (1991) showed that the basic characteristics of the inner-region of turbulent boundary layers over a wall roughened with sand grains were not significantly different from that on the smooth-wall. Low-speed streaks and turbulent burst events including the sweep and ejection events were also found in the rough-wall turbulent boundary layer, similar to those in the smooth-wall turbulent boundary layers. Similar to the finding of Grass (1971), Ching et al. (1995b) and Djenidi et al. (1999) showed that the low-speed streak structure over a *d*-type rough-wall is not too different from that on the smooth-wall. The appearance and the

break-up of the streak patterns were similar to the low-speed streaks observed by Kline et al. (1967).

Although flow visualization techniques have shown that the basic structures of the near-wall low-speed streaks over the smooth- and rough-wall turbulent boundary layers are similar, the inherent turbulent quantities are different. This is most significant in the near-wall region, say within $y^+ \leq 100$ (Antonia, 1994; Mochizuki and Osaka, 1998). Also, the wall shear stress (τ_w) on rough-walls is different from that on smooth-walls (Andreopoulus and Wood, 1982; Elavarasan et al., 1996; Pearson et al., 1998). Antonia and Luxton (1971a) introduced the concept of an internal layer (δ_i) in a turbulent boundary layer for a sudden change in wall boundary condition. The internal layer is defined as the region within the turbulent boundary layer where the effects of the change in boundary condition are felt. Several types of rough-walls have been studied, including turbulent boundary layers over sand-grain roughness (Andreopoulus and Bradshaw, 1981), riblet surfaces (Choi et al., 1993; Bechert et al., 1997; Lee and Lee, 2001), *k*- and *d*-type rough-walls (Perry et al., 1969; Bandyopadhyay and Watson, 1988; Antonia and Djenidi, 1997), and transverse V-grooves (Tantirige et al., 1994). The effect of simple perturbations (short-roughness, 2D bump, and single transverse square groove) on turbulent boundary layers have also been studied by many researchers (Andreopoulus and Wood, 1982; Choi and Fujisawa, 1993; Webster et al., 1996; Pearson et al., 1997, 1998).

2.3.1 k-type Rough Wall

The *k*-type rough-wall (Fig. 2.7) is defined as containing transverse 2D rectangular grooves with $w/k > 1$. The usefulness of this type of roughness is its ability to

enhance the turbulence intensities in the near-wall region (Bandyopadhyay and Watson, 1988). Many studies on turbulent boundary layers over this type of roughness have been performed (e.g. Perry et al., 1969; Antonia and Luxton, 1971b; Bandyopadhyay and Watson, 1988). The flow is strongly affected by the roughness height (k), which is also believed to be the most appropriate scaling parameter for the length scale in the wall-region. Bandyopadhyay and Watson (1988) showed that the second and third moments were increased by up to 13 and 50 percent, respectively, over a k-type rough-wall. The increase in the second moment over this type of rough-wall was also observed by Antonia and Luxton (1971b). The skin friction over a k-type rough-wall was found to be higher than that on the smooth-wall (Bandyopadhyay and Watson, 1988).

2.3.2 d-type Rough Wall

A d-type rough-wall (Fig. 2.8) is characterized by regularly spaced two-dimensional square grooves placed normal to the flow, one element width apart ($w = d$) in the streamwise direction (Antonia, 1994; Elavarasan et al., 1996). Bandyopadhyay (1986) and Bandyopadhyay and Watson (1988) also used the d-type rough-wall term for $w/d < 1$. The d-type rough wall is particularly interesting because of the possibility that the boundary layer over this roughness type may be exactly self-preserving (Djenidi et al., 1994). Also, it has been suggested that the drag over this rough-wall should not be much different from that over a smooth-wall, and could even be smaller (Tani et al., 1987; Osaka and Mochizuki, 1988). The d-type rough-wall has also been studied as a means of surface drag reduction by combining this surface with other potential drag reducing devices such as LEBUs (Bandyopadhyay, 1986).

Using flow visualization, Townes and Sabersky (1966) showed that there was a significant interaction between the flow in the grooves of the *d*-type rough-wall and the outer flow. They identified several phases of activities: ejections of fluid out of the groove, inflows into the groove, and periods of relative calm where the outer layer skims over the groove. Djenidi et al. (1994) speculated that the near-wall quasi-streamwise vortices are responsible for the ejections of fluid out of the groove, and also responsible for the increase in the Reynolds stress ($\langle -uv \rangle$). The observations of Townes and Sabersky were corroborated by Ching et al. (1995b), who showed that passage of near-wall quasi-streamwise vortices over the grooves triggered the ejections of fluid out of the groove. They also showed that the streak structure on the *d*-type rough-wall is somewhat similar to that on the smooth-wall. Figure 2.9 shows a time sequence of fluid ejection from the groove to the overlying layer (Elavarasan et al., 1996).

There were significant differences in the mean velocity (U), turbulent intensities (u' and v'), and Reynolds stress ($\langle -uv \rangle$) over the *d*-type roughness when compared with the smooth-wall case (Antonia, 1994; Mochizuki and Osaka, 1998; Djenidi et al., 1999). Antonia found a decrease in U^+ in the region $y^+ \leq 100$ and increases in u'^+, v'^+ and $\langle -u^+v^+ \rangle$ over the *d*-type rough-wall compared to that over the smooth-wall. Antonia argued that the increases in u'^+, v'^+, and $\langle -u^+v^+ \rangle$ must be associated with the increase in the wall shear stress, although the latter was not explicitly described. Mochizuki and Osaka (1998), using a *d*-type rough-wall with insertion of longitudinal ribs inside the grooves, found a reduction in u' compared to that observed in the smooth-wall. Djenidi et al. (1999) showed that τ_w exhibits a periodic behavior with a wavelength that resembles the periodicity of the surface geometry. The τ_w attains a maximum at a location just

downstream of the crest leading edge (groove trailing edge) and a minimum at a location just upstream of the crest leading edge. The total surface drag over the *d*-type rough-wall, however, was not compared to the smooth-wall case.

The study of turbulent boundary layers over the *d*-type rough-wall has been extended to sparse *d*-type roughness, where the grooves are spaced several element widths apart. For the sparse *d*-type roughness, a drag reduction of approximately 3 percent has been reported at low R_θ when the spacing is 20 widths apart (Tani et al., 1987; Matsumoto, 1994). Coustols and Savill (1991) attributed the reduction to the beneficial modifications of the turbulence structure in the near-wall region between consecutive grooves.

2.3.3 Riblets

Longitudinal riblets (Fig. 1.2) have received much attention because of their potential for drag reduction (Walsh, 1980, 1990; Bacher and Smith, 1986; Choi et al., 1993; Lee and Lee, 2001). It is believed that riblets are able to dampen the quasi-streamwise vortices. It is hypothesized that the formation of counter rotating vortices at the longitudinal riblet peaks can reduce considerably the re-generation of low-speed streaks in the near-wall region. This in turn reduces the bursting frequency in the near-wall region, resulting in a reduction in the wall shear stress (τ_w) (Bacher and Smith, 1986). If the riblet spacing is smaller than the typical diameter of the dynamically significant streamwise vortices, a reduction in wall shear stress is obtained (Choi et al., 1993; Lee and Lee, 2001). With this riblet size, the streamwise vortices cannot penetrate into the riblet valley so that only a limited wetted area interacts with the vortices. Choi et

al. (1993) found a riblet space of 20 wall units for drag reduction, while Bacher and Smith (1986) and Bechert et al. (1997) found a spacing of 15 wall units. In a recent experimental study, Lee and Lee (2001) found that the riblet spacing should be about 25 wall units to obtain a surface drag reduction using longitudinal riblets with a semi-circular groove cross section.

There have been a large number of studies on the effects of riblets on the characteristics of a turbulent boundary layer. The studies include probe measurements (e.g. Antonia, 1994; Grek et al., 1995; Bechert et al., 1997), flow visualizations (e.g. Bacher and Smith, 1986), and numerical simulations (e.g. Choi et al., 1993; Tullis and Pollard, 1994). The wall-normal turbulence intensity (v'^+) over the riblet surface was not significantly different from the smooth-wall cases, while a slight decrease in the peak of u'^+ below the smooth-wall value was observed (Choi et al., 1993; Antonia, 1994; Grek et al., 1995). A significant decrease in $\langle -u^+v^+ \rangle$ over the riblet surface compared to the smooth-wall value has also been reported (Choi et al., 1993; Antonia, 1994; Lee and Lee, 2001). The reduction in $\langle -u^+v^+ \rangle$ over the riblets is believed to be related to the drag reduction mechanism.

From flow visualization, Bacher and Smith (1986) showed that the structure of the streaks over a riblet surface is not too different from that observed over a flat plate in the region $y^+ > 15$. In the region $y^+ < 15$, on the other hand, the low-speed streak structure over the riblet surface is significantly different from the smooth-wall case. In this region, the streak spacing over the riblet surface is significantly reduced, and the lateral movement of the streaks is suppressed considerably compared to that on a flat plate. This finding is supported by Choi et al. (1993) from direct numerical simulations. The latter

authors found that the effect of the riblets on the turbulence characteristics is limited in the region $y^+ < 20$ in cases $s^+ = 20$, and in the region $y^+ < 60$ in cases $s^+ = 40$, where s^+ ($\equiv su_\tau/\nu$) is the normalized riblet spacing, indicating that the effect of the riblets penetrates farther away from the wall as the riblet size increases. Lee and Lee (2001) reported that the effect of the riblets with $s^+ = 25.2$ diminished beyond $y^+ = 30$.

Turbulent boundary layers over a surface with different transverse grooves have also been studied. The transverse groove geometries include convex curved (Walsh, 1980), small amplitude rigid waves (Cary et al., 1980), and triangular (Timin, et al., 1983; Tantirige, 1989). Turbulence intensity amplification over these surface geometries was reported. The exchange of the fluid within the groove and the outer flow was strongly affected by the presence of the turbulence fluctuation in the outer flow (Timin et al., 1983; Tantirige, 1989). Drag characteristics on the grooved-walls did not differ significantly from the corresponding smooth-wall, although a small drag reduction was reported at low R_θ ($R_\theta \approx 900$) (Walsh, 1980).

2.3.4 Short Roughness/Perturbation

There have been several investigations of the response of a turbulent boundary layer to a perturbation by a single transverse groove, which includes a square groove (Choi and Fujisawa, 1993; Elavarasan et al., 1996; Pearson et al., 1997) and a V-shaped groove (Tantirige et al., 1994). Choi and Fujisawa (1993) found a small decrease in C_f (approximately 3.5 percent) just downstream of a transverse square groove of size $d/\delta_0 =$ 0.4. They speculated that the reduction was caused by the existence of quasi-stable vortex flows within the groove. The C_f relaxed back to the smooth-wall value at x/d =100 (or

$x/\delta_0 = 40$) downstream of the groove. The mean velocity and turbulence intensity profiles were observed to relax back to the smooth-wall profiles at $x/d = 5$ (or $x/\delta_0 = 2$). For a groove with smaller d/δ_0 (0.125 and 0.17), Elavarasan et al. (1996) and Pearson et al. (1997) found a significant increase in C_f (approximately 100 and 200 percent, respectively) just downstream of the groove (Fig. 2.10). The sudden increase was followed by a decrease below the smooth-wall value (by approximately 50 percent), and an oscillatory relaxation to the smooth-wall value beyond $x/\delta_0 = 2$. They speculated that the intense local pressure gradients emanating from the downstream edge of the groove were responsible for the sudden increase in C_f, and the reduction was due to a weakening of the streamwise vorticity due to the removal of the wall. Intuitively, the experiments of Choi and Fujisawa (1993) should yield the most pronounced effect of the groove on the turbulent boundary layer, since they used the largest groove size. However, Choi and Fujisawa (1993) inferred τ_w from the Clauser-chart (log-law) technique, while Elavarasan et al. (1996) and Pearson et al. (1997) estimated it from the slope of the mean velocity profile at the wall from laser Doppler velocimetry (LDV) measurements. It has been argued that in this instance, the Clauser-chart technique may not be appropriate since the boundary layer is not in equilibrium just downstream of the groove.

An increase in u' downstream of the groove was discernible, up to $y/\delta \leq 0.1$, in the studies of Pearson et al. (1997) and Elavarasan et al. (1996). On the contrary, Choi and Fujisawa (1993) found a reduction in u' by approximately 10 percent in the same y/δ region. Tantirige et al. (1994) found that for a V-shaped groove there is an increase of the turbulence intensity (u') due to the presence of the groove. This increase suggests that there is an increase in the rate of exchange of the mass between the outer flow and the

flow within the groove. There is very little information on the wall-normal turbulence intensity (v') downstream of a single transverse square groove. However, the effect of an impulsive step on v' in a turbulent boundary layer has been studied. For example, Andreopoulus and Wood (1982) studied a turbulent boundary layer altered by a short length of surface roughness. They found an increase in the maximum value of v'/U_0 and u'/U_0 up to approximately 200 percent over the smooth-wall reference value. The increase in v'/U_0 and u'/U_0 were related to the increase in the turbulent energy production. The increase in v'/U_0 and u'/U_0 were also associated with an increase in the Reynolds stress ($\langle -uv \rangle/(U_0)^2$). Both v'/U_0 and u'/U_0 had not relaxed back to the smooth-wall value at the streamwise location $x/\delta_0 = 35$, where the maximum values were still approximately 20 percent higher than the corresponding smooth-wall value. The C_f distribution (obtained from the Clauser-chart technique) showed an impulsive increase of approximately 200 percent over the upstream value due to the presence of the roughness strip. At $x/\delta_0 = 3.5$, C_f reached a minimum of approximately 70 percent of the value upstream of the strip, and then gradually relaxed back to the smooth-wall value at $x/\delta_0 = 20$.

Webster et al. (1996) investigated the effect of a 2D bump on a turbulent boundary layer at $R_\theta = 4030$. There was approximately a 100 percent increase in v'/U_0 over the upstream reference value at a location $x/\delta_0 = 10$ downstream of the bump leading edge. Unlike v'/U_0, the maximum value of u'/U_0 occurred at $x/\delta_0 \approx 4.2$, and was approximately 130 percent of the reference value. The increase in v'/U_0 and u'/U_0 were associated with the development of the internal layers triggered by the leading and trailing edges of the bump. At the last measurement location ($x/\delta_0 = 14$), both v'/U_0 and u'/U_0 had not relaxed back to the corresponding undisturbed surface values. The C_f was

found to increase by approximately 70 percent over the bump, and did not differ significantly from the upstream value in the region downstream of the bump. Based on their arguments, favorable followed by adverse pressure gradients above the bump were responsible for the rapid increase and decrease in C_f above the bump. The increases in turbulence intensities were associated with the discontinuity due to the presence of the bump.

A reduction up to approximately 50 percent in C_f at the interface between the smooth-surface and a short perturbing roughness was reported by Pearson et al. (1998). This reduction in C_f was followed by an increase up to approximately 60 percent in C_f above the roughness element before it relaxed back to the smooth-wall value at approximately one δ downstream of the step change. Although the studies of Andreopulus and Wood (1982), Webster et al. (1996), and Pearson et al. (1998) showed an increase in C_f at the top of the roughness element, the evolution of C_f as it passes over the element behaves differently. For the case of the flow perturbed by a 2D bump (Webster et al., 1996), C_f shows a valley extending up to approximately 50 percent of the bump chord length. The increase in C_f over the short roughness element for Andreopoulus and Wood (1982) and Pearson et al. (1998), however, seems to be abrupt before it relaxes back to the corresponding smooth-wall value.

It is clear from the previous investigations that the effect of a transverse groove on a turbulent boundary layer, and its relaxation processes is still not clearly understood. It has been argued that the groove geometry and size could be optimized to obtain a small drag reduction (Ching and Parsons, 1999). Based on the results of Pearson et al. (1997), Ching and Parsons argued the surface drag reduction can be enhanced by using a sparse

d-type roughness. By assuming the wall shear stress distribution between consecutive grooves is qualitatively similar to that of Pearson et al. (1997), Ching and Parsons proposed a distribution of τ_w on the sparse *d*-type roughness as shown in Fig. 2.11. If the area under the overshoot can be reduced while the area under the undershoot is increased, the total surface drag could be decreased. This could possibly be used in active boundary layer control schemes, where 2D slots or grooves are used for adding momentum to the layer. A better understanding of the interaction between the grooves and the boundary layer structure, however, needs to be obtained to determine the important scaling parameters.

2.4 Simulations and Experimental Techniques

Numerical studies of turbulent boundary layers have been performed for approximately the last four decades. More recently the use of direct numerical simulations (DNS) and large eddy simulations (LES) have provided considerable insight into the structure of turbulent boundary layers. In DNS, all scales of motion are resolved, while in LES, only the large scales are resolved, while the smaller scales are modeled. DNS was initiated in the 1970s (Joslin, 1997), and presently, DNS is capable of solving flows at low Reynolds numbers, including compressible and reacting flows (Moin and Mahesh, 1998). Today, LES can be used to solve turbulent flows at higher Reynolds numbers and in more complex geometries than DNS (Piomelli and Balaras, 2002).

DNS is a powerful tool to solve turbulence problems, especially at low Reynolds numbers and for unbounded flows, where separation between the largest and the smallest scales is not large. As the Reynolds number increases, or in the case of wall-bounded

flows, the scale separation is very large, and DNS is limited by computational speed and memory. LES is currently more suitable to solve wall-bounded turbulent flows at moderate Reynolds numbers. DNS and LES still remain largely research tools; the use of LES in more realistic wall-bounded turbulent flows, such as in ship hydrodynamics or in aircraft aerodynamics, where the Reynolds number is very high, is still impractical (Piomelli and Balaras, 2002). Numerical simulations of turbulence have several advantages over experimental techniques, especially when the experimental conditions are difficult to simulate.

Studies of turbulent boundary layers on smooth-walls using DNS (Spalart, 1988; Moin and Mahesh, 1998) and LES (Wu et al., 1995) have provided a more complete picture of turbulent boundary layer structures. The near-wall vortical structures and streak patterns educed from the numerical simulations are in excellent agreement with those obtained from flow visualization (Kline et al., 1967; Falco, 1980a, b, 1991; Head and Bandyopadhyay, 1981). Numerical simulations of turbulent boundary layers over non-smooth-walls have also been performed. Choi et al. (1993) and Goldstein et al. (1995) investigated the turbulent flow over a riblet surface using DNS. They showed that the riblet surface can be used to reduce drag, with a reduction up to 4 percent (Goldstein et al., 1995). Suppression of the transversal movement of quasi-streamwise vortices and the inability of the near-wall vortical structures to penetrate the riblet valley were conjectured to be responsible for the drag reduction. In a recent study, Cui et al. (2000) investigated turbulent flow characteristics over *d*- and *k*-type rough-walls using LES. They found that the effect of the *d*-type rough wall is confined to the near-wall region, while the effect of

the *k*-type rough-wall penetrated into the outer region of the boundary layer. These findings are consistent with previous experimental results.

Although DNS and LES have provided much information about the structure of turbulence, the capabilities are still limited. To investigate the structures of turbulent boundary layers on more complex geometries and at high Reynolds numbers, one must still resort to experiments. Experiments continue to yield much information on the dynamics of near-wall turbulence and are still powerful tools for studying turbulent boundary layers. Details of the sub-layer structure of a turbulent boundary layer were first obtained experimentally, especially from flow visualization (Kline et al., 1967, Fig. 2.3). Ching et al. (1995a) used laser Doppler velocimetry (LDV) to characterize the turbulence intensities in three orthogonal directions, and obtained the correlation coefficients between two orthogonal turbulence intensities and the Reynolds stress anisotropy tensors. Recently, in addition to the hot-wire/hot-film sensors and laser Doppler anemometry/velocimetry, particle-tracking velocimetry (PTV) and particle image velocimetry (PIV) can provide a more complete field of measurements (i.e. 2D and 3D flow fields). The main drawback of experimental techniques is the inability to measure all required turbulent data, especially the pressure, at an instant of time (Rogallo and Moin, 1984). Although experimental techniques can be used at much higher Reynolds numbers than numerical simulations, model design and cost often become a major consideration.

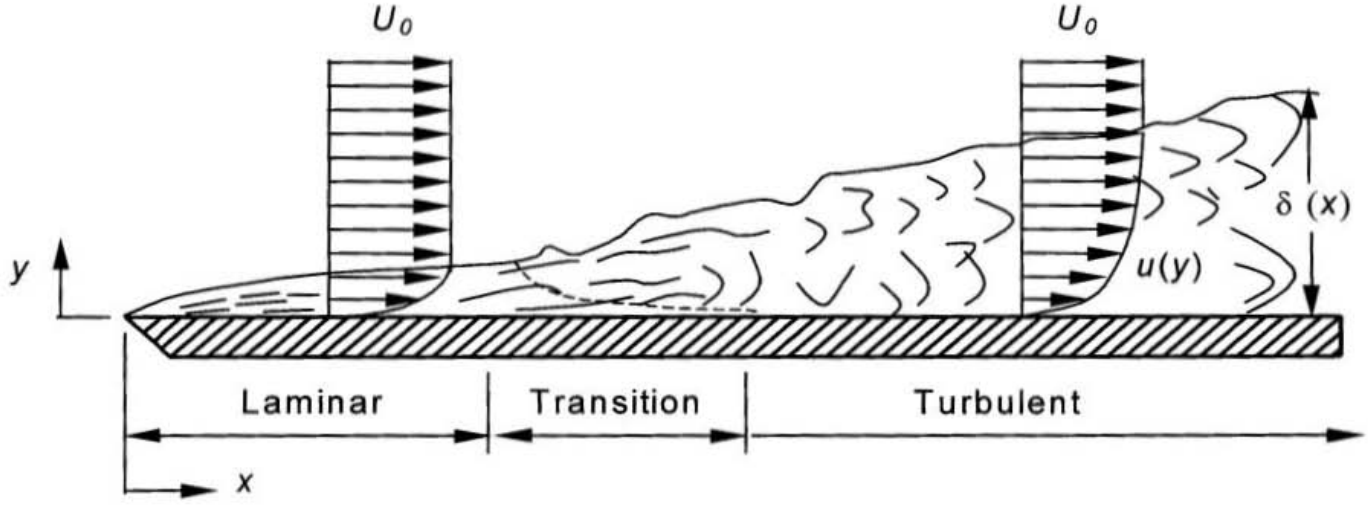

Fig. 2.1 Development of a boundary layer on a flat plate.

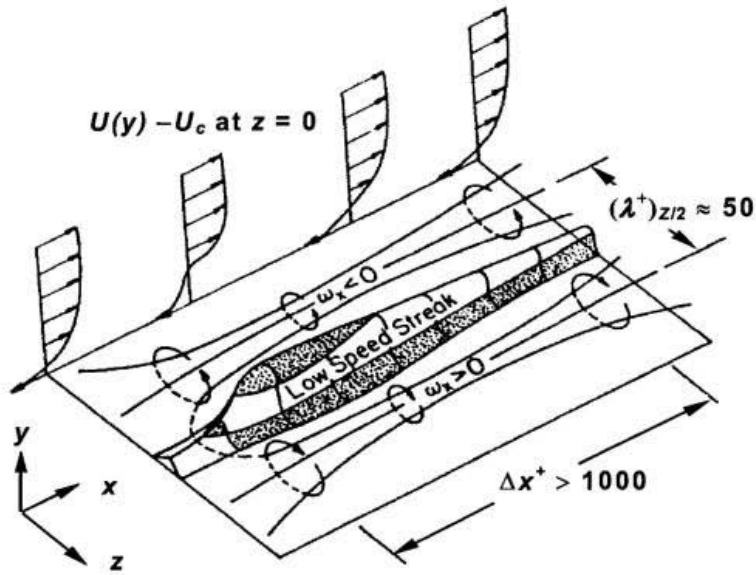

Fig. 2.2 Model of counter rotating streamwise vortices together with the resulting low-speed streak (Reproduced from Blackwelder and Eckelmann, 1979).

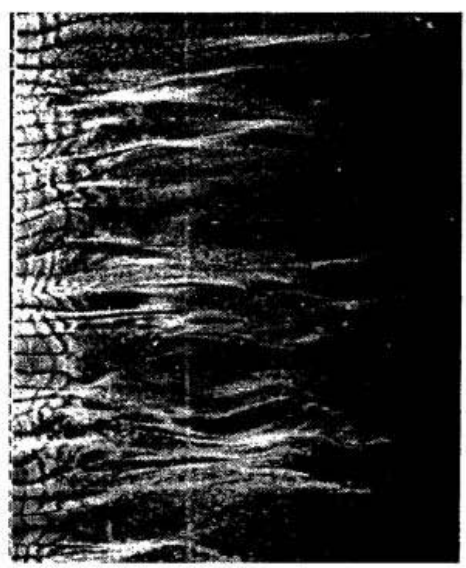

Fig. 2.3 Low- and high-speed streaks in the viscous sublayer ($y^+ = 2.7$). Flow direction is from left to right. (Reproduced from Kline et al., 1967).

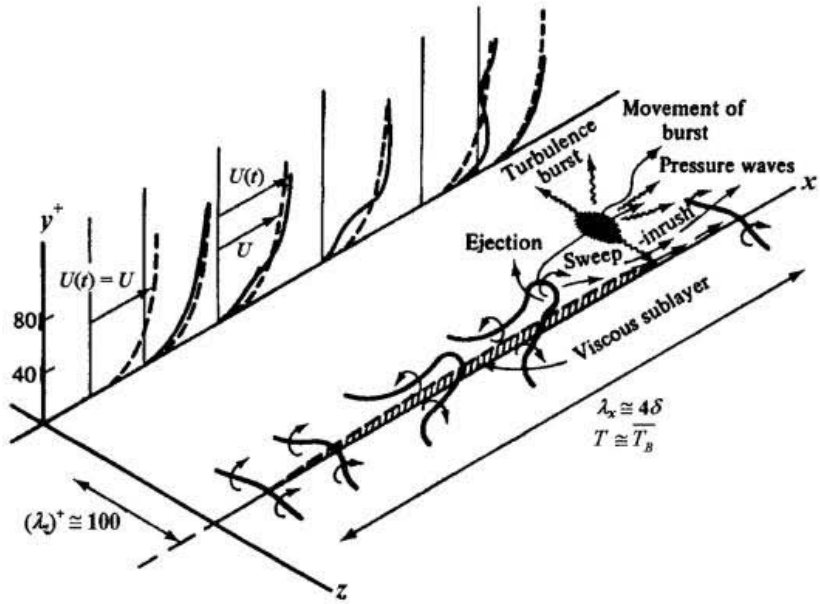

Fig. 2.4 Conceptual model of a cycle of the bursting process in the near-wall region (Reproduced from Hinze, 1975).

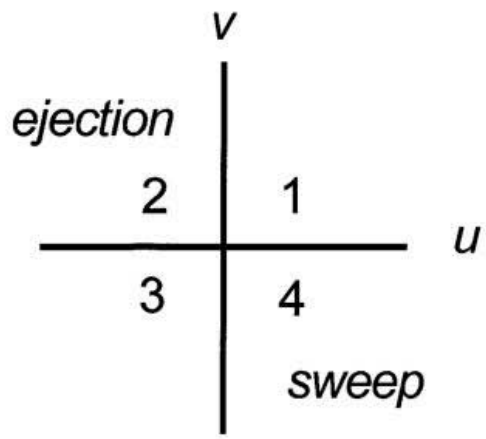

Fig. 2.5 Quadrants of the instantaneous *uv*-plane (Reproduced from Robinson, 1991)

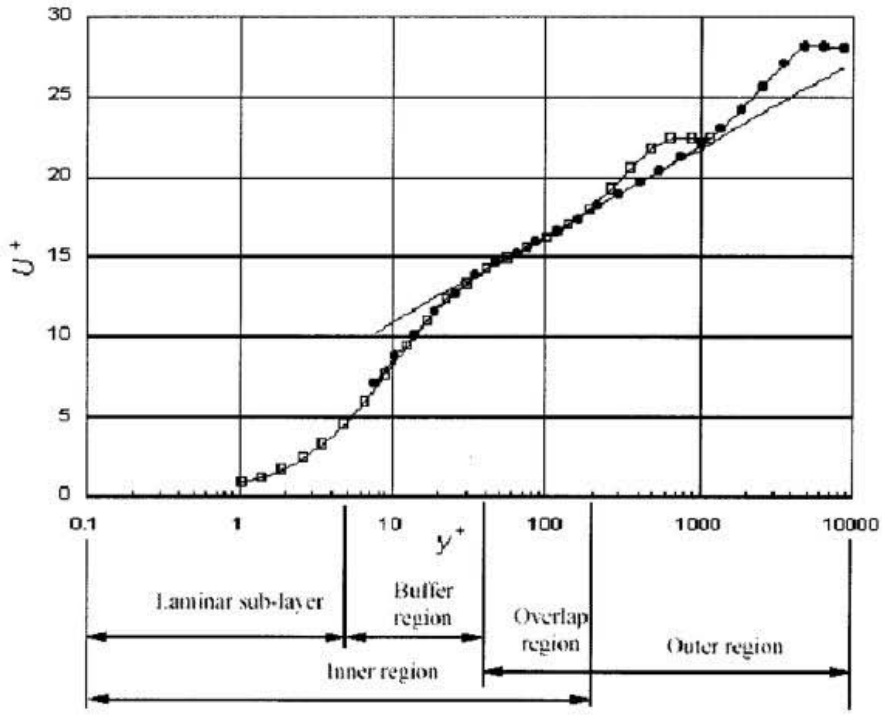

Fig. 2.6 A typical plot of mean velocity distribution in a turbulent boundary layer over a smooth-wall under zero pressure gradient. Data from DeGraff and Eaton (2000): □, $R_\theta = 1430$; •, $R_\theta = 13000$. ——, $U^+ = (1/0.425)ln(y^+) + 5.50$.

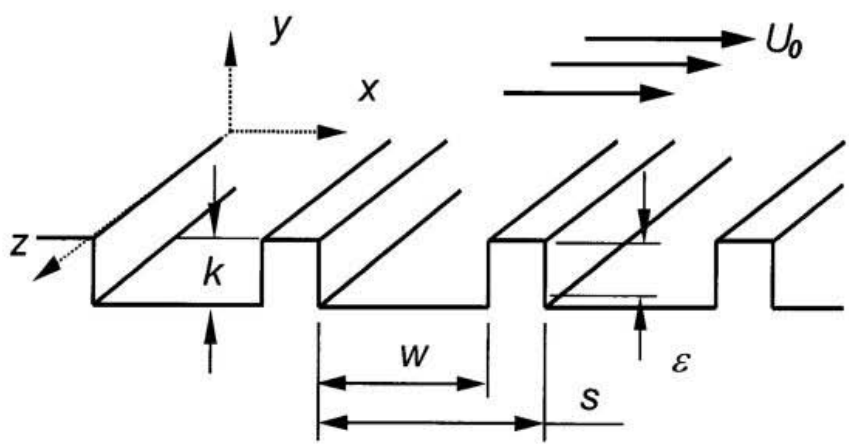

Fig. 2.7 *k*-type roughness (Reproduced from Perry et. al., 1969).

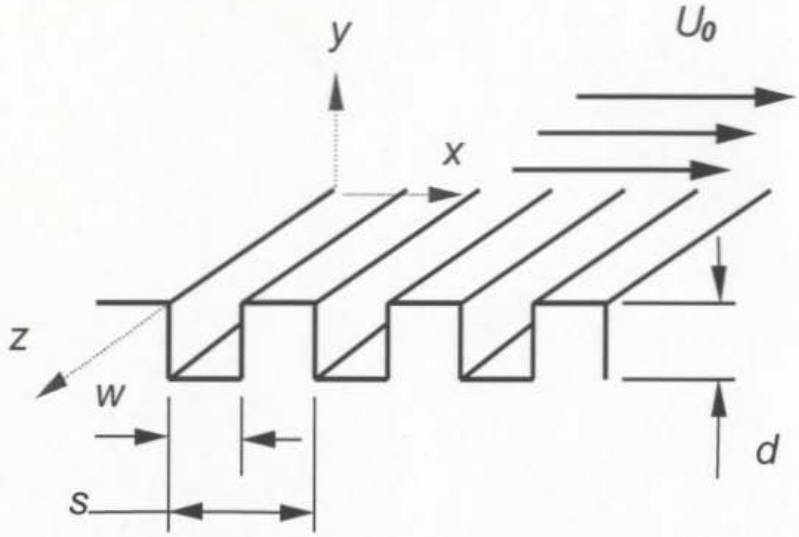

Fig. 2.8 *d*-type roughness (Reproduced from Antonia, 1994).

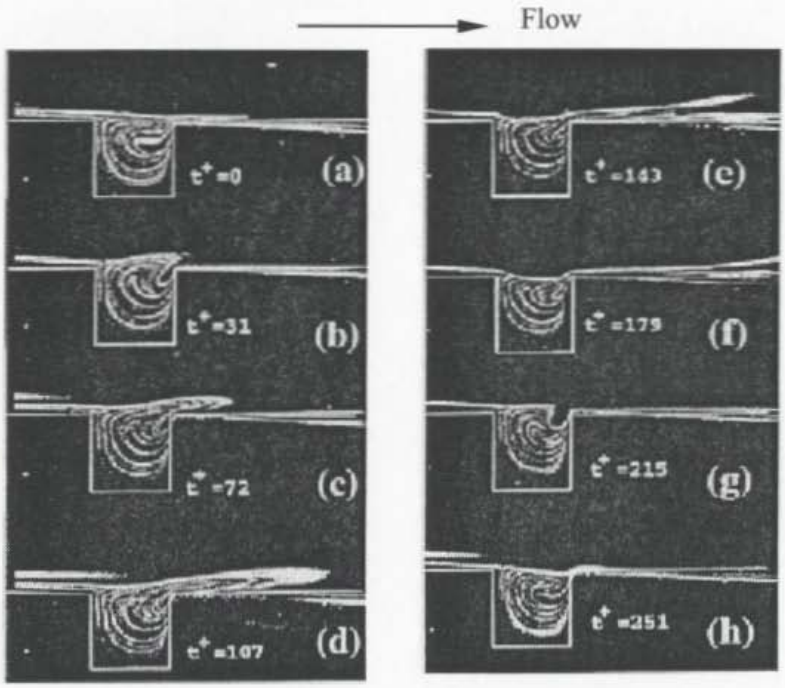

Fig. 2.9 A time sequence of fluid ejection from a square groove (Reproduced from Elavarasan et al., 1996)

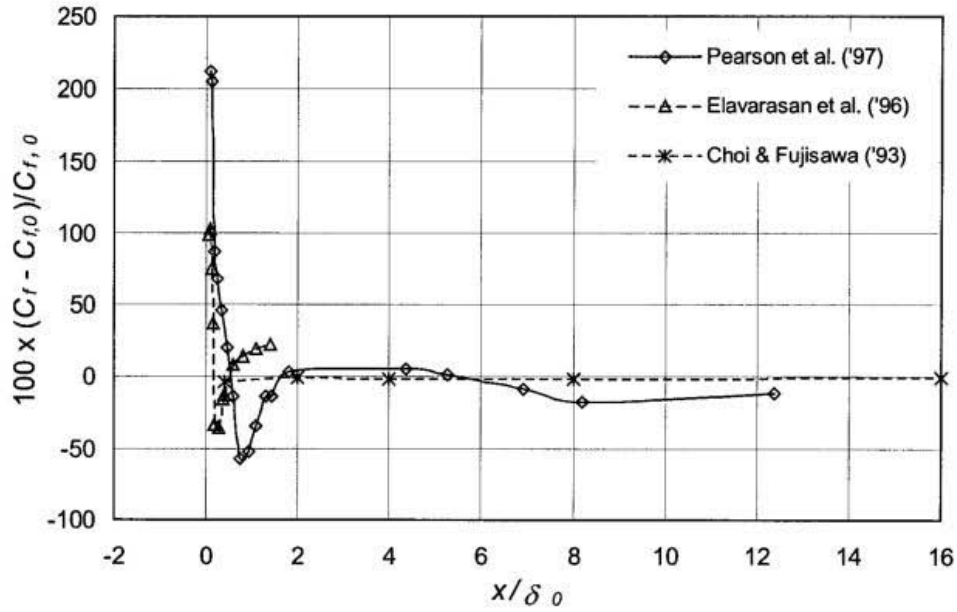

Fig. 2.10 Skin friction distribution of a turbulent boundary layer on the flat-plate with a single transverse square groove.

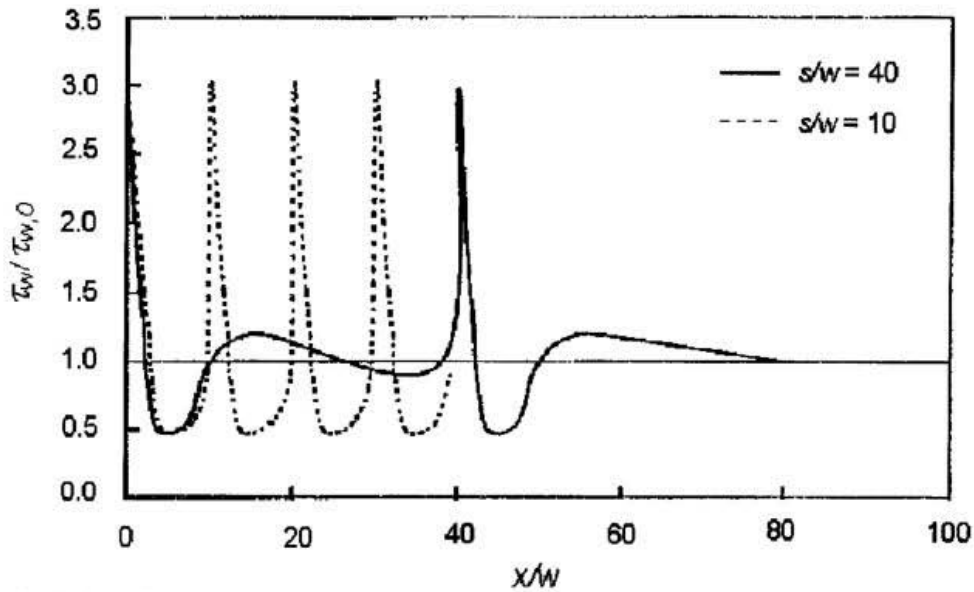

Fig. 2.11 Schematic diagram of wall shear stress distribution for $s/w = 40$ and 10. (Reproduced from Ching and Parsons, 1999).

Chapter 3

Experimental Facility, Data Reduction Procedures, and Experimental Uncertainties

A description of the wind tunnel and test plate configuration is presented in this chapter. The instrumentation, including the Preston tube arrangement for the wall shear stress measurements and the data acquisition system is described. Details of the data reduction procedures for the velocity, wall shear stress and turbulent bursting phenomenon are also described. The turbulence quantities were obtained from hot-wire anemometry using single- and X-wire sensors. The hot-wire calibration techniques for both sensors are presented, followed by techniques to estimate wall shear stress (τ_w) and the growth of the internal layer (d_i). The methodology for estimating the sweep and ejection events and the bursting frequency are described briefly. Finally, this chapter is concluded by a presentation of the experimental uncertainties.

3.1 Experimental Facility

3.1.1 Wind Tunnel and Hot Wire Anemometry

The experiments were performed in an open circuit low speed wind tunnel at Memorial University of Newfoundland. The wind tunnel has a 0.91m × 0.91m test section and is over 20m long, allowing investigation of relatively thick boundary layers (Figs. 3.1.1a and 3.1.1b). This alleviates to some extent the spatial resolution problems of hot-wire anemometry. A centrifugal blower driven by a 19 kW motor is used in the wind tunnel. The air passes through a screened diffuser and a large settling chamber with three single-piece precision screens. The air is accelerated into the test section through a 5:1 contraction. The velocity in the test section is changed using motorized variable angle inlet vanes on the blower. The maximum freestream velocity that can be achieved is approximately 15m/s. The freestream turbulence intensity is no larger than 0.5% at all velocities. The roof of the test section may be adjusted to compensate for boundary layer growth along the test section walls. A false floor/flat plate with a transverse groove machined across the entire span was installed in the test section and was used as the test surface. The false floor/flat plate was fabricated in such a manner to allow the size and shape of the groove to be changed conveniently.

Experiments were performed at two freestream velocities of 2.0m/s and 5.5m/s corresponding to Reynolds numbers, based on the momentum thickness just upstream of the groove, of R_θ = 1000 and 3000, respectively. At each freestream velocity, measurements were made on a smooth-wall flat plate and a flat plate with a single transverse groove. The boundary layer was tripped at the leading edge of the plate using a roughness strip consisting of a piece of 100mm wide sandpaper (series 0811) and a

1.5mm diameter cylindrical rod. Three different shaped (square, semicircular and triangular) grooves, with three different sizes (5, 10 and 20mm) for each shape were used. The depth to width ratio (d/w) was unity for each groove (see Fig. 1.3). Measurements were made at several x-locations downstream of the groove at both R_θ. The flat plate is made of 25mm thick acrylic and is mounted horizontally on the floor of the wind tunnel. The leading edge of each transverse groove was located at a distance of 2.5m from the roughness strip (see Fig. 3.1.1b and c). In terms of the boundary layer thickness just upstream of the grooves (δ_0), the groove sizes are $0.067\delta_0$, $0.133\delta_0$ and $0.267\delta_0$, respectively, at $R_\theta = 1000$. The ratio of the groove depth to the tunnel span (d/L) is 1:45 for the largest groove, which is similar to the studies of Elavarasan et al. (1996) and Pearson et al. (1997), and better than that in the study of Choi and Fujisawa (1993, d/L = 1:12). The ratio of δ_0/L is approximately 1:12 and is smaller than those in the studies of Choi and Fujisawa, Elavarasan et al., and Pearson et al., where δ_0/L is approximately 1:5, 1:6, and 1:8, respectively. Hence, the boundary layer in the present study can be considered to be two-dimensional at the centerline, where all measurements were made.

The turbulence measurements were obtained using single and X-wire hot-wire anemometry. A DANTEC 55P05 single-wire boundary layer type probe connected to a DANTEC 55M01 standard bridge was used for the boundary layer measurements. The sensor is a 5μm diameter (~ 0.03 wall unit) Platinum-plated tungsten (Pt-plated tungsten) wire with an effective (active) length (l_e) of 1.25mm. In terms of wall units (ν/u_τ), the wire length is approximately 8 and 18 wall units, respectively, at R_θ = 1000 and 3000. The ends of the wire are copper and gold plated to a diameter of approximately 30μm.

For the X-wire measurements, an X-wire from Auspex Corporation was used. The distance between the two wires is approximately 0.5mm, corresponding to approximately 3 wall units. This wire distance is considered to be large enough to avoid thermal wake interference between wires, based on the observation of Zhu and Antonia (1995). The wires were operated at an overheat ratio of 1.5. The frequency response of the wires was about 30 kHz as determined from a standard square-wave test.

The hot-wire probe is traversed in the wall-normal direction using a specially designed traversing mechanism with a Mitutoyo height gauge. The traverse mechanism is installed on rails mounted on the roof of the tunnel to move it in the streamwise direction. The traverse mechanism has a maximum span of approximately 46cm and a minimum linear division of 0.01mm. The probe (wire-sensor) can be brought to within approximately 0.05mm from the wall. The distance of the wire-sensor from the wall was determined using a reflection method. A theodolite was used to measure the angle between the sensor and its reflection on the wall. The distance from the wall is calculated from this angle and the distance of the theodolite to the probe. In the wall-region, the uncertainty of the probe distance from the wall is estimated to be no worse than 6.3 and 14.9 percent at the low and high R_θ, respectively.

3.1.2 Preston Tube

A Preston tube was used to measure the wall shear stress for the smooth-wall case. The tube is placed on the test surface, parallel to the free-stream velocity (Fig. 3.1.2). Static pressure (p_L) is obtained using the static pressure tap (hole) of a Pitot-static tube located 150mm above the wall. The opening of the Preston tube is located at the same streamwise location as the static pressure tap. The Preston tube is attached to the

stem of the Pitot-static tube. The differential pressure ($\Delta p = p_H - p_L$), where p_H is the total pressure from the Preston tube, is measured using a micro-manometer (FURNESS FCO12) with accuracy ± 0.01 Pa.

3.1.3 Data Acquisition

A schematic of the data acquisition system is shown in Fig. 3.1.3. The hot-wire signals are passed through a signal conditioning unit (SCU) before being sampled by the analog to digital (A/D) converter. The signals are digitized using a 16 channel 12 bit Keithley 570 System A/D converter, interfaced to a Pentium personal computer. For the turbulent measurements, the hot-wire was operated for 10 seconds at sampling rates of 4 kHz and 6 kHz for R_θ= 1000 and 3000, respectively. For the hot-wire calibrations, the velocity is measured using a 8360-M-GB VelociCalc® Plus TSI air velocity meter, which has resolution of 0.01 m/s and accuracy of 3 percent (TSI Incorporated, 1998). An HP 5420b digital spectrum analyzer and an oscilloscope were used to monitor the hot-wire signals on-line. The analyzer consists of three parts: a 54470B type digital filter, a 54410A type A/D converter, and a display unit. The A/D converter can handle an analog input signal up to 25.6 kHz in frequency and ± 10 VDC peak in amplitude.

3.2 Data Reduction Procedures

3.2.1 Hot Wire Calibrations

Proper hot-wire calibrations are important for accurate velocity measurements using hot-wire anemometry. The calibrations are performed both before and after the measurements to ensure that the results obtained are valid. The velocity for the hot-wire

calibration is measured using a 8360-M-GB VelociCalc® Plus TSI air velocity meter, hereafter referred to as the 'TSI-instrument'. The 'TSI-instrument' was periodically calibrated against the Pitot-tube to ensure that the 'TSI-instrument' was working well. This is important to make sure that the hot-wire calibrations were stable. The analog output of the hot-wire anemometer is directly sampled into a personal computer using an A/D converter. The output of the hot-wire anemometer is also connected to a spectrum analyzer and an oscilloscope to check the signal-to-noise ratio. The measurements are taken only if there is no significant noise in the signal. Data were sampled at a frequency of 20 Hz for 60 seconds and were time-averaged to obtain mean values for each point. For each calibration curve, ten to seventeen data points are used.

A third order polynomial is employed for the functional relationship between the hot-wire signal (Volts) and the velocity, U. This can be expressed as

$$U(E) = c_0 + c_1 E + c_2 E^2 + c_3 E^3, \tag{3.1}$$

where U is obtained from the 'TSI-instrument', while E is the anemometer output. The constants c_0, c_1, c_2, and c_3 are obtained by a least-squares curve fit to the data. The calibration procedure for an X-wire is more involved than that of a single-normal (SN) wire, where both a yaw and velocity calibration were performed using the 'effective angle method' of Browne et al. (1989). Each sensor (wire) is connected to an anemometer unit, and the outputs from the two anemometers are recorded simultaneously along with the velocity recorded from the 'TSI-instrument'. A more complete description of the calibration of the single-normal (SN) and X-wires, including the data reduction program is presented in Appendix A.

3.2.2 Wall Shear Stress (τ_w), Friction Velocity (u_τ) and Skin Friction Coefficient (C_f)

An accurate estimation of the wall shear stress is necessary to predict the skin friction drag associated with boundary layers. The wall shear stress (τ_w) is estimated in four different ways: from the Clauser-chart (log-law) technique, a power-law approximation of the velocity profile, slope of mean velocity profile at the wall, and from Preston tube measurements. The relation between the wall shear stress (τ_w), and the friction velocity (u_τ) can be expressed as:

$$\tau_w = \rho (u_\tau)^2. \tag{3.2}$$

The skin friction coefficient (C_f) is defined as:

$$C_f = \frac{\tau_w}{0.5\rho U_0^2}. \tag{3.3}$$

a) Clauser-chart (log-law) technique

The Clauser-chart (log-law) technique assumes a universal mean velocity profile in the overlap region. The Clauser-chart technique is only appropriate if the Reynolds number is sufficiently high ($R_\theta \geq 1500$) for a log-law region to exist. At low R_θ, the existence of the log region is questionable (Ching et al., 1995a). The basic equation for the log-law technique is expressed as:

$$\frac{U}{u_\tau} = \frac{1}{\kappa}\ln\left(\frac{u_\tau y}{\nu}\right) + B. \tag{3.4}$$

Eq. (3.4) is linear when U/u_τ is plotted as a function of $\ln(yu_\tau/\nu)$. The u_τ is then determined using a trial and error method so that the left-hand side term in Eq. (3.4) collapses well with the measured data in the overlap region. In the current study, $\kappa = 0.41$ and $B = 4.9$ at $R_\theta = 1000$ and $\kappa = 0.43$ and $B = 5.5$ at $R_\theta = 3000$ are adopted. The constants κ and B are obtained from the best fit to the experimental data, and there is no formal basis to obtain unique values for κ and B. In the study of DeGraaff and Eaton (2000) over a wide range of Reynolds number ($R_\theta = 1430$ to 31,000), it was found that κ varies from 0.39 to 0.45, while B remains flexible so that the error between the data and the log-law is minimized.

b) Power-law technique

An advantage of using the power-law technique to estimate u_τ at low R_θ turbulent boundary layers was reported by Djenidi et al. (1997). Following Barenblatt's (1993) arguments of incomplete similarity, Ching et al. (1995a) showed that u_τ can be expressed as:

$$u_\tau = U_0 \left\{ \frac{1}{\exp(3/2\alpha)} \left(\frac{\exp(3/2\alpha)}{C} \right)^{1/(1+\alpha)} \right\}, \tag{3.5}$$

where α and C are calculated with the following equations:

$$\alpha = \frac{3}{2\ln R_\delta}, \tag{3.6}$$

and

$$C = \frac{1}{\sqrt{3}} \ln R_\delta + \frac{5}{2}. \tag{3.7}$$

Djenidi et al. (1997) showed that u_τ determined from Eq. (3.5) was within ± 0.57 percent to that obtained from Preston tube measurements for $R_\theta = 940$. At higher R_θ ($R_\theta \geq 3000$), on the other hand, the power-law fit in the overlap region is poor, and it is difficult to obtain a good fit to the experimental data using the power-law approximation.

c) Slope of U at the wall

The wall shear stress can also be calculated from the slope of mean velocity (U) at the wall:

$$\tau_w = \mu \left(\frac{\partial U}{\partial y} \right)_{y=0}. \tag{3.8}$$

This technique needs accurate data very close to the wall i.e. $y^+ \leq 3.0$. Djenidi and Antonia (1993), using LDA, showed that u_τ can be determined using this technique to an accuracy of order $\pm$ 3 percent at low Reynolds numbers ($R_\theta \leq 1320$). Due to the effect of heat conduction from the wire to the wall, measurements in this region are very difficult with hot-wire anemometry, especially at high R_θ, where the linear sub-layer is very thin. At the lower R_θ, at least four to five data points can be obtained in the range $1 \leq y^+ \leq 5$ using a single-normal hot-wire. At the higher R_θ, however, only about three data points fall on the linear line $U^+ = y^+$ in the layer, and the data in the range $y^+ \leq 2.5$ show a spurious increase due to the wall conduction effect. A correction can be made for the

effect of wall conduction to obtain more data points in the region $y^+ \leq 5.0$ to allow for a more accurate estimate of u_τ.

The effect of wall conduction on hot-wire signals in the proximity of the wall have been studied, and methods for correcting the signal have been proposed (Wills, 1962; Bhatia et al., 1982; Azad and Burhanuddin, 1983; Krishnamoorthy et al., 1985; Janke, 1987). Recently, Lange et al. (1999) and Durst et al. (2001, 2002) proposed a simpler scheme for the correction factors for the hot-wire signal in the near-wall region, and this method is used in this thesis. The correction factor (C_u) is defined as the ratio of the correct local velocity (U_c) to the measured velocity (U_{meas}):

$$C_u = \frac{U_c}{U_{meas}}, \tag{3.9}$$

and is expressed in the exponential form as:

$$C_u = 1.0 - exp(-Ay^{+D}), \tag{3.10}$$

where A and D are experimental constants determined from a fit to the data. Figure 3.2.1 shows the values of C_u in the near-wall region for the present experiments, together with the fit to the experimental data. Beyond $y^+ = 4$, C_u is practically equal to unity. The nondimensional uncorrected data of mean velocity on the smooth-wall flate plate is shown in Fig. 3.2.2, where u_τ was obtained from the log-law technique. Estimation of u_τ using the log-law technique for the smooth-wall turbulent boundary layer is accurate when the Reynolds number is sufficiently high ($R_\theta \geq 1500$) that the overlap region extends one decade or more in the wall-normal direction.

When the near-wall mean velocity data is corrected for the wall conduction effect, approximately six data points can be obtained in the range $y^+ \leq 5$ at both R_θ. The u_τ estimated from the mean velocity gradient at the wall is within ± 4 percent of the value obtained from the log-law technique for the smooth-wall case. The distributions of U^+ in the near-wall region before and after correction are shown in Figs. 3.2.3 and 3.2.4. Data from DNS (Spalart, 1988) and the line $U^+ = y^+$ are also shown in the figures for comparison. The present data, after correction, show a very good collapse with the two lines in the region $y^+ \leq 5$. The C_u obtained from this technique is used to correct the mean velocity in the near-wall region for the turbulent boundary layer developing downstream of the transverse grooves. Finally, the corrected mean velocity profiles in the linear sub-layer are used to estimate u_τ for the grooved-wall profiles since the use of the log-law technique may not be appropriate in this case.

d) Preston tube technique

A Preston tube was also used to determine the wall shear stress for the smooth-wall case to corroborate the other techniques. This method was introduced by Preston (1954), who suggested a non-dimensional relationship between the differential pressure at the wall (Δp) and the wall shear stress (τ_w)

$$\frac{\Delta p}{\rho}\frac{d^2}{\nu^2} = F\left[\frac{d^2\tau_w}{\rho\nu^2}\right], \tag{3.11}$$

where Δp is the pressure difference between the total pressure at the wall (which is sensed by the Preston tube) and the static pressure (which is sensed by the Pitot-static

tube). Patel (1965) proposed three relationships for F in Eq. (3.11) that are valid in three Reynolds number ranges:

$$\text{A) } y^* = 0.50x^* + 0.037, \quad y^* < 1.5, \text{ and } u_\tau d/2\nu < 5.6, \tag{3.12a}$$

$$\text{B) } y^* = 0.8287 - 0.1381x^* + 0.1437x^{*2} - 0.0060x^{*3}, \quad 1.5 < y^* < 3.5 \text{ and } 5.6 < u_\tau d/2\nu < 55, \tag{3.12b}$$

$$\text{C) } x^* = y^* + 2\log_{10}(1.95\,y^* + 4.10), \quad 3.5 < y^* < 5.3 \text{ and } 55 < u_\tau d/2\nu < 800, \tag{3.12c}$$

where $x^* = \log_{10}\left(\frac{\Delta p d^2}{4\rho\nu^2}\right)$ and $y^* = \log_{10}\left(\frac{\tau_w d^2}{4\rho\nu^2}\right)$, respectively. Although there is a drawback of using Patel's calibration since it is in an implicit form Eq. (3.12c), this is the most frequently used compared to the other available calibration equations.

Bechert (1995), proposed a more general Preston tube calibration formula

$$\tau^+ = [28.44(\Delta p^+)^2 + 6.61 \times 10^{-6}(\Delta p^+)^{3.5}]^{1/4}, \tag{3.13}$$

where τ^+ and Δp^+ are defined as $\tau_w d^2/(\rho\nu^2)$ and $\Delta p d^2/(\rho\nu^2)$, respectively. This formula is in excellent agreement with data obtained by Head and Ram (1971). Bechert's calibration equation is valid within a wide range of Δp^+ ($10^2 < \Delta p^+ < 10^{10}$). At low Δp^+ ($< 10^3$), Eq. (3.13) over predicts wall shear stress (τ_w) by about 6 percent from the experimental data of Head and Ram, while at higher Δp^+ ($> 10^3$) it compares well with the experimental data. Bechert's equation is easier to use since it has only a single expression for a wide range of Δp^+ compared to three for Patel's calibration.

3.2.3 Internal Layer Growth (d_i)

When there is a sudden change in the wall boundary condition, the effect of the step change on the turbulent characteristics propagates outward into the boundary layer. The region within which the effects are significant is usually termed the internal layer (d_i). The thickness of d_i just downstream of a step change is approximately 0.1δ (see, for example, Antonia and Luxton, 1971a), hence it is well within the log/overlap region. For a sudden change from smooth-to-rough surface, Antonia and Luxton found that within the internal layer the turbulence level and turbulence production were increased.

The growth of the internal layer (d_i) due to the presence of the groove in this case is determined using the method of Antonia and Luxton (1971a,b). This is illustrated with reference to Fig. 3.2.5, which shows the U/U_0 profiles downstream of the 20mm square (SQ)-groove at R_θ = 3000. Within the internal layer, the shear stress distribution just downstream of the step change (i.e. downstream of the groove trailing edge in the present study), must vary between the shear stress at the wall and the shear stress at the edge of the internal layer (Antonia and Luxton, 1971a). Based on dimensional arguments, Antonia and Luxton (1971a) suggested that the mean velocity profile (U) must be affected by the gradient of wall shear stress ($d\tau_w/dx$) and the distance from the solid boundary (y). Using simple mathematical manipulations, one can obtain a linear functional relationship between U and $y^{1/2}$ (Antonia and Luxton, 1971a,b). When U/U_0 is plotted against $y^{1/2}$, there is a location indicating a sudden change in the slope of the non-dimensional mean velocity profiles, called a 'knee' point. In the inner and outer regions, the profiles are linear, with the slope in the inner region being much larger than that in the outer region. The intersection between the straight lines representing the inner and outer regions of the mean velocity profiles is used to define the edge of the internal layer in this

thesis. The distribution of the internal layer (d_i) downstream of the 20mm SQ-groove at R_θ = 3000 obtained from this method is also shown in Fig. 3.2.5 (inset). The complete results of the distribution of d_i downstream of the different sized and shaped transverse grooves are presented in chapter 5 and 6.

3.2.4 Sweep and Ejection Events and Burst Detection

Sweep and ejection events, which are parts of the bursting process in wall-bounded turbulent flows, play an important role in the dynamics of the Reynolds stresses, turbulence production, and turbulent kinetic energy dissipation (Coustols and Savill, 1991). The term burst was used by Kim et al. (1971) to describe the ejection from the wall of low-speed fluid embedded in the near-wall region. An ejection is initiated when a low-speed streak lifts slowly from the wall and oscillates in a three-dimensional manner with a final break up.

Several techniques have been employed to detect the frequency of bursts or ejection occurrence in the near-wall region. In the *uv* quadrant-splitting technique (Wallace et al., 1972; Willmarth and Lu, 1972) ejections are defined as $\langle uv \rangle_2$, where subscript 2 represents the second quadrant. The second quadrant ($\langle uv \rangle_2$) is associated with negative streamwise ($-u$) and positive wall-normal ($+v$) velocity fluctuations, and this quadrant contributes the most to the total Reynolds stress ($\langle -uv \rangle$). The second quadrant reflects low-speed fluid moving away from the wall. Blackwelder and Kaplan (1976) used a variable-time interval-averaging (VITA) technique to detect the burst and sweep processes. The detection criterion is based on the large variance in the streamwise velocity fluctuation (u). Chen and Blackwelder (1978) modified the VITA technique proposed by Blackwelder and Kaplan using a slope condition such that ejections will be

detected only if there are accelerations in the streamwise direction. Lu and Willmarth (1973) used the *U*-level technique, later modified by Luchik and Tiederman (1987), to detect ejections in a turbulent boundary layer. Lu and Willmarth (1973) used the streamwise velocity signal (u) at the edge of the sub-layer as the detection criterion. They observed that if u was low and decreasing, an ejection occurred. The *U*-level technique from Lu and Willmarth (1973) and the modified *U*-level (*mu*-level) from Luchik and Tiederman (1987) used u' as the threshold level.

Bogard and Tiederman (1986) evaluated the effectiveness of the above techniques to detect ejection and bursts in a channel flow. The evaluation was made by direct comparison between hot-film probe measurement and flow visualization. It was concluded that the second-quadrant technique was the most reliable to detect the burst and time interval between two consecutive ejections. This particular technique, hence, is used to detect the bursts in the turbulent boundary layer in this thesis.

An ejection is only detected if the $|uv|/u'v'$ signal exceeds a certain threshold level (H), and uv resides in the second-quadrant (Wallace et al., 1972; Willmarth and Lu, 1972). The threshold level (H) is determined using the equation recommended by Comte-Bellot et al. (1978), i. e.:

$$H = \langle -uv \rangle_2 / u'v'. \tag{3.14}$$

The procedure used to calculate the ejection and burst frequencies is summarized as follow:

(1) ejections are detected if $|uv|/u'v' \geq H$;

(2) the time between two consecutive detected ejections (T_e) is calculated;

(3) the duration of each detected ejection is calculated, and the average (T_o) is obtained;

(4) all detected ejections for which $T_e \leq T_o$ are removed;

(5) the maximum T_e (τ_{max}) is calculated by comparing the probability distribution of T_e to the exponential distribution;

(6) the detected ejections with $T_e \leq \tau_{max}$ are grouped into a single burst;

(7) the number of bursts (N_b) within the sampling time (T_s) is calculated to obtain the bursting frequency (f_B) , i.e. $f_B = N_b / T_s$.

Figure 3.2.6 shows a typical streamwise and wall-normal velocity fluctuation and the corresponding Reynolds stress at $y^+ = 14$ obtained from X-wire measurement for a sampling time (T_s) of 10s at a sampling frequency (f_s) of 4 kHz. Only 1/100 of the total samples is shown in the figure for clarity. In Fig. 3.2.7, the contributions of the first, second, third and fourth quadrants of $\langle -uv \rangle$ signal to the Reynolds stress are shown, together with the threshold line (Eq. 3.14). For the second quadrant ($\langle -uv \rangle_2$), it is obvious that there are four significant spikes and one less intense spike higher than the threshold line. After applying the detection criterion (Eq. 3.14), Fig. 3.2.8 is obtained, which shows five detection functions equal to unity. Applying the detection function to the whole domain of the sampling time, one can obtain the time interval between two consecutive ejections (T_e), and then obtain its average ($T_{e,m}$).

The duration of each ejection is calculated by taking the difference between the start and end times of the ejection. The mean ejection duration (T_o) is calculated for the whole sampling period, and it is assumed that all ejections with a period less than T_o are false signals. Figure 3.2.9 shows the histogram of the distribution of time between two

consecutive ejections, T_e, at $y^+ = 14$ for $T_e \geq T_o$. The exponential density function is also shown in the figure for comparison.

According to Bogard and Tiederman (1986), ejections with separation time less than τ_{max} can be grouped into a single burst event, where τ_{max} is determined as follows: The probability distribution of T_e is plotted as shown in Fig. 3.2.10 together with the exponential distribution function (straight line). The average duration of each ejection (T_o) and the average period between ejections ($T_{e,m}$) are used to normalize T_e in the exponential function. The deviation from the exponential function is then chosen as the location of the τ_{max}. From Fig. 3.2.10, it can be seen that the deviation of the probability distribution of T_e from the exponential distribution takes place at $[1- exp(-(T_e - T_o)/(T_{e,m} - T_o)] \approx 0.8$, and the corresponding value of τ_{max} is approximately 0.05s. The complete results of the sweep and ejection processes and the corresponding bursting frequency (f_B) are presented in Chapters 4, 5, and 6 for the smooth- and grooved-walls.

So far only the second quadrant contribution to the Reynolds stress has been described; contributions to the Reynolds stress are also made by the first, third, and fourth quadrants. The first quadrant ($\langle uv \rangle_1$) is associated with both positive streamwise ($+u$) and wall-normal ($+v$) velocity fluctuations, the third quadrant ($\langle uv \rangle_3$) with both negative streamwise ($-u$) and wall-normal ($-v$) velocity fluctuations, while the fourth quadrant ($\langle -uv \rangle_4$), is associated with positive streamwise ($+u$) and negative wall-normal ($-v$) velocity fluctuations. The fourth quadrant is referred to as the sweep by Wallace et al. (1972) and Willmarth and Lu (1972), while the first and third quadrants are referred to as outward interaction and wall-ward interaction. From Fig. 3.2.7, it is clear that the contribution of $\langle -uv \rangle_4$ to the total Reynolds stress is comparable to the contribution of

$\langle -uv \rangle_2$, while the contributions of $\langle uv \rangle_1$ and $\langle uv \rangle_3$ to the total $\langle -uv \rangle$ are much less than those from $\langle -uv \rangle_2$ or $\langle -uv \rangle_4$. Table 3.1 shows relative contributions of $\langle uv \rangle_1$, $\langle -uv \rangle_2$, $\langle uv \rangle_3$, and $\langle -uv \rangle_4$ to the total Reynolds stress ($\langle -uv \rangle$) at a particular x-location at $y^+ = 14$. The two "positive stress producing motions" (Wallace et al., 1972), $\langle -uv \rangle_2$ and $\langle -uv \rangle_4$, contribute more than 100 percent to the total Reynolds stress ($\langle -uv \rangle$), while the other two "negative stress producing motions", $\langle uv \rangle_1$ and $\langle uv \rangle_3$, contribute in the opposite way to the positive stress producing motions to make 100 percent of the total Reynolds stress.

Table 3.1 Relative contributions of $\langle uv \rangle_1$, $\langle -uv \rangle_2$, $\langle uv \rangle_3$, and $\langle -uv \rangle_4$ to the total Reynolds stress ($\langle -uv \rangle$). $R_\theta = 1000$.

Variable	Symbol	Magnitude (m^2/s^2)	Percentage of the total Reynolds stress ($-\langle uv \rangle$)
Total Reynolds stress	$\langle -uv \rangle$	0.004787	100.0
Quadrant 1	$\langle uv \rangle_1$ or q_1	-0.000743	-15.5
Quadrant 2	$\langle -uv \rangle_2$ or q_2	0.003719	77.7
Quadrant 3	$\langle uv \rangle_3$ or q_3	-0.001183	-24.7
Quadrant 4	$\langle -uv \rangle_4$ or q_4	0.002994	62.5

The decomposition of the Reynolds stress into the four quadrants, i.e. $\langle uv \rangle_1$, $\langle -uv \rangle_2$, $\langle uv \rangle_3$, and $\langle -uv \rangle_4$, are written as q_1, q_2, q_3 and q_4, with the corresponding normalized values by inner variable (u_τ) denoted as q_1^+, q_2^+, q_3^+ and q_4^+. Figure 3.2.11 shows the distributions of the stress producing motions across a typical boundary layer at a particular streamwise location, where the individual stress producing motion is normalized by the local friction velocity, u_τ. It can be seen that there are non-negligible contributions from the two negative stress producing motions to the total Reynolds stress across the layer.

3.3 Experimental Uncertainties

All measurement uncertainties are analyzed based on the method outlined by Yavuzkurt (1984), Moffat (1982) and Coleman and Steele (1989). The details of the method and some numerical examples of the experimental uncertainties are presented in Appendix C. The uncertainties are calculated at 95% confidence and presented relative to the local values in Table 3.2.

Table 3.2. Experimental uncertainties

Flow variable	Uncertainty (%)	
	$R_\theta = 1000$	$R_\theta = 3000$
Mean velocity (U): - Outer region	1.7	1.7
- Wall-region	8.7	2.1
Streamwise turbulence intensity (u'):		
- Outer region	1.7	1.7
- Wall-region	8.7	2.1
Wall-normal turbulence intensity (v'):		
- Outer region	7.0	n/a[¶]
- Wall-region	9.8	n/a[¶]
Reynolds stress ($\langle -uv \rangle$)		
- Outer region	10.4	n/a[¶]
- Wall-region	14.6	n/a[¶]
Boundary layer thickness (δ)	0.6	0.3
Wall-distance (y)		
- Outer region	0.2	0.2
- Wall-region	6.3	14.9
Skin friction coefficient (C_f)[*]	11.2	15.4

[¶] No X-wire measurements were taken at $R_\theta = 3000$.
[*] Obtained from the slope of U at the wall.

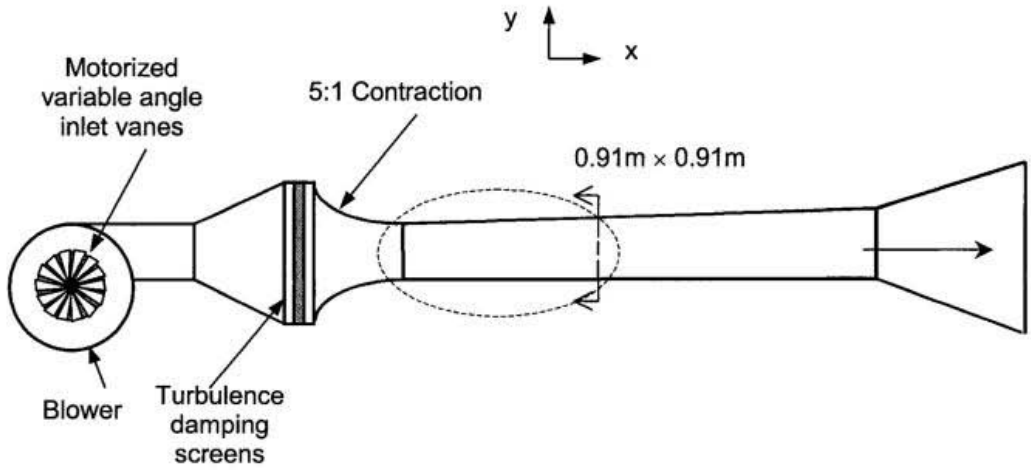

Fig. 3.1.1a Wind tunnel with its components.

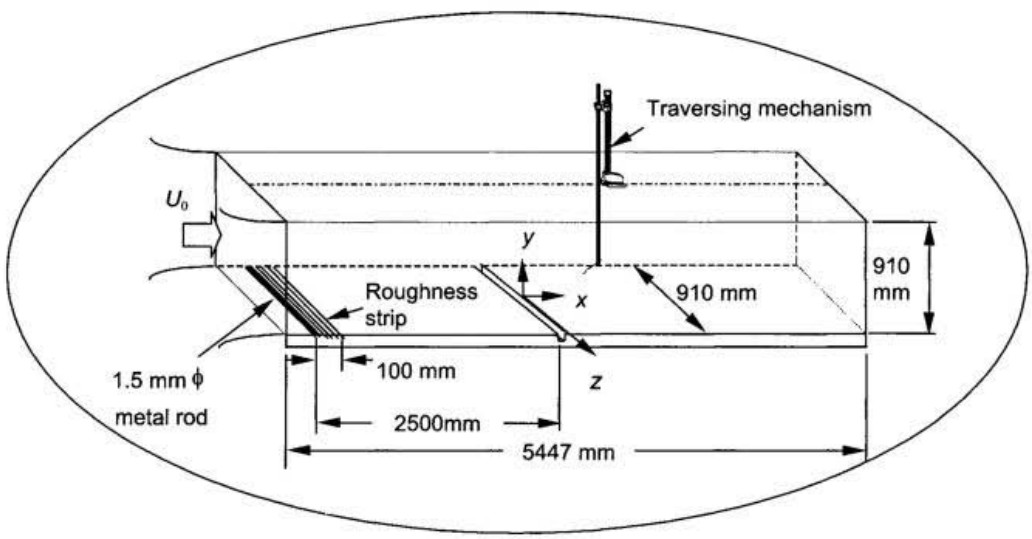

Fig. 3.1.1b Detailed test section.

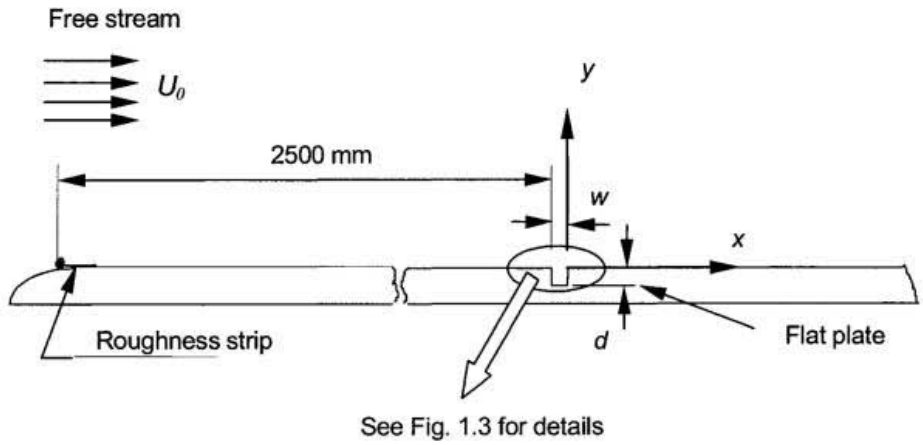

Fig. 3.1.1c A schematic diagram of the test-plate showing a single transverse groove.

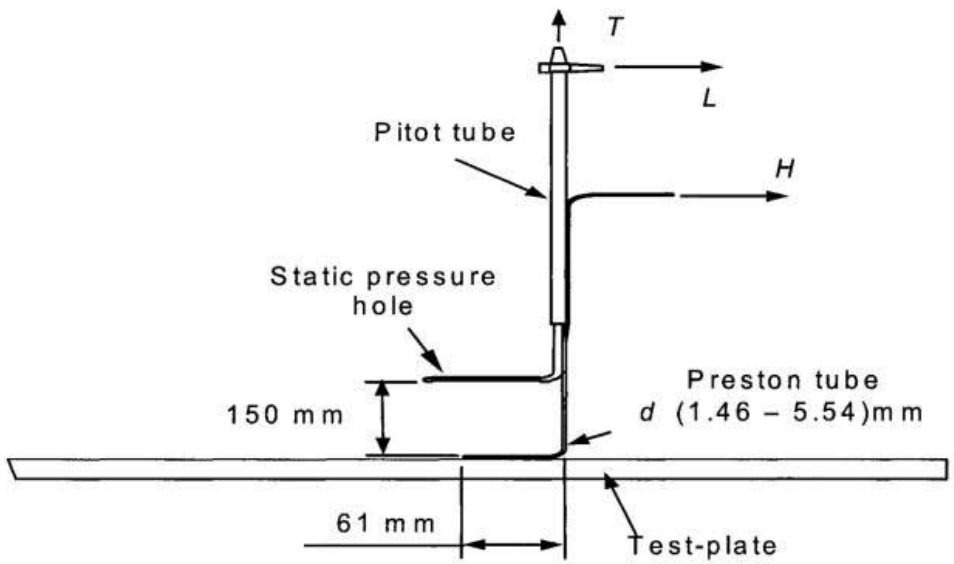

Fig. 3.1.2 Preston tube arrangement. H is the total pressure from Preston tube, L is the static pressure from static hole of the Pitot-static tube, and T is the stagnation pressure from the Pitot-static tube.

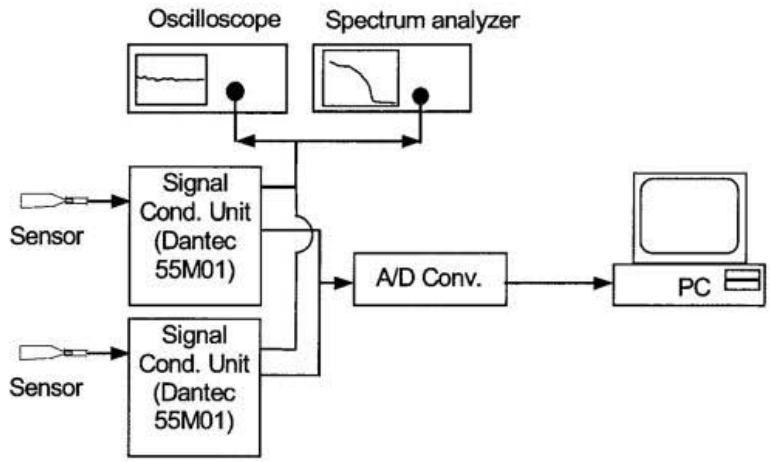

Fig. 3.1.3 Data Acquisition System.

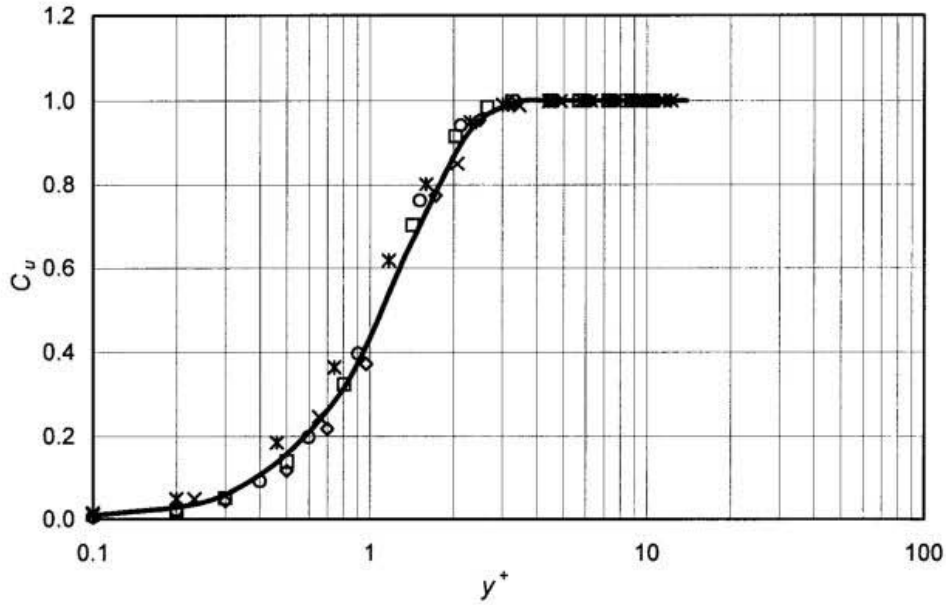

Fig. 3.2.1 Velocity correction coefficient (C_u) due to wall conduction effect in the hot-wire measurements at various R_θ. ○, R_θ = 900; □, = 1000; ◇, = 2500; ×, = 4000; ∗, = 4200. _____, the best fitted line ($C_u = 1 - \exp(-Ay^{+B})$), A = 0.574, B = 1.846.

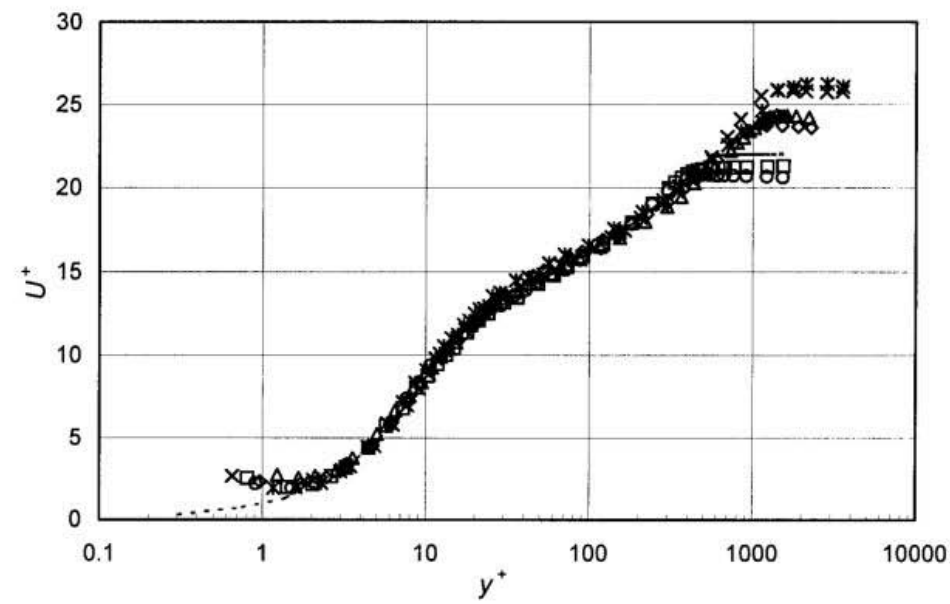

Fig. 3.2.2 Uncorrected mean velocity on the smooth-wall flate plate. ○, R_θ = 900; □, = 1000; ◇, = 2500; Δ, = 3100; ×, = 4000; ∗, = 4200. - - - -, DNS data (Spalart, 1988).

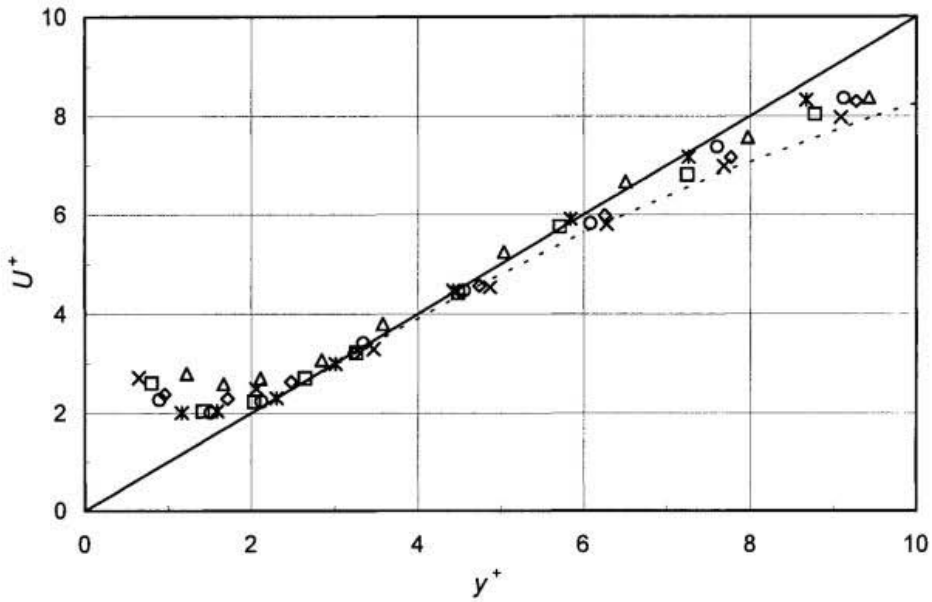

Fig. 3.2.3 Uncorrected near-wall mean velocity profiles. ○, R_θ = 900; □, = 1000; ◇, = 2500; Δ, = 3100; ×, = 4000; ∗, = 4200. _____, $U^+ = y^+$; - - - -, DNS data (Spalart, 1988).

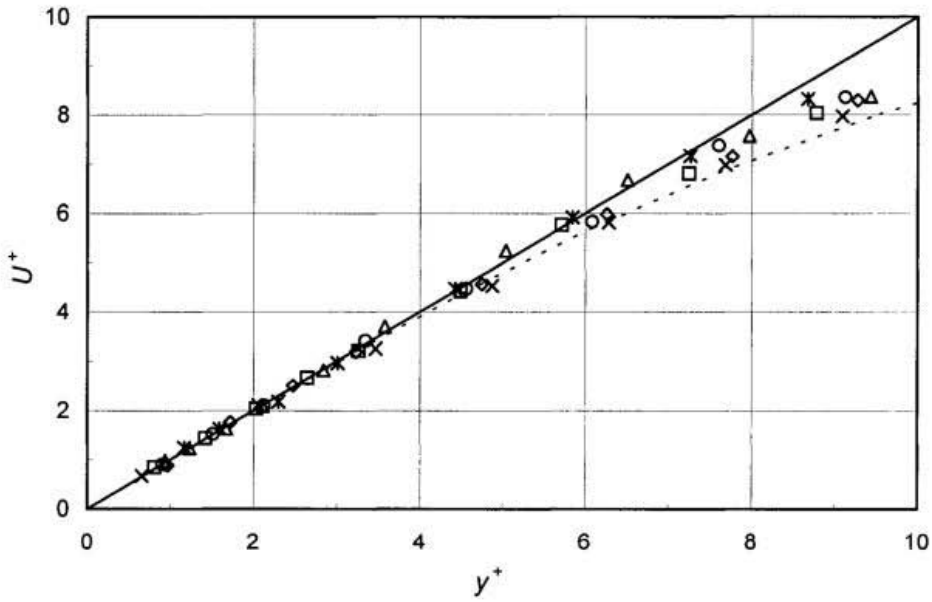

Fig. 3.2.4 Corrected near-wall mean velocity profiles. ○, R_θ = 900; □, = 1000; ◇, = 2500; Δ, = 3100; ×, = 4000; ∗, = 4200. _____, $U^+ = y^+$; - - - -, DNS data (Spalart, 1988).

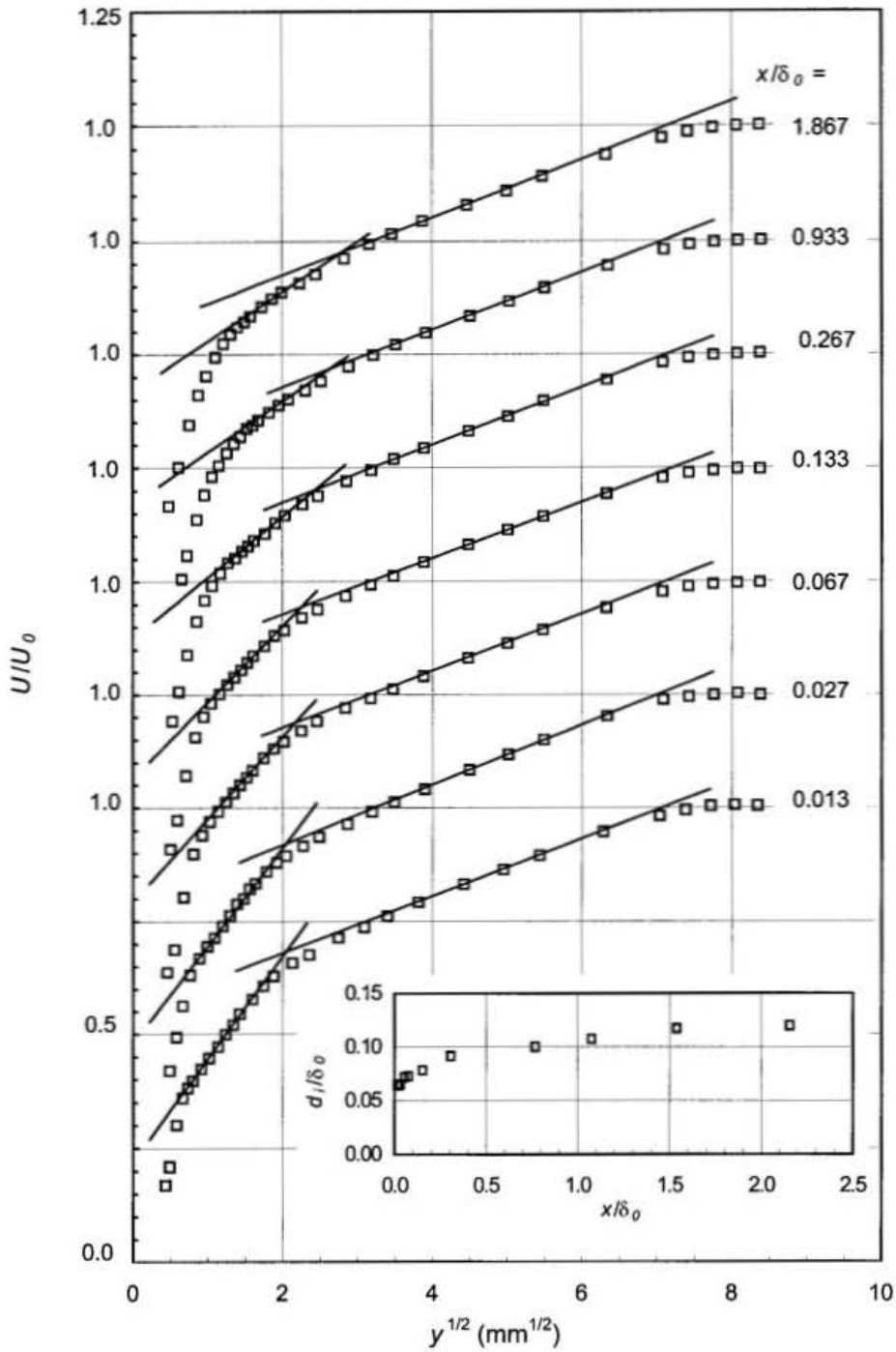

Fig. 3.2.5 Mean velocity profiles plotted as a function of $y^{1/2}$. $R_\theta = 3000$, $d = 20$mm, SQ-groove. Inset: The corresponding internal layer growth downstream of the groove.

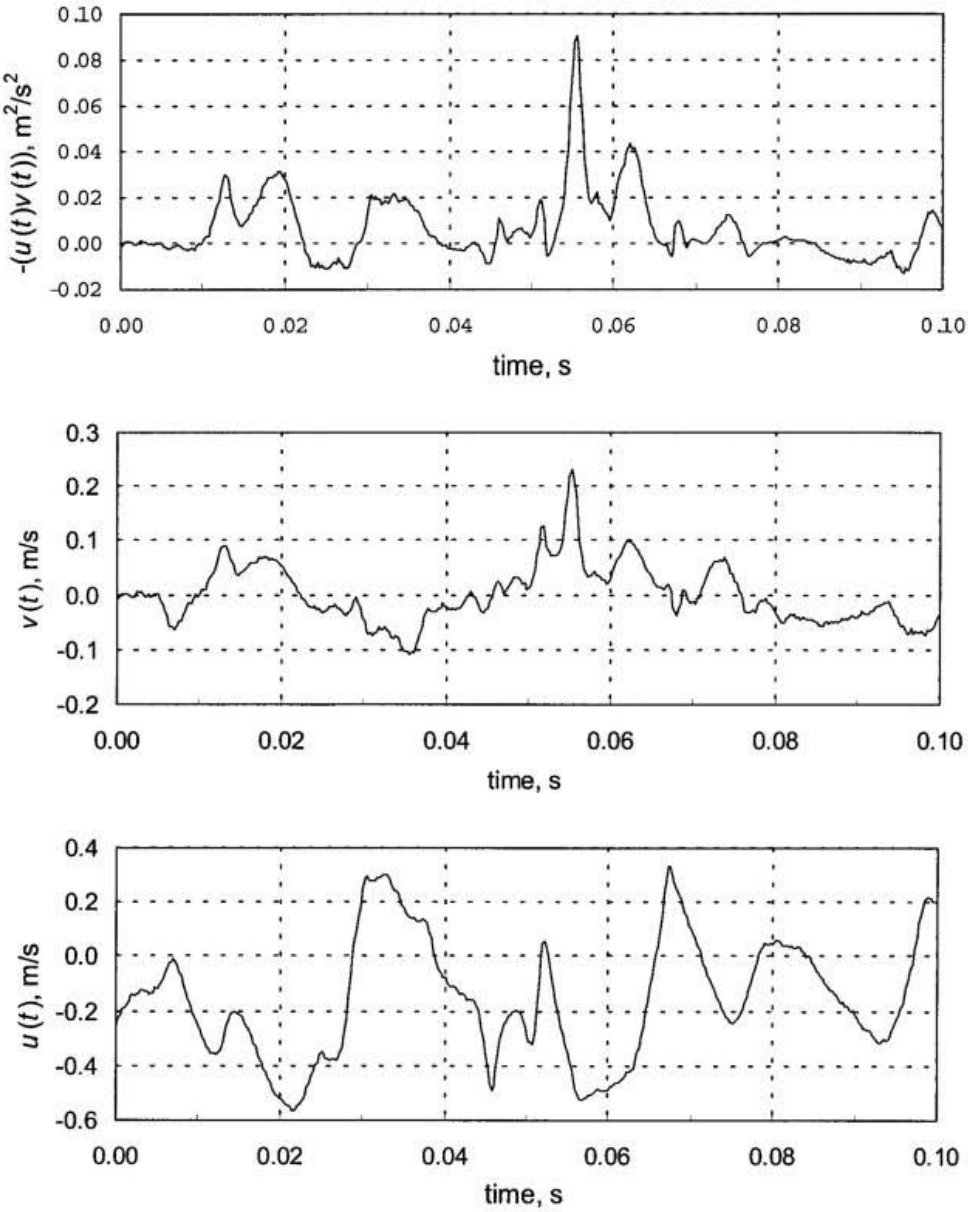

Fig. 3.2.6 Typical streamwise and wall-normal velocity fluctuations and the instantaneous Reynolds stress product of a wall-bounded turbulent flow. Sample time = 10 seconds, $y^+ = 14$.

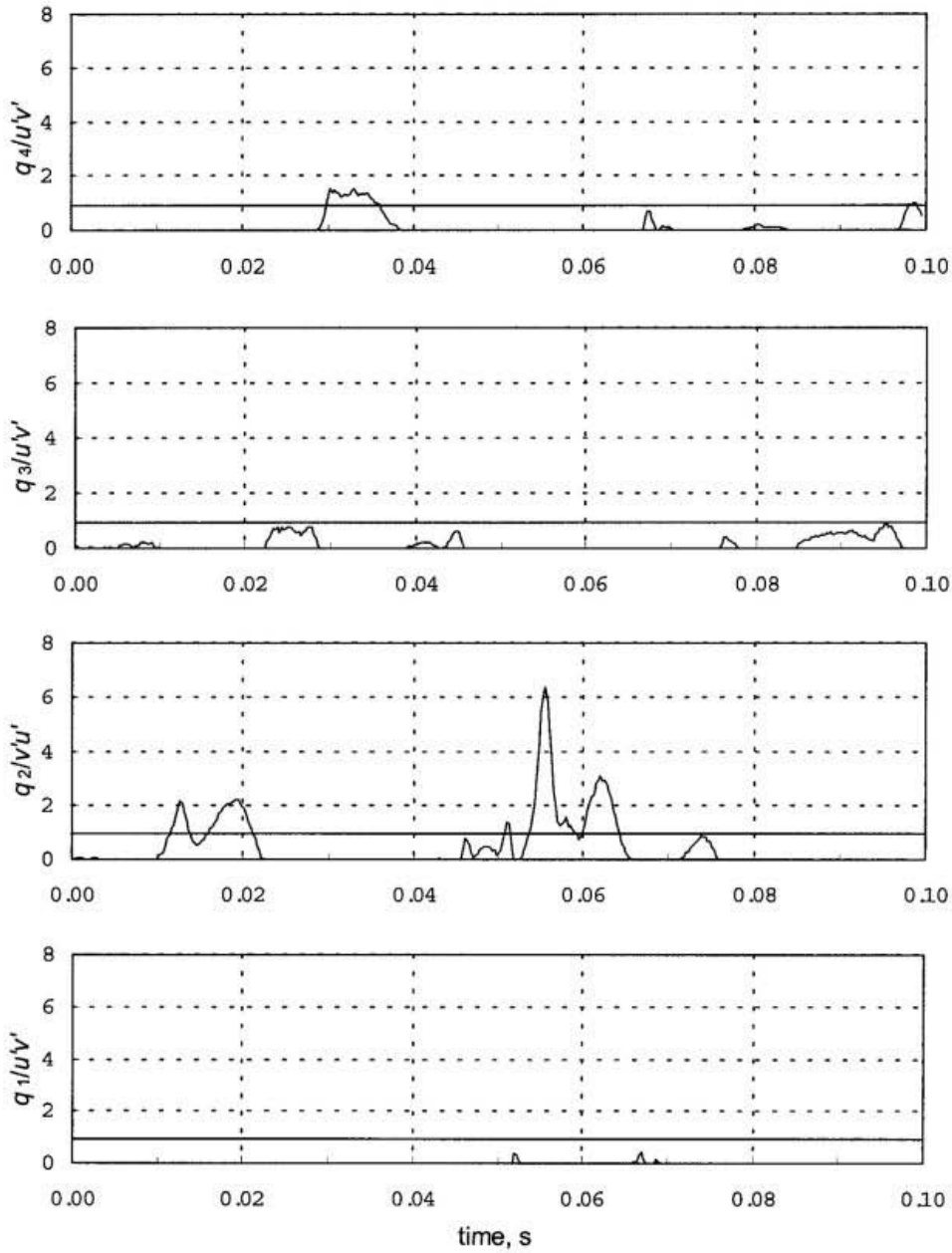

Fig. 3.2.7 Contributions of the first, second, third and fourth quadrant signals to the Reynolds stress. Horizontal lines are the threshold level lines, $H = 0.92$. Sample time = 10 seconds, $y^+ = 14$.

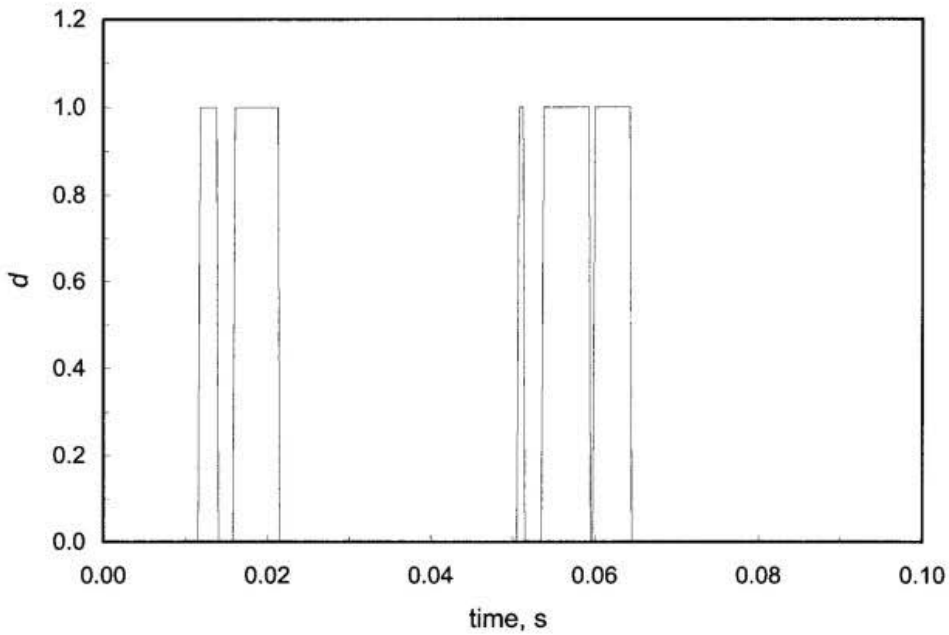

Fig. 3.2.8 Detection function of the signal shown in Fig. 3.2.7, after the threshold level is applied. Sample time = 10 seconds, $y^+ = 14$.

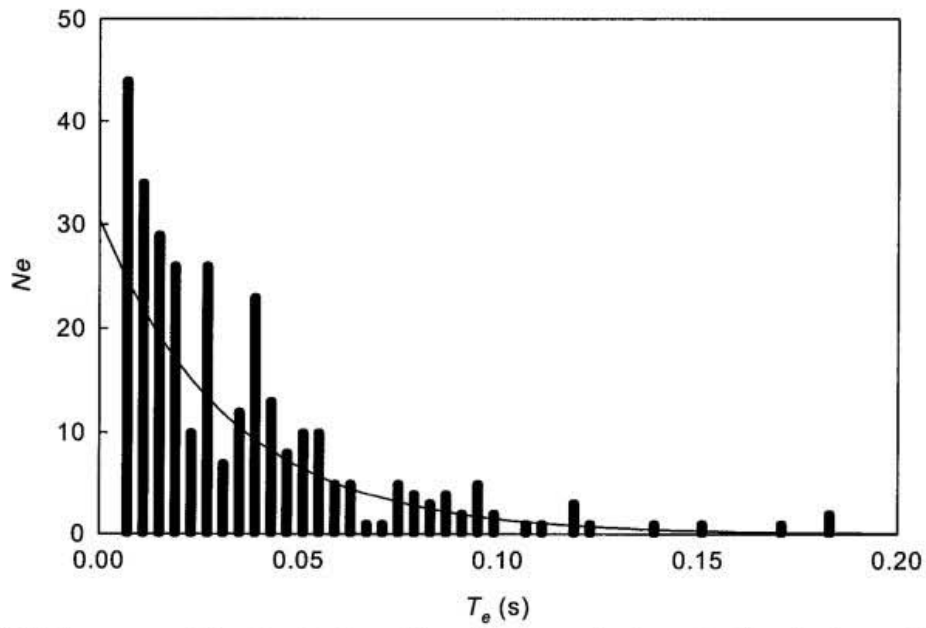

Fig. 3.2.9 Histogram of the distribution of time between ejections, T_e. Sample time = 10 seconds, $y^+ = 14$. Mean $T_e = 0.0282$s, for $T_e \geq T_o$. Solid curve: exponential function.

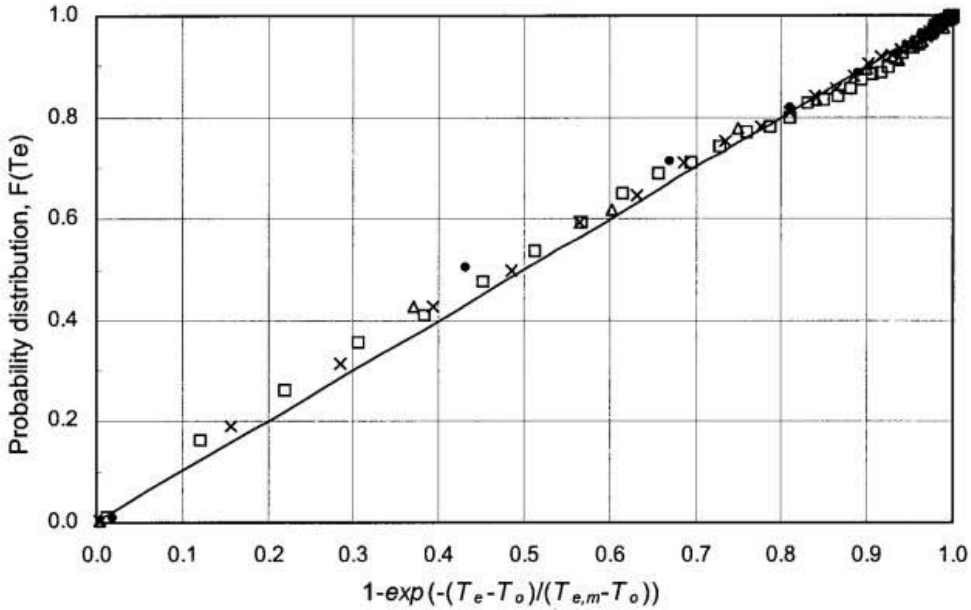

Fig. 3.2.10 Probability distribution of T_e compared to the exponential distribution (solid line) for $T_e \geq T_o$. Sample time = 10 seconds, $y^+ = 14$. SQ-groove data: Δ, d = 5mm; ×, d = 10mm; □, d = 20mm; smooth-wall: •. $T_{e,m}$ = mean of T_e.

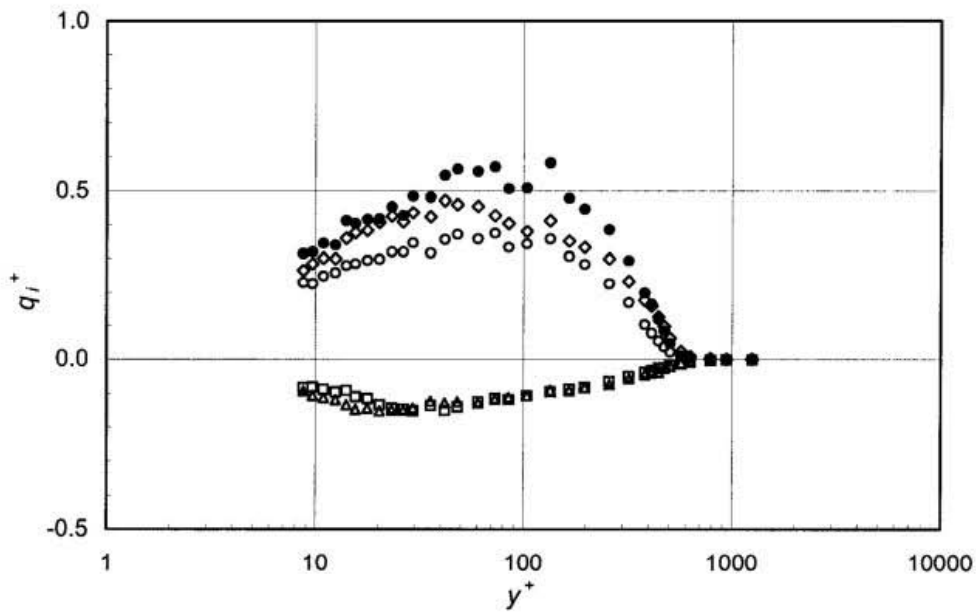

Fig. 3.2.11 Contributions of the stress producing motions ($q_i^+ = q_i/(u_\tau)^2$) across a smooth-wall turbulent boundary layer to the total Reynolds stress ($\langle -uv \rangle$). □, i = 1; ◇, i = 2; Δ, i = 3; ○, i = 4; •, i = total.

Chapter 4

Smooth-Wall Turbulent Boundary Layer Results

The initial set of experiments was performed on a turbulent boundary layer over a smooth-wall. This provides a baseline data set against which the turbulent boundary layer over the different grooves can be compared. The smooth-wall experiments were also intended to provide some basic measurements to validate the experimental techniques by comparing the experimental data with DNS data. One emphasis of the smooth-wall experiments was to examine several different techniques to estimate the wall shear stress (τ_w). The experiments were performed at freestream velocities of 2.0 and 5.5m/s, corresponding to R_θ in the range 1000 to 1900 at the lower velocity, and 3000 to 4200 at the higher velocity. Experimental conditions and flow parameters are provided in Table 4.1. At both R_θ, the static pressure variation along the test section is negligibly small, with $(p - p_0)/0.5\rho(U_0)^2 < 4\%$, where p_0 is the reference static pressure at the location 2500mm downstream of the trip (Fig. 4.1). At $U_0 = 2.0$m/s, δ varies from 75mm at $x/\delta_0 =$

0.013 to 130mm at $x/\delta_0 = 27$, while at $U_0 = 5.5$m/s, it varies from 65mm at $x/\delta_0 = 0.013$ to 105mm at $x/\delta_0 = 27$. The momentum thickness (θ) varies from 7.6mm to 15mm at $U_0 = 2.0$m/s, while at $U_0 = 5.5$m/s, it varies from 7.5mm to 12mm at the same x/δ_0-range. Results are presented for the distribution of the friction velocity (u_τ) and skin friction coefficient (C_f) along the wall. The mean velocity (U), turbulence intensities (u' and v'), Reynolds stress ($\langle -uv \rangle$), turbulent energy spectra, sweep and ejection events, and bursting frequency are also presented. In general, the present smooth-wall results are in good agreement with previous measurements and DNS data.

Table 4.1 Experimental conditions and flow parameters

	U_0 (m/s)	
	2.0	5.5
R_δ	$(1.0 - 1.7) \times 10^4$	$(2.3 - 3.7) \times 10^4$
R_θ	$(0.9 - 1.9) \times 10^3$	$(2.7 - 4.2) \times 10^3$
u_τ (m/s)¶	0.0980	0.238
δ_0 (m)¶¶	0.075	0.065
θ_0 (m)¶¶¶	0.0076	0.0075
T (C)§	20	20
ν (m^2/s)§§	1.51×10^{-5}	1.51×10^{-5}

¶: u_τ at $x/\delta_0 = -1.0$. ¶¶: defined at $U/U_0 = 0.99$. ¶¶¶: θ at $x/\delta_0 = -1.0$.
§: Typical air temperature with ±2°C. §§ ±1% with temperature changes.

4.1 Wall Shear Stress (τ_w)

The wall shear stress (τ_w) on a smooth-wall turbulent boundary layer can be measured using either direct or indirect techniques. An example of a direct technique is the use of floating elements, which provides a direct reading of the 'local' wall shear

stress. One disadvantage of this technique, however, is that a slight misalignment of the sensor surface will result in a large error. In addition, the presence of the gap around the sensing element creates difficulties with the measurements (Hanratty and Campbell, 1983). There are several indirect τ_w measurement techniques, including the Clauser-chart technique, power-law technique, slope of the mean velocity at the wall ($(dU/dy)_{y=0}$), and Preston tube measurements.

The Clauser-chart (log-law) technique can be used reliably to estimate wall shear stress (τ_w) at higher R_θ. The use of this technique at low Reynolds numbers, however, is more tenuous. Both DNS (Spalart, 1988) and experimental (Ching et al., 1995a) data indicate that the log region is very narrow at low R_θ. The power-law technique can provide a good estimate of τ_w in low Reynolds numbers ($R_\theta \leq 2000$, see for example, Djenidi et al., 1997). At low Reynolds numbers, the power-law represents the mean velocity in the overlap region accurately. The wall shear stress (τ_w) can also be estimated from $(dU/dy)_{y=0}$. There are several difficulties, however, associated with this method as described in Section 3.2. At the higher R_θ, τ_w was also estimated using a Preston tube. This method was not feasible at the lower R_θ because the differential pressure transducer available was out of range. For this R_θ, the dynamic pressure ratio ($\equiv 0.5\ \rho U^2/0.5\rho U_0^2$) near the wall is of the same order as the minimum reading of the differential pressure transducer.

Measurements of wall shear stress (τ_w) over rough-walls are more difficult to obtain than over smooth-walls. For example, separation bubbles may occur in boundary layers over rough-walls. Also, turbulent boundary layers over rough-walls may not be in an equilibrium condition. Therefore, the use of log-law, power-law, and Preston tube

techniques to estimate τ_w over rough-walls is less appropriate than the use of $(dU/dy)_{y=0}$. A pitfall of estimating τ_w from $(dU/dy)_{y=0}$ using HWA measurements is the wall conduction problem, which creates a spurious increase in U as the wall is approached. Hence, the mean velocity (U) must be corrected before estimating τ_w using the $(dU/dy)_{y=0}$ technique. The wall conduction correction parameters were obtained from the smooth-wall measurements, where 'valid' values of τ_w were deduced from the log-law technique. Details of the procedure were presented in chapter 3, and the validity of estimating τ_w using the $(dU/dy)_{y=0}$ technique over a smooth-wall is confirmed by comparing τ_w obtained from the power-law technique and Preston tube measurements. The correction factor due to the wall conduction effect obtained in the smooth-wall measurements is then assumed to be valid for the grooved-wall turbulent boundary layer.

Before presenting results for C_f from the four methods (log-law, power-law, $(dU/dy)_{y=0}$ and Preston tube measurement), the Preston tube measurements are analyzed in some details. Similar to the log-law technique, the validity of estimating τ_w in turbulent boundary layers using Preston tube measurements relies on the existence of the log region. The tube diameter, therefore, must be small enough to be completely submerged within the log region of the layer, however, the tube diameter must be large enough so that the available equipment can measure Δp accurately. Therefore, there should be a range of tube sizes for which the Preston tube technique can be used effectively to estimate τ_w for given flow conditions. The main difficulty of this technique is obtaining the most appropriate calibration equation for the given tube diameter. Preston (1954) suggested a non-dimensional relationship between Δp and τ_w (Eq. 3.11). He then proposed the following calibration equation:

$$y^* = 0.875x^* - 1.396, \quad (4.1)$$

for $4.1 \leq x^* \leq 6.5$. Since then, several different calibration equations for Preston tubes have been proposed (Smith and Walker, 1958; Patel, 1965; Bechert, 1995). A summary of several calibration equations is provided by McAllister et al. (1982). In a preliminary study of τ_w measurements using the Preston tube technique, several tubes with different outside diameters were used to estimate τ_w on a smooth-wall turbulent boundary layer. The calibration equations of Patel (Eq. 3.12) and Bechert (Eq. 3.13) were used to calculate τ_w. It was found that there was a significant effect of the tube diameter on the calculated τ_w obtained from either equation. Hence, dependence of the results on the tube diameter was further investigated.

Preston tubes with five different outside diameters (1.46, 1.82, 3.23, 4.76 and 5.54mm) were used to investigate the effect of the tube diameter on existing calibration curves. The free stream velocity was kept constant at 5.5m/s, and the measurements were made at fourteen streamwise locations, corresponding to R_θ in the range 2800 to 4100. The ratios of tube diameter (d) to the boundary layer thickness (δ) are 0.022, 0.027, 0.048, 0.071 and 0.082. In terms of wall units ($d^+ = du_\tau/\nu$), the tube diameters are 21.6, 26.9, 47.9, 70.5 and 82.1 (see Table 4.2).

Skin friction coefficients (C_f) obtained from the five different tubes using the calibrations of Patel (1965) and Bechert (1995) are compared in Fig. 4.1.1. For the smaller diameter tubes ($d^+ = 21.6$ and 26.9), C_f values from Bechert's equation are less than Patel's, while for the larger diameter tubes, Bechert's calibration yields larger values than those obtained from Patel's calibration. The maximum difference in C_f obtained

from the two calibrations is approximately 6.7 percent and occurs for $d^+ = 82.1$. The C_f values from the two calibration equations are almost equal for $d^+ = 47.9$, with an average difference of approximately 0.09 percent. Table 4.3 shows the average of the maximum difference in C_f obtained from Patel's and Bechert's calibration equations for the different diameter tubes.

Table 4.2. Average difference in C_f obtained from Patel's and Bechert's calibration equations.

Tube diameter, d (mm)	d/δ	du_τ/ν	Average difference in C_f (%)
1.46	0.022	21.6	3.16
1.82	0.027	26.9	3.35
3.23	0.048	47.9	-0.09
4.76	0.071	70.5	-6.44
5.54	0.082	82.1	-6.69

For comparison with the Preston tube measurements, reference τ_w values are obtained from the log-law technique. The log-law line represents the mean velocity (U) well into the overlap region for $R_\theta \geq 2500$, and for the smooth-wall case, τ_w can be deduced from this technique accurately. The U profiles at nine streamwise locations are shown in Fig. 4.1.2, and the τ_w values obtained from this technique are hereafter referred to as the "log-law" data.

The C_f distribution from the five different tubes using Bechert's calibration is shown in Fig. 4.1.3 together with the "log-law" data. While the trend of the C_f distribution from the five tubes is similar, they all decrease more rapidly with streamwise

distance than the "log-law" data. The maximum deviation from the "log-law" data occurs at the last streamwise location for the 1.46mm diameter tube, and is approximately 13 percent. At any given streamwise location, there is a significant difference in the estimated value of C_f from the five different tubes. In general, Bechert's (1995) calibration equation gives a larger value of C_f for a larger tube diameter. The average difference in C_f measured from the largest and the smallest tubes is approximately 17.7 percent (see Table 4.3).

Table 4.3. Average of the maximum difference in C_f measured from the largest and the smallest tubes (see Figs. 4.1.3, 4.1.4, and 4.1.6).

Calibration equation	$\Delta\tau_{w,max}$ or $\Delta C_{f,max}$ (%)
Bechert	17.71
Patel	8.04
Present	5.30

The distribution of C_f for the five tubes obtained from Patel's (1965) calibration equation is shown in Fig. 4.1.4. The maximum difference in C_f measured from the largest and the smallest tubes in this case is approximately 8 percent (see Table 4.3). In general, Patel's calibration equation is less sensitive to the tube diameter than Bechert's calibration equation. In this case, C_f also decreases more rapidly than the "log-law" data. Bechert's calibration equation, however, is simpler to use since it uses a single equation for a wide range of Δp^+ ($\equiv \Delta p d^2/(\rho \nu^2)$) instead of three different equations based on different Δp^+ used by Patel, see section 3.2.

A new calibration equation was obtained using the present measurements to overcome the tube diameter dependence of Patel's and Bechert's calibration equations.

The calibration equation is obtained by fitting the experimental data to the "log-law" data. The calibration equation consists of three non-dimensional parameters: Δp^+, τ^+, and $R_{e,d}$, where Δp^+ and τ^+ are as defined in Eq. (3.13), and $R_{e,d} \equiv U_0 d / \nu$. The inclusion of the Reynolds number ($R_{e,d}$) makes the calibration equation less sensitive to the tube diameter. The new calibration equation is given by:

$$\frac{\log_{10}(\tau^+)}{(R_{e,d})^{0.135}} = 0.767 \ln(\log_{10}[\Delta p^+]) + 0.0097, \qquad (4.2)$$

and is valid in the range $3.6 < x^* < 5.3$ (or $1.8 \times 10^4 < \Delta p^+ < 7.6 \times 10^5$) for tubes in the range $20 < d^+ < 82$ or $0.02 < d/\delta < 0.08$. The fit of the data to the calibration equation is shown in Fig. 4.1.5. The streamwise distribution of C_f using the new calibration equation is shown in Fig. 4.1.6, and the average of the maximum scatter of the measured C_f is reduced to approximately 5.3 percent. The U profiles at $R_\theta = 3100$ normalized with u_τ from the different diameter tubes using the present calibration equation are in good agreement in the overlap region to the "log-law" line (Fig. 4.1.7).

Briefly, both Bechert's and Patel's calibration equations are sensitive to the tube diameter, with Patel's calibration being less dependent on the tube diameter. A new calibration equation has been obtained empirically which is less dependent on the tube diameters than previous calibration curves. The maximum difference in the τ_w measurements from the different tubes using Bechert's, Patel's, and present calibrations are approximately 17.7, 8.0, and 5.3 percent, respectively (Table 4.3).

The C_f distributions obtained from the power-law, $(dU/dy)_{y=0}$ and the log-law techniques at $R_\theta = 1000$ are shown in Fig. 4.1.8. In general, the C_f obtained from the

three different techniques are in good agreement, although the C_f obtained from the power-law technique overpredicts the log-law and the $(dU/dy)_{y=0}$ techniques by approximately 3 percent beyond $x/\delta_0 \approx 9.0$. The C_f distribution obtained from the $(dU/dy)_{y=0}$, log-law and Preston-tube techniques at $R_\theta = 3000$ is shown in Fig. 4.1.9. The results from the three techniques are well within ± 3 percent. The power-law, log-law and Preston tube techniques may not be appropriate to estimate u_τ just downstream of the groove since the boundary layer is not in equilibrium. The $(dU/dy)_{y=0}$ technique, on the other hand, is more appropriate in this case if the effect of wall conduction on U can be eliminated. As the C_f in the smooth-wall measurements can be estimated reliably from the log-law, power-law and Preston tube measurements, a near-wall correction factor has been sought to correct the grooved-wall U. The grooved-wall C_f is then obtained from the $(dU/dy)_{y=0}$ technique applied to the corrected U in the laminar sub-layer region. Unless otherwise stated, the u_τ estimated from $(dU/dy)_{y=0}$ is used as the normalizing parameter in this thesis, for both the smooth- and grooved-wall boundary layers.

4.2 Mean Velocity Profiles (U)

The normalized mean velocity profiles are presented in Fig. 4.2.1. The experimental profiles at the lower R_θ are in good agreement with the DNS data (Spalart, 1988). Very close to the wall, the experimental data deviates from the DNS data due to the wall conduction effect, and uncertainty of the spatial location of the probe (Djenidi et al. 1997). In the wake region, a small deviation of the experimental data from the DNS data is discernible due to the difference in the Reynolds number. The U^+ profiles at the higher R_θ agree well with the DNS profile ($R_\theta = 1410$) up to $y^+ \approx 250$, and then deviate

from the DNS data due to the difference in Reynolds number. The U^+ profiles obtained from LDV (Degraff and Eaton, 2000) at $R_\theta = 2900$ and from HWA (Purtell et al., 1981) at $R_\theta = 1840$ are also in good agreement with the present data except very close to the wall and at the outermost region (Fig. 4.2.1). The U^+ at the lower R_θ is compared with the DNS data (Spalart, 1988) and the power-law distribution in Fig. 4.2.2. It can be seen from this figure that the power-law closely describes the velocity profile, except in the region close to the wall ($y^+ \leq 30$).

The outer layer similarity is verified by normalizing U with the freestream velocity (U_0) and plotting against y/δ for five representative x-locations (Fig. 4.2.3). For both R_θ, there is good collapse of the profiles. The $1/6^{th}$ power-law curve represents the profiles well for either R_θ in most of the layer. The curve collapses well with the profiles at R_θ=1000 in the range $0.05 \leq y/\delta \leq 1.0$ and in the range $0.02 \leq y/\delta \leq 1.0$ for $R_\theta = 3000$.

Clauser (1956) used the friction velocity, u_τ, to nondimensionalize a family of turbulent boundary layer profiles. When $(U_0 - U)/u_\tau$ was used as the ordinate, the profiles which originally depended on Reynolds number and surface roughness, collapsed into a single profile. In mathematical form, this can be expressed as

$$\frac{U - U_0}{u_\tau} = g\left(\frac{y}{\delta}\right) = \frac{1}{\kappa}\ln\left(\frac{y}{\delta}\right) + E, \tag{4.3}$$

and is called the velocity-defect law. For a turbulent boundary layer under zero pressure gradient, the velocity defect $(U - U_0)/u_\tau$ is solely a function of y/δ. The velocity-defect law, Eq. (4.3), is plotted in Fig. 4.2.4. The plot shows a logarithmic behavior in the overlap region with the same slope as U^+. The value of y-intercept (E) is chosen so that

Eq. (4.3) matches well with experimental data in the overlap region. For the present smooth-wall measurements, E = -1.8 and -2.5 at R_θ = 1000 and 3000, respectively.

4.3 Turbulence Measurements

4.3.1 Streamwise Turbulence Intensity (u')

The u'^+ profiles along the streamwise direction for the smooth-wall at both R_θ are shown in Fig. 4.3.1 together with the DNS data from Spalart (1988). Although there is some experimental scatter in the data, the u'^+ profiles are similar to the DNS profile. The smooth-wall data from Purtell et al. (1981) and LDV data from DeGraaff and Eaton (2000) at similar Reynolds numbers are also shown for comparison. There is a good collapse of the profiles in the region $y^+ \leq 30$ at either R_θ. Moreover, the peak value of u'^+ (u'^+_{max}) occurs at $y^+ \approx 14$ with $u'^+_{max} \approx 2.7$, which is in agreement with the DNS data. In the region close to the wall ($y^+ \leq 3$), the uncertainty of the probe distance from the wall is highlighted, because of the log scale used for the abscissa. At the lower R_θ, the difference in R_θ between the experimental and DNS data (R_θ = 1410) is reflected in the region $y^+ \geq 30$. At this R_θ range, the present data are, however, in good agreement with data from Purtell et al. up to $y^+ \approx 200$, with the difference in R_θ highlighted in the outer region ($y^+ \geq 200$). At the higher R_θ, the present data show a good collapse with data from DeGraff and Eaton up to $y^+ \approx 400$. The rightward shift of the experimental data for $y^+ \geq 200$ compared to the DNS data is due to the higher R_θ (Perry and Abbel, 1975; Purtell et al., 1981).

4.3.2 Wall-Normal Turbulence Intensity (v')

The wall-normal turbulence intensity profiles on the smooth-wall are presented in Fig. 4.3.2 for five representative x-locations. Only the data at the lower R_θ are presented due to the limitation of the spatial resolution of the probe. The LDV data of DeGraaff and Eaton (2000), Djenidi et al. (1999) and DNS data (Spalart, 1988) are also presented for comparison. Within a major portion of the layer, the present data are lower than the DNS data, and also from the experimental data of DeGraaff and Eaton, and Djenidi et al. The peak values of v'^+ are approximately 90 percent of the DNS data. Hot-wire data from Roach and Brierley (R_θ = 1431) (see Fernholz and Finley, 1996) also exhibited the maximum value for v'^+ of 90 percent of the DNS data of Spalart. There are several difficulties in measuring v'^+ using X-wires. The wire separation and physical length of each sensor are important parameters for accurate measurements (Zhu and Antonia, 1995; Ligrani and Bradshaw, 1987; Elsner et al., 1993). The X-wire measurements of Antonia et al. (1995) for $(v'^+)_{max}$ were approximately 76 percent of the DNS data. The attenuation in v^+ is probably due to the angle of the instantaneous velocity vector exceeding the effective angle of the wire.

4.3.3 Reynolds Stress ($\langle -uv \rangle$)

The Reynolds stress ($\langle -uv \rangle/(U_0)^2$) profiles along the streamwise direction for the smooth-wall at the lower R_θ (R_θ = 950, 1050 and 1250) are shown in Fig. 4.3.3 along with the profile from Klebanoff (1955). The present data at the three Reynolds numbers collapse fairly well in the outer region ($y/\delta \geq 0.2$), but they exhibit more scatter in the region $y/\delta \leq 0.2$. The scatter in the $\langle -uv \rangle/(U_0)^2$ data in the region $y/\delta \leq 0.2$ is more severe

than the data scatter for u' and v' (Figs. 4.3.1 and 4.3.2). In general there is a good collapse between the present $\langle -uv \rangle/(U_0)^2$ profiles with that of Klebanoff (1955), except in the region $y/\delta \leq 0.04$. The decrease in $\langle -uv \rangle/(U_0)^2$ as the wall is approached was also observed by Roach and Brierley (see Fernholz and Finley, 1996) at similar R_θ. The decrease in $\langle -uv \rangle/(U_0)^2$ in the wall region, however, was not observed by Klebanoff (1955).

4.3.4 Turbulence Energy Spectra ($E(k_1)$)

The energy spectra of the streamwise velocity fluctuations (u') at different locations in the layer are presented in Figs. 4.3.4 and 4.3.5. Following the method of Klebanoff (1955), the energy spectrum ($E_1(k_1)/(u')^2$) is plotted against the wave number k_1 (k_1 is the one dimensional wave number defined as $2\pi f/U$, where f and U are frequency and local mean velocity, respectively). The energy spectrum is defined as (Hinze, 1975)

$$E_1(k_1) = \frac{U}{2\pi} E_1(f), \tag{4.4}$$

so that

$$(u')^2 = \int_0^\infty E_1(k_1) dk_1 . \tag{4.5}$$

The spectra of u' are spread out over approximately two decades in wave number at the lower R_θ, and approximately three decades at the higher R_θ. The energy at the lower wave number decreases as the wall is approached, because the energy containing eddies are larger at the lower wave number (i.e. lower frequency) than eddies at the

higher wave number. As the wall is approached, the large eddy motions are damped, resulting in a lower energy in the large eddies at distances closer to the wall.

The energy spectrum of the wall-normal velocity fluctuations (v') on the smooth-wall is presented in Fig. 4.3.6. The spectra of v' are spread out over three decades in both wave number and energy level at this R_θ. Similar to the u' spectrum, the energy level for the v' spectrum at the lower wave number also decreases as the wall is approached. In the proximity of the wall, the turbulent eddies with higher wave numbers contain more energy than the turbulent eddies at locations remote from the wall. From Figs. 4.3.4 to 4.3.6, it can be concluded that in the near-wall region the turbulent eddies with higher wave numbers contain more energy, while at distances away from the wall, the eddies with lower wave numbers contain more energy. The -5/3 and -1-slopes are also shown in Figs. 4.3.4 to 4.3.6 for comparison. The most dominant energy-containing eddies closely follow the -1-slope rather than the -5/3-slope. The -5/3-slope is most likely for high Reynolds number turbulent flows where the extent of the inertial range is wider than that in low Reynolds number flows. The Reynolds numbers for the present study is relatively low, and it is not surprising that the spectra follow the -1-slope.

4.4 Sweep and Ejection Events and Bursting Frequency

The method used to calculate the sweep and ejection events and the bursting frequency was described in Section 3.2.4. Figures 4.4.1a and 4.4.1b show the distribution of the ejection (q_2^+) and sweep (q_4^+) events across the layer for the smooth-wall turbulent boundary layers. The distribution of the outward interaction (q_1^+) and wall-ward interaction (q_3^+) across the layer are also shown in the figures. The data were taken at

several streamwise locations that cover R_θ from 900 to 1900. All quadrants contributing to the Reynolds stress (q_1^+ to q_4^+) show self-similarity in the inner region ($y^+ \leq 100$ or $y/\delta \leq 0.2$) within the R_θ range of this study. In the region $y^+ \geq 200$ (or $y/\delta \geq 0.4$), on the other hand, the Reynolds number effect on q_1^+ to q_4^+ is apparent in Figs. 4.4.1a and 4.4.1b. This effect is reflected by the rightward shift in the q_1^+ to q_4^+ profiles at the two highest R_θ (R_θ = 1400 and 1900) in that region.

Figure 4.4.2 shows the downstream distribution of the maximum time duration (τ_{max}) during which a single ejection or a group of ejections can be considered as one burst on the smooth-wall turbulent boundary layer. The corresponding ratio between the mean duration of ejections to the average time between two consecutive ejections ($T_o/T_{e,m}$) and the normalized bursting frequency (f_B^+) is also shown in the figure. The value of τ_{max} is nearly constant at 0.05 seconds (Table 4.4). The $T_o/T_{e,m}$ ratio is also practically constant along the streamwise direction with an average of approximately 0.1. The f_B is calculated using the second quadrant method as described by Bogard and Tiederman (1986), and is obtained at $y^+ \approx 14$. The bursting frequency (f_B) is normalized using inner variables (ν and u_τ), i.e. $f_B^+ = f_B \nu/(u_\tau)^2$. The value of f_B^+ is nearly constant at 0.011 in the present smooth-wall study. The threshold level, calculated from Eq. (3.14), is practically constant at approximately 0.9 with a standard deviation of 0.05.

The formation of bursts can also be expressed in terms of the average time between bursts ($\overline{T_B}$). In Table 4.5, the normalized average time between bursts ($\overline{T_B}^+$) of the present study (R_δ = 10000; R_θ = 1000) for the smooth-wall is compared with results of previous studies (Bogard and Tiederman, 1986; Luchik and Tiederman, 1987; Kim and Spalart, 1987; Rao et al., 1971; Kim et al., 1971). The $\overline{T_B}^+$ in the studies of Bogard and

Tiederman, Luchik and Tiederman, and Kim and Spalart were obtained from the second quadrant ($(uv)_2$) analysis, and hence provides a good reference to validate the present results. Although the studies of Rao et al. and Kim et al. used a different method from that used in the present study to estimate $\overline{T_B}^+$ (they used the visual counting method), the results compare favorably. The present $\overline{T_B}^+$ is in good agreement with the result of Luchik and Tiederman, but less than the result of Bogard and Tiederman, and greater than the result of Kim and Spalart. The difference in $\overline{T_B}^+$ between the present result and the results of Bogard and Tiederman and Kim and Spalart may be associated with the difference in the Reynolds numbers used in the experiments.

Table 4.4. Recorded smooth-wall burst data. $y^+ = 14$, $U_0 = 2.0$m/s. Sampling time: 10 seconds.

x (mm)	H	$T_{e,m}$ (s)	T_o (s)	τ_{max} (s)	f_B (s^{-1})	$T_o/T_{e,m}$
1	0.9155	0.03049	0.002966	0.04697	6.8	0.09728
10	0.9227	0.03294	0.003467	0.05267	6.5	0.10525
40	0.9110	0.03167	0.003105	0.05351	6.2	0.09804
70	0.9704	0.03211	0.003285	0.05139	6.6	0.10230
100	0.8903	0.02926	0.003043	0.04804	6.3	0.10400
140	0.9383	0.03214	0.003189	0.05039	6.6	0.09922
250	0.9270	0.03049	0.002880	0.04908	6.6	0.09446
500	0.9491	0.03178	0.003364	0.04736	7.0	0.10585
700	0.8200	0.03206	0.002993	0.04919	5.5	0.09336
1000	0.8370	0.03180	0.002995	0.05240	6.3	0.09418
1400	0.8297	0.03141	0.003130	0.04933	6.7	0.09965
2000	0.8859	0.03359	0.003190	0.04999	6.8	0.09497

4.5 Summary

The characteristics of a turbulent boundary layer on the smooth-wall were investigated experimentally. The experiments were performed to obtain a baseline data

set for comparison with the turbulent boundary layers over the grooved-walls. The smooth-wall experiments were also intended to validate the methods of analysis used in the present study through comparison with the existing literature. The mean quantities, including the streamwise mean velocity (U) and wall shear stress (τ_w), compare favorably with the literature. Moreover, the turbulence intensities (u' and v'), Reynolds stress ($\langle -uv \rangle$) and turbulent energy spectra are also in good agreement with the literature. The near-wall turbulent burst analysis also shows consistent results with previous studies. Finally, a new correlation for Preston tube calibration has been obtained empirically. The new calibration correlation is less dependent on the tube diameter than the calibration curves from Patel (1965) and Bechert (1995).

Table 4.5. The normalized average time between bursts ($\overline{T_B}^+ = \overline{T_B} u_\tau^2 / \nu$)

	$\overline{T_B}^+$	Reynolds number	Note
Bogard and Tiederman (1986)	140	$Re_h = U_m h/\nu = 8200$ $R_\theta = U_0\theta/\nu = 420$	Channel flow
Luchik and Tiederman (1987)	90	$9400 \le Re_h \le 17800$	Channel flow
Kim and Spalart (1987)	60	$300 \le R_\theta \le 1400$	Boundary layer flow
Rao et al. (1971)	71	$R_\theta = 1000$	Boundary layer flow
Kim et al. (1971)	118	$R_\theta = 1100$	Boundary layer flow
Present study	88	$R_\delta = 10000$; $R_\theta = 1000$	Boundary layer flow

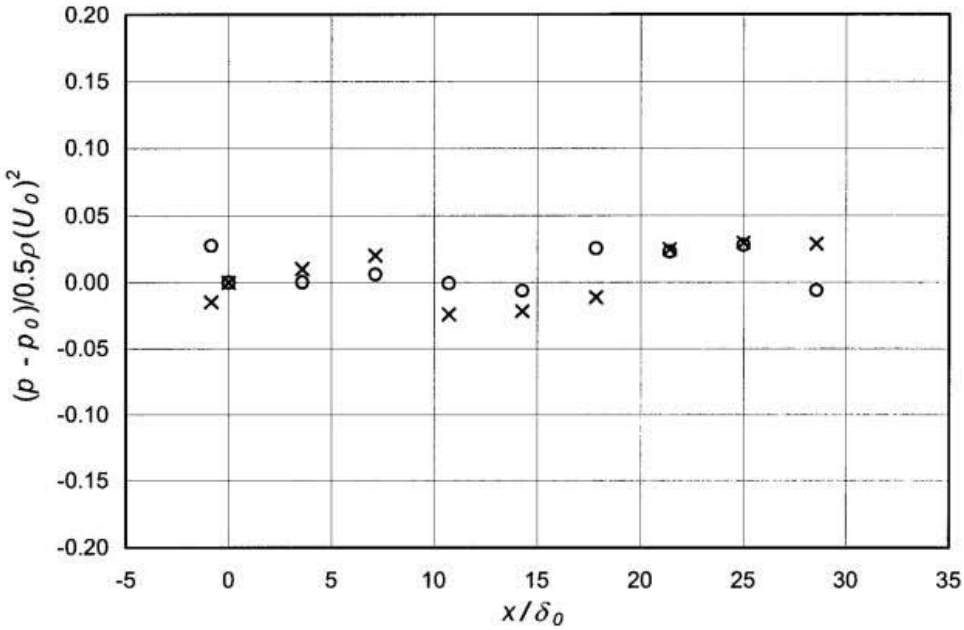

Fig. 4.1 Static pressure distribution along the centerline of the test section. Symbols: ×, $R_\theta = 1000$; ○, $R_\theta = 3000$.

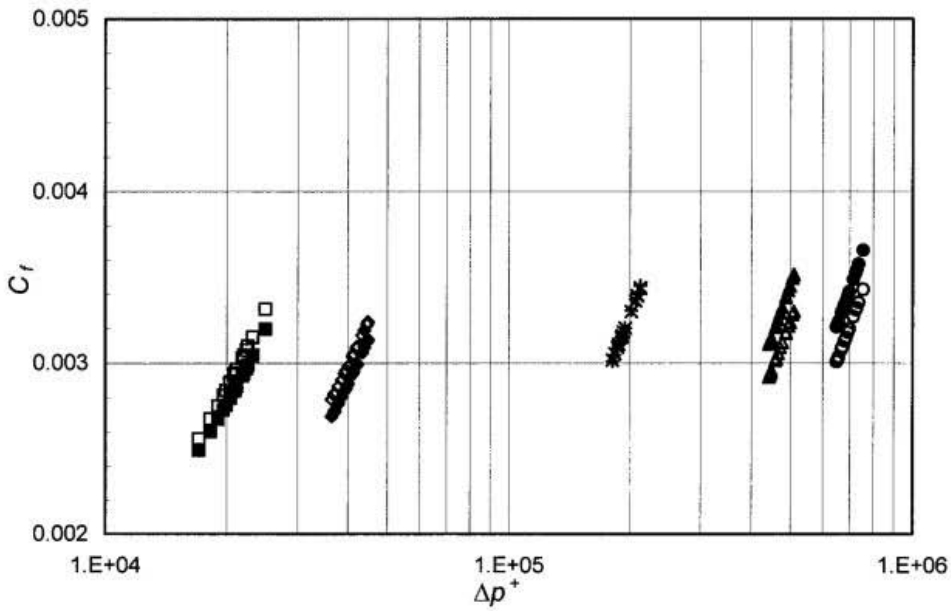

Fig. 4.1.1 Comparison of C_f based on Patel's and Bechert's calibration equations.
Patel : □, d = 1.46; ◇, d = 1.82; ×, d = 3.23; △, d = 4.76; ○, d = 5.54.
Bechert : ■, d = 1.46; ◆, d = 1.82; +, d = 3.23; ▲, d = 4.76; ●, d = 5.54.
d is in mm.

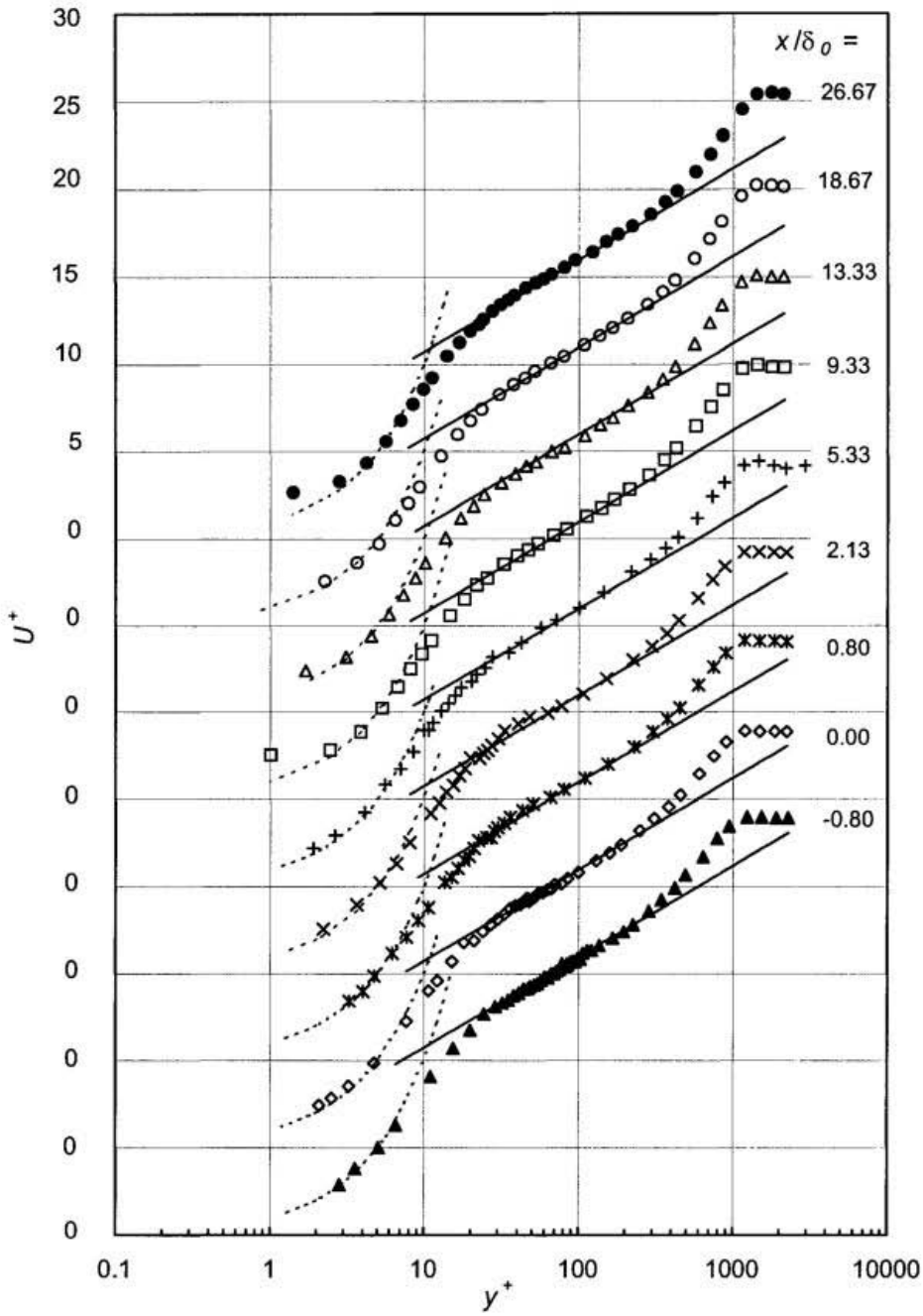

Fig. 4.1.2 Mean velocity profiles in the overlap region of a turbulent boundary layer.
▲, R_θ = 2840; ◇, 2870; *, 2980; ×, 3050; +, 3090; □, 3100; Δ, 3200; ○, 3400;
●, 4050; ———, Log-law: $U^+ = (1/0.43)\ln(y^+) + 5.50$; - - - -, $U^+ = y^+$.

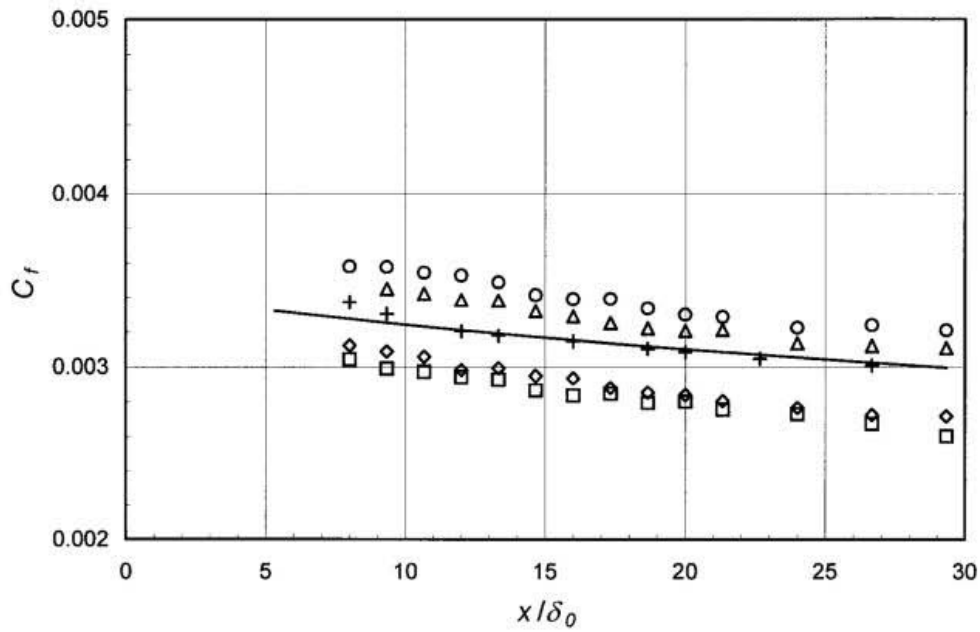

Fig. 4.1.3 Skin friction coefficient distribution obtained from Bechert's calibration equation. □, d = 1.46mm; ◇, 1.82mm; +, 3.23mm; Δ, 4.76mm; ○, 5.54mm; _____, "log-law" data.

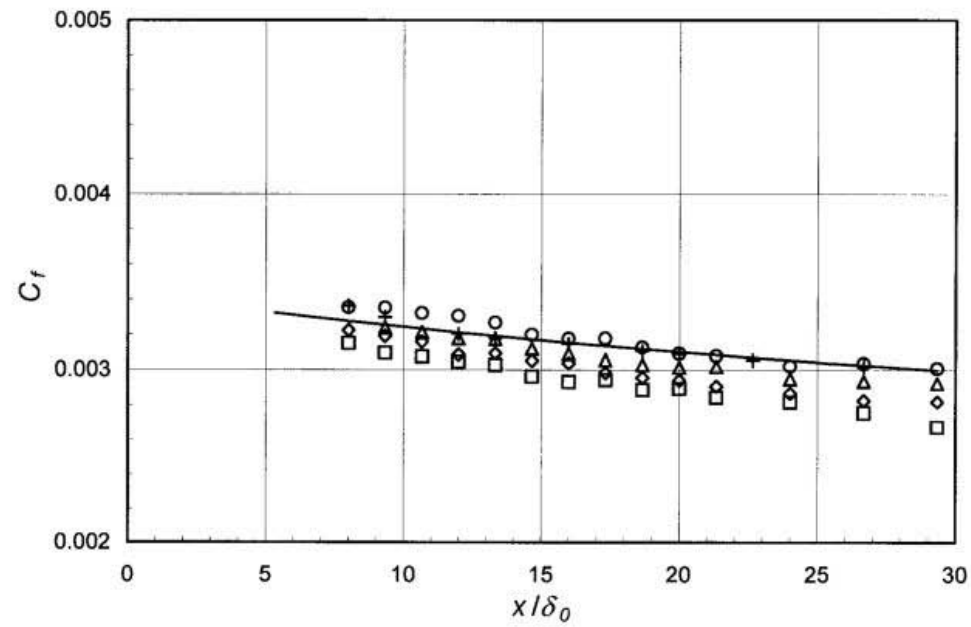

Fig. 4.1.4 Skin friction coefficient distribution obtained from Patel's calibration equation. □, d = 1.46mm; ◇, 1.82mm; +, 3.23mm; Δ, 4.76mm; ○, 5.54mm; _____, "log-law" data.

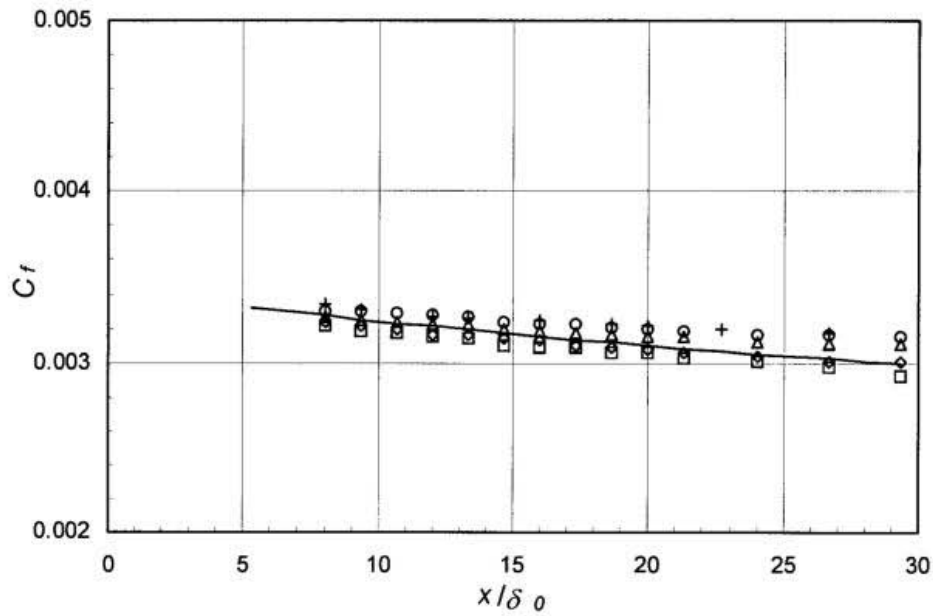

Fig. 4.1.6 Skin friction coefficient distribution obtained from the present calibration equation. □, d = 1.46mm; ◇, 1.82mm; +, 3.23mm; Δ, 4.76mm; ○, 5.54mm; _____, "log-law" data.

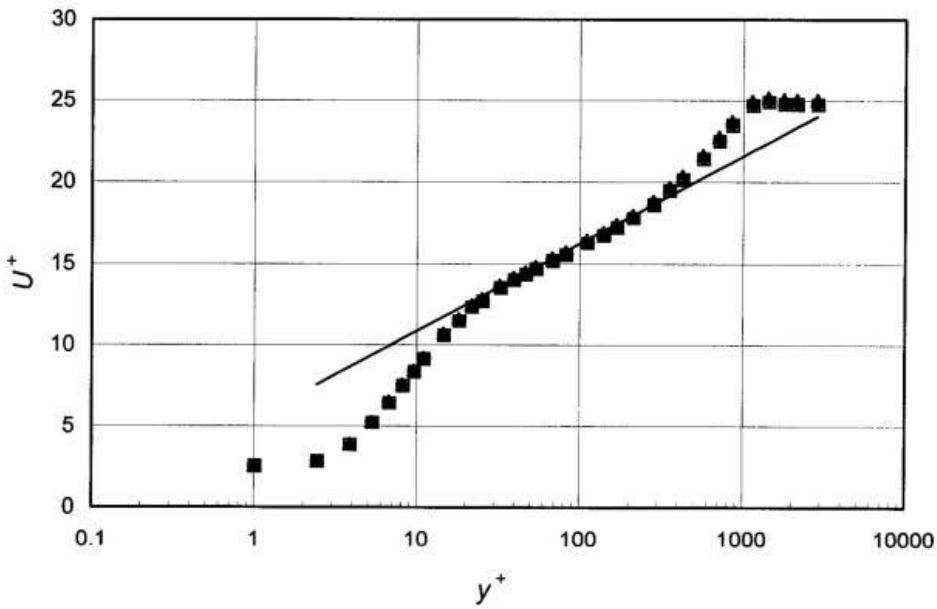

Fig. 4.1.7 Mean velocity profiles normalized using u_τ obtained from the present calibration equation (R_θ= 3100). □, d = 1.46mm; ◇, 1.82mm; +, 3.23mm; Δ, 4.76mm; ○, 5.54mm; ——, Log-law: $U^+ = (1/0.43)\ln(y^+) + 5.50$.

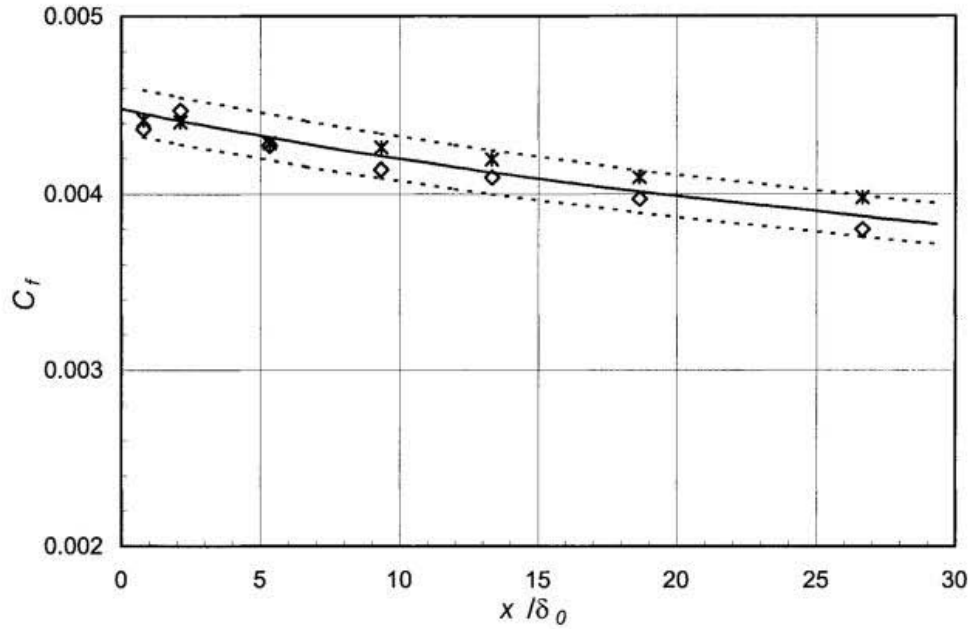

Fig. 4.1.8 Skin friction coefficient on the smooth-wall at R_θ = 1000 to 1900. ∗, power-law; ◇, slope of U at the wall; ———, log-law C_f, - - - - -, ±3% band from the log-law C_f. U_0 = 2.0m/s.

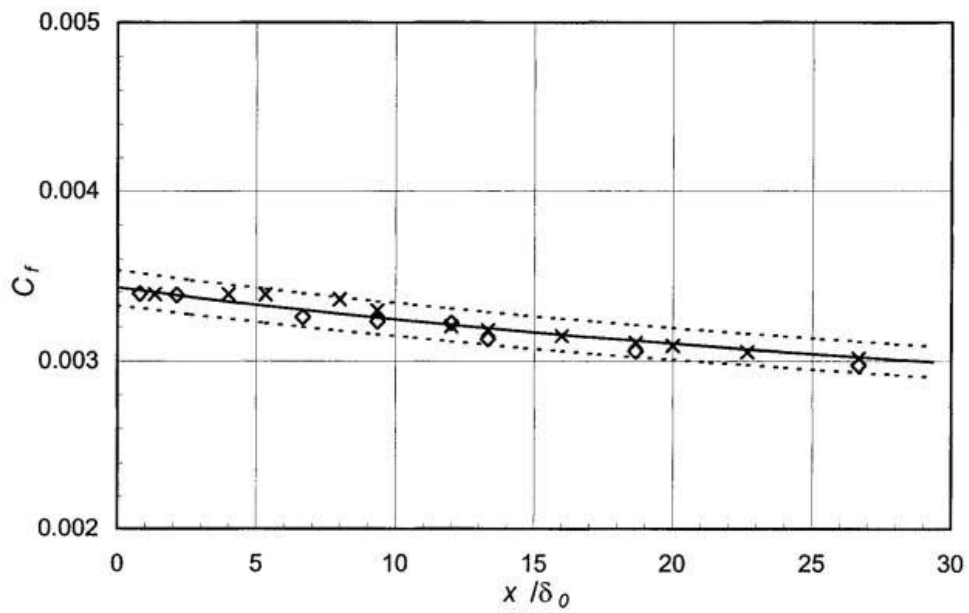

Fig. 4.1.9 Skin friction coefficient on the smooth-wall at R_θ = 2800 to 4100. ×, Preston tube; ◇, slope of U at the wall; ———, log-law C_f, - - - -, ±3% band from the log-law C_f. U_0 = 5.5m/s.

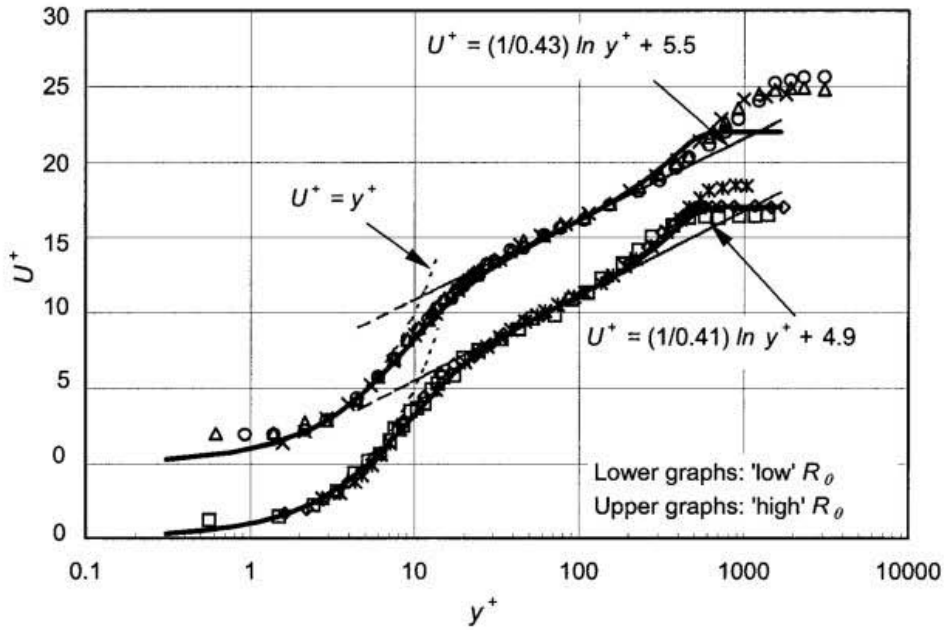

Fig. 4.2.1 Mean velocity profiles over a smooth-wall. Symbols: □, R_θ = 1030; ◇, 1250; Δ, 3200; ○, 4200; ∗, Purtell et al. (1981), R_θ = 1840; ×, DeGraaff and Eaton (2000), R_θ = 2900; ———, DNS (Spalart, 1988), R_θ =1410.

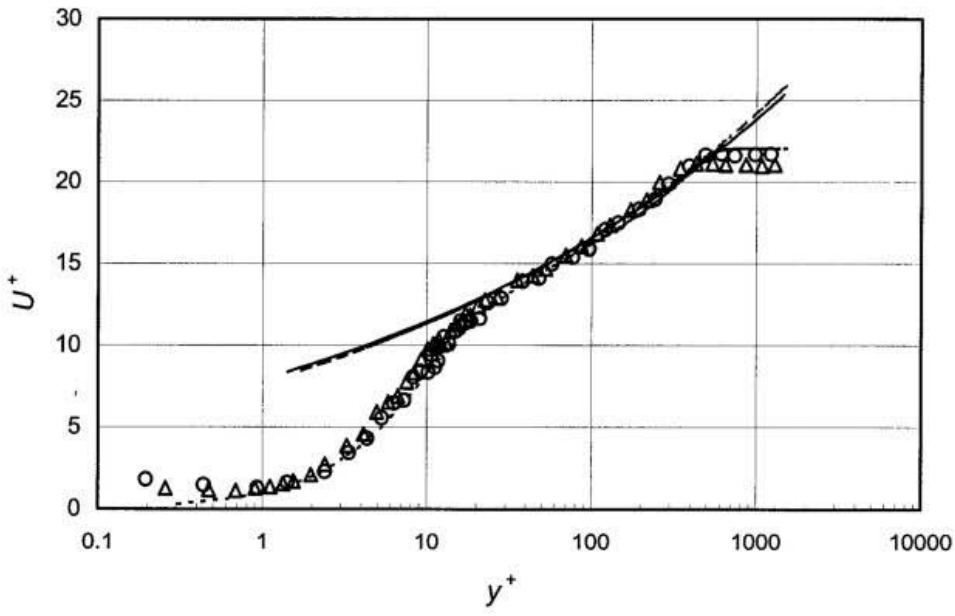

Fig. 4.2.2 Comparison between mean velocity profiles at lower R_θ with the power-law lines and the DNS data (Spalart, 1988). Δ, R_θ = 830; ○ = 1250. Power-law lines: -- —— --, R_θ = 830; _____, =1250. - - - -, DNS (R_θ =1410).

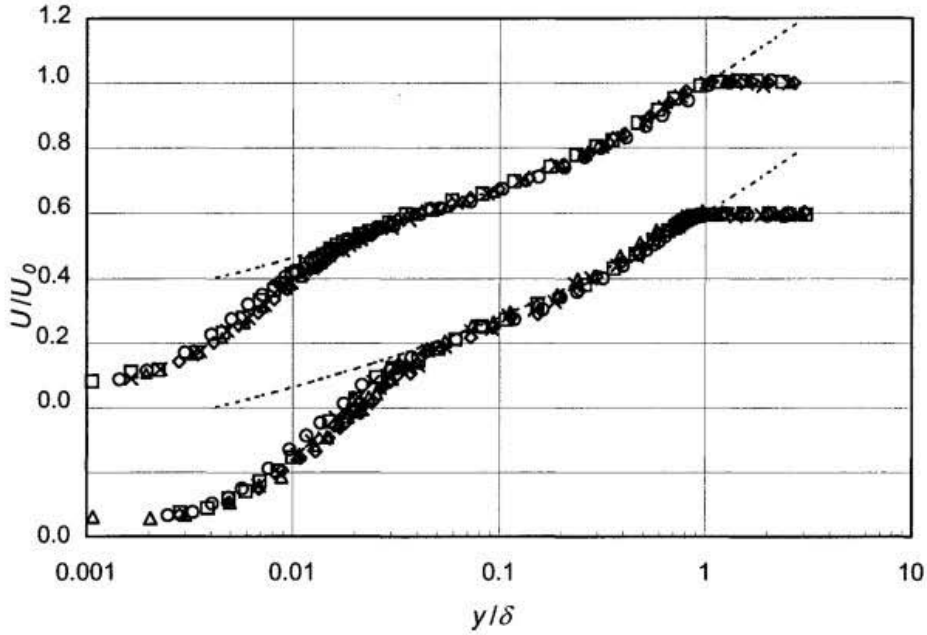

Fig. 4.2.3 Mean velocity profiles in terms of outer variables. The lower and the upper graphs represent the lower and higher Reynolds number family profiles (R_θ = 1000 to 1900 and R_θ = 3000 to 4200), respectively. - - - -, 1/6 power-law line.

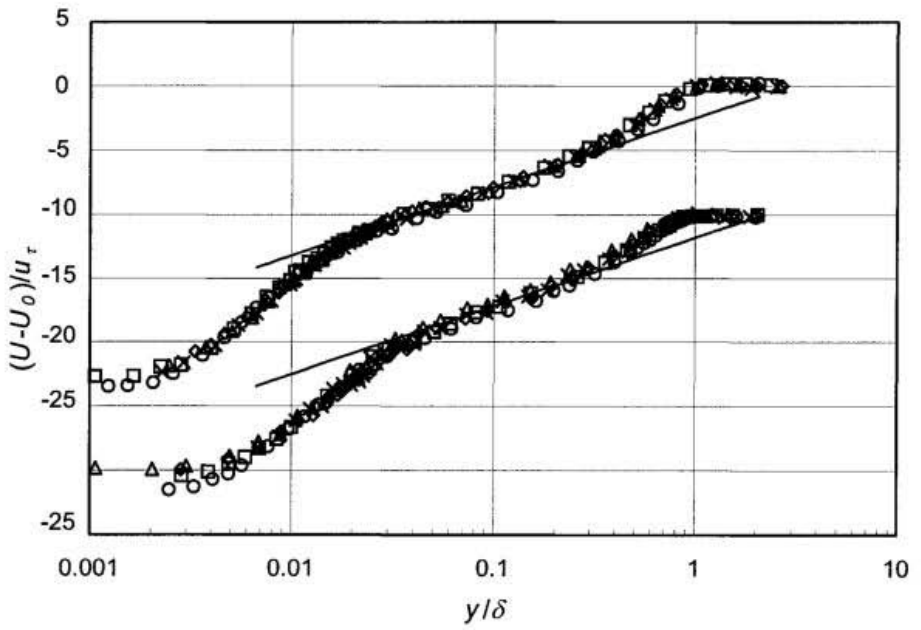

Fig. 4.2.4 Velocity defect plots. Upper graphs: higher R_θ family profiles. Lower graphs: lower R_θ family profiles. _____, log-line. Vertical scale is for the upper graphs.

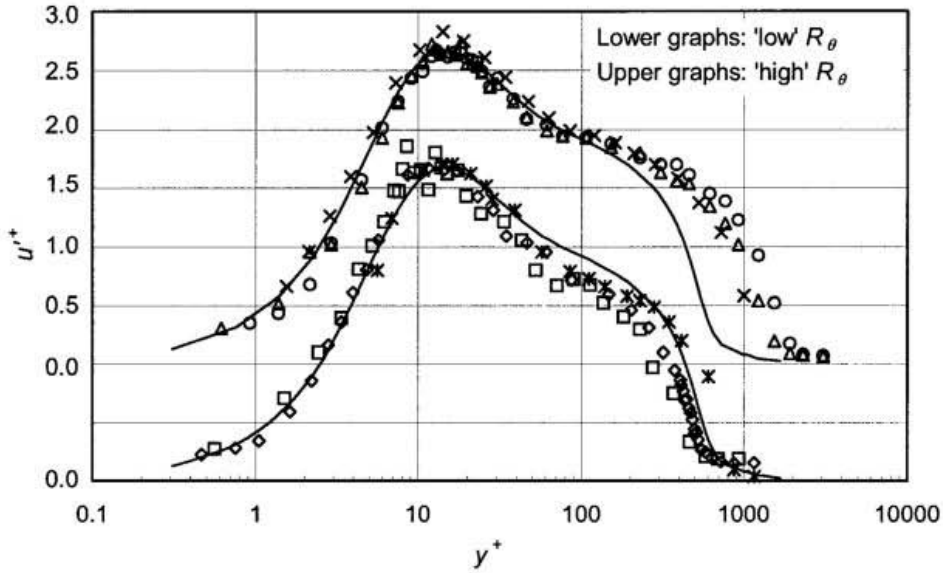

Fig. 4.3.1 Streamwise turbulence intensity profiles over a smooth-wall. Symbols: □, R_θ = 1030; ◇, 1250; Δ, 3200; ○, 4200; ∗, Purtell et. al (1981), R_θ = 1840; ×, DeGraaff and Eaton (2000), R_θ = 2900; ——, DNS (Spalart, 1988), R_θ =1410.

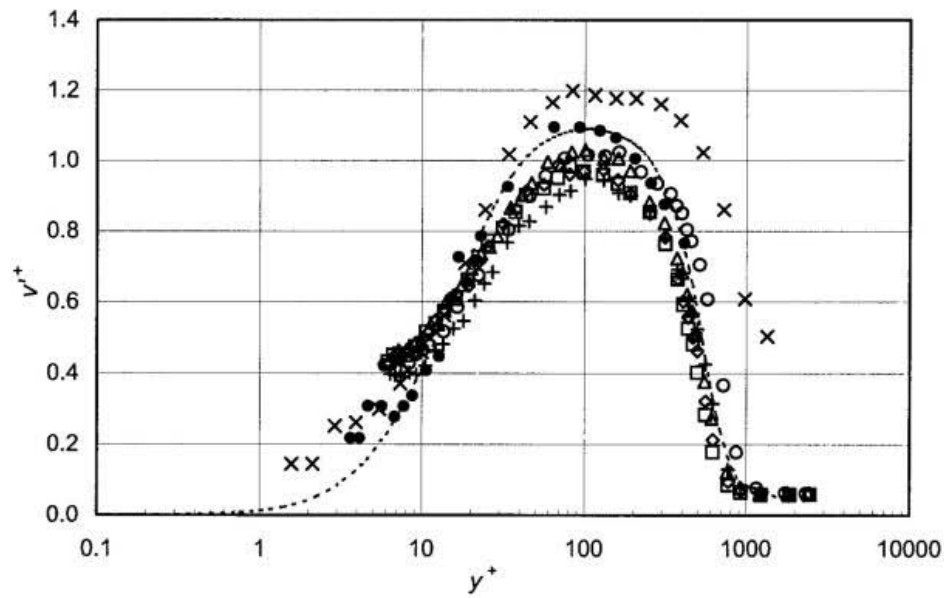

Fig. 4.3.2 Wall-normal turbulence intensity profiles over a smooth-wall. Symbols: □, R_θ = 960; ◇, 1050; Δ, 1150; +, 1350; ○, 1900; •, Djenidi et. al (1999), R_θ = 1400; × DeGraaff and Eaton (2000), R_θ = 2900; - - - -, DNS (Spalart, 1988), R_θ =1410.

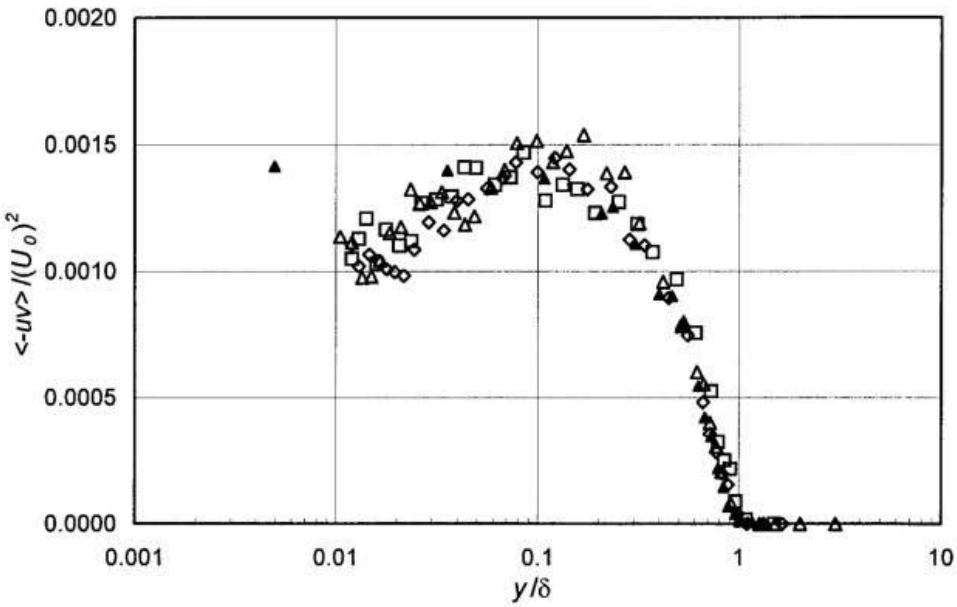

Fig. 4.3.3 Reynolds stress distribution on the smooth-wall. Symbols: □, R_θ = 950; ◇, 1050; △, 1250; ▲; Klebanoff (1955) data.

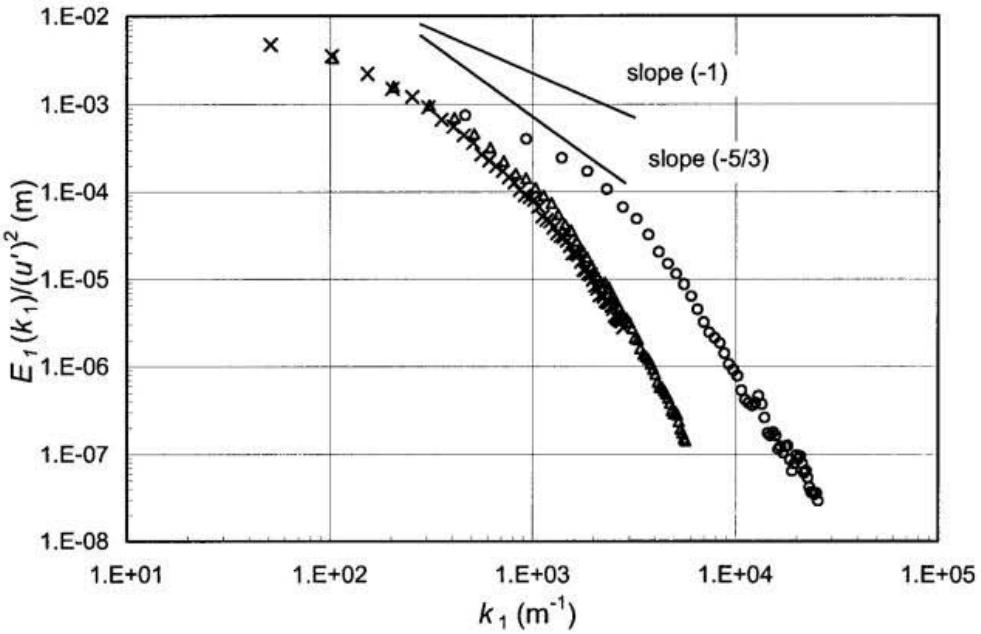

Fig. 4.3.4 Energy spectra of the streamwise velocity fluctuation at $R_\theta = 1000$. Symbols: ×, $y/\delta = 0.80$; Δ, $y/\delta = 0.02$; ○, $y/\delta = 0.004$;

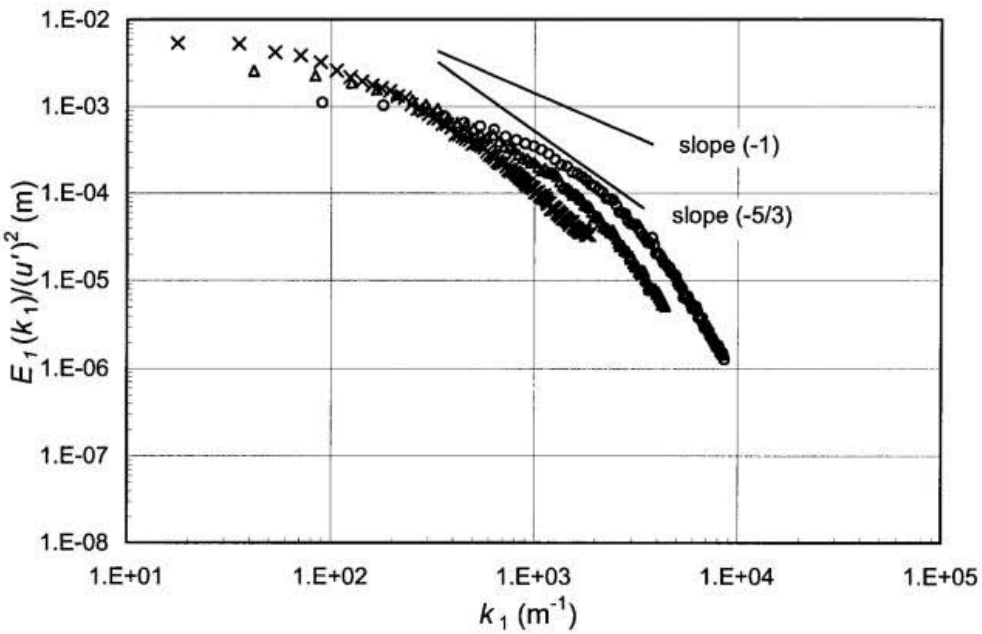

Fig. 4.3.5 Energy spectra of the streamwise velocity fluctuation at $R_\theta = 3000$. Symbols: ×, $y/\delta = 0.87$; Δ, $y/\delta = 0.02$; ○, $y/\delta = 0.003$;

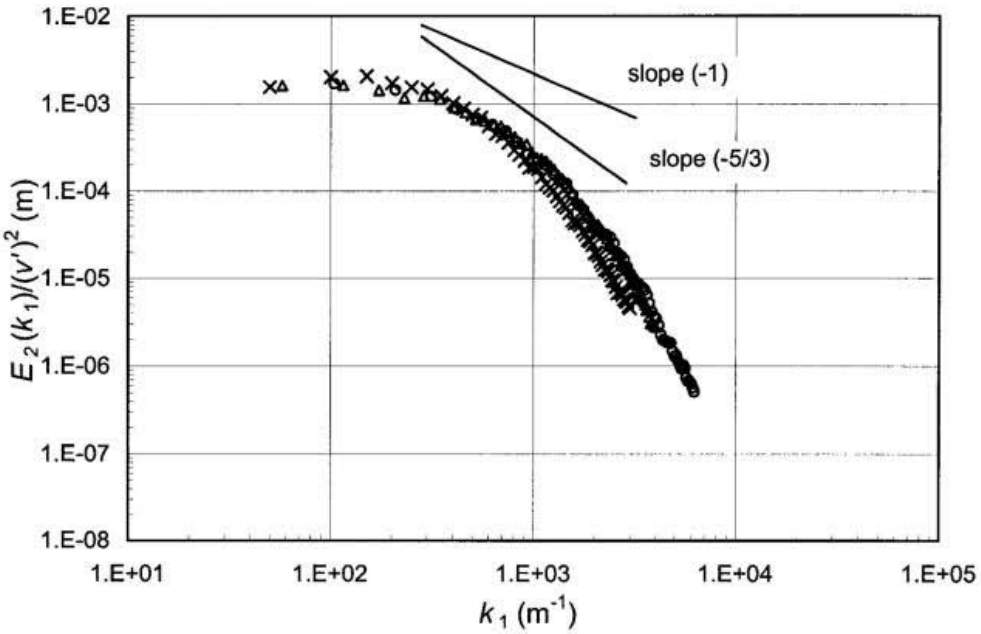

Fig. 4.3.6 Energy spectra of the wall-normal velocity fluctuation at $R_\theta = 1000$. Symbols: ×, $y/\delta = 0.80$; Δ, $y/\delta = 0.35$; ○, $y/\delta = 0.02$;

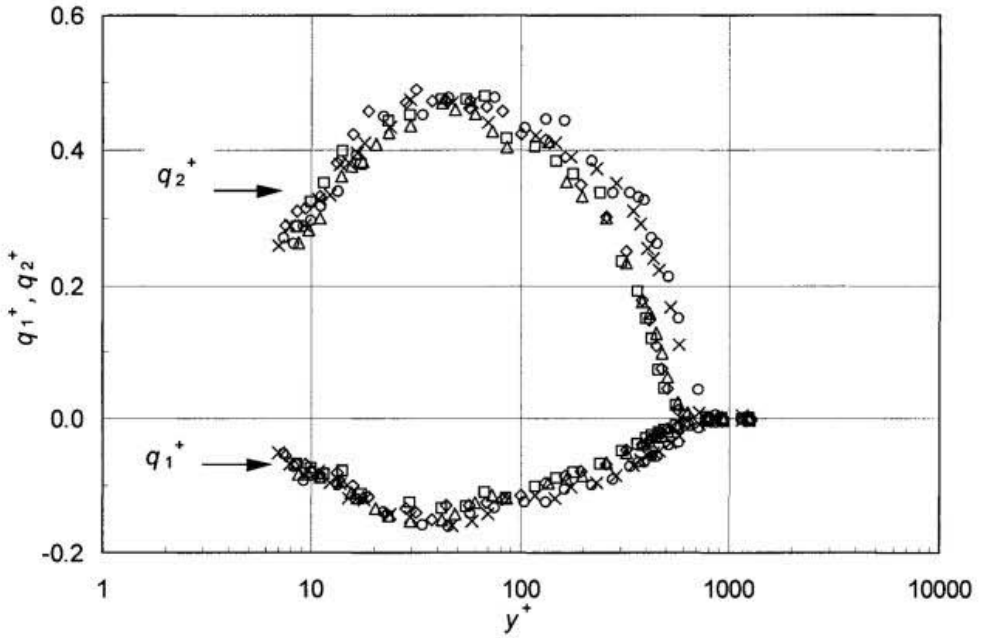

Fig. 4.4.1a Distribution of the first and second quadrants (q_1^+ and q_2^+) within the smooth-wall turbulent boundary layer. □, $R_\theta = 900$; ◇, $R_\theta = 950$; △, $R_\theta = 1050$; ×, $R_\theta = 1400$; ○, $R_\theta = 1900$. Lower graphs: q_1^+; upper graphs: q_2^+.

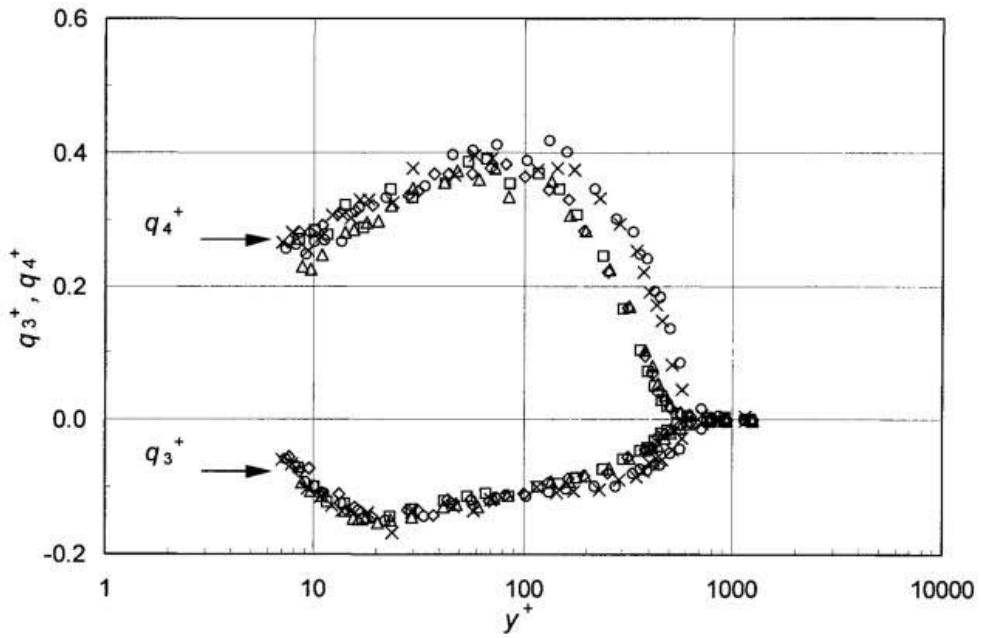

Fig. 4.4.1b Distribution of the third and fourth quadrants (q_3^+ and q_4^+) within the smooth-wall turbulent boundary layer. Symbols are as in Fig. 4.4.1a.
Lower graphs: q_3^+; upper graphs: q_4^+.

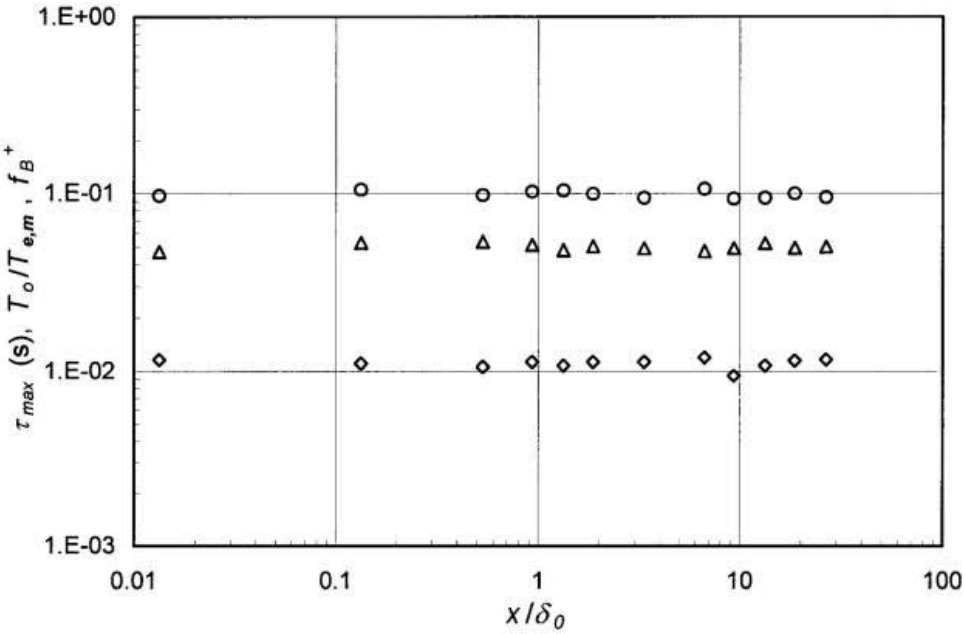

Fig. 4.4.2 Distribution of τ_{max}, $T_o/T_{e,m}$, and f_B^+ in the smooth-wall turbulent boundary layer at $R_\theta = 1000$. Sample time = 10 seconds. $y^+ = 14$. Δ, τ_{max}; ○, $T_o/T_{e,m}$; ◇, f_B^+.

Chapter 5

Results and Discussion: Effect of Groove Size

In this chapter, the experimental results of the turbulent boundary layer over the transverse square groove (SQ), semicircular base groove (SC), and triangular groove (TR) are presented and discussed. In sections 5.1 to 5.3, results from the different shaped grooves with the three different sizes are presented. In section 5.4, the results are discussed and summarized. The skin friction coefficient (C_f), mean velocity (U) and the growth of the internal layer (d_i) downstream of the grooves are presented. The streamwise and wall-normal turbulence intensities (u' and v'), Reynolds stress ($\langle -uv \rangle$), turbulence energy spectra ($E(k_1)$), sweep and ejection events and bursting frequency are also discussed. The emphasis in this chapter is on the effect of the groove size on the turbulence parameters. The effects of the three different shaped grooves are compared in the next chapter. The results over the grooved-wall are compared to the results from the

corresponding smooth-wall. The present experimental conditions and flow parameters together with related previous studies are given in Table 5.1.

Table 5.1. Experimental conditions and flow parameters

	d (mm)	U_0 (m/s)	R_θ	d/δ_0	$d^+ = u_\tau d/\nu$	d/w
Choi and Fujisawa (1993)¶	10	7.0	1250	0.400	210	1.0
Elavarasan et al. (1996)¶	5	0.4	1300	0.125	100	1.0
Pearson et al. (1997)¶	5	0.4	1320	0.170*	100	1.0
Present study	5	2.0	1000	0.067	32	1.0
(SQ-, SC- and TR-	10	2.0	1000	0.133	64	1.0
grooves)	20	2.0	1000	0.267	128	1.0
	5	5.5	3000	0.083	74	1.0
	10	5.5	3000	0.167	148	1.0
	20	5.5	3000	0.333	296	1.0

¶ Square groove experiments.
* Based on δ at 50 mm upstream of the groove leading edge.

5.1 Mean Measurements

5.1.1 Skin Friction Coefficient (C_f)

The distributions of $(C_f - C_{f,0})/C_{f,0}$ downstream of the SQ-, SC- and TR-grooves for the three different groove sizes are shown in Fig. 5.1.1a to 5.1.1f, where $C_{f,0}$ is the skin friction coefficient on the corresponding smooth-wall. The effect of all three groove shapes and sizes on C_f is qualitatively similar at both R_θ. At R_θ = 1000, there is an increase in C_f just downstream of the grooves followed by a decrease in C_f below the

smooth-wall value in the range $1 \leq x/\delta_0 \leq 3$. The C_f has relaxed back to the smooth-wall value at $x/\delta_0 \approx 4.0$ (Figs. 5.1.1a, 5.1.1c and 5.1.1e). The increase in C_f is more pronounced at $R_\theta = 3000$ (Figs. 5.1.1b, 5.1.1d and 5.1.1f). For the SQ-groove case, the maximum increase in C_f over the corresponding smooth-wall value for the 20, 10 and 5mm grooves are approximately 24, 14 and 4 percent at $R_\theta = 1000$. At $R_\theta = 3000$, the corresponding increase for the three sizes are 46, 26 and 10 percent. The local maximum increase and decrease in C_f for the SQ-, SC- and TR-grooves are presented in Table 5.1.1. For a given groove shape, a higher d^+ results in a higher increase in C_f just downstream of the grooves. On average, the maximum C_f is increased by approximately three times as the groove size is increased from 5 to 20mm.

The sharp rise in C_f just downstream of a SQ-groove was also observed by Pearson et al. (1997) and Elavarasan et al. (1996). Tani (1968), Andreopoulus and Wood (1982) and Pearson et al. (1998) found the same indication of a sharp rise in C_f after a sudden change in surface roughness. The present measurements, however, show a maximum increase in C_f of only 24 percent for the largest groove ($d/\delta_0 \approx 0.3$) compared to 100 percent and 200 percent, respectively, in the studies of Elavarasan et al. (1996) and Pearson et al. (1997), which were performed at approximately the same R_θ. The d/δ_0 of the present study is considerably larger than that of Elavarasan et al. and Pearson et al. The cause of the significant difference in the peak value of C_f of the present study and those two previous studies is not clear at this stage. The effect of d/δ_0 (and d^+) on $(C_f - C_{f,0})/C_{f,0}$ is presented in Table 5.1.1 together with the data from Elavarasan et al. (1996) and Pearson et al. (1997). It may be conjectured, that d/δ_0 must be larger than 0.1

(or $d^+ \geq 100$) to significantly affect the inner region of a turbulent boundary layer, and thus the wall shear stress (τ_w). The small local reduction in C_f of about 6 percent in the immediate vicinity of the SQ-groove (for $R_\theta = 1000$) is much smaller compared to the findings of Elavarasan et al. and Pearson et al., which found a reduction of approximately 50 percent.

Table 5.1.1. Effect of d/δ_0 and d^+ on $((C_f - C_{f,0})/C_{f,0})_{max}$ and $((C_f - C_{f,0})/C_{f,0})_{min}$

	R_θ	d/δ_0	$d^+ = u_\tau d/\nu$	$((C_f - C_{f,0})/C_{f,0})_{max}$ (%)			$((C_f - C_{f,0})/C_{f,0})_{min}$ (%)		
Pearson et al. (1997)[¶]	1320	0.170*	100	200			-50		
Elavarasan et al. (1996)[¶]	1300	0.125	100	100			-50		
	Groove shapes			SQ	SC	TR	SQ	SC	TR
	1000	0.067	32	4	12	5	-6	-5	-6
		0.133	64	14	16	12	-5	-8	-6
		0.267	128	24	22	20	-4	-11	-6
Present study	3000	0.083	74	10	9	9	-5	-8	-2
		0.167	148	26	12	27	-8	-8	-4
		0.333	296	46	32	27	-11	-8	-6

[¶] Square groove experiments.

* Based on δ at 50 mm upstream of the groove leading edge.

For the 20mm SQ- and TR-grooves (Figs. 5.1.1a and 5.1.1e), C_f relaxes back to the corresponding smooth-wall value in an oscillatory manner at $R_\theta = 1000$. Pearson et al. also found this oscillatory relaxation downstream of a square groove. The relaxation of C_f

is complete at approximately $3\delta_0$, while Pearson et al. found the relaxation of C_f takes much longer ($12\delta_0$). For the smaller SQ- and TR-grooves and all the SC-grooves (Figs. 5.1.1a, 5.1.1c and 5.1.1e), the oscillatory behavior is absent.

5.1.2 Streamwise Mean Velocity (U)

Mean velocity profiles at seven representative x-locations normalized using outer variables (U_0 and δ) over the SQ-, SC- and TR-grooves at R_θ = 1000 and 3000 are presented in Figs. 5.1.2a to 5.1.2f. The profiles for the corresponding smooth-wall (with no groove) are also presented in these figures for comparison. Mean velocity measurements were also performed farther downstream of the groove up to $x/\delta_0 \approx 27$ for the three different shaped and sized grooves at both R_θ. Although the profiles are not shown here, they show good collapse with the corresponding smooth-wall profiles beyond $x/\delta_0 \approx 1.867$.

At the lower R_θ, the effect of the grooves on U/U_0 is very weak. The U/U_0 profiles downstream of the three groove shapes for d = 10 and 5mm collapse with the smooth-wall profile (Fig. 5.1.2a, 5.1.2c and 5.1.2e). There is a small discernible increase in U/U_0 in the region $y/\delta \leq 0.01$ for the 20mm groove immediately downstream of the SQ-groove (x/δ_0 = 0.013), with the profiles farther downstream showing good collapse with the smooth-wall profiles (Fig. 5.1.2a). For the SC-groove, the profile of the 20mm groove falls below the corresponding smooth-wall profile in the log-region at $x/\delta_0 = 0.013$ (Fig. 5.1.2c). The profiles relax back to the corresponding smooth-wall profiles very quickly. For the TR-groove, the U/U_0 profiles also decrease in the buffer region just downstream

of the 20mm groove, while the profiles are shifted up slightly in the region $y/\delta \leq 0.01$, before they relax back to the smooth-wall profiles at $x/\delta_0 = 0.267$ (Fig. 5.1.2e).

At the higher R_θ, the effect of the grooves on U/U_0 is more pronounced (Fig. 5.1.2b, 5.1.2d and 5.1.2f). For the SQ-groove, the effect of the 5mm groove on U/U_0 is less significant than the effect of the 10 and 20mm grooves, especially at locations closer to the groove ($x/\delta_0 = 0.013$). An increase in U/U_0 up to approximately 20 percent for the SQ-groove with d = 10 and 20mm is discernible in the region $y/\delta \leq 0.01$ at $x/\delta_0 = 0.013$ (Fig. 5.1.2b). A decrease in U/U_0 in the buffer region is observed for the 20mm groove, which is absent for the smaller grooves. By $x/\delta_0 \approx 1.0$, the U/U_0 profiles have relaxed back to the smooth-wall profile. For the SC-groove, there is a small increase in U/U_0 from the smooth-wall profile in the region $y/\delta \leq 0.01$ at $x/\delta_0 = 0.013$ due to the 20mm groove. The effect of the 10 and 5mm grooves on U/U_0 cannot be differentiated and the U/U_0 profiles downstream of the grooves collapse well with the smooth-wall profiles. A decrease in U/U_0 downstream of the 20mm SC-groove is discernible in the region $0.015 \leq y/\delta \leq 0.06$ up to $x/\delta_0 = 0.267$ (Fig. 5.1.2d).

The U/U_0 profiles over the TR-grooves behave slight differently from those over the SQ- and SC-grooves at the higher R_θ. The U/U_0 profiles over the 5mm groove are not distinguishable from U/U_0 profiles on the smooth-wall in the region $y/\delta \geq 0.03$ (Fig. 5.1.2f). In the range $y/\delta \leq 0.02$, however, the U/U_0 profiles for the 5mm groove are shifted down from the smooth-wall profiles up to $x/\delta_0 = 0.067$. On the contrary, the U/U_0 profiles for the 10 and 20mm grooves are shifted up slightly in this region with the shift being larger for the 20mm groove. The downward shift in U/U_0 for the 20mm groove is

discernible in the region $0.02 \leq y/\delta \leq 0.06$ up to $x/\delta_0 = 0.133$, whereas the shift for the 10 and 5mm grooves is not clear here. Beyond $x/\delta_0 = 0.267$, the U/U_0 profiles for all sized grooves collapse well with the smooth-wall profile.

While the mean velocity profiles (U/U_0) for the different groove shapes and sizes indicate that relaxation back to the smooth-wall profiles is complete at $x \approx 2.0\delta_0$ (Fig. 5.1.2a to 5.1.2f), the wall shear stress (τ_w) shows a deviation from the smooth-wall value up to $x \approx 3\delta_0$. This indicates that $(dU/dy)_{y=0}$, is much more sensitive to the perturbation since τ_w is determined from the $(dU/dy)_{y=0}$. This is in agreement with the suggestion of Smits and Wood (1985) that the relaxation length depends on the order of the statistical moment of the turbulence quantities. For example, the wall shear stress (τ_w), which is deduced from $(dU/dy)_{y=0}$, should relax slower than the mean velocity (U).

The mean velocity profiles normalized using inner variables (u_τ and ν) are shown in Fig. 5.1.3a to 5.1.3f. The log-law lines for the smooth-wall profiles are also shown in the figures for comparison. There is a considerable shift of the profiles from the smooth-wall profiles at locations away from the wall, especially for the 20mm groove. At the lower R_θ, the effect of the 5 and 10mm grooves on U^+ is not significant (Figs. 5.1.3a, 5.1.3c and 5.1.3e), with the exception of the 10mm SC-groove at $x/\delta_0 = 0.133$ and 0.267. At these two particular locations, the profiles are shifted down, reflecting an increase in C_f. At $R_\theta = 1000$, the largest downward shift of U^+ profiles occurs at $x/\delta_0 = 0.267$ and 0.067, respectively, for the SQ- and SC-grooves (Fig. 5.1.3a and 5.1.3c). For the TR-groove (Fig. 5.1.3e), a shift in U^+ is not as clear as for the SQ- and SC-grooves, because C_f in this case is not much different from the corresponding smooth-wall values. At $R_\theta =$

3000, the effect of the grooves on U^+ is more significant, with the largest downward shift at $x/\delta_0 = 0.013$ for all groove shapes with $d = 20$mm (Figs. 5.1.3b, 5.1.3d and 5.1.3f). At this particular x-location, small downward shifts in U^+ due to the 10mm groove for all shapes are observed, while the effect of the 5mm groove is not significant.

5.1.3 Internal Layer (d_i)

The growth of the internal layer (d_i) as a response of the turbulent boundary layer to the presence of the grooves is shown in Figs. 5.1.4a to 5.1.4f. The d_i was determined using the method of Antonia and Luxton (1971a,b), see Section 3.2.3. The rate of growth of d_i is higher for $R_\theta = 3000$ than that for $R_\theta = 1000$. The higher rate of growth of d_i at $R_\theta = 3000$ is a consequence of the more pronounced effect of the groove on the boundary layer at the higher R_θ, where d^+ of the groove is more than twice that at the lower R_θ (see Table 5.1.1). For a given groove shape and R_θ, the initial rate of growth of d_i is a function of the groove size. The initial rate of growth of d_i is very rapid and followed by a much slower growth rate beyond $x/\delta_0 = 0.5$.

For all three groove shapes, d_i is affected by the groove size (d) at both R_θ. For example, at the lower R_θ, at $x/\delta_0 = 1.9$, $d_i/\delta_0 \approx 0.09$, 0.08 and 0.075, respectively, for $d =$ 20, 10 and 5mm. At the higher R_θ for the SQ-groove, d_i/δ_0 is approximately 0.12, 0.11 and 0.10 for $d = 20$, 10 and 5mm, respectively, at $x/\delta_0 = 2$. At the same x-location and at the higher R_θ, the d_i/δ_0 for the SC- and TR-grooves are slightly smaller than that for SQ-groove, with d_i/δ_0 approximately 0.11, 0.10 and 0.09, respectively, for $d = 20$, 10 and

5mm, respectively, for both SC- and TR-grooves. The dependence of d_i on d for a given R_θ and groove shape is consistent with the effect of the groove size on C_f and U.

The distribution of the internal layer thickness (d_i) of the present study is slightly different from the results obtained by Elavarasan et al. (1996). Although the normalized thickness of d_i (i.e. d_i/δ_0) is similar in both studies, the rate of growth of d_i is different (Figs. 5.1.4a and 5.1.4b). The d_i in the study of Elavarasan et al. (R_θ= 1300) grows faster than that for the present study in the region $x/\delta_0 \leq 0.1$. In the region $x/\delta_0 \geq 1.0$, however, the rate of growth of d_i is almost similar for both studies. This difference is probably reflected in the difference in the maximum increase in C_f just downstream of the groove in the two studies as discussed in section 5.1.1.

5.2 Turbulence Measurements

5.2.1 Streamwise Turbulence Intensity (u')

The streamwise turbulence intensity (u'/U_0) profiles downstream of the different sized grooves are presented in Figs. 5.2.1a to 5.2.1f. At R_θ = 1000, there is an increase in u'/U_0 immediately downstream of the SQ-groove (x/δ_0 = 0.013) in the region $0.007 \leq y/\delta \leq 0.02$ (Fig. 5.2.1a). The increase is more pronounced for the larger sized groove. For the 20mm groove, there is a discernible peak in the region where u'/U_0 is increased. This peak is not present at the next measurement location (x/δ_0 = 0.047), as the effect of the groove on u'/U_0 weakens as it propagates out in the layer. There is, however, an increase in u'/U_0 for all three sized grooves in the region $0.007 \leq y/\delta \leq 0.03$ at this x-location. The increase is still discernible at x/δ_0 = 0.067 for the two larger sized grooves, while u'/U_0

has relaxed back to the smooth-wall profile for the 5mm groove. For the SC-groove, u'/U_0 is increased significantly in the region $0.005 \leq y/\delta \leq 0.03$ for the 20mm groove at the first three x-locations ($x/\delta_0 = 0.013$, 0.047 and 0.067) (Fig. 5.2.1c). At $x/\delta_0 = 0.013$ and 0.047, the increase in u'/U_0 is a function of d, where the increase is maximum for $d =$ 20mm and minimum for $d =$ 5mm. With the 20 and 10mm grooves, the maximum increase in u'/U_0 is up to approximately 20 and 10 percent, respectively, in the region $0.005 \leq y/\delta \leq 0.03$. At the same x-locations, the increase in u'/U_0 due to the 5mm groove in the region $0.008 \leq y/\delta \leq 0.02$ is approximately 5 percent. The increase in u'/U_0 at $x/\delta_0 =$ 0.067 due to the 5 and 10mm groove is, however, comparable. The u'/U_0 does not increase significantly above the maximum value for the corresponding smooth-wall case. For the TR-groove, the increase in u'/U_0 is a function of the groove size up to $x/\delta_0 =$ 0.067, and is independent of the groove size at $x/\delta_0 = 0.267$ and beyond (Fig. 5.2.1e). At the lower R_θ, the effect of the 5mm groove is less pronounced than that of the 10 and 20mm grooves. With the 20 and 10mm grooves, u'/U_0 is increased up to approximately 25 percent and 20 percent, respectively, over the local smooth-wall value in the region $y/\delta \leq 0.05$. With the 5mm groove, however, the increase in u'/U_0 is approximately 10 percent in the region $y/\delta \leq 0.025$. Moreover, the maximum value $(u'/U_0)_{max}$ for the 20mm groove is approximately 13 percent higher than the corresponding smooth-wall value at $x/\delta_0 =$ 0.013, 0.047 and 0.067. The $(u'/U_0)_{max}$ for the 10mm is also increased up to approximately 10 percent at $x/\delta_0 = 0.047$, while $(u'/U_0)_{max}$ for the 5mm groove does not increase above the smooth-wall value. The relaxation of u'/U_0 for all grooves is not complete by $x/\delta_0 = 1.867$ at $R_\theta = 1000$.

At $R_\theta = 3000$, the 20mm groove also has a more significant effect on u'/U_0 than the 10 and 5mm grooves for the three different shaped grooves. At $x/\delta_0 = 0.013$, the increase in u'/U_0 due to the 20mm SQ-groove is discernible in the range $0.004 \leq y/\delta \leq 0.06$ (Fig. 5.2.1b), with the maximum increase being about 30 percent over the corresponding smooth-wall value, and occurs at $y/\delta \approx 0.005$. At $x/\delta_0 = 0.013$, an increase in u'/U_0 in the region $0.005 \leq y/\delta \leq 0.01$ up to approximately 10 and 8 percent, respectively, for the 10 and 5mm SQ-grooves is observed. At $x/\delta_0 = 0.267$, the u'/U_0 profiles for the 10 and 5mm grooves are not distinguishable, whereas the u'/U_0 profile for the 20mm groove is different. The profile for the latter groove size is shifted down in the region $0.002 \leq y/\delta \leq 0.01$ and shifted up in the region $0.03 \leq y/\delta \leq 0.1$. The relaxation is complete at $x/\delta_0 = 1.867$ for the three different sized SQ-grooves at this R_θ. There is an increase in u'/U_0 in the range $0.005 \leq y/\delta \leq 0.01$ immediately downstream of the SC-groove with $d = 20$mm (Fig. 5.2.1d), with the maximum increase about 10 percent over the corresponding smooth-wall value. At $x/\delta_0 = 0.267$, u'/U_0 is increased in the range $0.025 \leq y/\delta \leq 0.09$, while it is shifted slightly down in the region $y/\delta \leq 0.02$. The downward shift of u'/U_0 is persistent up to $x/\delta_0 = 0.933$, before it recovers to the smooth-wall value at $x/\delta_0 = 1.867$. The u'/U_0 profiles for the 10 and 5mm SC-groove at $x/\delta_0 = 0.013$ and 0.047 cannot be differentiated from the smooth-wall profiles. The profiles for the latter groove sizes are, however, shifted down in the range $y/\delta \leq 0.01$ at locations $0.067 \leq x/\delta_0 \leq 0.933$, before they relax back to the smooth-wall profile at $x/\delta_0 = 1.867$. For the 20 and 10mm TR-grooves, u'/U_0 is increased by about 20 and 10 percent, respectively, in the range $0.006 \leq y/\delta \leq 0.07$ at $x/\delta_0 = 0.013$ (Fig. 5.2.1f). For the 20mm

TR-groove, at $x/\delta_0 = 0.267$, an increase in u'/U_0 in the range $0.04 \leq y/\delta \leq 0.08$ and a decrease in u'/U_0 in the region $0.01 \leq y/\delta \leq 0.03$ is still discernible. The profiles for the 10 and 5mm grooves relax back to the smooth-wall profile by $x/\delta_0 = 0.267$, while it takes much longer for the 20mm groove, with relaxation complete at $x/\delta_0 = 1.867$.

The distribution of u'_{max} normalized by u'_{max} on the smooth-wall ($u'_{max,sw}$) downstream of the grooves are shown in Figs. 5.2.2a to 5.2.2f. For the SQ- and SC-grooves, u'_{max} does not significantly increase above the $u'_{max,sw}$ at either R_θ (Figs. 5.2.2a to 5.2.2d), with u'_{max} within ± 8 percent of $u'_{max,sw}$. For the TR-groove, on the contrary, there is an increase in u'_{max} up to approximately 13 percent over the $u'_{max,sw}$ at $R_\theta = 1000$, especially at locations immediately downstream of the groove for the 20mm groove (Fig. 5.2.2e).

The u'^+ profiles ($u'^+ \equiv u'/u_\tau$) for the different grooves are shown in Figs. 5.2.3a to 5.2.3f together with the corresponding u'^+ profiles on the smooth-wall. For the SQ- and SC-grooves, the effect of the 10 and 5mm grooves on u'^+ are less pronounced compared to the 20mm groove at $R_\theta = 1000$ (Figs. 5.2.3a and 5.2.3c). For the 20mm SQ- and SC-grooves, as x/δ_0 increases, there is a downward shift of the profiles due to the increase in C_f. The downward shift in u'^+ for the SQ-groove is highest at $x/\delta_0 = 0.267$, reflecting the high C_f at this location. A downward shift in u'^+ is also seen for the SC-groove (Fig. 5.2.3c), although the shift is not as large as that for the SQ-groove. In the case of the TR-groove (Fig. 5.2.3e), the u'^+ profiles for all three sizes collapse with the corresponding

smooth-wall profile. This is due to the increase in u' being on the same order of magnitude as the increase in u_τ at the particular streamwise location.

At $R_\theta = 3000$, in general, the u'^+ profiles collapse with the corresponding smooth-wall profile for all three groove shapes, except for the largest groove ($d = 20$mm). For the largest groove, an upward shift in u'^+ is still discernible at $y^+ \approx 40$ at $x/\delta_0 = 0.013$ for all shapes, although the u_τ is significantly increased at this location. This means that the increase in u' for the 20mm groove is much larger than that for the smaller grooves for all three groove shapes.

5.2.2 Wall-Normal Turbulence Intensity (v')

The wall-normal turbulence intensity profiles (v'/U_0) at $R_\theta = 1000$ are shown in Figs. 5.2.4a to 5.2.4c. The increase in v'/U_0 is more significant than the increase in u'/U_0 with the 20mm groove for all three different shaped grooves. The effect of the smaller grooves (5 and 10mm) on v'/U_0, however, is much less significant. For the 20mm SQ-groove, (v'/U_0) is increased by up to approximately 50 percent in the region $y/\delta \leq 0.1$ at $x/\delta_0 = 0.013$ (Fig. 5.2.4a), compared to a corresponding increase of approximately 30 percent for u'/U_0. For the 20mm SQ-groove, the increase is still discernible in the region $y/\delta \leq 0.1$ at $x/\delta_0 = 1.867$. The profiles for the smaller sized grooves have collapsed with the smooth-wall profile at this x-location. For the 20 and 10mm SC-groove, v'/U_0 is increased up to approximately 25 percent in the region $y/\delta \leq 0.05$ at $x/\delta_0 = 0.013$ (Figs. 5.2.4b), while the effect of the 5mm groove is not discernible. At $x/\delta_0 = 1.867$, the v'/U_0 profiles for the 20 and 10mm SC-grooves have not completely relaxed back to the

smooth-wall profile. For the 20mm TR-groove, the increase in v'/U_0 is approximately 25 percent over the corresponding smooth-wall value at $x/\delta_0 = 0.013$. For this groove, the v'/U_0 profile has not relaxed back to the smooth-wall profile by $x/\delta_0 = 1.867$. The effect of the grooves on v'/U_0 is less pronounced as x increases for all three groove shapes (Figs. 5.2.4a to 5.2.4c). It can be speculated that the sudden absence of the solid wall due to the groove amplifies v'/U_0. The larger groove should, therefore, result in a higher increase in v'/U_0 than the smaller groove. It should be noted that the measurements for (v'/U_0) were obtained only for the lower R_θ due to the inability of obtaining near-wall measurements at the higher R_θ with the present X-wire.

5.2.3 Reynolds Stress ($\langle -uv \rangle$)

The Reynolds stress ($\langle -uv \rangle/(U_0)^2$) profiles at $R_\theta = 1000$ are presented in Figs. 5.2.5a to 5.2.5c. The scatter in the data in the region $y/\delta \leq 0.1$ is similar to the studies of Antonia (1994), Antonia et al. (1995) and Mochizuki and Osaka (1998). Despite the scatter in the data, certain features are clearly seen, especially for the largest groove size. For example, at the location just downstream of the groove ($x/\delta_0 = 0.013$), there is an increase in $\langle -uv \rangle/(U_0)^2$ due to the 20mm groove for all three shapes. The increase in $\langle -uv \rangle/(U_0)^2$ for all three groove shapes at $x/\delta_0 = 0.013$ is also associated with an increase in u'/U_0 and v'/U_0. For the TR-groove, an increase in $\langle -uv \rangle/(U_0)^2$ due to the 10mm groove is also discernible. As the downstream distance increases, $\langle -uv \rangle/(U_0)^2$ for all three groove sizes collapses better but is higher than the corresponding smooth-wall value in the region $y/\delta \leq 0.1$. For the 20mm groove for all shapes, an increase in $\langle -uv \rangle/(U_0)^2$ by

approximately 40 percent is observed in the region $y/\delta < 0.1$ at $x/\delta_0 = 1.867$. The relaxation of $\langle -uv \rangle/(U_0)^2$ takes longer than that for u'/U_0 and v'/U_0, as $\langle -uv \rangle/(U_0)^2$ is not relaxed completely at $x/\delta_0 = 1.867$. Andreopoulus and Wood (1982) also found that the maximum increase in $\langle -uv \rangle/(U_0)^2$ occurred further downstream at $x/\delta_0 \approx 3.5$, instead of just downstream of the step change. Webster et al. (1996) found that the maximum increase in $\langle -uv \rangle/(U_0)^2$ occurred even farther downstream of the step change at $x/\delta_0 \approx 10$.

5.2.4 Turbulence Energy Spectra ($E(k_1)$)

Representative turbulence energy spectra for u', on the smooth- and grooved-walls at $R_\theta = 1000$ and 3000 for the three different shaped grooves are shown in Figs. 5.2.6a to 5.2.6f. The spectra are at the streamwise location immediately downstream of the grooves ($x/\delta_0 = 0.013$) and at the y-location where the turbulence intensity is maximum ($y/\delta \approx 0.03$; $y^+ \approx 14$). For $R_\theta = 1000$, the effect of the SQ-groove on the spectra of u' (or $E_1(k_1)/(u')^2$) is discernible at the higher k_1 range (Fig. 5.2.6a). At $k_1 \geq 2000\text{m}^{-1}$, $E_1(k_1)/(u')^2$ for the 5mm groove is lower than the smooth-wall and larger grooved-wall values. For the SC- and TR-grooves, the spectra for all groove sizes, on the other hand, collapse well over the entire k_1 range at $R_\theta = 1000$ (Figs. 5.2.6c and 5.2.6e).

At $R_\theta = 3000$, the effect of the grooves on $E_1(k_1)/(u')^2$ is to reduce the turbulent energy level at $k_1 \leq 500\text{m}^{-1}$ and to increase the energy level at $k_1 \geq 1000\text{m}^{-1}$ for the three groove shapes (Figs. 5.2.6b, 5.2.6d and 5.2.6f). The spectra of u' on the grooved-walls are decreased up to approximately 30 percent for $k_1 \leq 500\text{m}^{-1}$ and increased up to approximately 100 percent for $k_1 \geq 1000\text{m}^{-1}$. The spectra for the SQ- and SC- grooves

with d = 20mm are higher than for the spectra with d = 5mm and 10mm at $k_1 \geq 1000\text{m}^{-1}$. For the TR-groove, the spectrum of u' for the 20mm groove is also greater than for the smaller grooves in the range $k_1 \geq 2000\text{m}^{-1}$. The increase in the spectra of u' is consistent with the increase in u'/U_0 as discussed in the previous section. Direct comparison between $E_1(k_1)/(u')^2$ at the lower and higher R_θ reveals that as k_1 increases the energy content at the lower R_θ drops rapidly compared to that at the higher R_θ. For example, at a k_1 of approximately 2000m^{-1}, the energy content at the lower R_θ is already approximately one decade lower than that at the higher R_θ.

The spectra of v' (or $E_2(k_1)/(v')^2$) at R_θ = 1000 are spread over two decades in k_1 and over four decades in the energy level (Figs. 5.2.7a to 5.2.7c). The change in the spectra of v' with the groove size at a given k_1 is more significant than that for the spectra of u' at the same R_θ. For example, in the range $k_1 \geq 1000\text{m}^{-1}$, the spectra for d = 20mm is the highest, followed by the spectra for d = 10mm and 5mm. Also, at $k_1 \leq 400\text{m}^{-1}$, a decrease in $E_2(k_1)/(v')^2$ for the three grooves is observed, which is not discernible for $E_1(k_1)/(u')^2$. This is consistent with the results for u'/U_0 and v'/U_0, where the effect of the grooves on v'/U_0 is much more significant than that on u'/U_0. The decrease in the energy level at the lower k_1 for $E_2(k_1)/(v')^2$ is offset with an increase in the energy level at the higher k_1.

The –5/3 and –1-slopes are shown in Figs. 5.2.6a to 5.2.6f and Figs. 5.2.7a to 5.2.7c for comparison with the smooth-wall turbulent energy spectra. The most dominant energy containing eddies closely follow the –1-slope rather than the –5/3-slope. This is in

agreement with the finding of Klebanoff (1955) for the energy spectrum in the near-wall region of a turbulent boundary layer over a flat plate.

5.3 Sweep and Ejection Events and Bursting Frequency

Based on the quadrant decomposition (e.g. Wallace et al., 1972; Wilmarth and Lu, 1972; Brodkey et al., 1974), sweep and ejection events occur in the fourth and second quadrant, respectively. These two events contribute the most to the total Reynolds stress compared to the other two events (i.e. the first and third quadrants), as evident from the present results on the smooth-wall experiments (Sections 3.2.4 and 4.4). The distribution of the ejection and sweep events (q_2^+ and q_4^+, respectively) across the layer normalized by $(u_\tau)^2$ for the three different sized transverse SQ-grooves just downstream of the groove ($x/\delta_0 = 0.013$) are shown in Figs. 5.3.1a and 5.3.1b. Similar figures for the SC- and TR-grooves are shown in Figs. 5.3.1c and 5.3.1d and Figs. 5.3.1e and 5.3.1f, respectively. For the 20mm SQ-groove, there is a significant increase in q_2^+ and q_4^+ in the region $10 \leq y^+ \leq 100$ ($0.02 \leq y/\delta \leq 0.2$). The effect of the smaller grooves (5 and 10mm grooves) on q_2^+ and q_4^+ are, however, not discernible. The increases in q_2^+ and q_4^+ for the 20mm SQ-groove are in agreement with the increase in $\langle -uv \rangle/(U_0)^2$ (Fig. 5.2.5a). For the 20mm SC-groove, the increase in q_2^+ and q_4^+ is significant in the region $10 \leq y^+ \leq 30$ ($0.02 \leq y/\delta \leq 0.06$) (Figs. 5.3.1c and 5.3.1d). On the contrary, there is a reduction in q_2^+ due to the 5mm groove in the region $10 \leq y^+ \leq 200$ ($0.02 \leq y/\delta \leq 0.4$). This is consistent with the decrease in $\langle -uv \rangle/(U_0)^2$ for this case (Fig. 5.2.5b). In the case of the TR-grooves, a small decrease in q_2^+ and q_4^+ due to the 20mm groove is discernible in the region $50 \leq y^+ \leq 200$

($0.1 \leq y/\delta \leq 0.4$) (Figs. 5.3.1e and 5.3.1f). This decrease is caused by the high value of C_f for the 20mm TR-groove at this particular x-location. The effects of the 5 and 10mm grooves on q_2^+ and q_4^+ are not significant in this instance.

The distributions of q_1^+ and q_3^+ are shown in Figs. 5.3.2a to 5.3.2f. The effect of the 20mm groove on q_1^+ and q_3^+ is more significant than the effect of the 10 and 5mm grooves for the three different shaped grooves. For the SQ-groove, the effect of the 20mm groove on q_1^+ is felt up to $y^+ \approx 50$ ($y/\delta \approx 0.1$) (Fig. 5.3.2a), while the effect of this sized groove on q_3^+ is limited to the region $y^+ \leq 30$ ($y/\delta \leq 0.06$) (Fig. 5.3.2b). With the 20mm SQ-groove, the contributions of q_1^+, q_2^+, q_3^+ and q_4^+ to $\langle -uv \rangle/(U_0)^2$ are comparable, at least in the region very close to the wall (say $y^+ \leq 20$ or $y/\delta \leq 0.04$). This is not the case for the smaller groove sizes (5 and 10mm grooves), and also for the smooth-wall case, where in the region $y^+ \leq 20$ the contributions of q_1^+ and q_3^+ to $\langle -uv \rangle/(U_0)^2$ are much smaller than the contributions of q_2^+ and q_4^+. For the SC-grooves, the increase in both q_1^+ and q_3^+ is again more pronounced for the 20mm groove compared to the smaller grooves. There is an increase in q_1^+ and q_3^+ for the 10mm SC-groove in the range $y^+ \leq 20$, whereas the effect of the 5mm groove on q_1^+ and q_3^+ is not significant in this instance (Figs. 5.3.2c and 5.3.2d). For the TR-grooves, an increase in q_1^+ and q_3^+ in the range $y^+ \leq 14$ is observed, with the most pronounced being for the 20mm groove. In summary, q_1^+, q_2^+, q_3^+ and q_4^+ are affected the most by the 20mm groove, while the effects of the 5 and 10mm grooves are small.

The downstream distribution of bursting frequency (f_B) normalized using inner variables (ν and u_τ) at $R_\theta = 1000$ is shown in Fig. 5.3.3a to 5.3.3c. The f_B is calculated

using the second quadrant method as described by Bogard and Tiederman (1986), and is obtained at approximately the same y^+ value. For the present study, the y-location is chosen so that $y/\delta \approx 0.03$ ($y^+ \approx 14$), while Bogard and Tiederman obtained most measurements at $y^+ \approx 15$. The 20mm groove increases f_B^+ significantly, especially for the SQ-groove. On average, f_B^+ for the 20mm SQ-, SC- and TR-grooves are approximately 20, 16 and 9 percent, respectively, higher than f_B^+ over the smooth-wall case. The corresponding increases for the 10mm grooves are 5, 13 and 4 percent. The f_B^+ over the 5mm groove shows no significant difference from the smooth-wall case for the three different shaped grooves. The increase in f_B^+ for the two larger sizes for all three groove shapes is in agreement with the increase in the Reynolds stress ($\langle -uv \rangle/(U_0)^2$) (Figs. 5.2.5a to c).

5.4 Discussion and Summary

This discussion is focussed on the effect of the different groove sizes on the turbulent characteristics over the grooved-walls. In general, the mean quantities, including wall shear stress (τ_w), mean velocity (U) and the internal layer thickness (d_i), are affected the most by the largest groove (d = 20mm) for all three groove shapes. Similarly, the turbulent quantities, including turbulence intensities (u' and v'), Reynolds stress ($\langle -uv \rangle$) and turbulent energy spectra ($E(k_1)$), deviate the most from the corresponding smooth-wall values for the largest groove. All quadrants (q_1^+, q_2^+, q_3^+ and q_4^+) contributing to $\langle -uv \rangle$ and the bursting frequency (f_B^+) are significantly increased for

the 20mm groove. The effect of the smaller grooves (d = 5 and 10mm) on the mean and turbulent quantities, and on q_1^+, q_2^+, q_3^+, q_4^+ and f_B^+, on the contrary, is less significant for all three groove shapes at either R_θ.

There is a significant interaction between the flow in the groove and the boundary layer as first observed by Townes and Sabersky (1966). There are periodic ejections of fluid from the groove to the outer layer, and this is likely to affect the turbulence characteristics downstream of the groove. The ejection of fluid from a transverse square groove was also observed by Ching et al. (1995b). A schematic of the fluid ejection for the three grooves, adopted from Ching et al. (1995b), is shown in Fig. 5.4.1. In the study of Ching et al., one value of groove depth (d = 5mm) was used; therefore, the size of the ejected fluid out from the groove as shown in the diagram must be typical. In the present study, three different sized SQ-grooves were used with the ratios of the groove depth to the thickness of the oncoming boundary layer (δ_0) of approximately 0.07, 0.13 and 0.27 at R_θ = 1000. The thickness of the oncoming boundary layer (δ_0) relative to the groove size (d) is also shown in Fig. 5.4.1 for comparison. It can be conjectured that the typical size of the ejected fluid from the different sized grooves must scale with the groove size. Assume that the ejected fluid from the groove is carried a distance l_f over a height h_f (Fig. 5.4c). At a given R_θ, the ratio of l_f/δ_0 and h_f/δ_0 should increase with the groove size (Figs. 5.4.1b and 5.4.1c). The disturbance to the boundary layer near the groove caused by the largest groove should, therefore, be the most pronounced. The more intense disturbance from the larger grooves is reflected by the more pronounced effect of the grooves on the turbulent characteristics.

The difference of the mean and turbulence quantities over the grooved-wall from those on the smooth-wall is less distinguishable as the streamwise location increases, except for the groove with d = 20mm at the higher R_θ. For the latter groove size, the increases in U and u' propagate outward as x increases, before they relax at x/δ_0 = 1.867. Moreover, the effect of the groove diminishes as y increases, and by approximately y/δ = 0.1, the mean velocity and turbulence intensities are the same as the smooth-wall values. The Reynolds stress, on the other hand, recovers to the smooth-wall value by approximately y/δ = 0.5.

The main conclusions can be summarized as follows:

(1) At either R_θ, there is an increase in C_f just downstream of the grooves. For the SQ-groove at R_θ = 1000, the maximum increase of C_f is approximately 24, 14 and 4 percent, respectively, for d = 20, 10 and 5mm, compared to 22, 16 and 12 percent for the SC-groove and 20, 12 and 5 percent for the TR-groove. At R_θ = 3000, the maximum increase in C_f is approximately 46, 26 and 10 percent for the SQ-groove, 32, 12 and 9 percent for the SC-groove, and 27, 27 and 9 percent for the TR-groove. There is a small local reduction in C_f immediately after the increase, where the maximum reduction is about 11 percent.

(2) At the higher R_θ, there is an increase in U/U_0 with the groove size over the corresponding smooth-wall value in the near-wall region immediately downstream of the SQ- and SC-grooves. For the TR-groove, on the other hand, there is an increase in U/U_0 for the 10 and 20mm grooves, while the U/U_0 is decreased slightly for the 5mm

groove immediately downstream of the grooves. The effect of the grooves on U/U_0 is much less significant at the lower R_θ.

(3) For a given R_θ and groove shape, the height of d_i is proportional to the groove size. The internal layer grows rapidly immediately downstream of the groove, followed by a much slower growth rate beyond $x/\delta_0 = 0.5$.

(4) The effect of the 20mm groove on u'/U_0 and v'/U_0 is more significant than for the 10 and 5mm grooves. For the 20mm groove, an increase in u'/U_0 up to approximately 30 percent was observed, while the corresponding increases are approximately 10 and 8 percent for the 10 and 5mm grooves. The increase in u'/U_0 is more pronounced at the higher R_θ and propagates away from the wall as x increases. The effect of the grooves on v'/U_0 is more significant than that on u'/U_0, with the maximum increase of approximately 50 percent for v'/U_0 compared to approximately 20 percent for u'/U_0 at the same R_θ. The relaxation of v'/U_0 for the 20mm groove is not complete by $x/\delta_0 = 1.867$, while it has relaxed completely for the smaller grooves at this x-location.

(5) For a given groove shape, the effect of the groove on the Reynolds stress ($\langle -uv \rangle/(U_0)^2$) is more significant for the larger groove size than for the smaller grooves. The increase in $\langle -uv \rangle/(U_0)^2$ for the 20mm groove reaches up to approximately 40 percent over the corresponding smooth-wall value.

(6) The presence of the grooves modifies the turbulent energy content. The increase in $E_1(k_1)/(u')^2$ for $R_\theta = 3000$ and $E_2(k_1)/(v')^2$ for $R_\theta = 1000$ at the higher k_1 range for the 20mm groove is more significant than that for the 10 and 5mm grooves. For a given groove shape, the spectra of $E_1(k_1)/(u')^2$ at $R_\theta = 1000$ for all groove sizes are almost

the same as the spectra on the smooth-wall over the entire k_1 range, except for the 5mm SQ-groove. For the latter groove, a small decrease in $E_1(k_1)/(u')^2$ at $R_\theta = 1000$ is, however, discernible at the higher k_1.

(7) At $R_\theta = 1000$, the increase in the ejection and sweep events (q_2^+ and q_4^+) and the normalized bursting frequency (f_B^+) just downstream of the groove due to the 20mm groove are more pronounced. The f_B^+ immediately downstream of the 20 and 10mm SQ-grooves is approximately 20 and 5 percent higher, respectively, than the corresponding smooth-wall value. With $d = 20$ and 10mm, the increases in f_B^+ for the SC- and TR-grooves are smaller than the increase in f_B^+ for the SQ-groove. The effect of the 5mm groove for all shapes on f_B^+ is not significant.

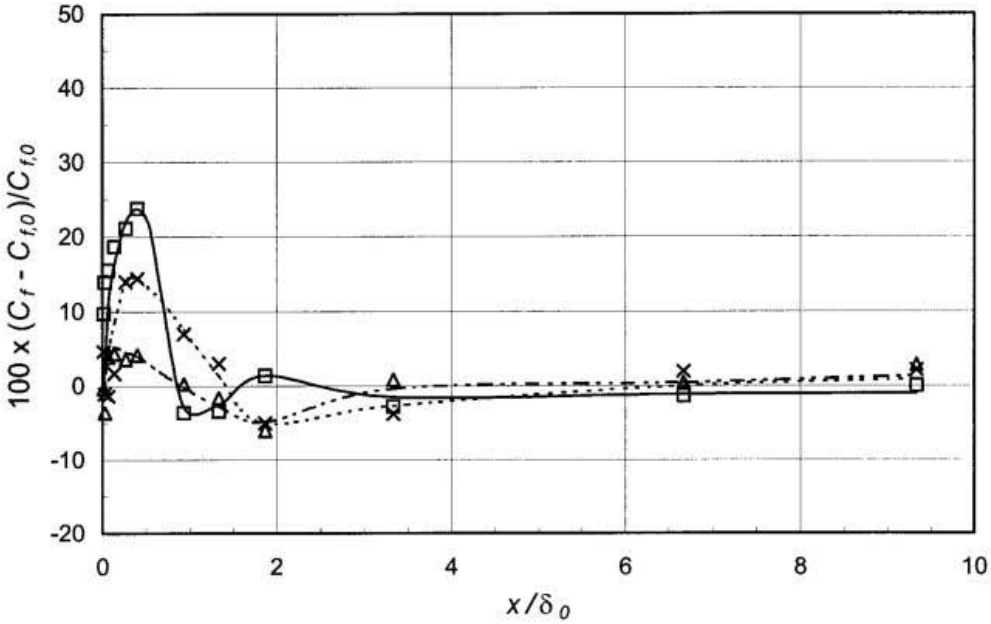

Fig. 5.1.1a Skin friction distribution downstream of the different sized SQ-grooves at R_θ = 1000: Δ, d = 5mm; ×, d = 10mm; □, d = 20mm.

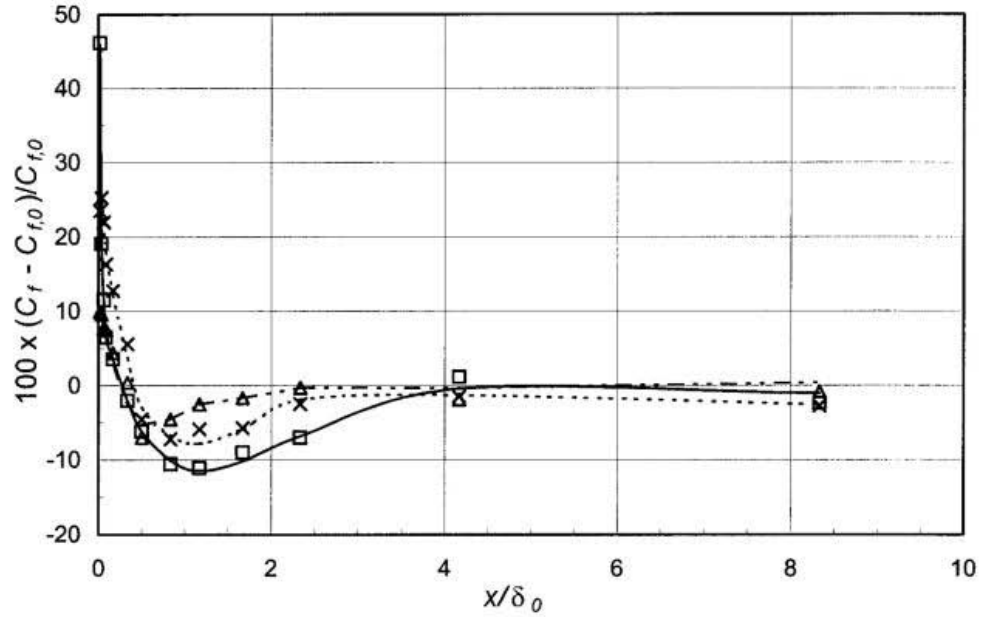

Fig. 5.1.1b Skin friction distribution downstream of the different sized SQ-grooves at R_θ = 3000. Δ, d = 5mm; ×, d = 10mm; □, d = 20mm.

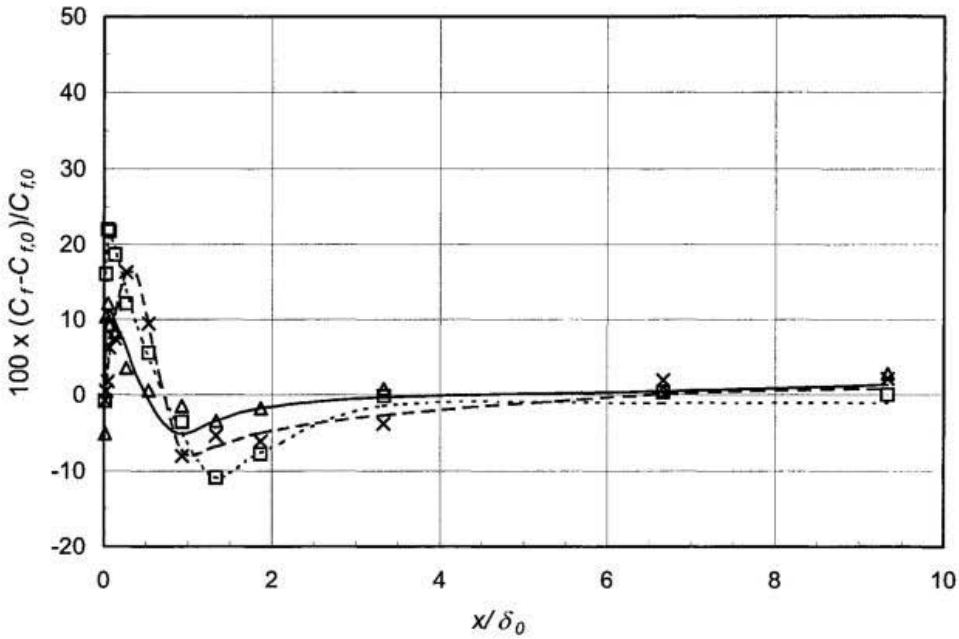

Fig. 5.1.1c Skin friction distribution downstream of the different sized SC-grooves at R_θ = 1000: Δ, d = 5mm; ×, d = 10mm; □, d = 20mm.

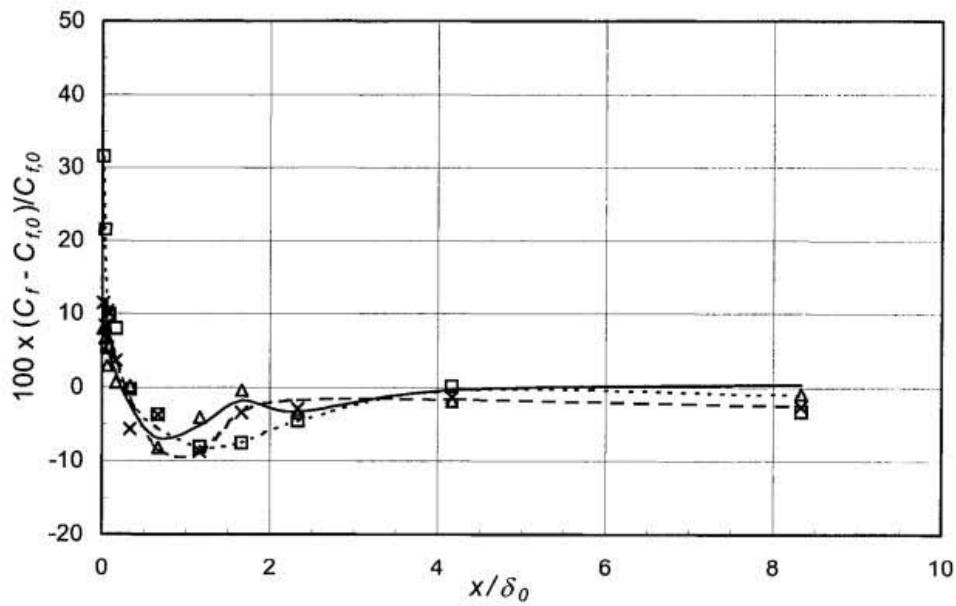

Fig. 5.1.1d Skin friction distribution downstream of the different sized SC-grooves at R_θ = 3000: Δ, d = 5mm; ×, d = 10mm; □, d = 20mm.

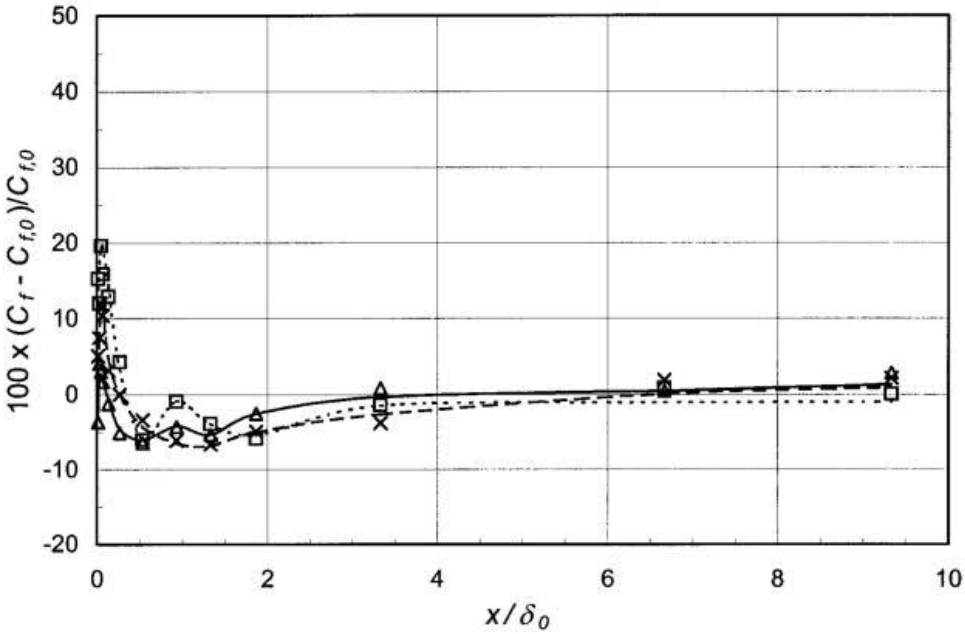

Fig. 5.1.1e Skin friction distribution downstream of three different sized TR-grooves at $R_\theta = 1000$: △, $d = 5$mm; ×, $d = 10$mm; □, $d = 20$mm.

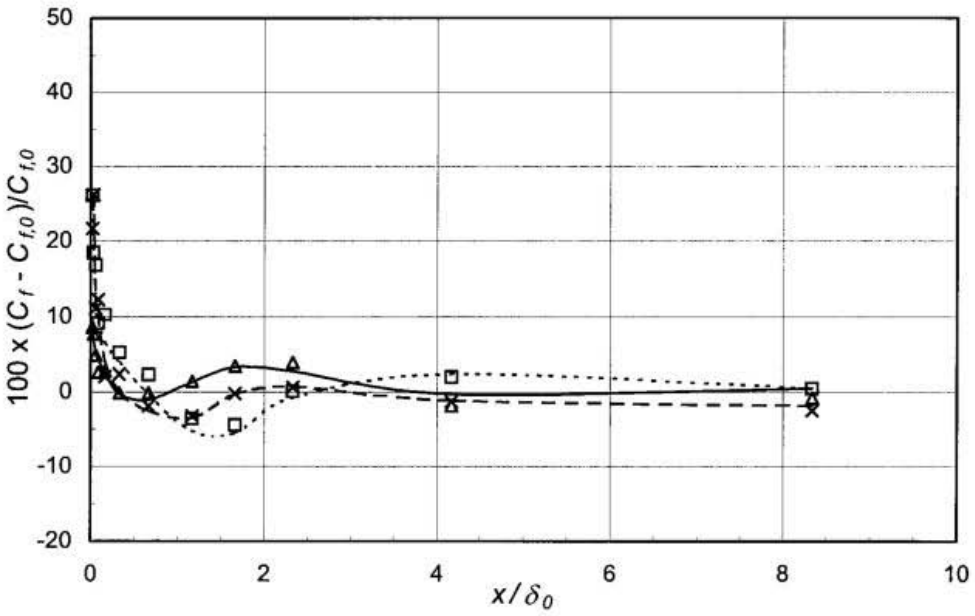

Fig. 5.1.1f Skin friction distribution downstream of three different sized TR-grooves at $R_\theta = 3000$: △, $d = 5$mm; ×, $d = 10$mm; □, $d = 20$mm.

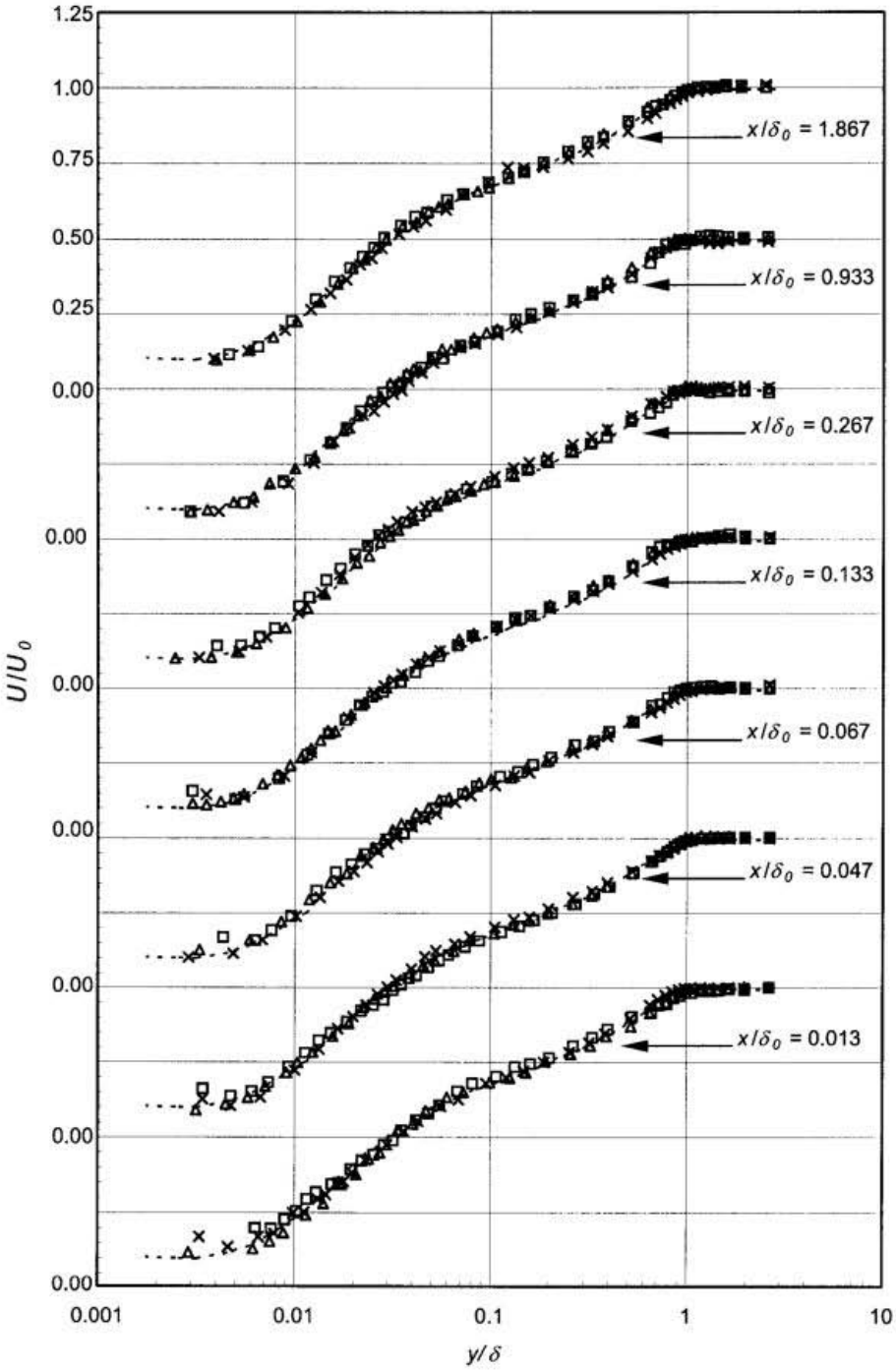

Fig. 5.1.2a Streamwise mean velocity profiles downstream of the SQ-grooves, $R_\theta = 1000$. △, d = 5mm; ×, d = 10mm; □, d = 20mm; ------, smooth-wall.

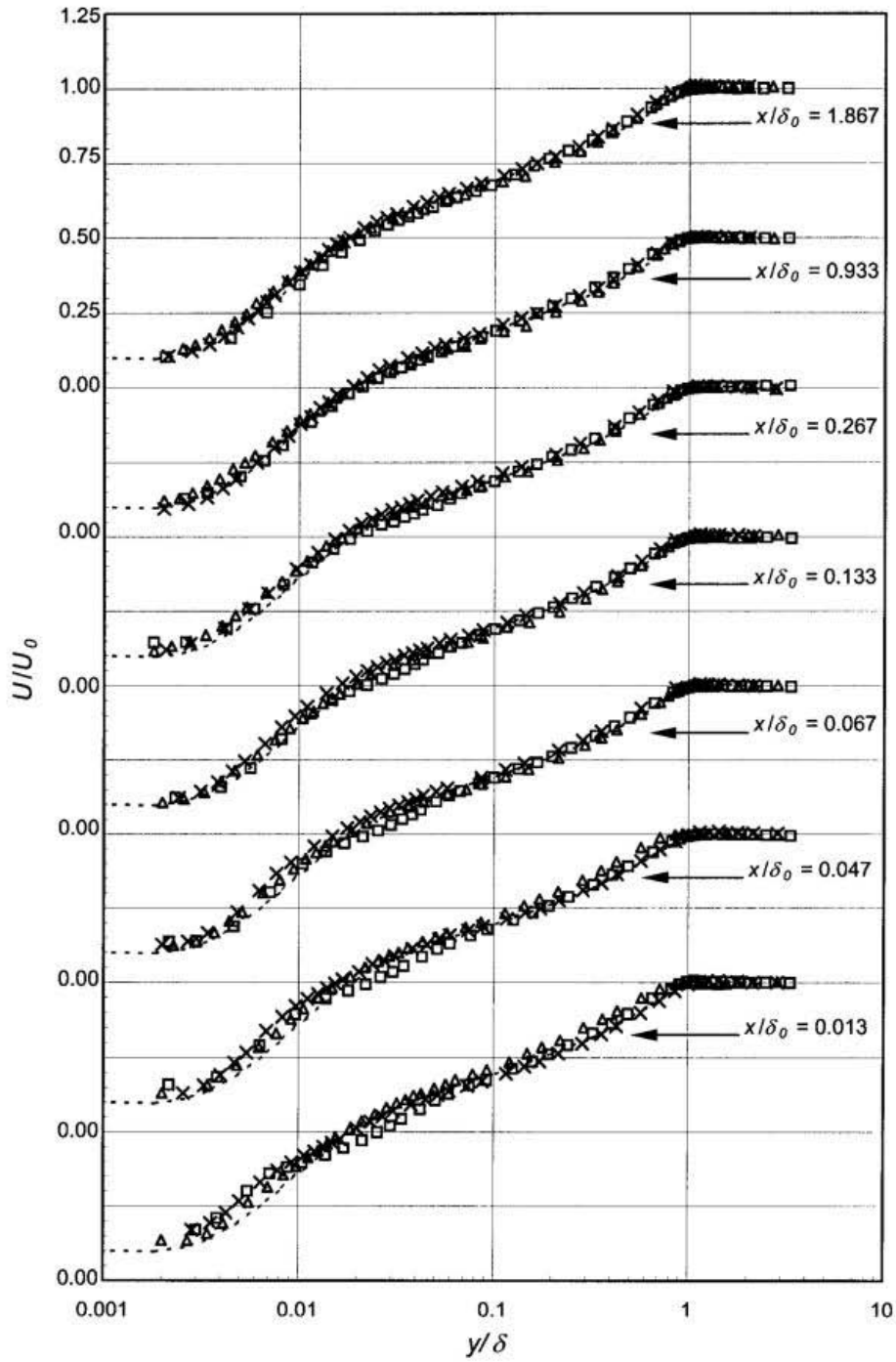

Fig. 5.1.2b Streamwise mean velocity profiles downstream of the SQ-grooves, $R_\theta = 3000$. △, $d = 5$mm; ×, $d = 10$mm; □, $d = 20$mm; -------, smooth-wall.

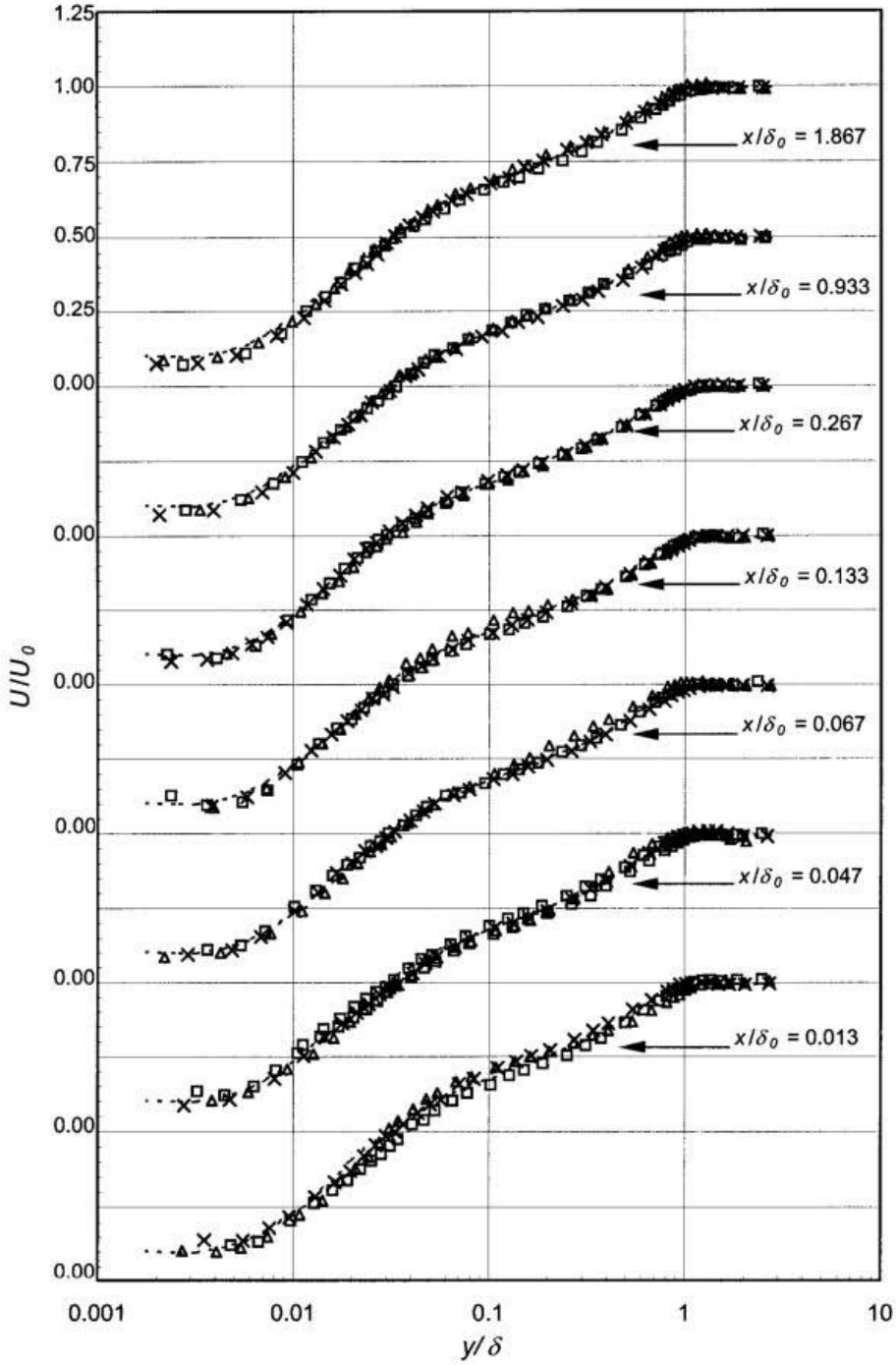

Fig. 5.1.2c Streamwise mean velocity profiles downstream of the SC-grooves, $R_\theta = 1000$. △, $d = 5$mm; ×, $d = 10$mm; □, $d = 20$mm; ------, smooth-wall.

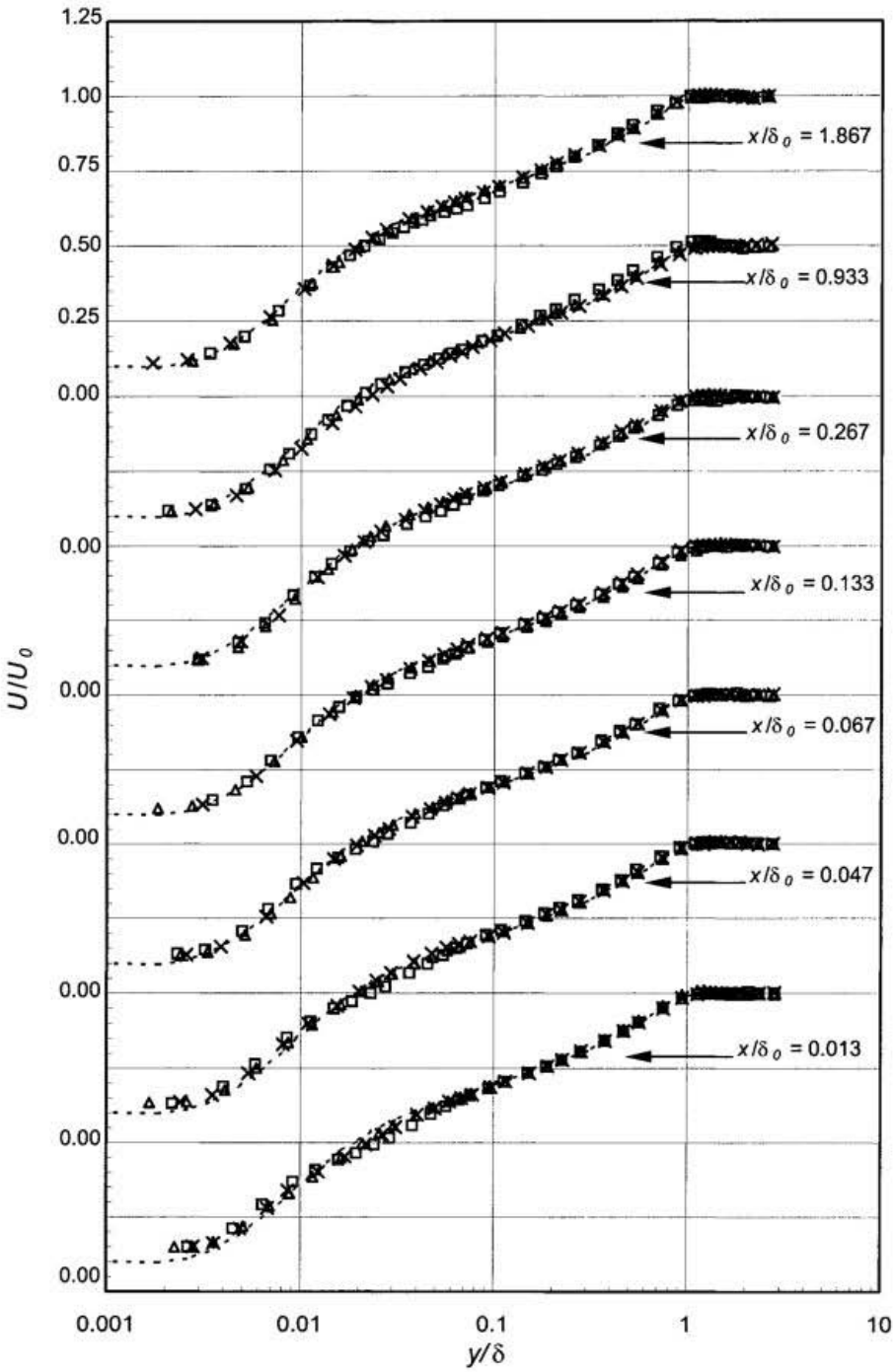

Fig. 5.1.2d Streamwise mean velocity profiles downstream of the SC-grooves, $R_\theta = 3000$. △, $d = 5$mm; ×, $d = 10$mm; □, $d = 20$mm; -------, smooth-wall.

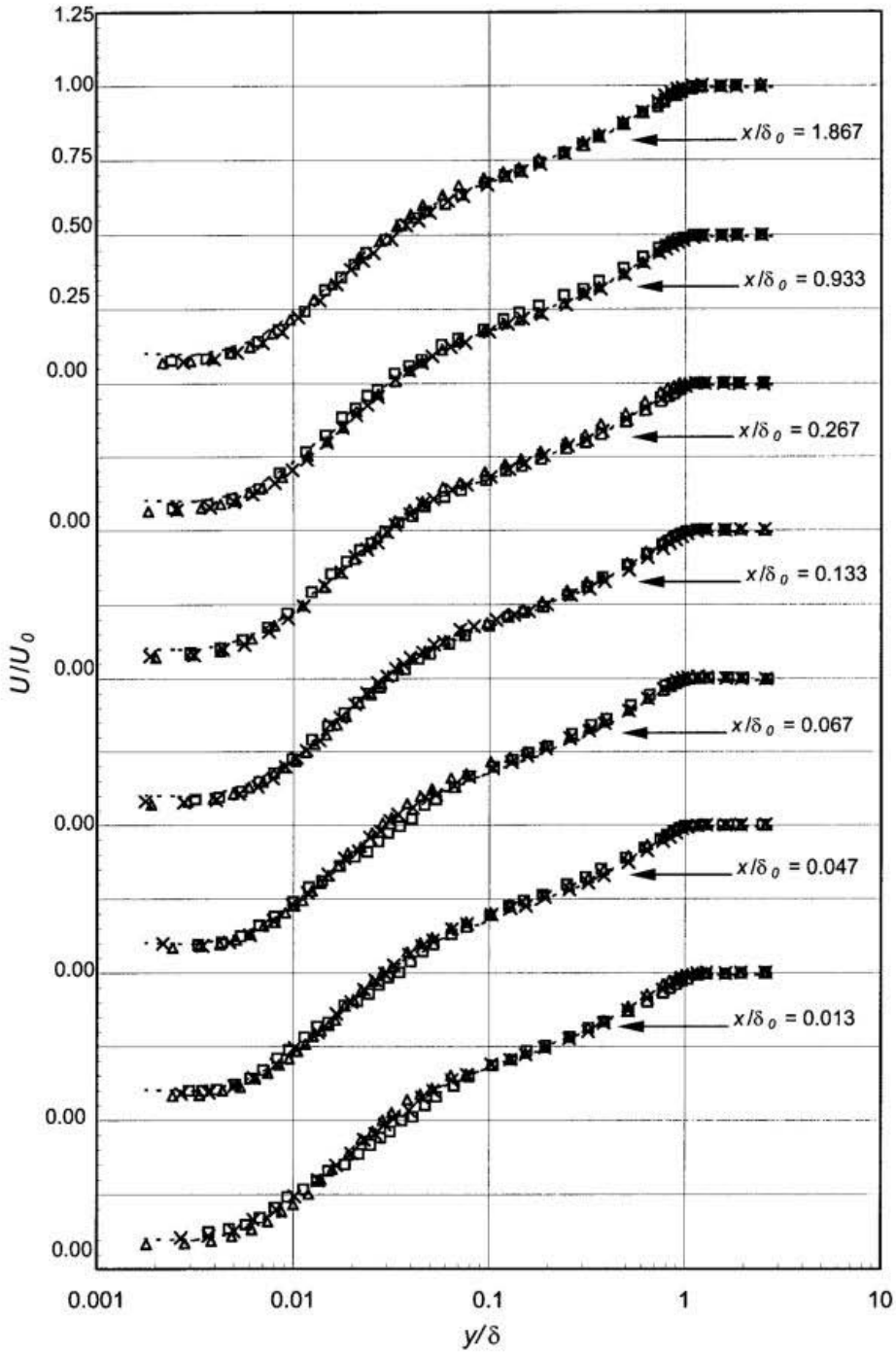

Fig. 5.1.2e Streamwise mean velocity profiles downstream of the TR-grooves, $R_\theta = 1000$. △, $d = 5$mm; ×, $d = 10$mm; □, $d = 20$mm; ------, smooth-wall.

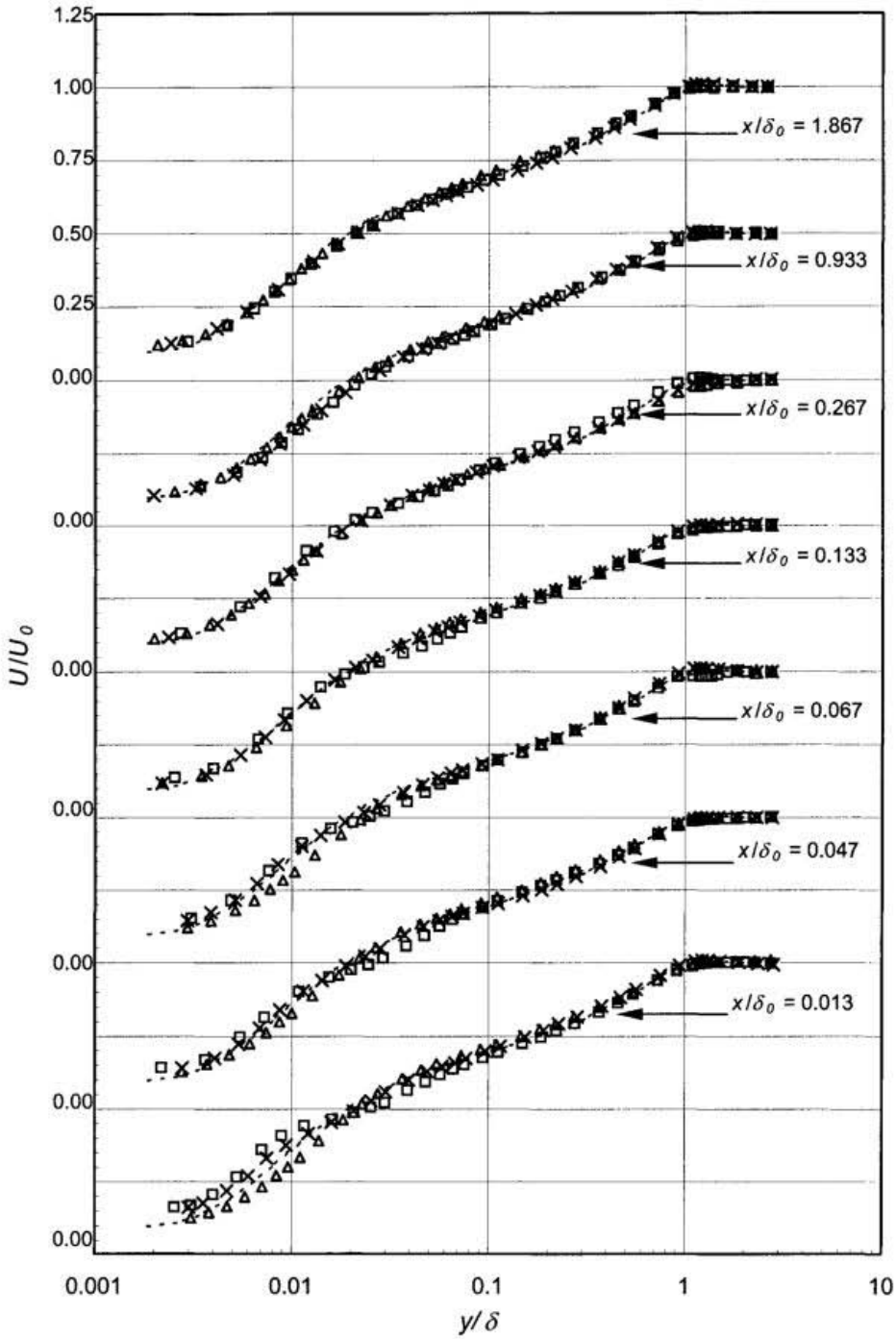

Fig. 5.1.2f Streamwise mean velocity profiles downstream of the TR-grooves, $R_\theta = 3000$. △, d = 5mm; ×, d = 10mm; □, d = 20mm; -------, smooth-wall.

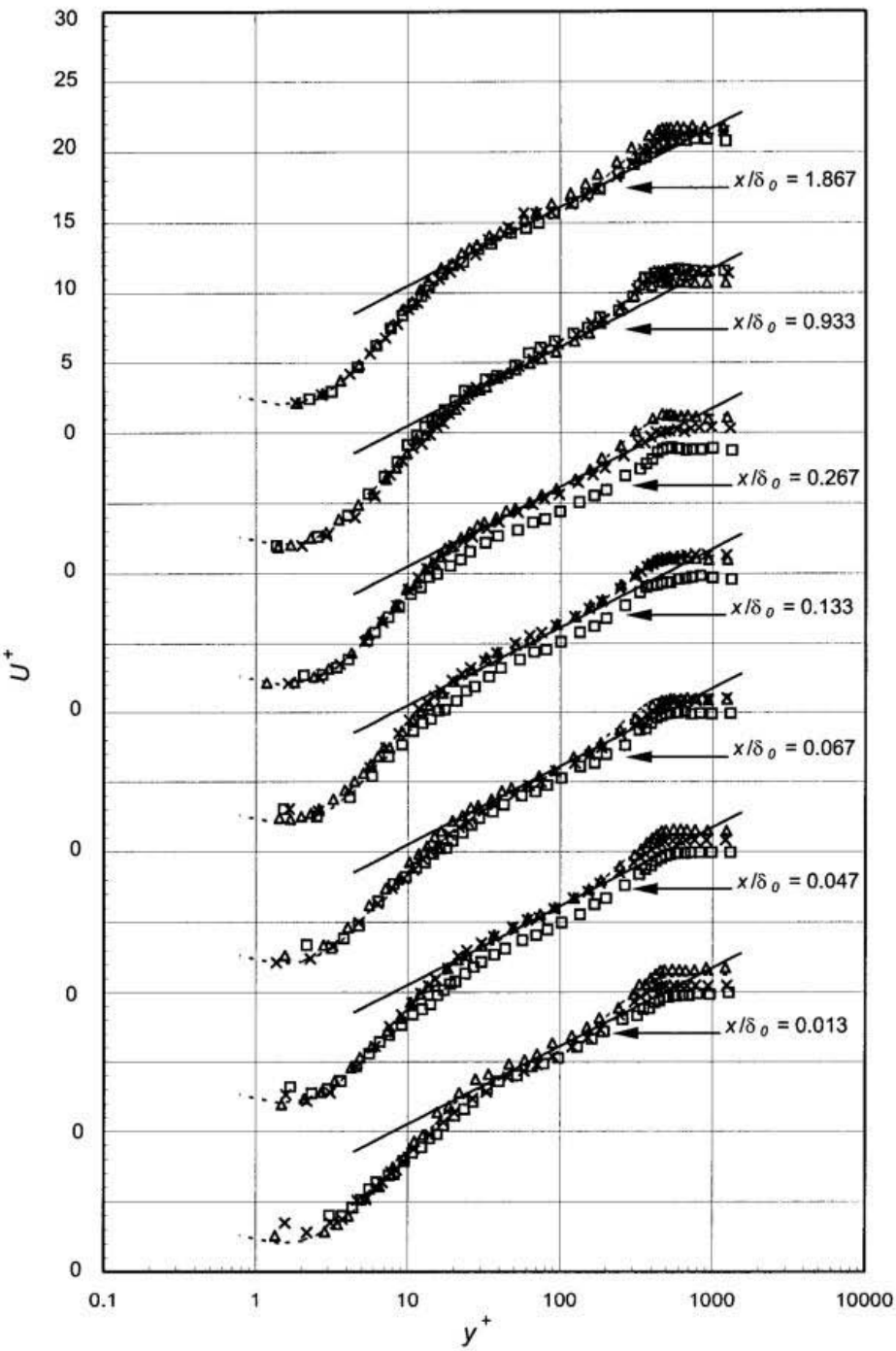

Fig. 5.1.3a Streamwise mean velocity profiles downstream of the SQ-grooves, R_θ = 1000. △, d = 5mm; ×, d = 10mm; □, d = 20mm; -------, smooth-wall. ——, Log-line, $U^+ = (1/0.41)\ ln\ y^+ + 4.9$.

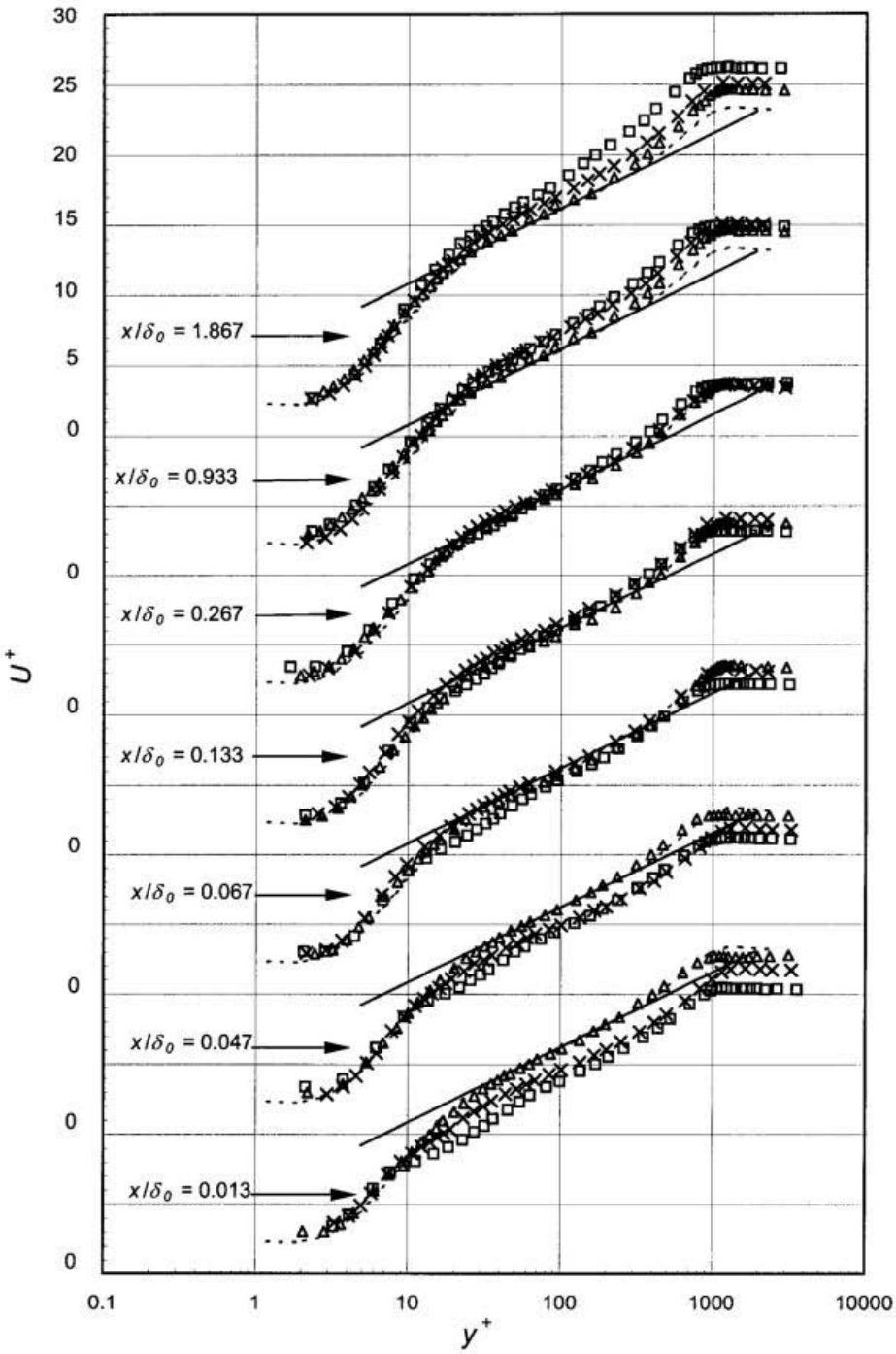

Fig. 5.1.3b Streamwise mean velocity profiles downstream of the SQ-grooves, R_θ = 3000. △, d = 5mm; ×, d = 10mm; □, d = 20mm; -------, smooth-wall. ———, Log-line: $U^+ = (1/0.43)\ ln\ y^+ + 5.5$.

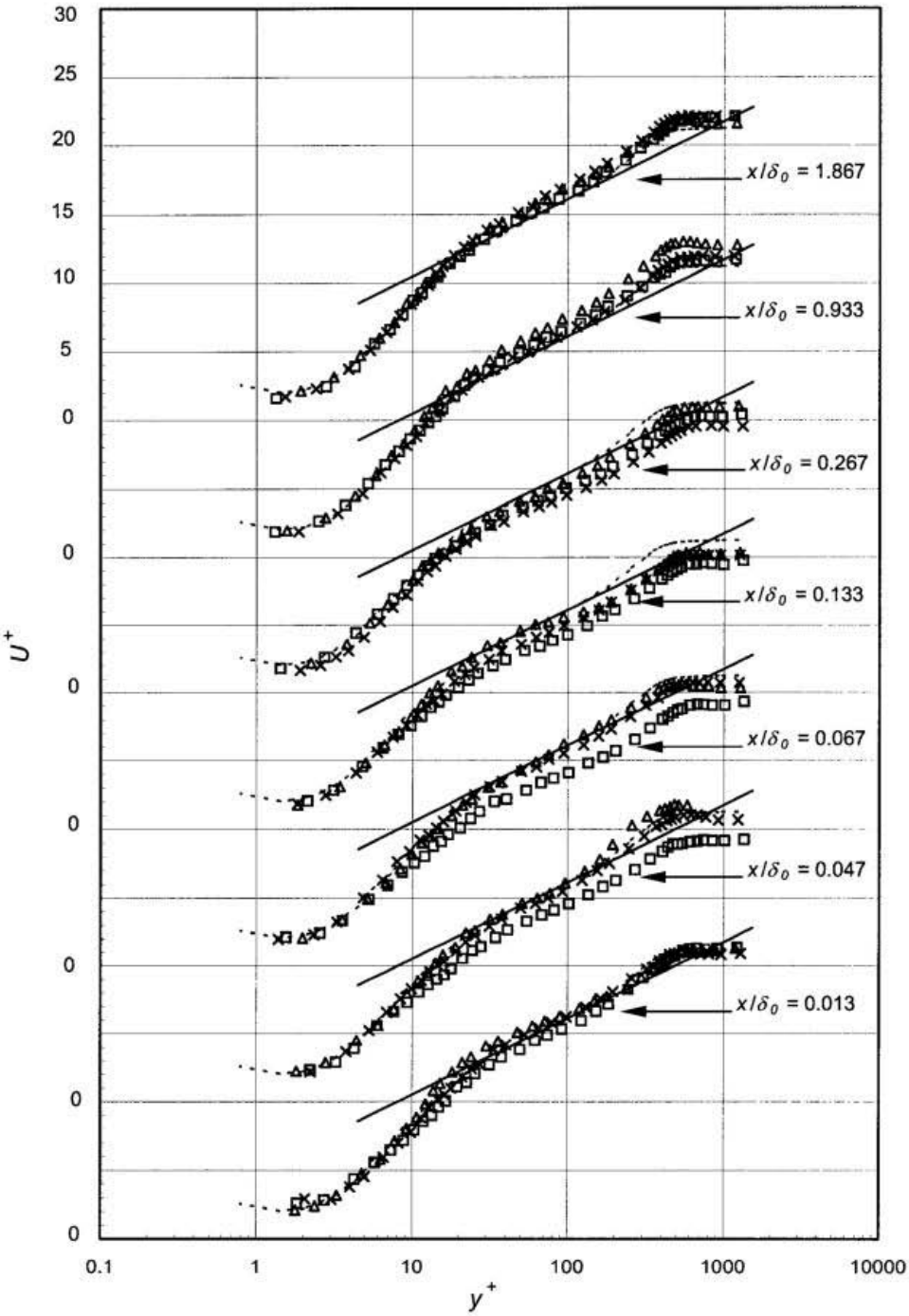

Fig. 5.1.3c Streamwise mean velocity profiles downstream of the SC-groove, $R_\theta = 1000$.
△, $d = 5$mm; ×, $d = 10$mm; □, $d = 20$mm; -------, smooth-wall.
———, Log-line: $U^+ = (1/0.41)\, ln\, y^+ + 4.9$.

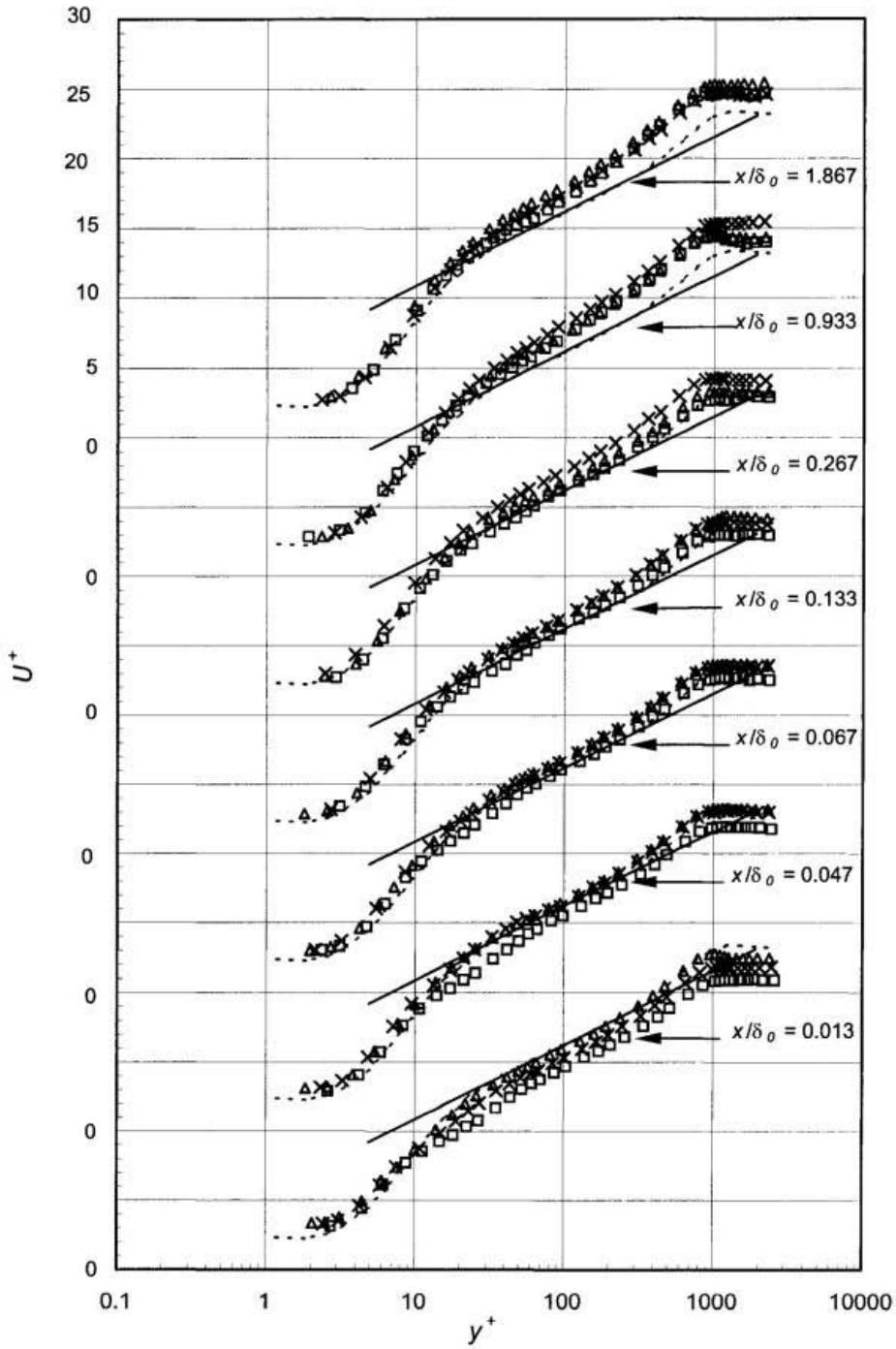

Fig. 5.1.3d Streamwise mean velocity profiles downstream of the SC-grooves, R_θ = 3000. △, d = 5mm; ×, d = 10mm; □, d = 20mm; -------, smooth-wall. ———, Log-line: $U^+ = (1/0.43)\ ln\ y^+ + 5.5$.

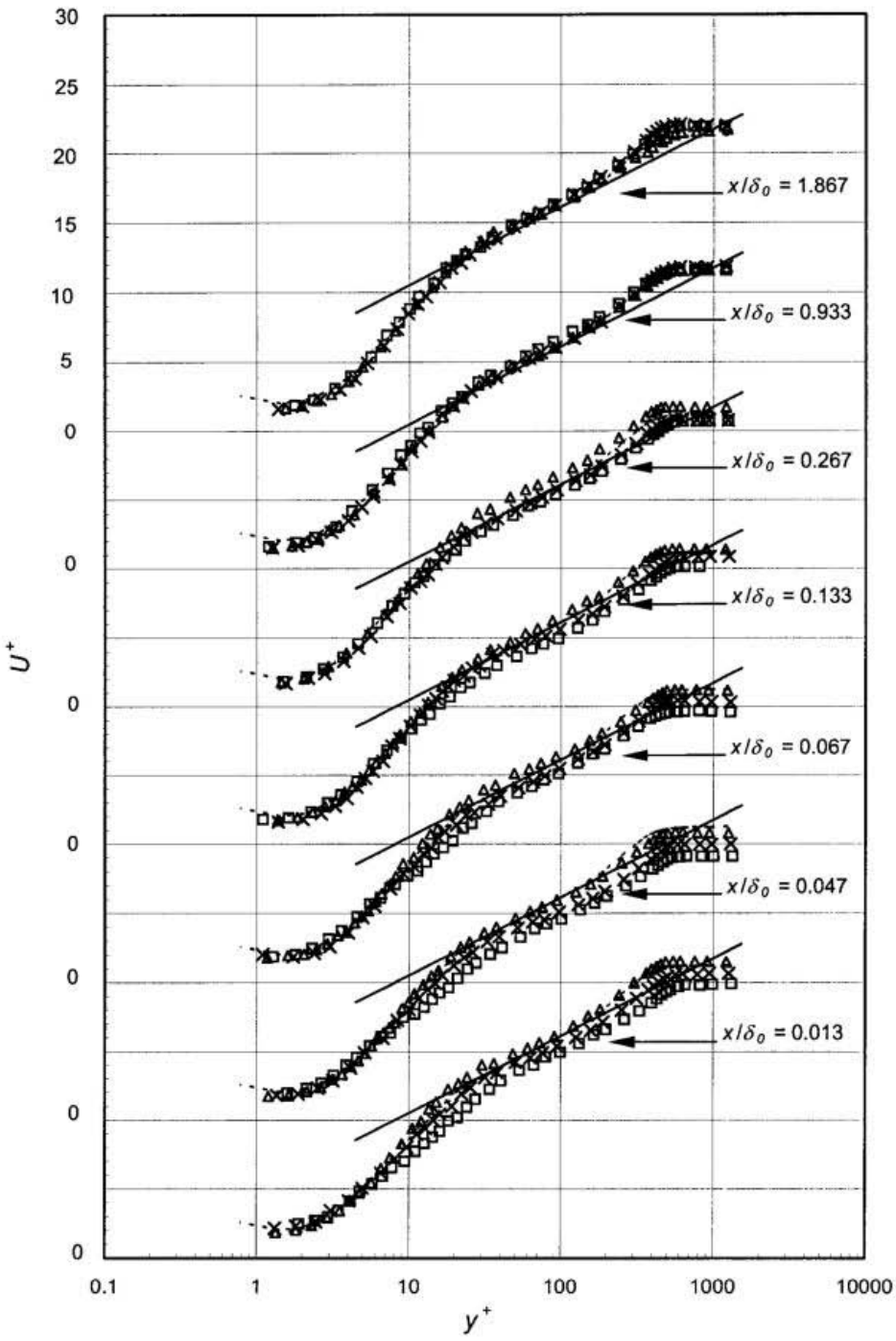

Fig. 5.1.3e Streamwise mean velocity profiles downstream of the TR-grooves, R_θ = 1000. △, d = 5mm; ×, d = 10mm; □, d = 20mm; -------, smooth-wall. ——, Log-line: $U^+ = (1/0.41)\, ln\, y^+ + 4.9$.

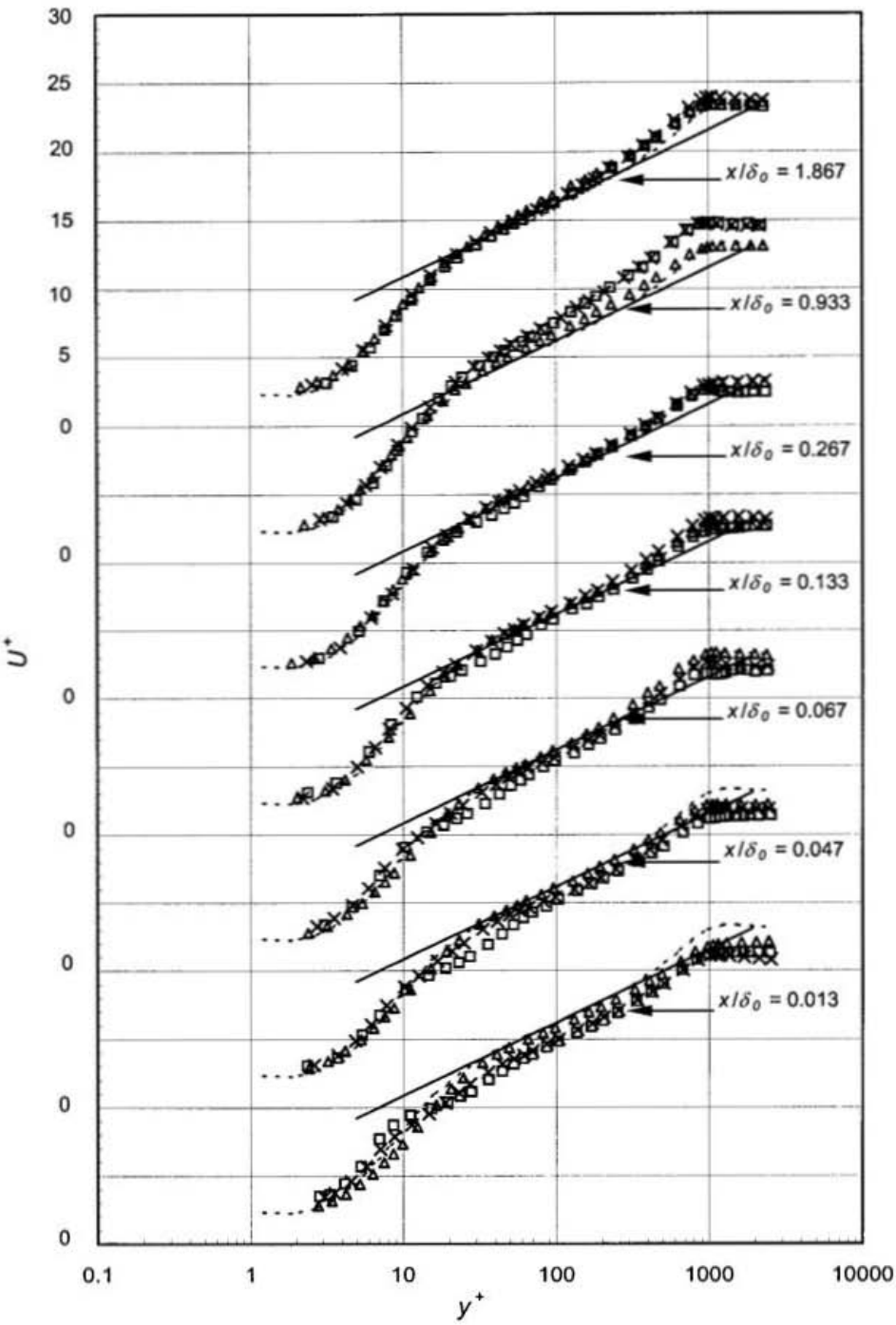

Fig. 5.1.3f Streamwise mean velocity profiles downstream of the TR-grooves, R_θ = 3000. △, d = 5mm; ×, d = 10mm; □, d = 20mm; -------, smooth-wall. ——, Log-line: $U^+ = (1/0.43)\ ln\ y^+ + 5.5$.

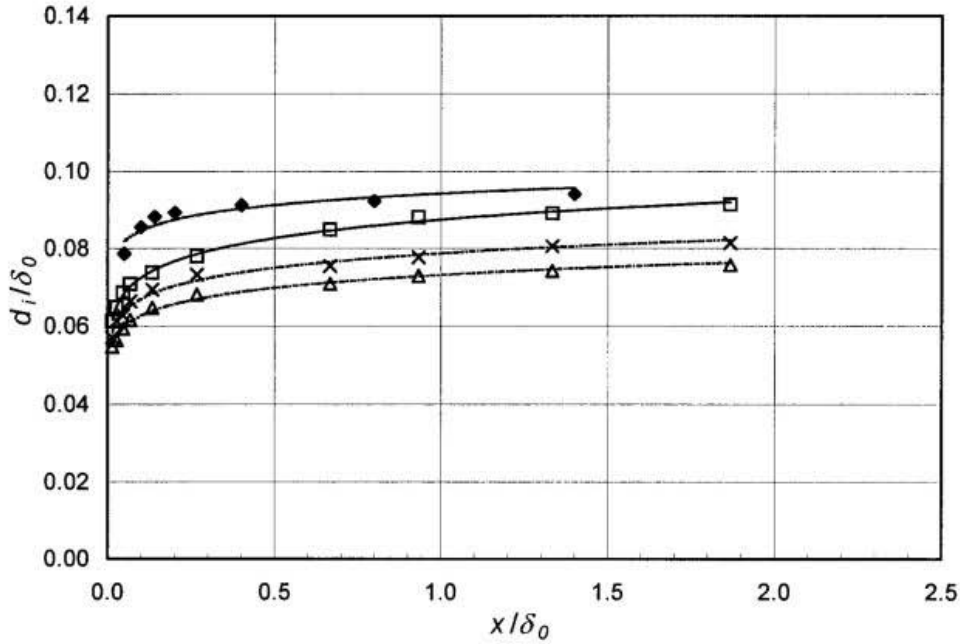

Fig. 5.1.4a Internal layer growth downstream of three different sized SQ-grooves at R_θ = 1000. △, d = 5mm; ×, d = 10mm; □, d = 20mm; ◆, data of Elavarasan et al. (1996, R_θ = 1300).

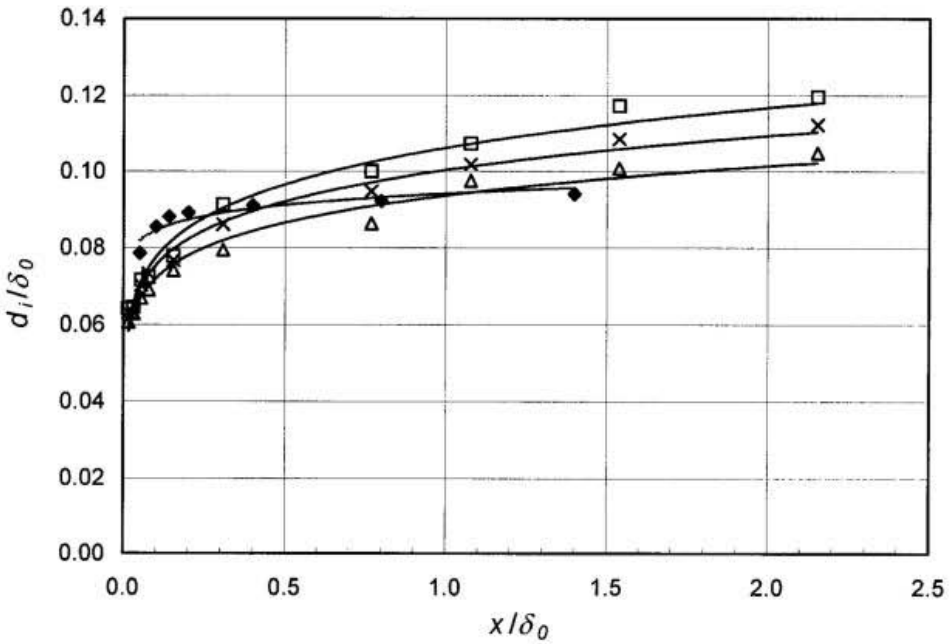

Fig. 5.1.4b Internal layer growth downstream of three different sized SQ-grooves at R_θ = 3000. △, d = 5mm; ×, d = 10mm; □, d = 20mm; ◆, data of Elavarasan et al. (1996, R_θ = 1300).

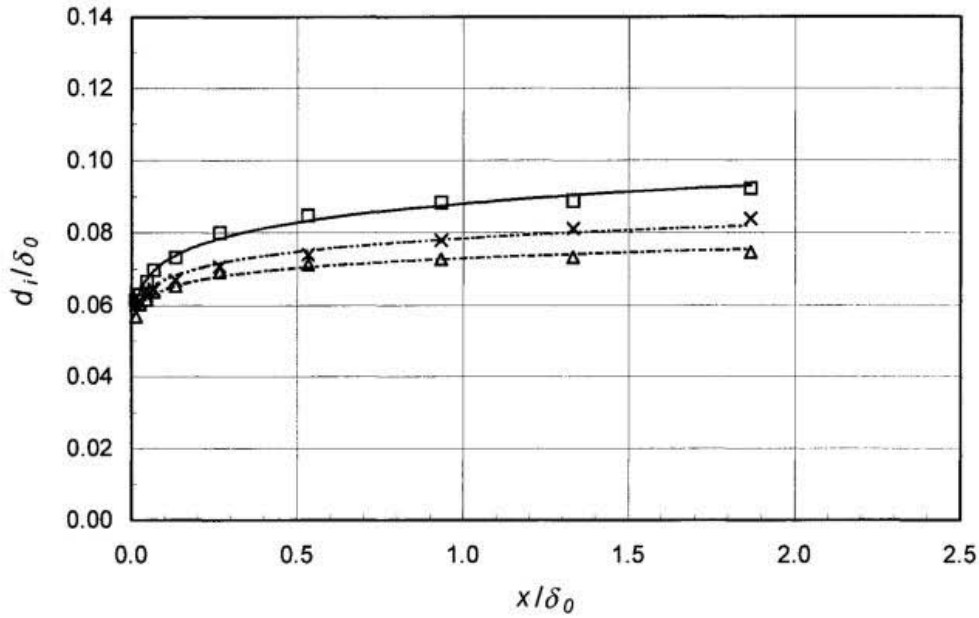

Fig. 5.1.4c Internal layer growth downstream of three different sized SC-grooves at R_θ = 1000. Δ, d = 5mm; ×, d = 10mm; □, d = 20mm.

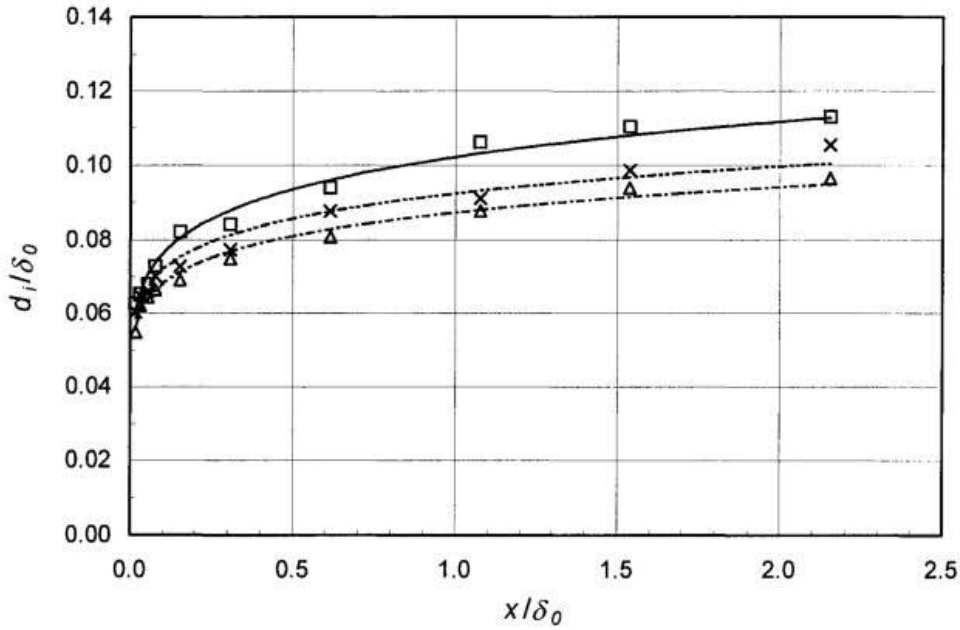

Fig. 5.1.4d Internal layer growth downstream of three different sized SC-grooves at R_θ = 3000. Δ, d = 5mm; ×, d = 10mm; □, d = 20mm.

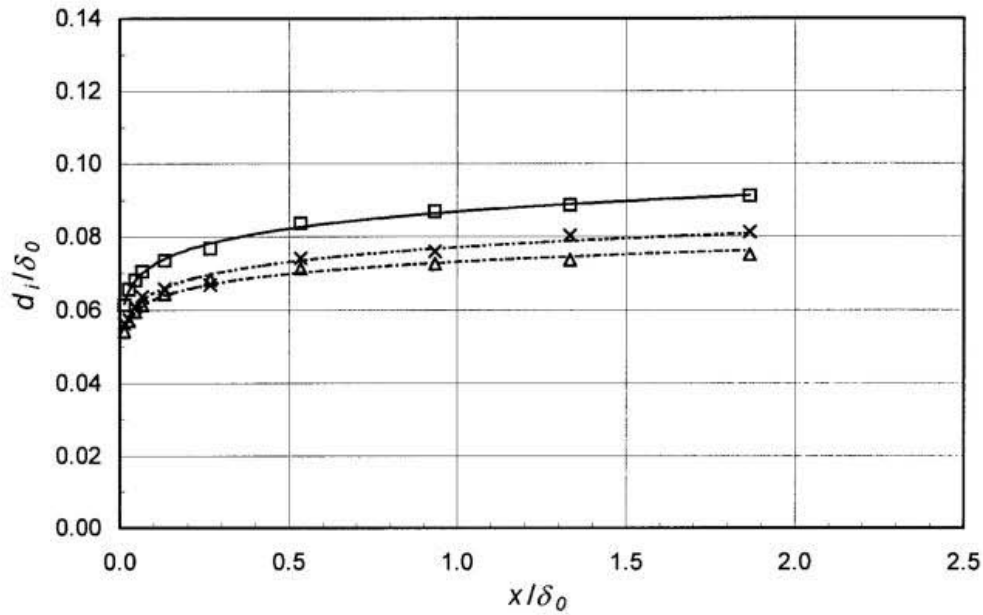

Fig. 5.1.4e Internal layer growth downstream of three different sized TR-grooves at R_θ = 1000. Δ, d = 5mm; ×, d = 10mm; □, d = 20mm.

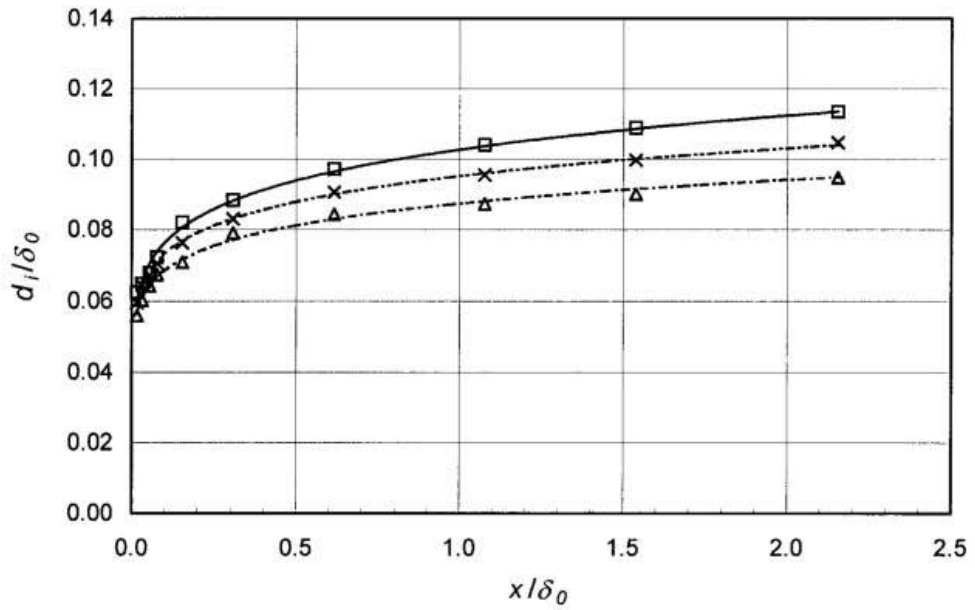

Fig. 5.1.4f Internal layer growth downstream of three different sized TR-grooves at R_θ = 3000. Δ, d = 5mm; ×, d = 10mm; □, d = 20mm.

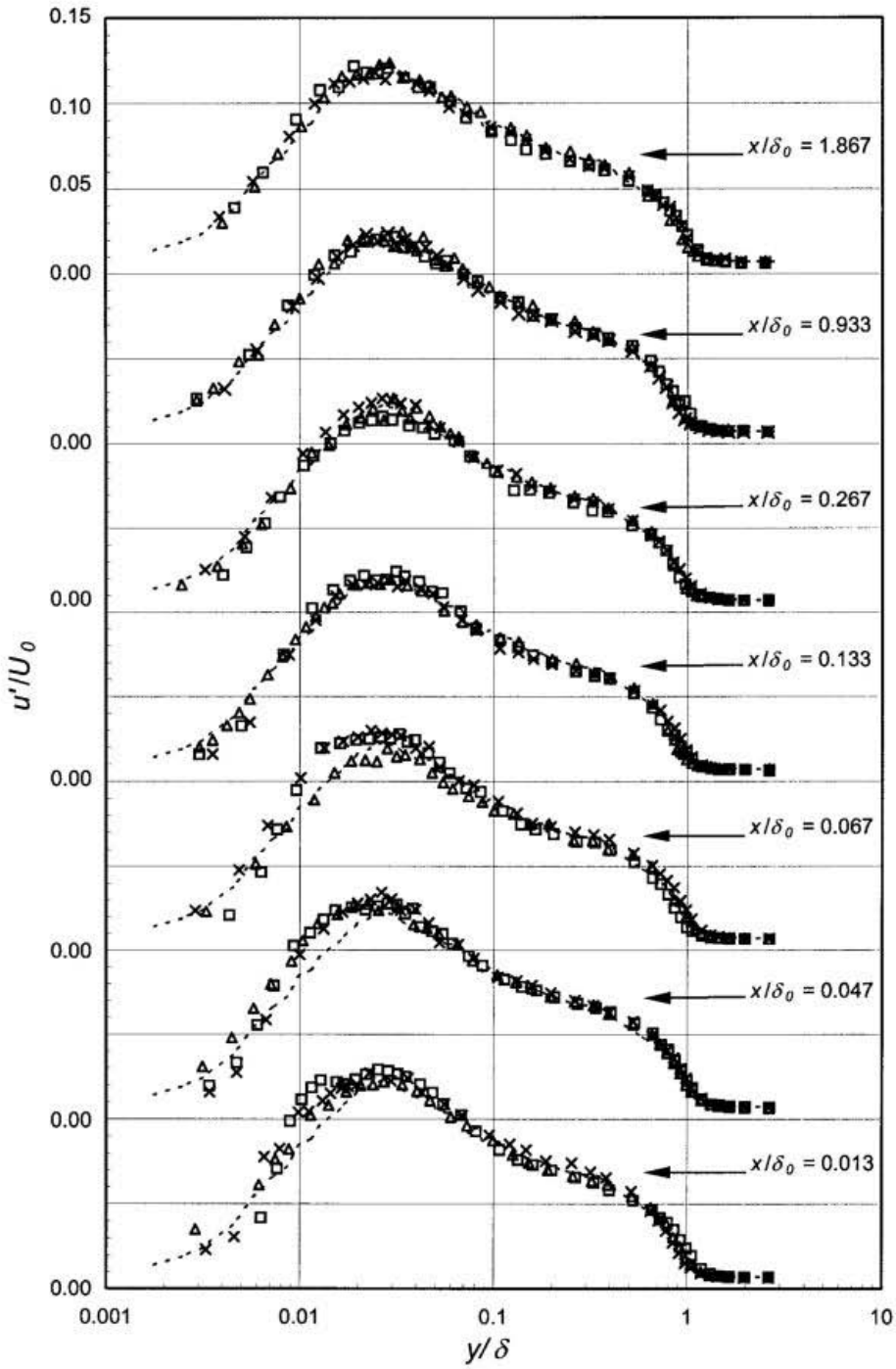

Fig. 5.2.1a Streamwise turbulence intensity profiles downstream of the SQ-grooves, R_θ = 1000. △, d = 5mm; ×, d = 10mm; □, d = 20mm; -----, smooth-wall.

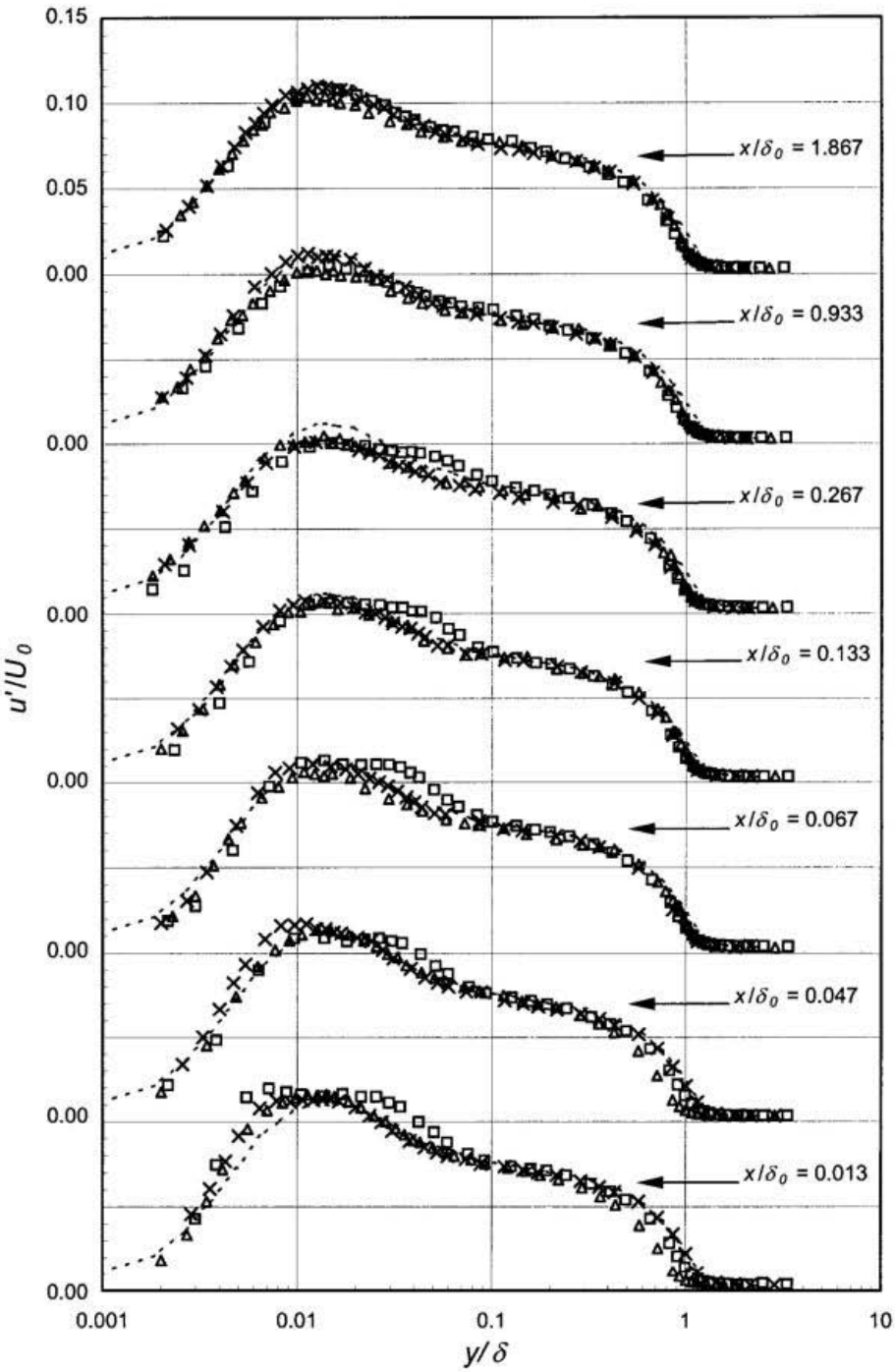

Fig. 5.2.1b Streamwise turbulence intensity profiles downstream of the SQ-grooves, R_θ = 3000. △, d = 5mm; ×, d = 10mm; □, d = 20mm; -----, smooth-wall.

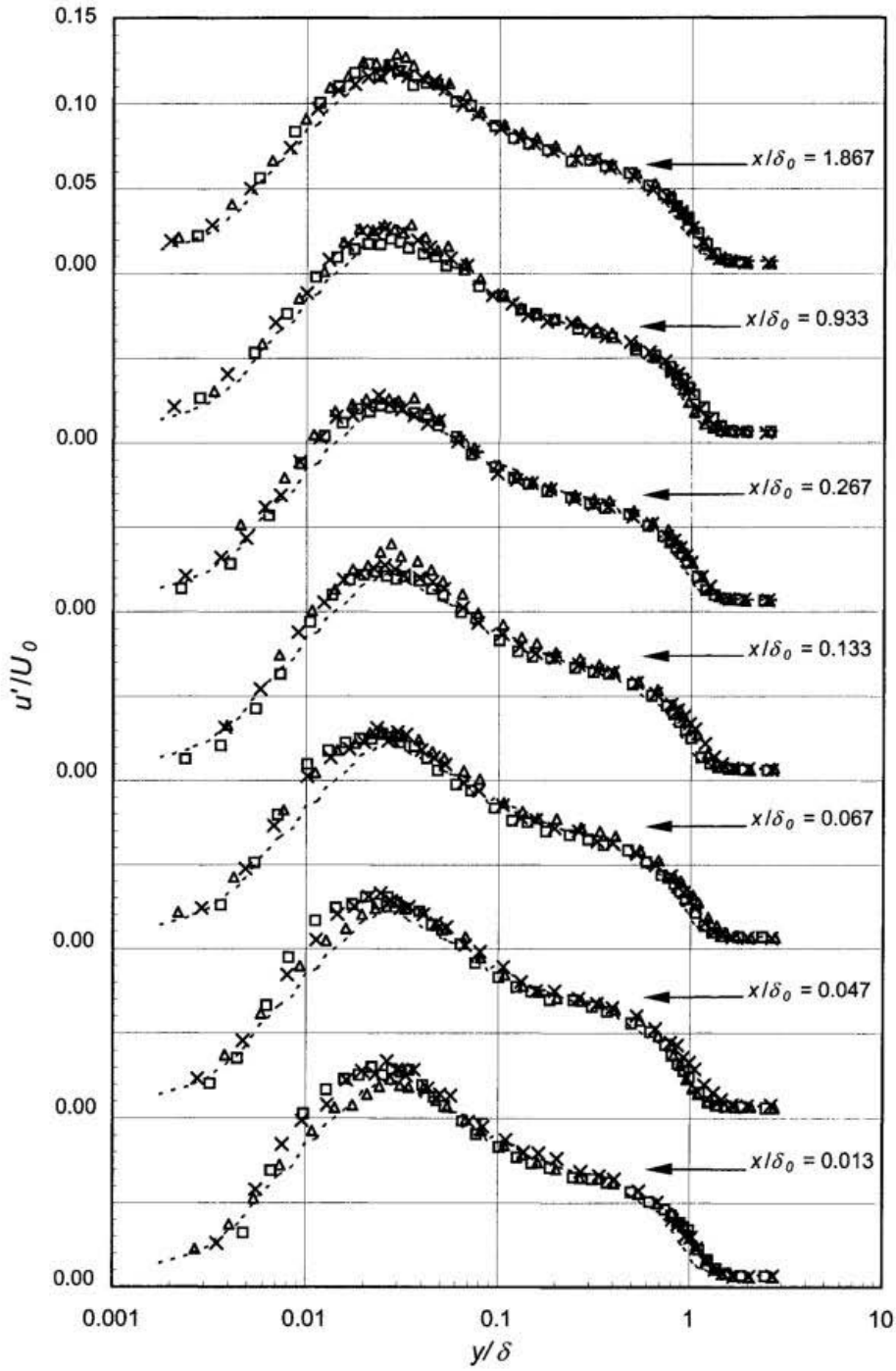

Fig. 5.2.1c Streamwise turbulence intensity profiles downstream of the SC-grooves, R_θ = 1000. △, d = 5mm; ×, d = 10mm; □, d = 20mm; -----, smooth-wall.

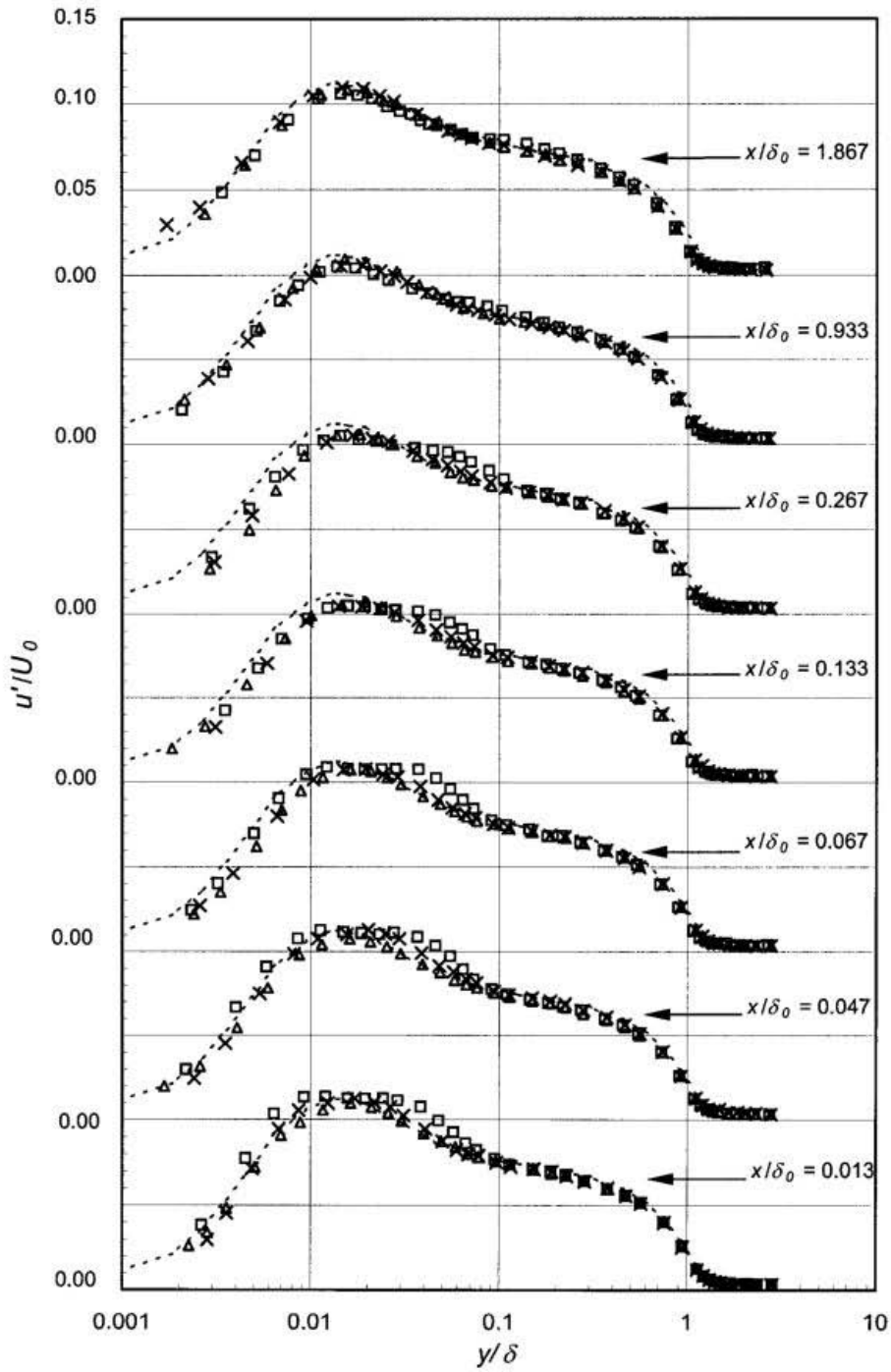

Fig. 5.2.1d Streamwise turbulence intensity profiles downstream of the SC-grooves, R_θ = 3000. △, d = 5mm; ×, d = 10mm; □, d = 20mm; -----, smooth-wall.

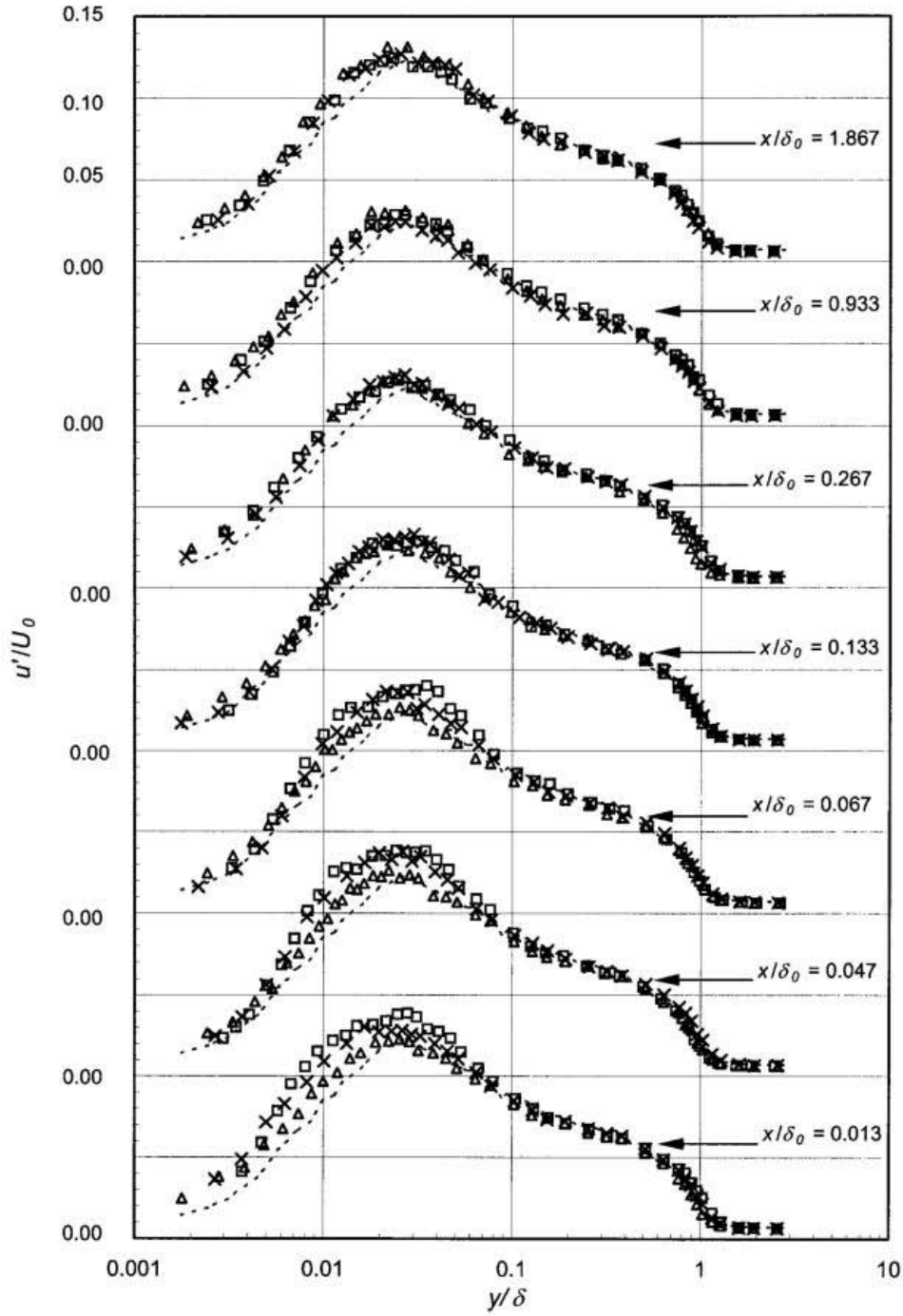

Fig. 5.2.1e Streamwise turbulence intensity profiles downstream of the TR-grooves, R_θ = 1000. △, d = 5mm; ×, d = 10mm; □, d = 20mm; ·····, smooth-wall.

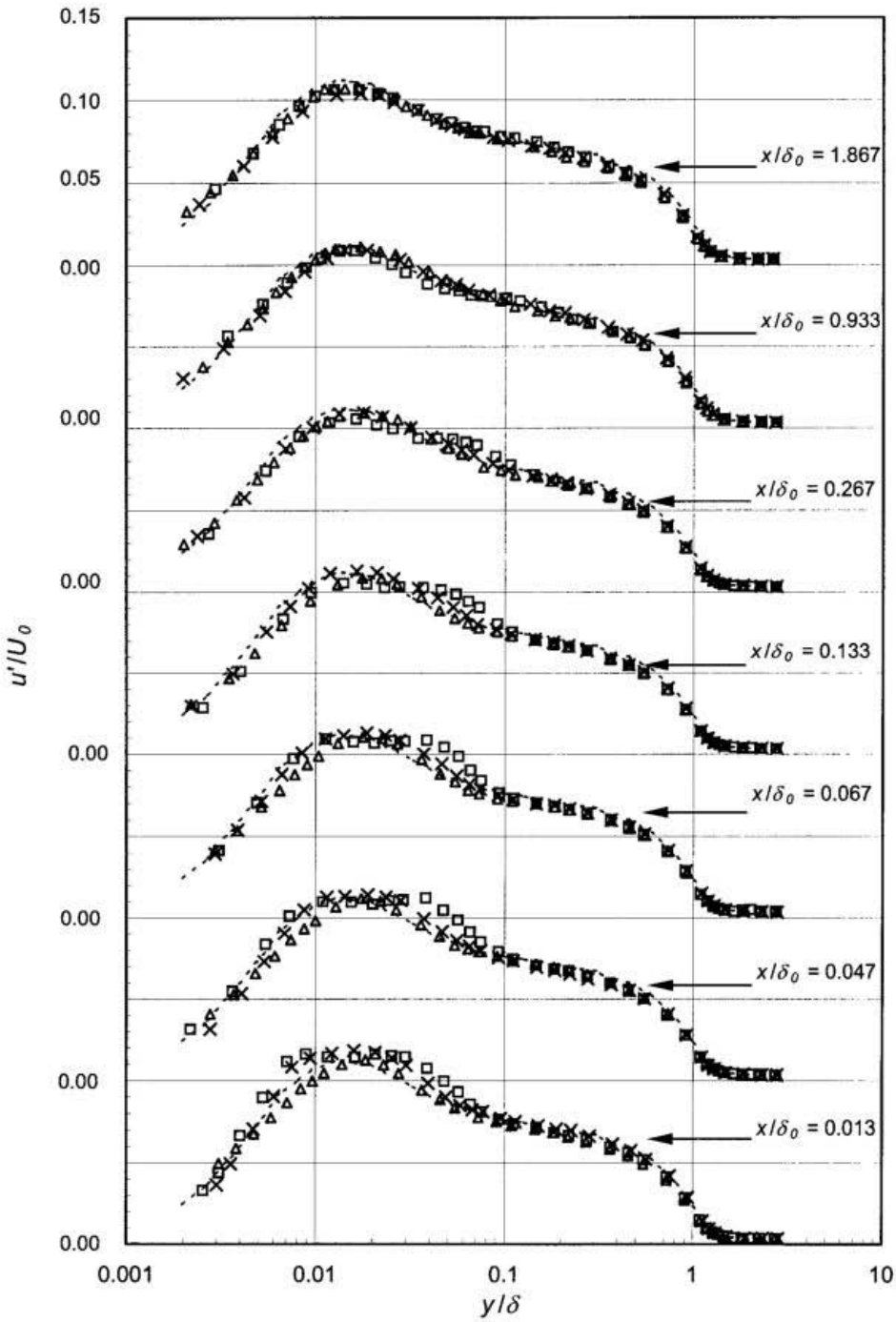

Fig. 5.2.1f Streamwise turbulence intensity profiles downstream of the TR-grooves, R_θ = 3000. △, d = 5mm; ×, d = 10mm; □, d = 20mm; -----, smooth-wall.

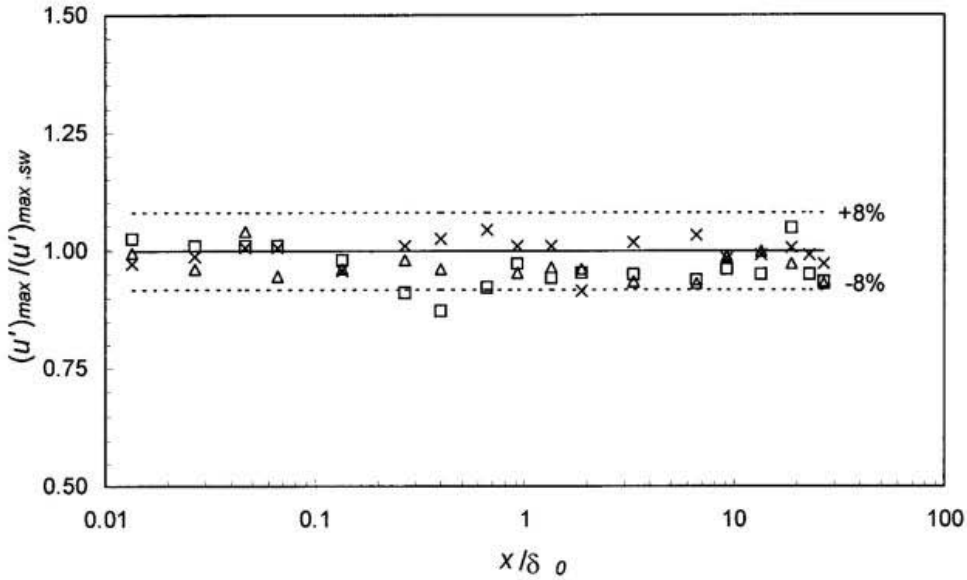

Fig. 5.2.2a Distribution of $(u')_{max}/(u')_{max,sw}$ as a function of x/δ_0 for the three different sized SQ-grooves, $R_\theta = 1000$. △, $d = 5$mm; ×, $d = 10$mm; □, $d = 20$mm. ——, $(u')_{max}/(u')_{max,sw} = 1.0$; - - - -, ± 8% variation.

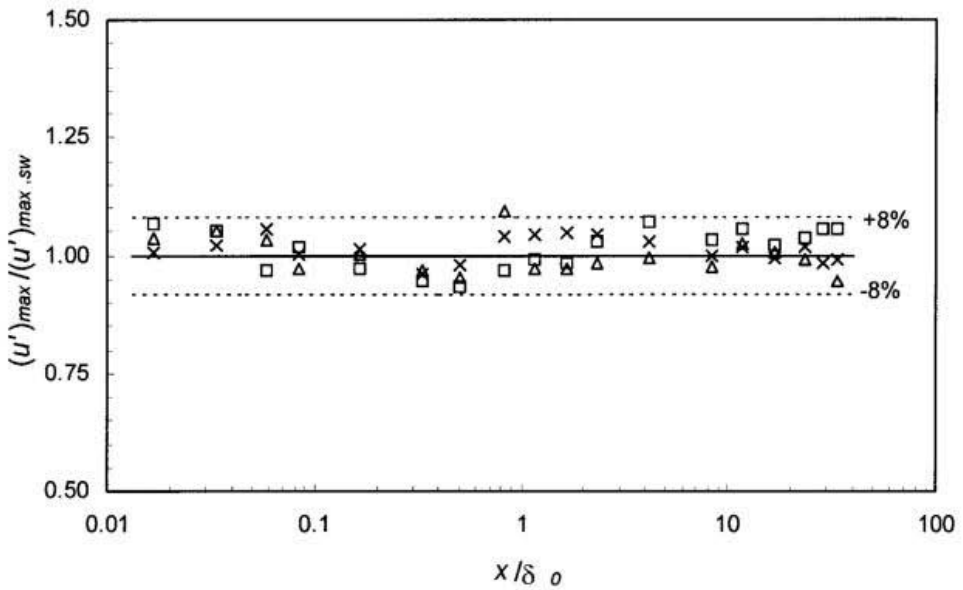

Fig. 5.2.2b Distribution of $(u')_{max}/(u')_{max,sw}$ as a function of x/δ_0 for the three different sized SQ-grooves, $R_\theta = 3000$. △, $d = 5$mm; ×, $d = 10$mm; □, $d = 20$mm. ——, $(u')_{max}/(u')_{max,sw} = 1.0$; - - - -, ± 8% variation.

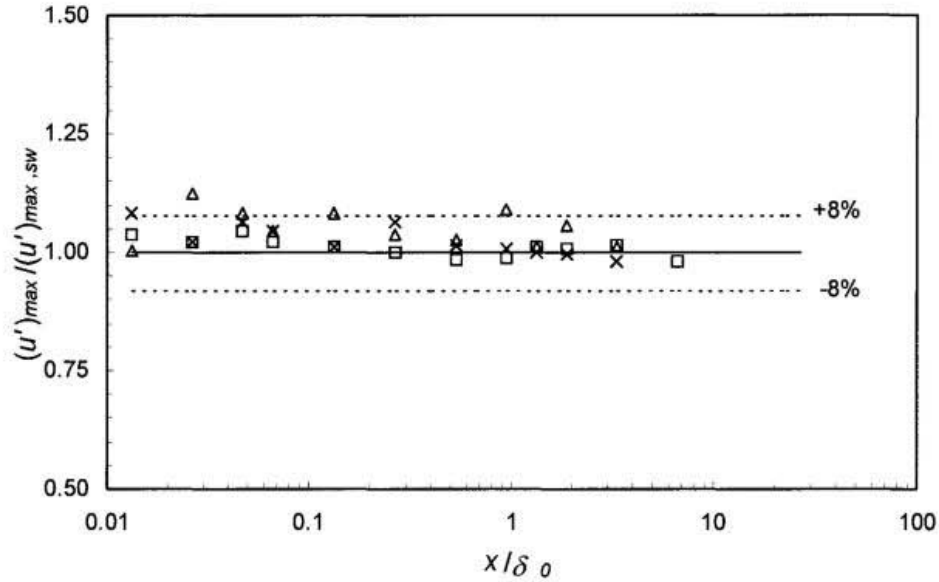

Fig. 5.2.2c Distribution of $(u')_{max}/(u')_{max,sw}$ as a function of x/δ_0 for the three different sized SC-grooves, $R_\theta = 1000$. △, $d = 5$mm; ×, $d = 10$mm; □, $d = 20$mm. ——, $(u')_{max}/(u')_{max,sw} = 1.0$; - - - -, ± 8% variation.

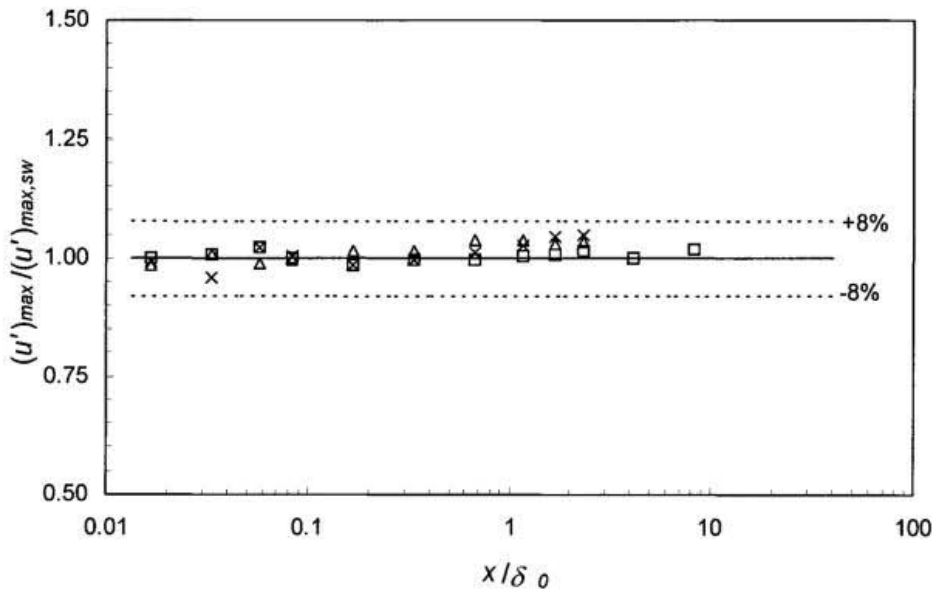

Fig. 5.2.2d Distribution of $(u')_{max}/(u')_{max,sw}$ as a function of x/δ_0 for the three different sized SC-grooves, $R_\theta = 3000$. △, $d = 5$mm; ×, $d = 10$mm; □, $d = 20$mm. ——, $(u')_{max}/(u')_{max,sw} = 1.0$; - - - -, ± 8% variation.

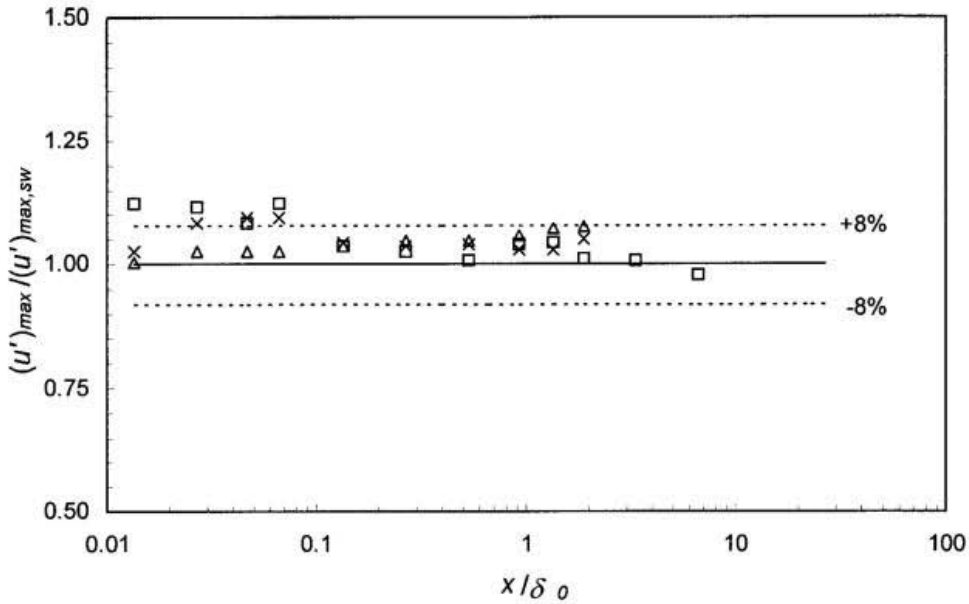

Fig. 5.2.2e Distribution of $(u')_{max}/(u')_{max,sw}$ as a function of x/δ_0 for the three different sized TR-grooves, $R_\theta = 1000$. △, $d = 5$mm; ×, $d = 10$mm; □, $d = 20$mm. ——, $(u')_{max}/(u')_{max,sw} = 1.0$; - - - -, ± 8% variation.

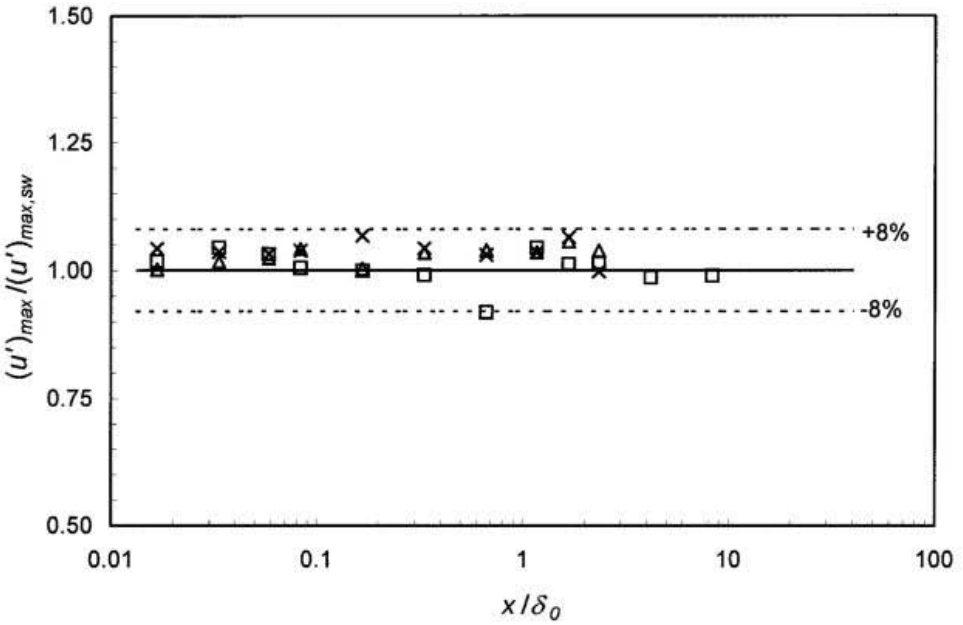

Fig. 5.2.2f Distribution of $(u')_{max}/(u')_{max,sw}$ as a function of x/δ_0 for the three different sized TR-grooves, $R_\theta = 3000$. △, $d = 5$mm; ×, $d = 10$mm; □, $d = 20$mm. ——, $(u')_{max}/(u')_{max,sw} = 1.0$; - - - -, ± 8% variation.

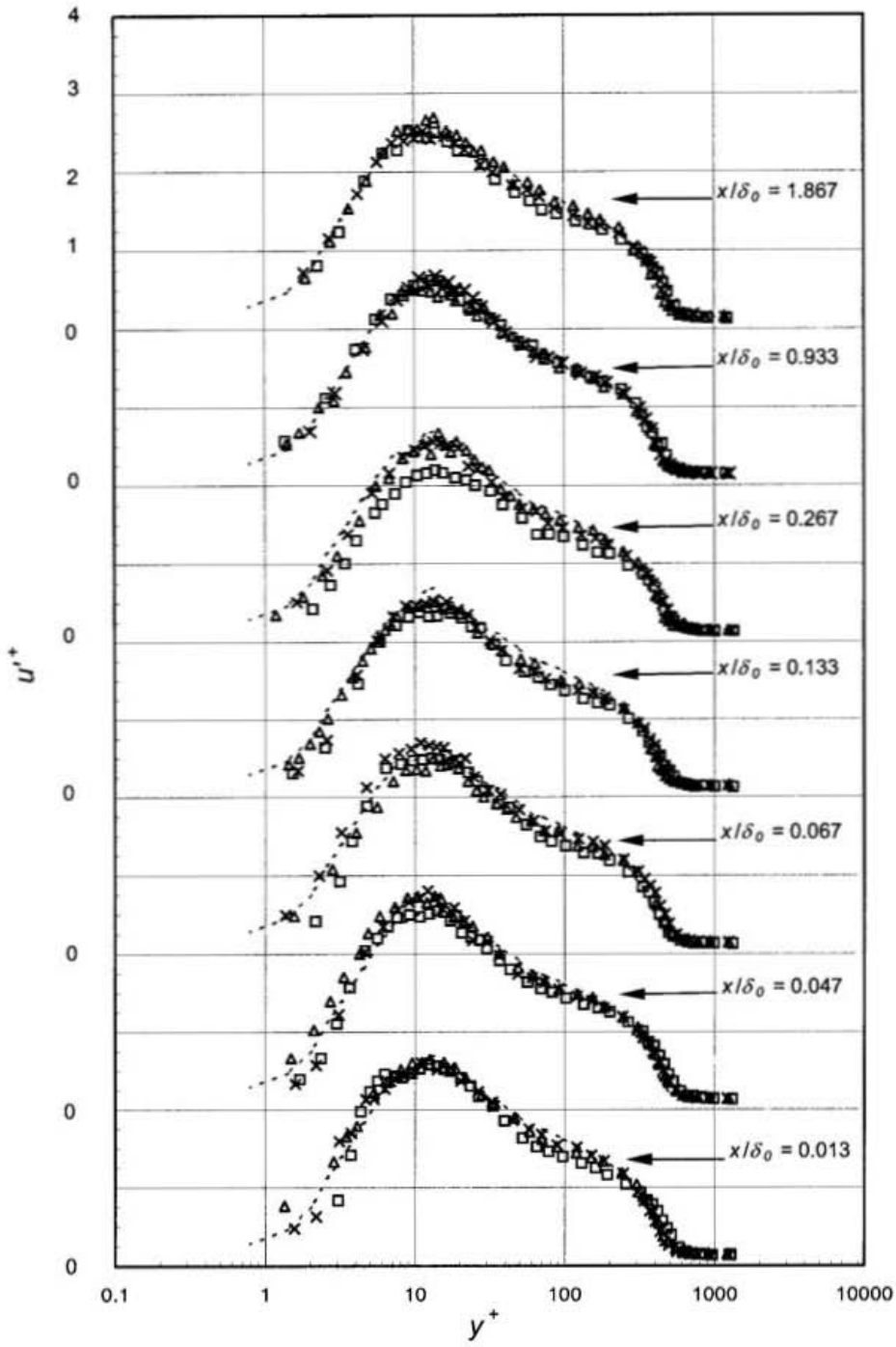

Fig. 5.2.3a Streamwise turbulence intensity profiles downstream of the SQ-grooves, R_θ = 1000. △, d = 5mm; ×, d = 10mm □, d = 20mm; -------, smooth-wall.

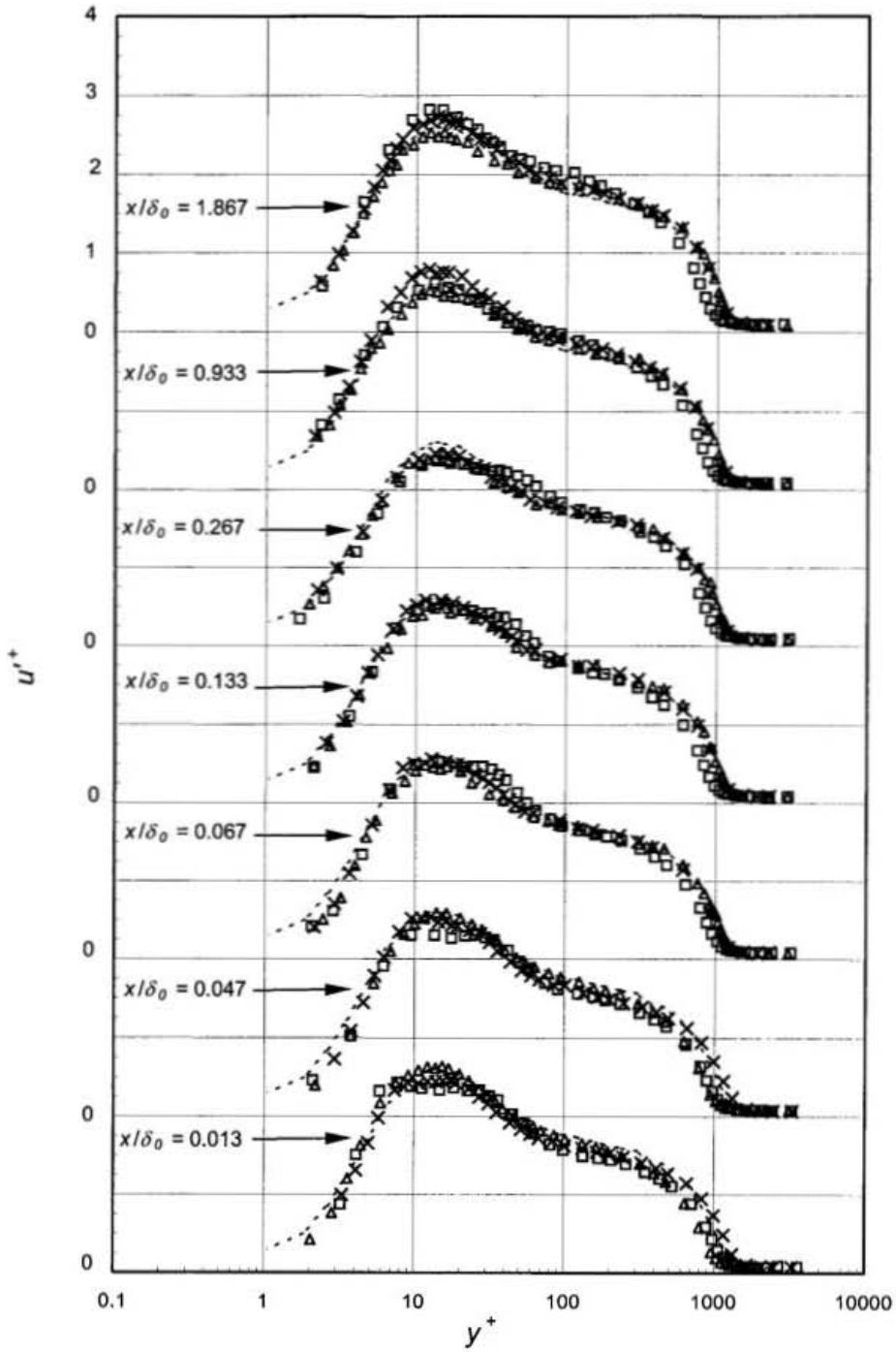

Fig. 5.2.3b Streamwise turbulence intensity profiles downstream of the SQ-grooves, R_θ = 3000. △, d = 5mm; ×, d = 10mm □, d = 20mm; -------, smooth-wall.

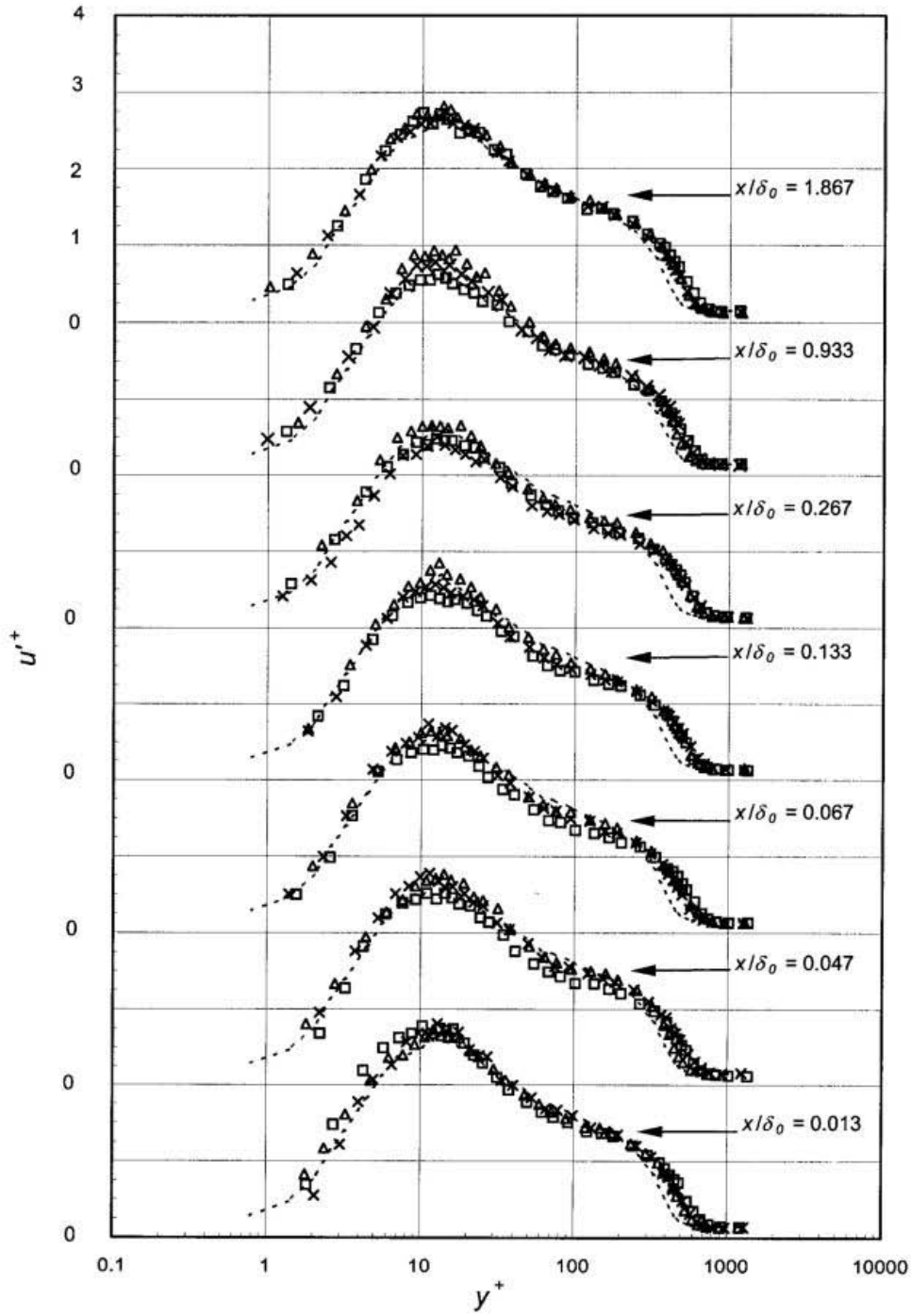

Fig. 5.2.3c Streamwise turbulence intensity profiles downstream of the SC-groove, R_θ = 1000. △, d = 5mm; ×, d = 10mm; □, d = 20mm ; -------, smooth-wall.

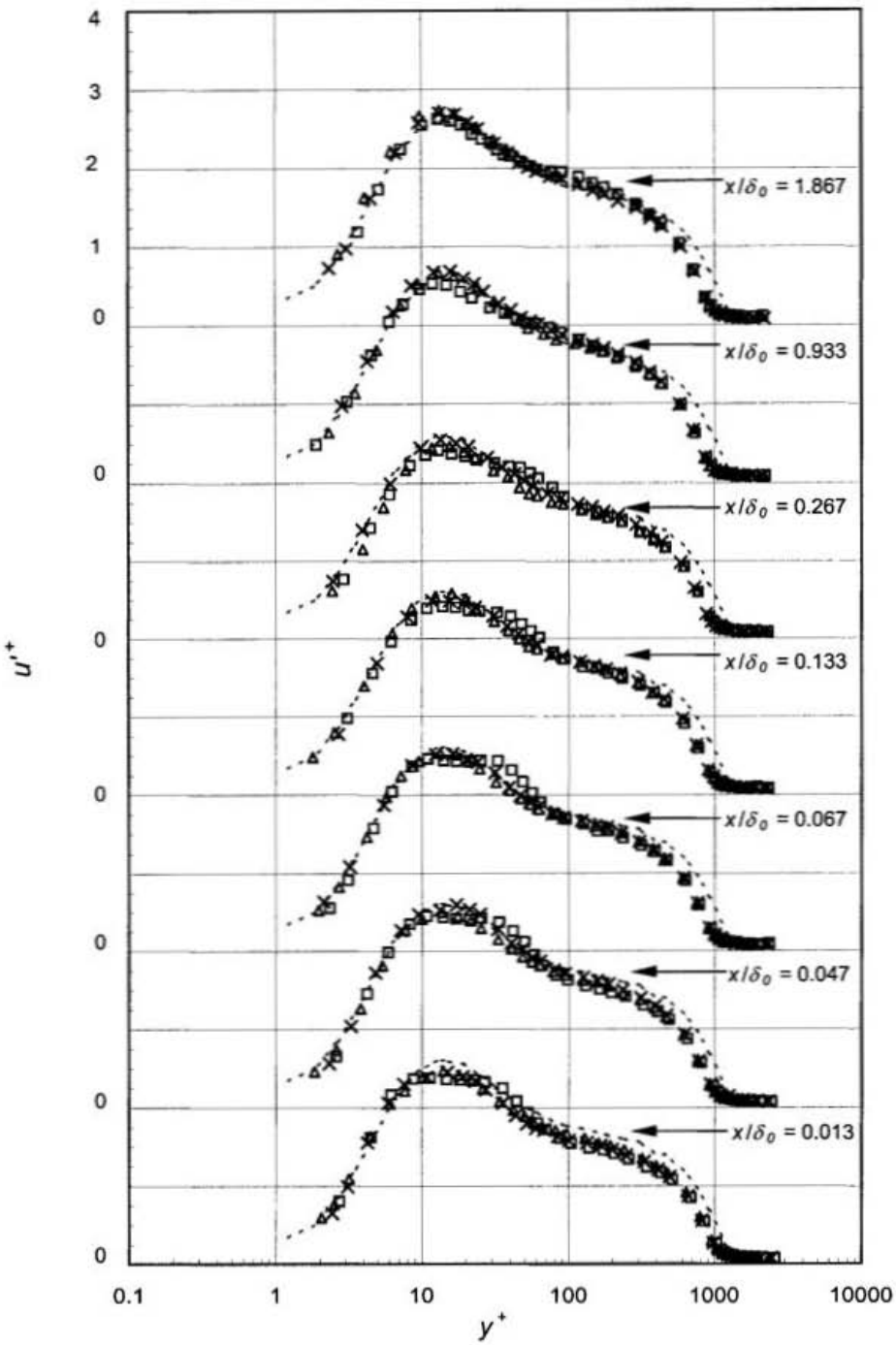

Fig. 5.2.3d Streamwise turbulence intensity profiles downstream of the SC-grooves, R_θ = 3000. △, d = 5mm; ×, d = 10mm □, d = 20mm; -------, smooth-wall.

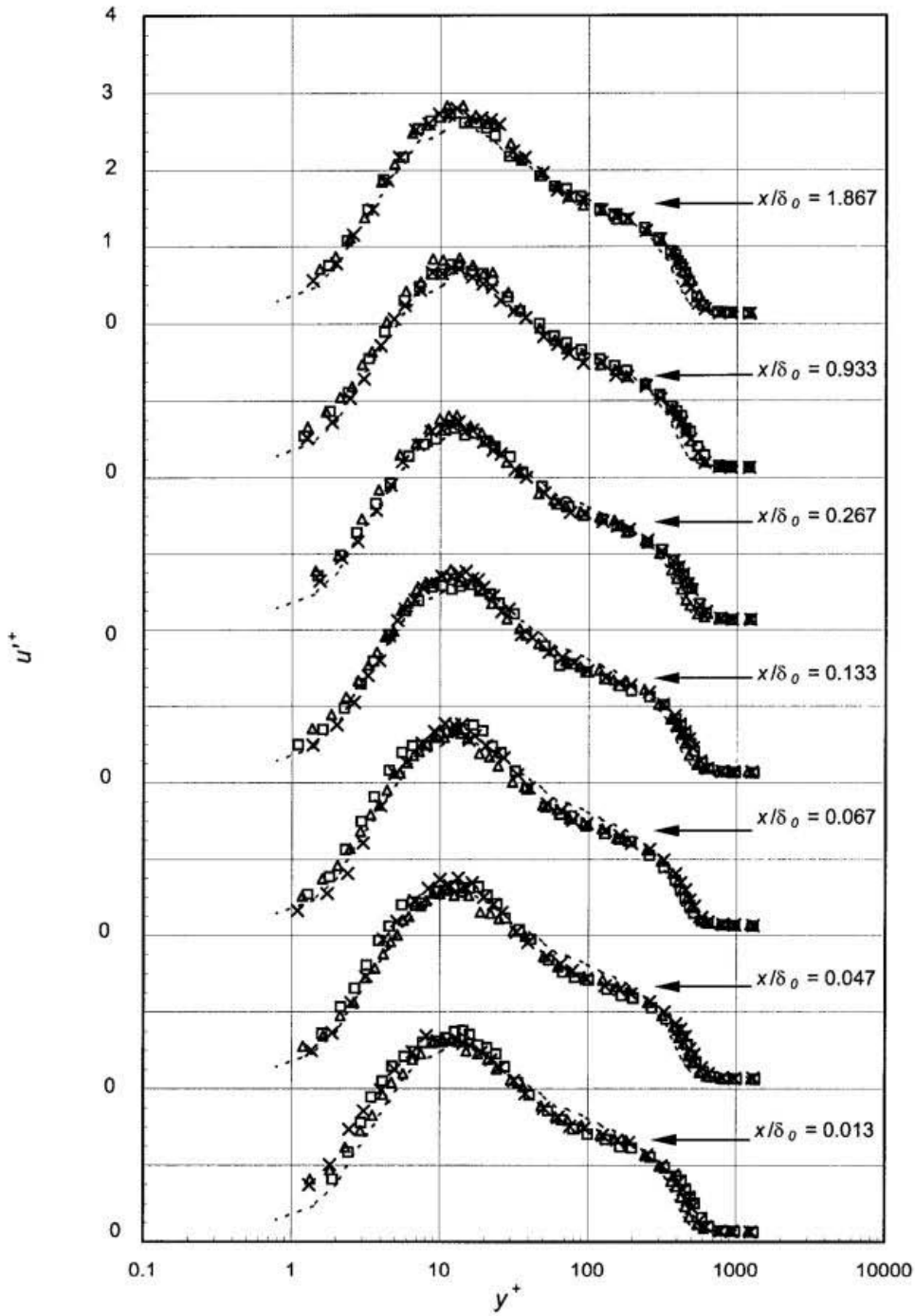

Fig. 5.2.3e Streamwise turbulence intensity profiles downstream of the TR-grooves, R_θ = 1000. △, d = 5mm; ×, d = 10mm; □, d = 20mm; -------, smooth-wall.

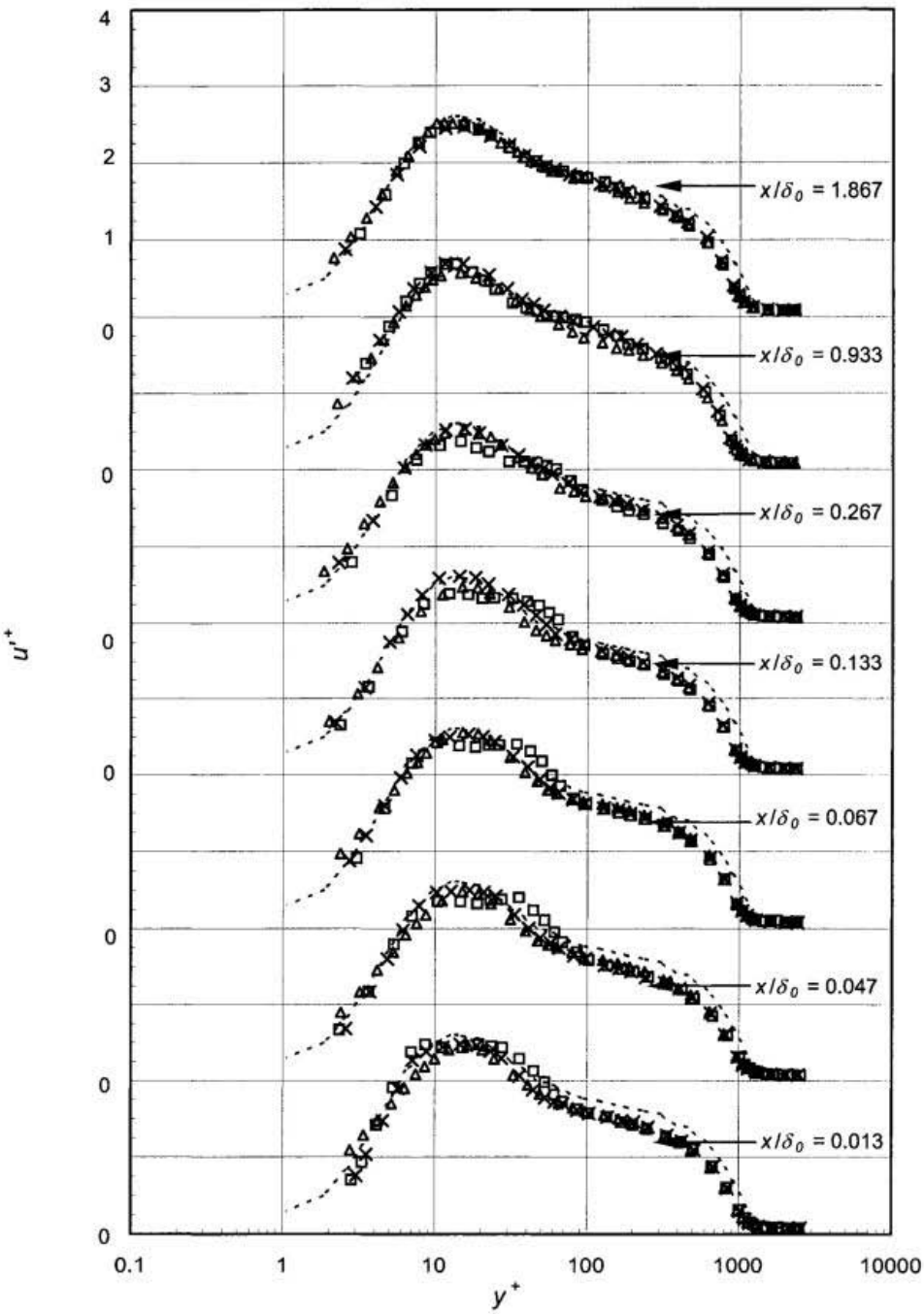

Fig. 5.2.3f Streamwise turbulence intensity profiles downstream of the TR-grooves, R_θ = 3000. △, d = 5mm; ×, d = 10mm □, d = 20mm; -------, smooth-wall.

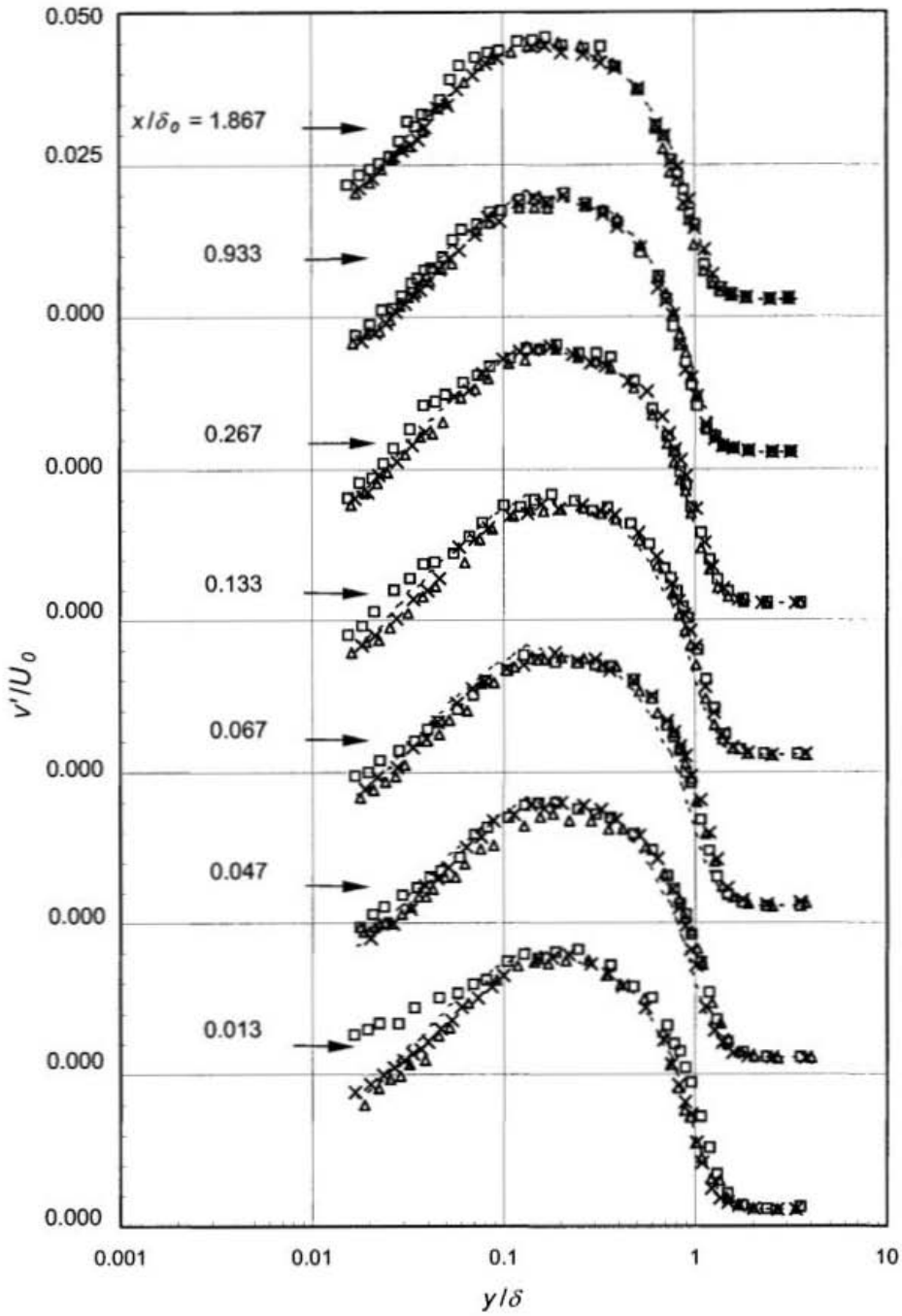

Fig. 5.2.4a Wall-normal turbulence intensity profiles downstream of the SQ-grooves, R_θ = 1000. △, d = 5mm; ×, d = 10mm; □, d = 20mm; ·····, smooth-wall.

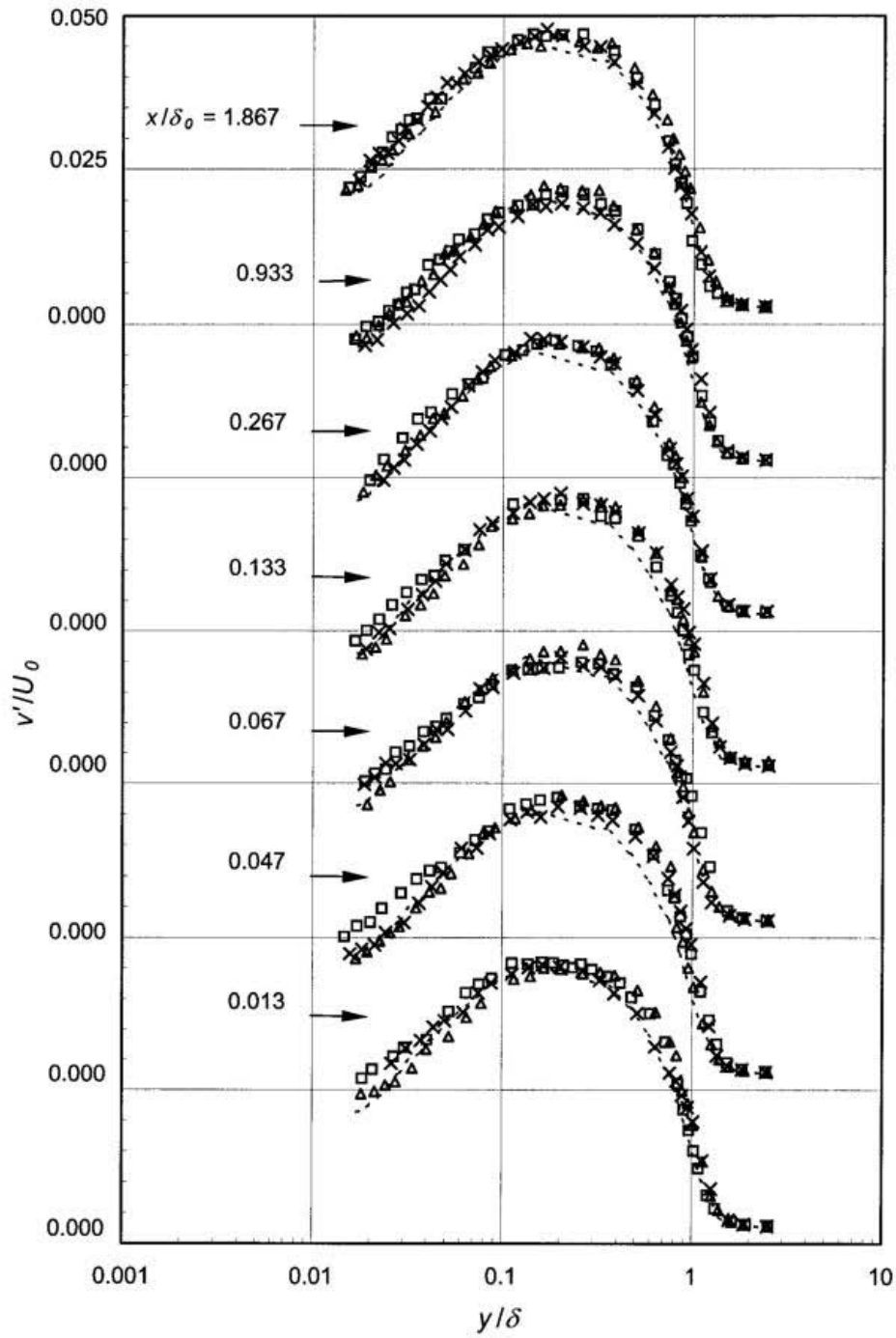

Fig. 5.2.4b Wall-normal turbulence intensity profiles downstream of the SC-groove, R_θ = 1000. △, d = 5mm; ×, d = 10mm; □, d = 20mm; ------, smooth-wall.

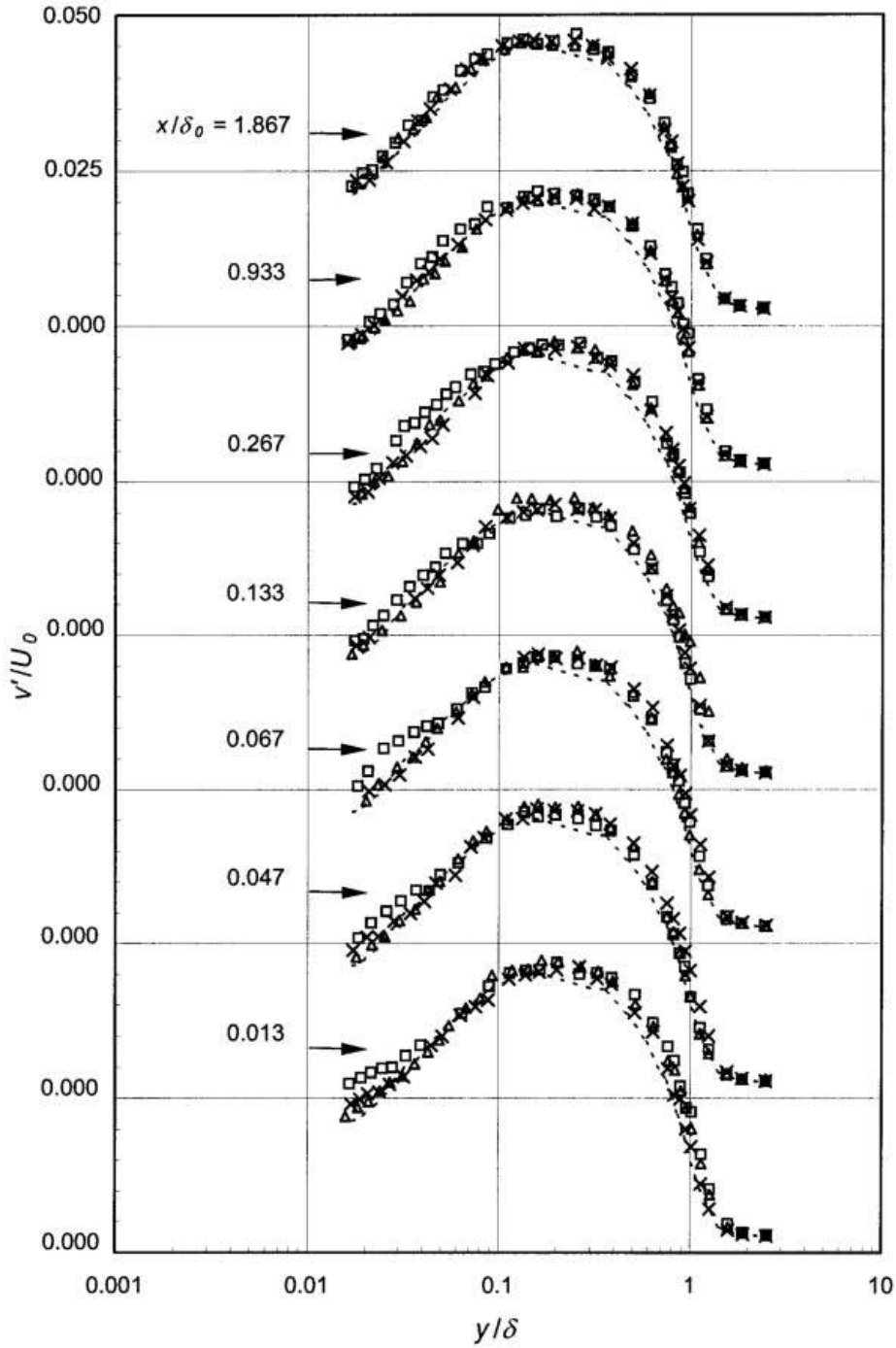

Fig. 5.2.4c Wall-normal turbulence intensity profiles downstream of the TR-grooves, R_θ = 1000. △, d = 5mm; ×, d = 10mm; □, d = 20mm; ------, smooth-wall.

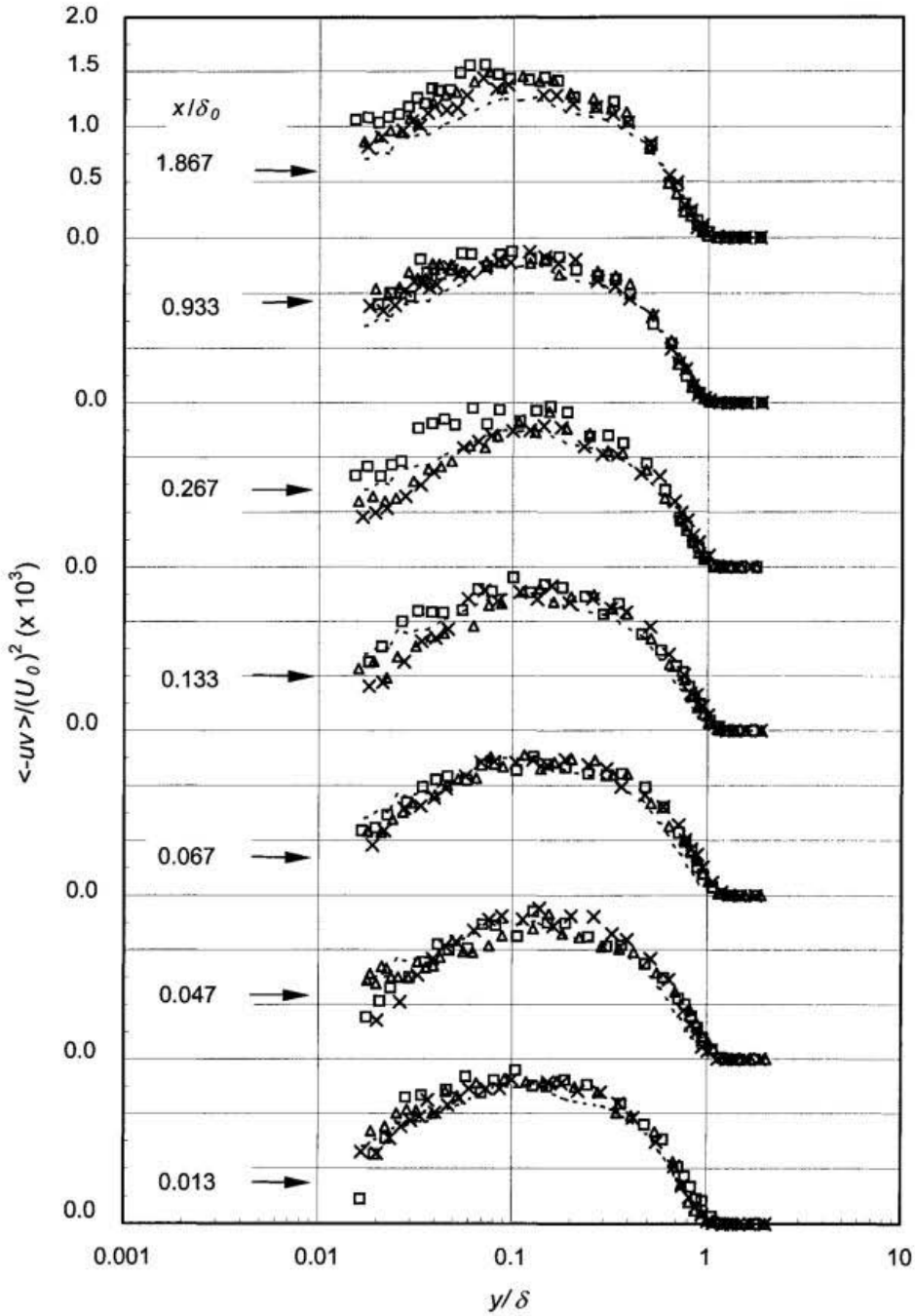

Fig. 5.2.5a Reynolds stress profiles downstream of the SQ-groove, $R_\theta = 1000$.
△, $d = 5$mm; ×, $d = 10$mm; □, $d = 20$mm; ------, smooth-wall.

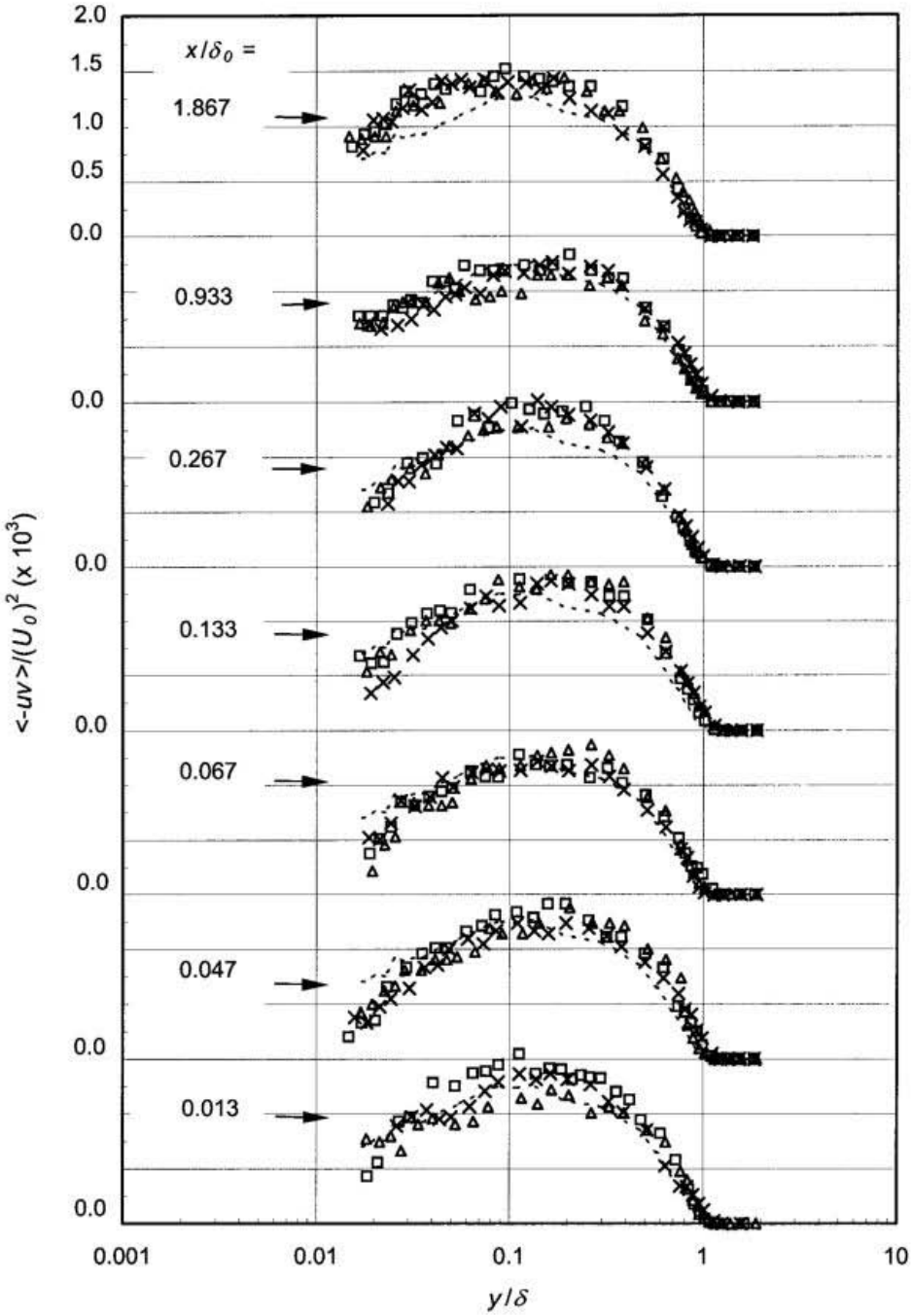

Fig. 5.2.5b Reynolds stress profiles downstream of the SC-groove, $R_\theta = 1000$.
△, d = 5mm; ×, d = 10mm; □, d = 20mm; ------, smooth-wall.

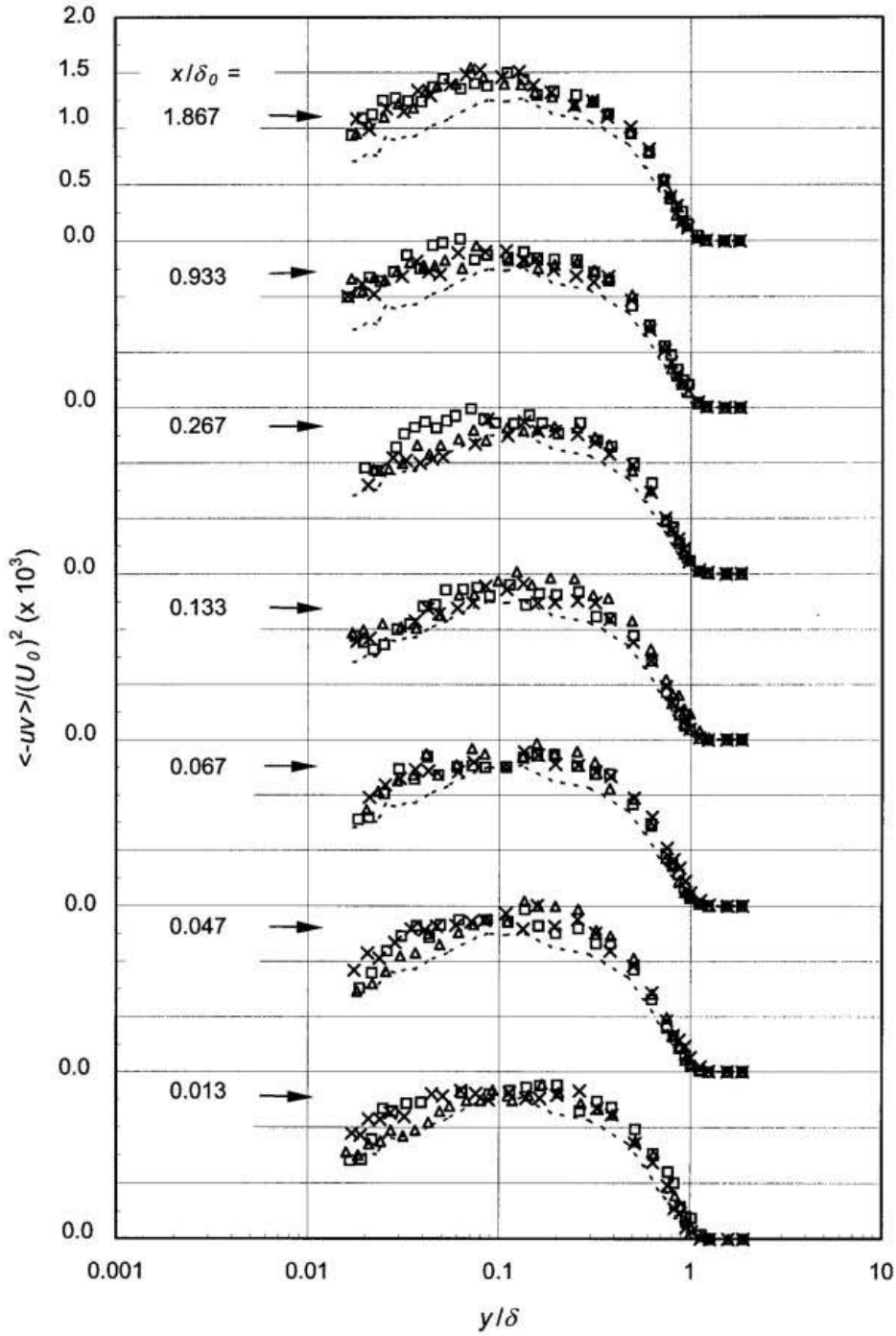

Fig. 5.2.5c Reynolds stress profiles downstream of the TR-groove, $R_\theta = 1000$.
△, $d = 5$mm; ×, $d = 10$mm; □, $d = 20$mm ; ------, smooth-wall.

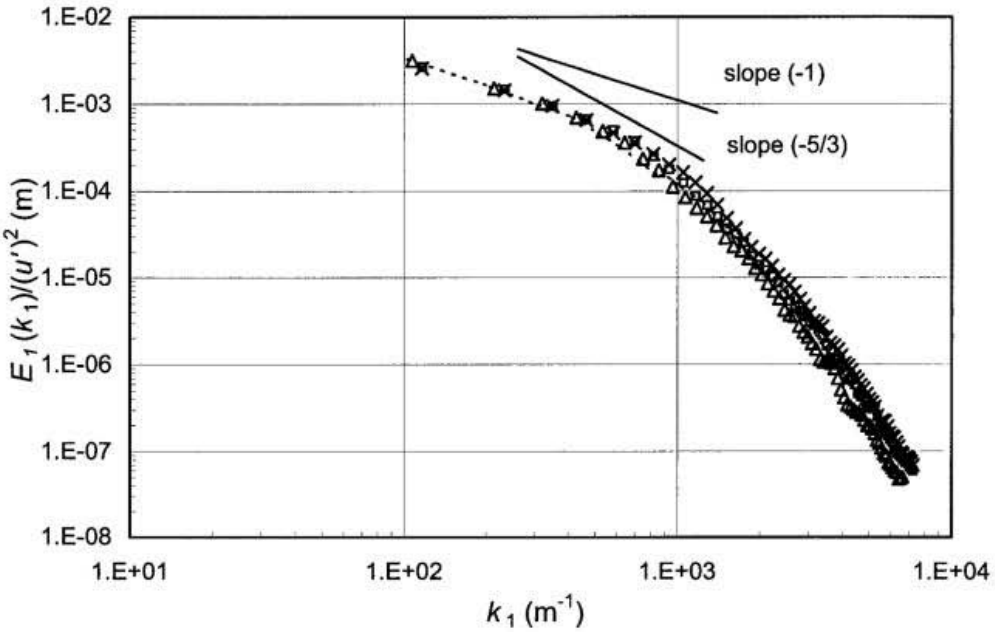

Fig. 5.2.6a Spectra of u' at a location where u'/U_0 is maximum ($y/\delta \approx 0.03$) and $x/\delta_0 =$ 0.013 for three different sized grooves: Δ, $d = 5$mm; ×, $d = 10$mm; □, $d =$ 20mm; ....., smooth-wall. $R_\theta = 1000$.

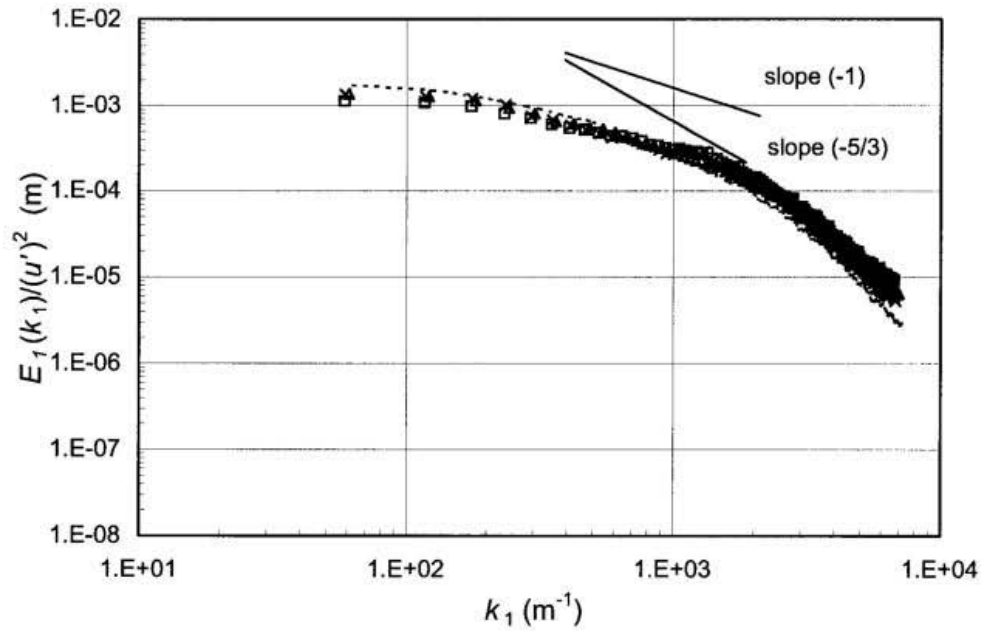

Fig. 5.2.6b Spectra of u' at a location where u'/U_0 is maximum ($y/\delta \approx 0.03$) and $x/\delta_0 =$ 0.013 for three different sized grooves: Δ, $d = 5$mm; ×, $d = 10$mm; □, $d =$ 20mm; ....., smooth-wall. $R_\theta = 3000$.

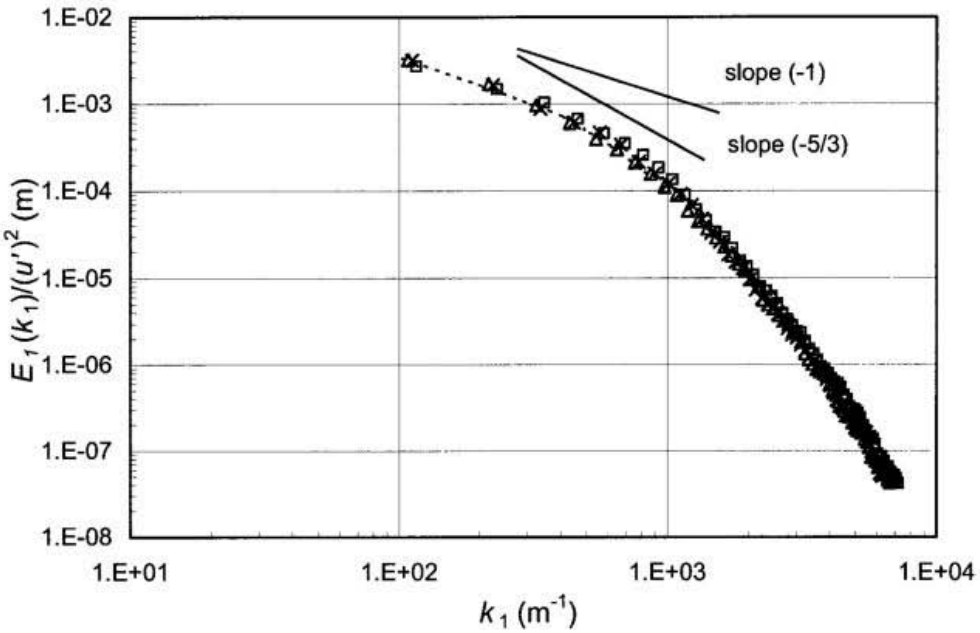

Fig. 5.2.6c Spectra of u' at a location where u'/U_0 is maximum ($y/\delta \approx 0.03$) and $x/\delta_0 =$ 0.013 for three different sized SC-grooves: Δ, $d = 5$mm; ×, $d = 10$mm; □, $d =$ 20mm; ....., smooth-wall. $R_\theta = 1000$.

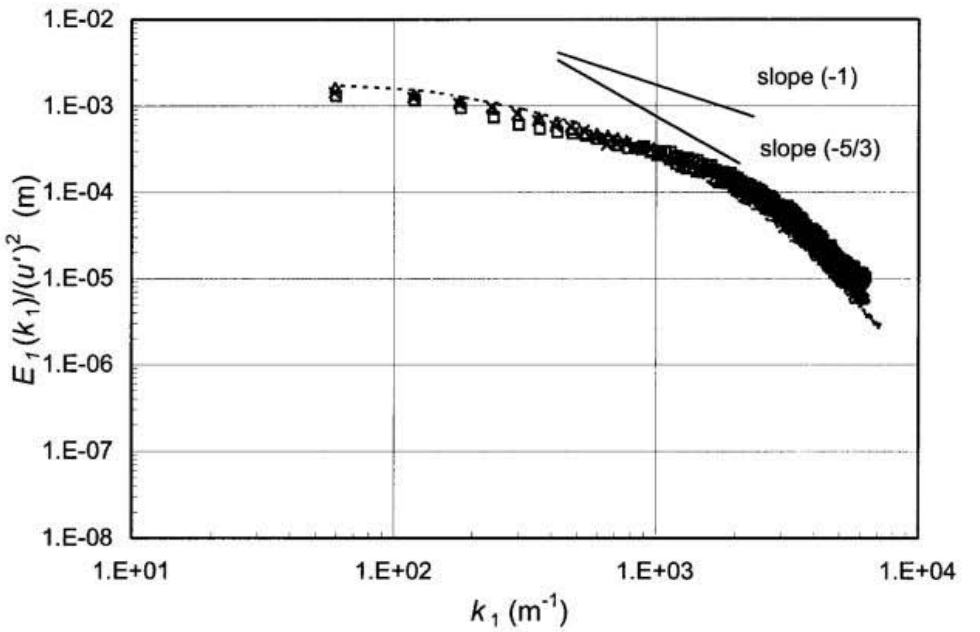

Fig. 5.2.6d Spectra of u' at a location where u'/U_0 is maximum ($y/\delta \approx 0.03$) and $x/\delta_0 =$ 0.013 for three different sized SC-grooves: Δ, $d = 5$mm; ×, $d = 10$mm; □, $d =$ 20mm; ....., smooth-wall. $R_\theta = 3000$.

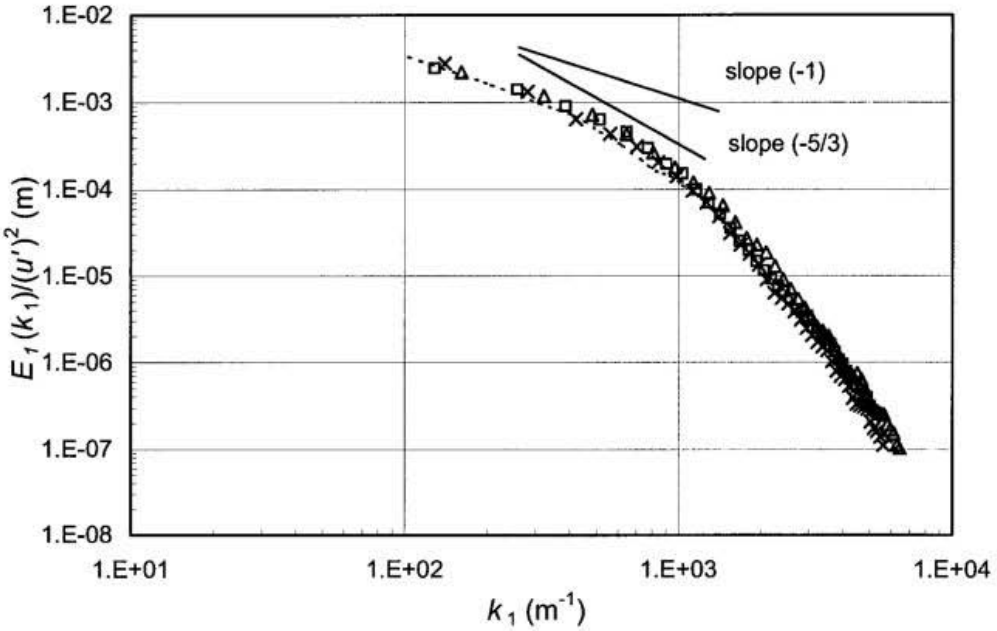

Fig. 5.2.6e Spectra of u' at a location where u'/U_0 is maximum ($y/\delta \approx 0.03$) and $x/\delta_0 =$ 0.013 for three different sized TR-grooves: △, $d =$ 5mm; ×, $d =$ 10mm; □, $d =$ 20mm; ....., smooth-wall. $R_\theta = 1000$.

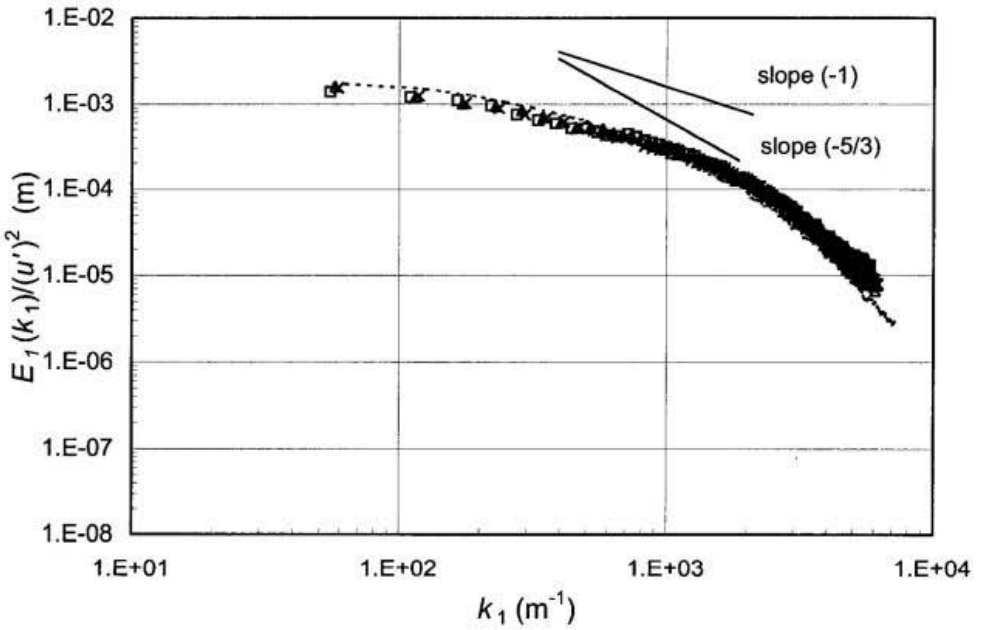

Fig. 5.2.6f Spectra of u' at a location where u'/U_0 is maximum ($y/\delta \approx 0.03$) and $x/\delta_0 =$ 0.013 for three different sized TR-grooves: △, $d =$ 5mm; ×, $d =$ 10mm; □, $d =$ 20mm; and ....., smooth-wall. $R_\theta = 3000$.

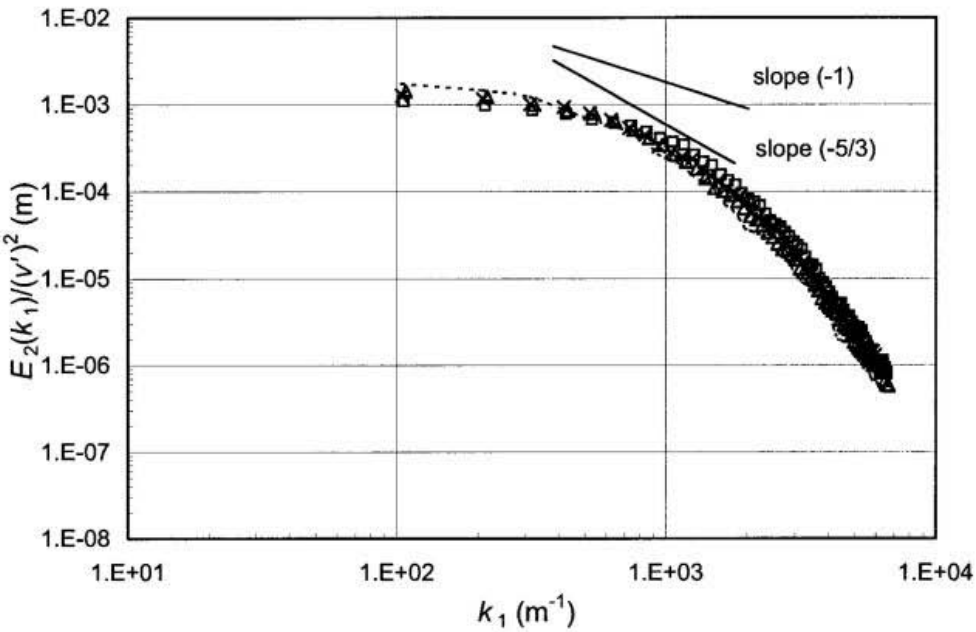

Fig. 5.2.7a Spectra of v' at a location where u'/U_0 is maximum ($y/\delta \approx 0.03$) and $x/\delta_0 =$ 0.013 for three different sized SQ-grooves at $R_\theta = 1000$: Δ, $d = 5$mm; ×, $d =$ 10mm; □, $d = 20$mm; ....., smooth-wall.

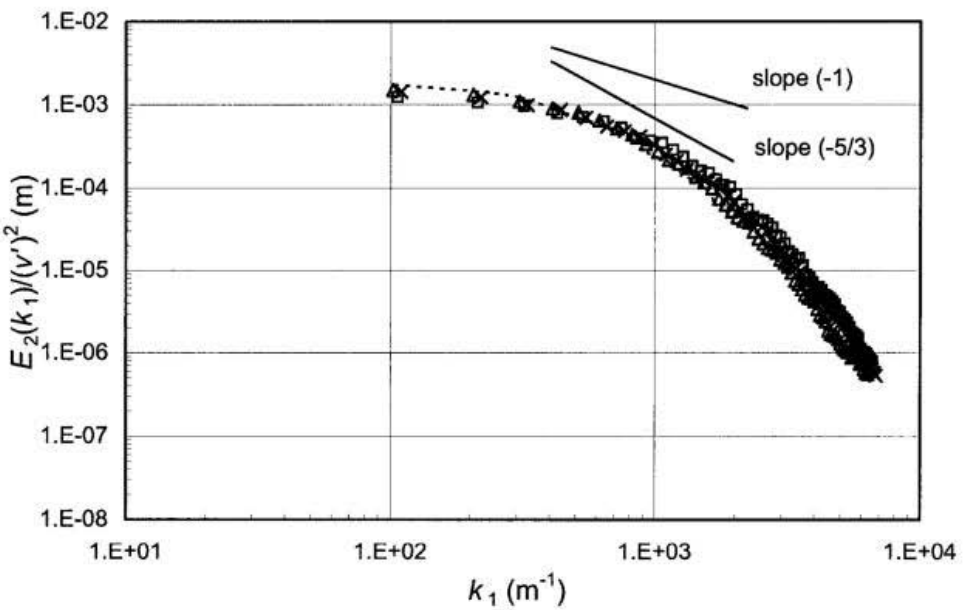

Fig. 5.2.7b Spectra of v' at a location where u'/U_0 is maximum ($y/\delta \approx 0.03$) and $x/\delta_0 =$ 0.013 for three different sized SC-grooves at $R_\theta = 1000$: Δ, $d = 5$mm; ×, $d =$ 10mm; □, $d = 20$mm; ....., smooth-wall.

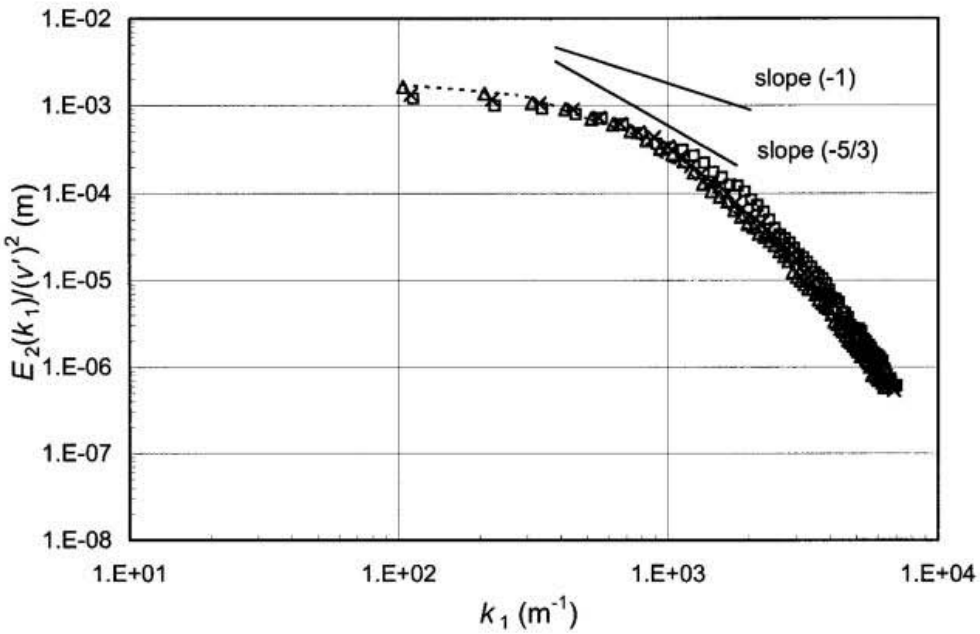

Fig. 5.2.7c Spectra of v' at a location where u'/U_0 is maximum ($y/\delta \approx 0.03$) and $x/\delta_0 =$ 0.013 for three different sized TR-grooves at $R_\theta = 1000$: Δ, $d = 5$mm; ×, $d =$ 10mm; □, $d = 20$mm; ....., smooth-wall.

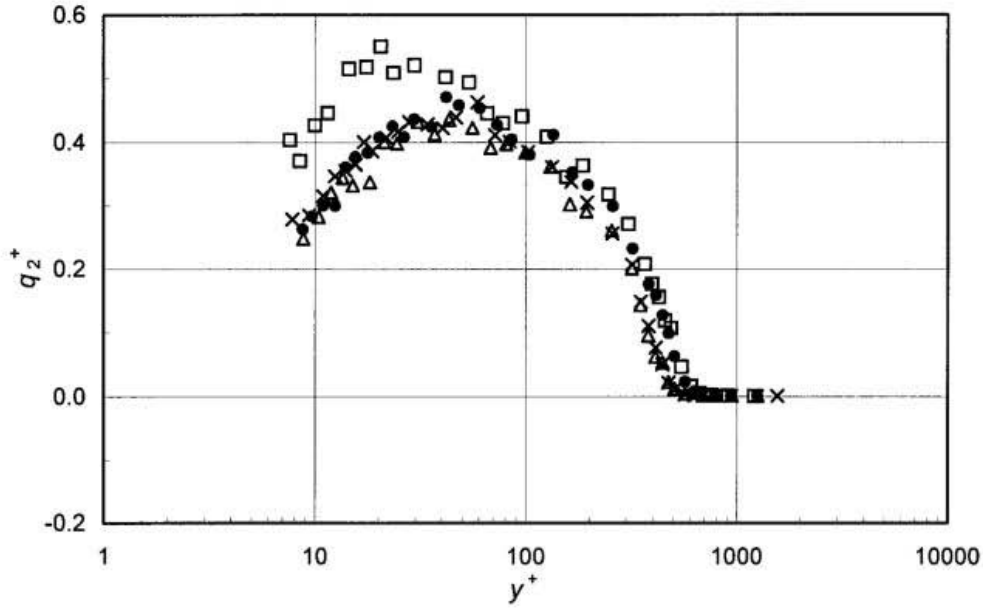

Fig. 5.3.1a Contribution of the second quadrant (q_2^+) to the Reynolds stress downstream of the different sized transverse SQ-grooves at $R_\theta = 1000$. △, $d = 5$mm; ×, $d = 10$mm; □, $d = 20$mm; •, smooth-wall.

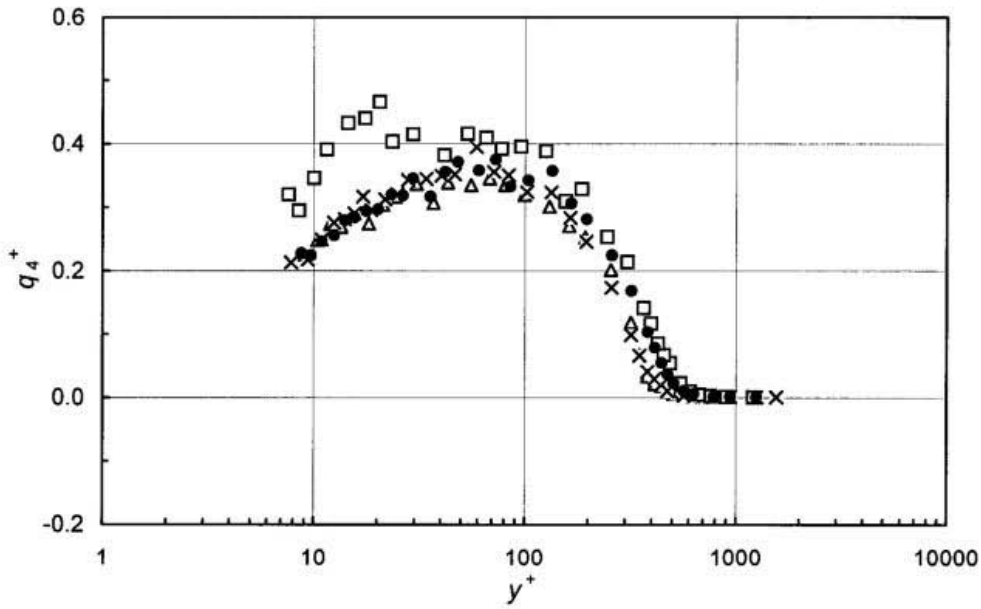

Fig. 5.3.1b Contribution of the fourth quadrant (q_4^+) to the Reynolds stress downstream of the different sized transverse SQ-grooves at $R_\theta = 1000$. △, $d = 5$mm; ×, $d = 10$mm; □, $d = 20$mm; •, smooth-wall.

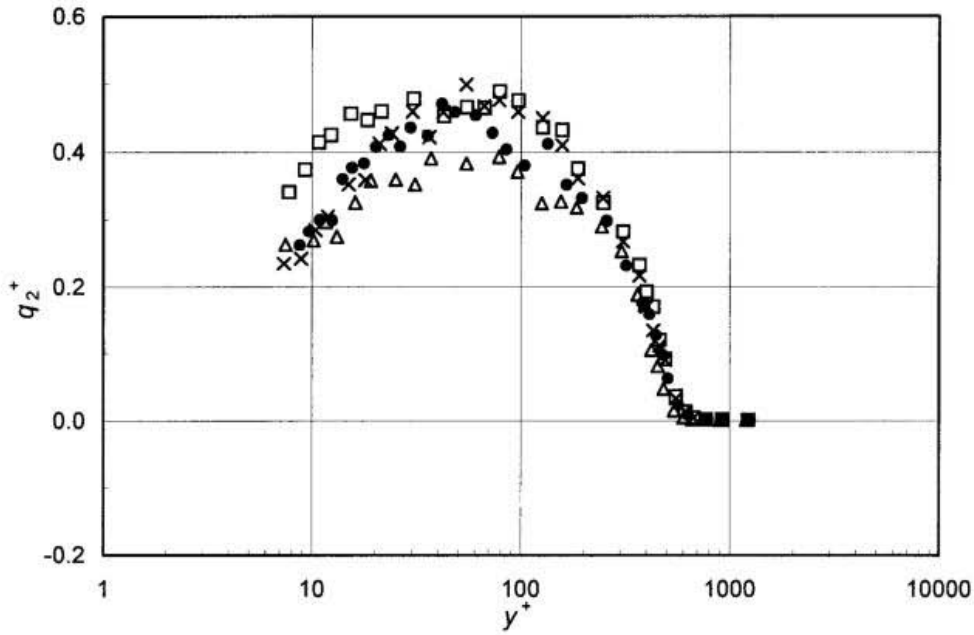

Fig. 5.3.1c Contribution of the second quadrant (q_2^+) to the Reynolds stress downstream of the different sized transverse SC-grooves at $R_\theta = 1000$. △, $d = 5$mm; ×, $d = 10$mm; □, $d = 20$mm; •, smooth-wall.

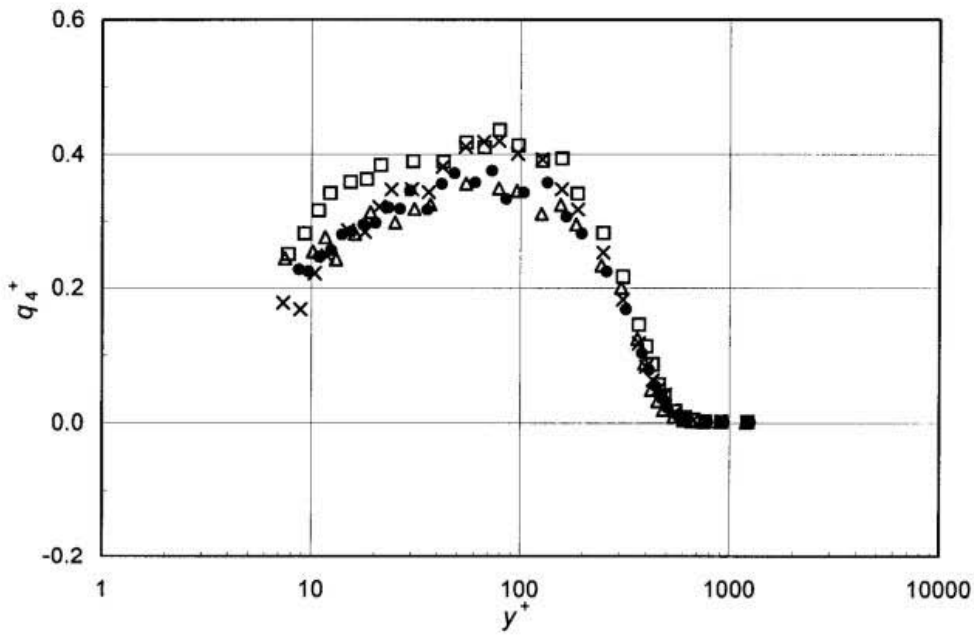

Fig. 5.3.1d Contribution of the fourth quadrant (q_4^+) to the Reynolds stress downstream of the different sized transverse SC-grooves at $R_\theta = 1000$. △, $d = 5$mm; ×, $d = 10$mm; □, $d = 20$mm; •, smooth-wall.

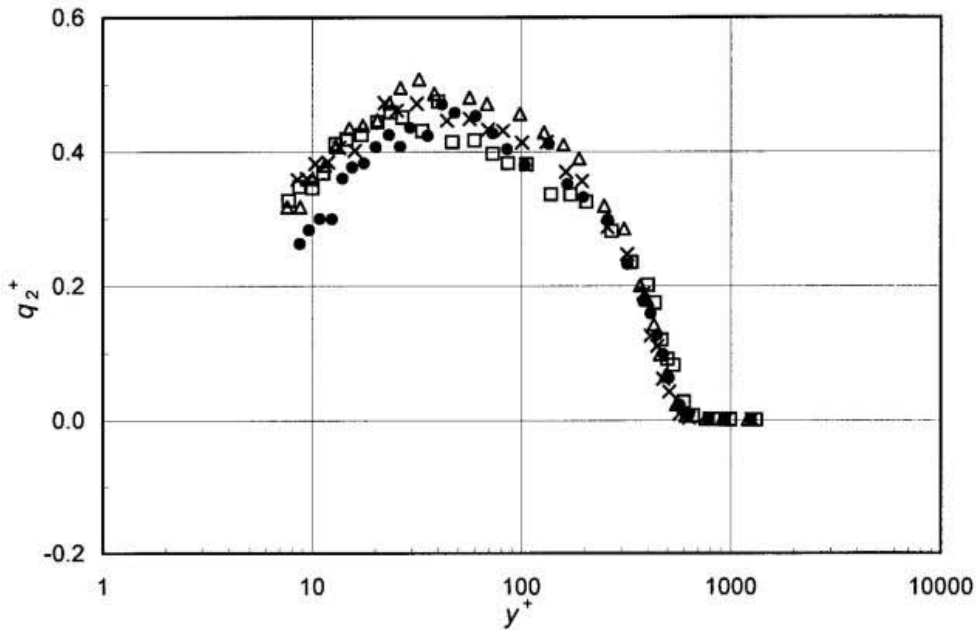

Fig. 5.3.1e Contribution of the second quadrant (q_2^+) to the Reynolds stress downstream of the different sized transverse TR-grooves at $R_\theta = 1000$. Δ, $d = 5$mm; ×, $d = 10$mm; □, $d = 20$mm; •, smooth-wall.

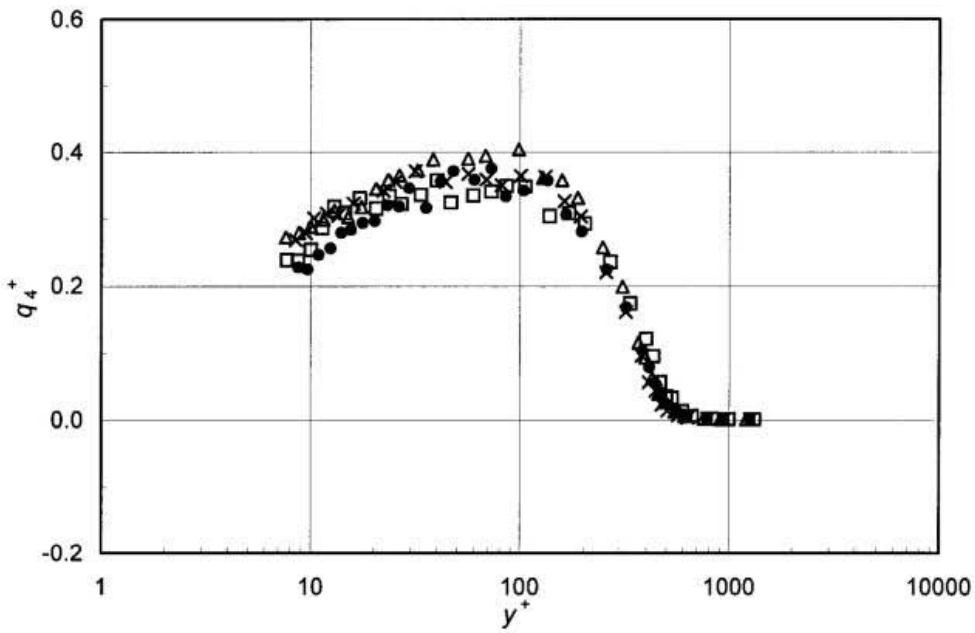

Fig. 5.3.1f Contribution of the fourth quadrant (q_4^+) to the Reynolds stress downstream of the different sized transverse TR-grooves at $R_\theta = 1000$. Δ, $d = 5$mm; ×, $d = 10$mm; □, $d = 20$mm; •, smooth-wall.

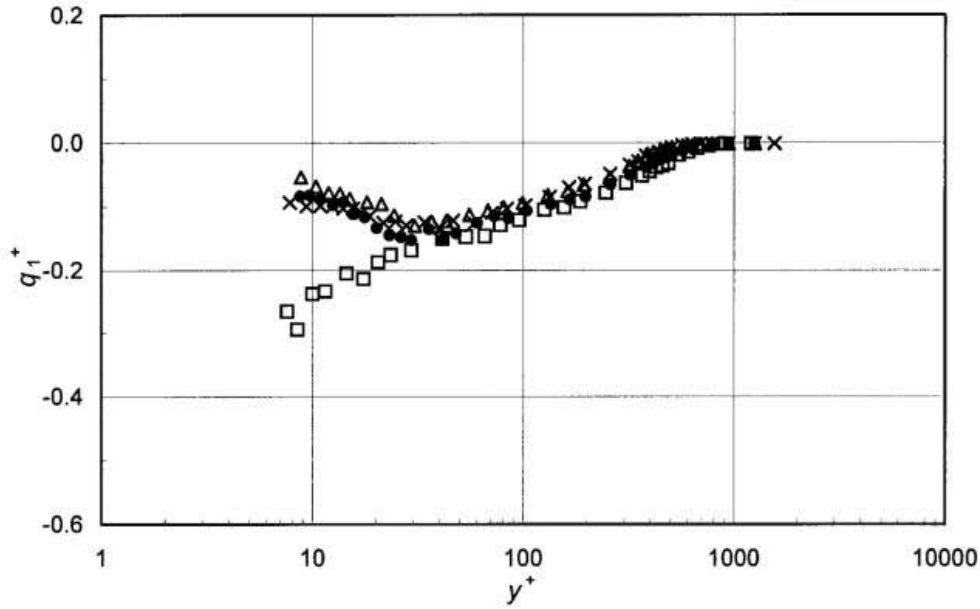

Fig. 5.3.2a Contribution of the first quadrant (q_1^+) to the Reynolds stress downstream of the different sized transverse SQ-grooves at $R_\theta = 1000$. △, $d = 5$mm; ×, $d = 10$mm; □, $d = 20$mm; •, smooth-wall.

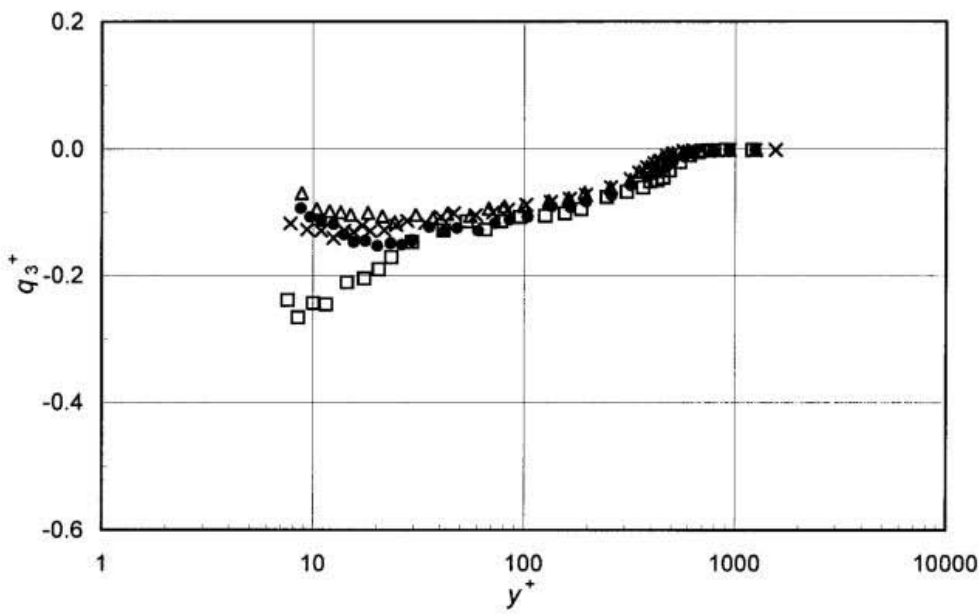

Fig. 5.3.2b Contribution of the third quadrant (q_3^+) to the Reynolds stress downstream of the different sized transverse SQ-grooves at $R_\theta = 1000$. △, $d = 5$mm; ×, $d = 10$mm; □, $d = 20$mm; •, smooth-wall.

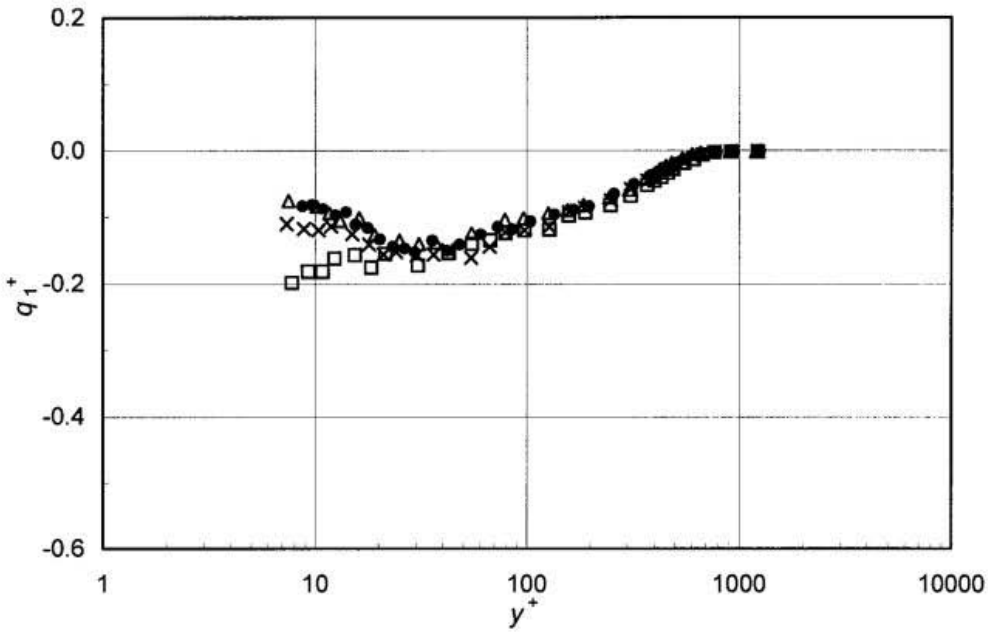

Fig. 5.3.2c Contribution of the first quadrant (q_1^+) to the Reynolds stress downstream of the different sized transverse SC-grooves at $R_\theta = 1000$. △, $d = 5$mm; ×, $d = 10$mm; □, $d = 20$mm; •, smooth-wall.

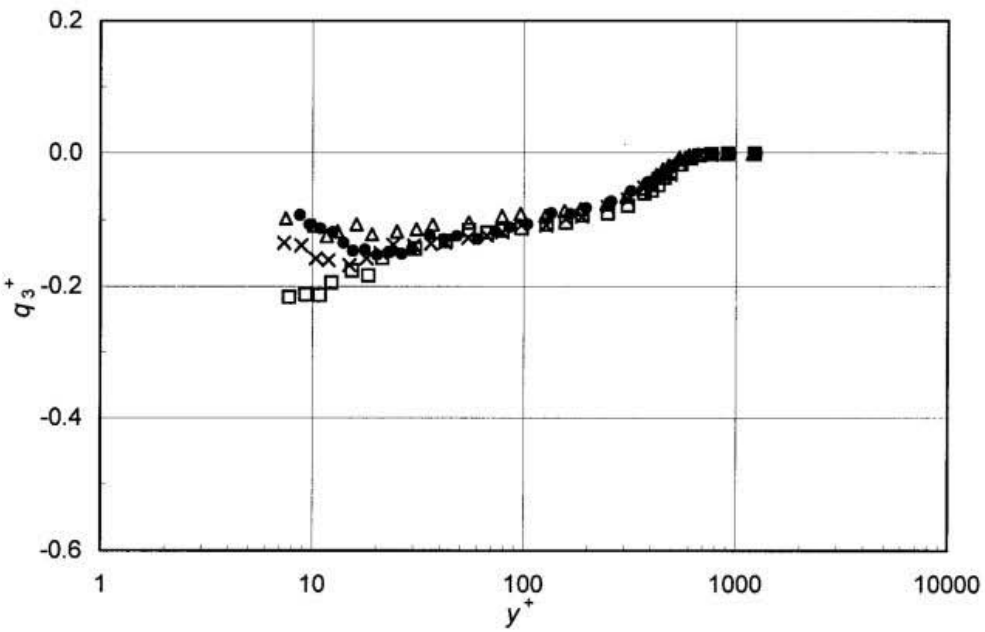

Fig. 5.3.2d Contribution of the third quadrant (q_3^+) to the Reynolds stress downstream of the different sized transverse SC-grooves at $R_\theta = 1000$. △, $d = 5$mm; ×, $d = 10$mm; □, $d = 20$mm; •, smooth-wall.

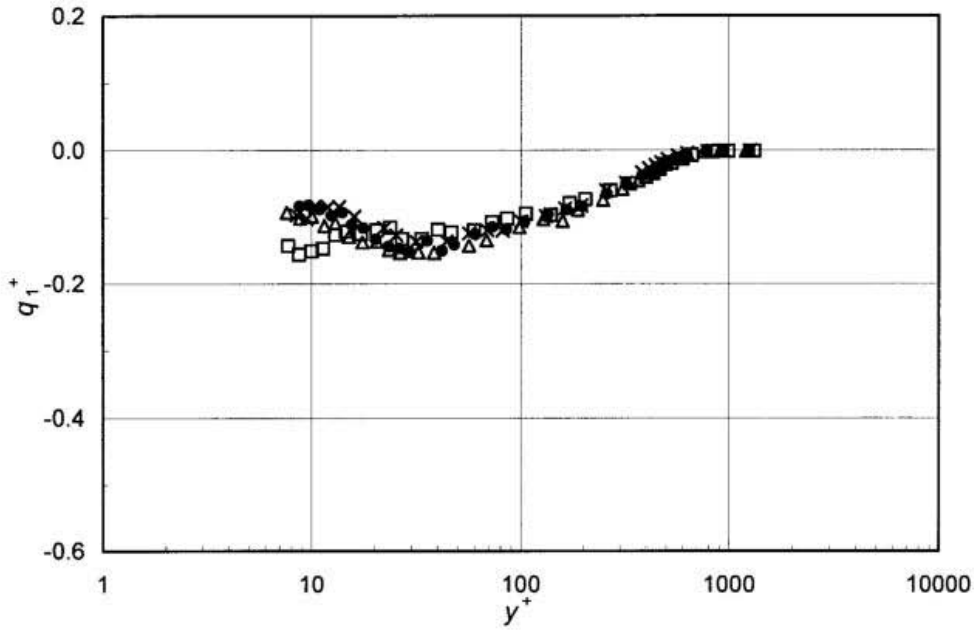

Fig. 5.3.2e Contribution of the first quadrant (q_1^+) to the Reynolds stress downstream of the different sized transverse TR-grooves at $R_\theta = 1000$. △, $d = 5$mm; ×, $d = 10$mm; □, $d = 20$mm; •, smooth-wall.

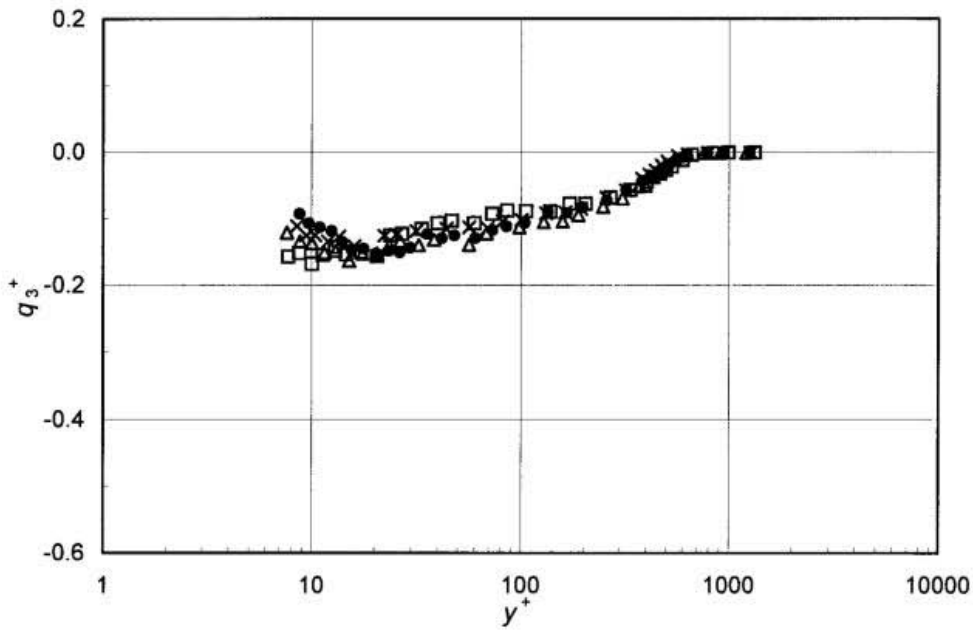

Fig. 5.3.2f Contribution of the third quadrant (q_3^+) to the Reynolds stress downstream of the different sized transverse TR-grooves at $R_\theta = 1000$. △, $d = 5$mm; ×, $d = 10$mm; □, $d = 20$mm; •, smooth-wall.

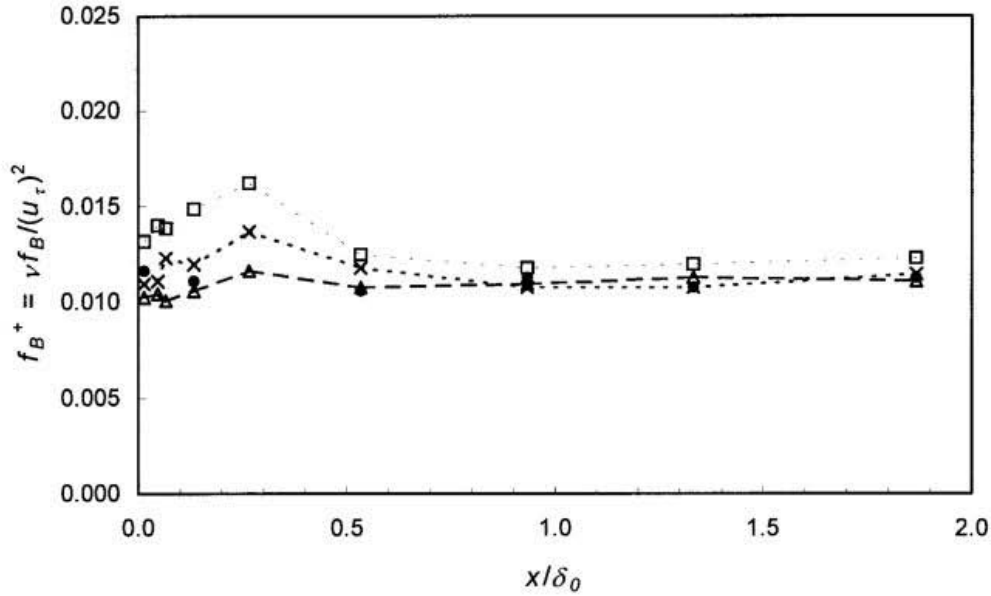

Fig. 5.3.3a Distribution of bursting frequency ($f_B^+ = \nu f_B/(u_\tau)^2$) downstream of the different sized SQ-grooves at $R_\theta = 1000$. Δ, $d = 5$mm; ×, $d = 10$mm; □, $d = 20$mm; •, smooth-wall.

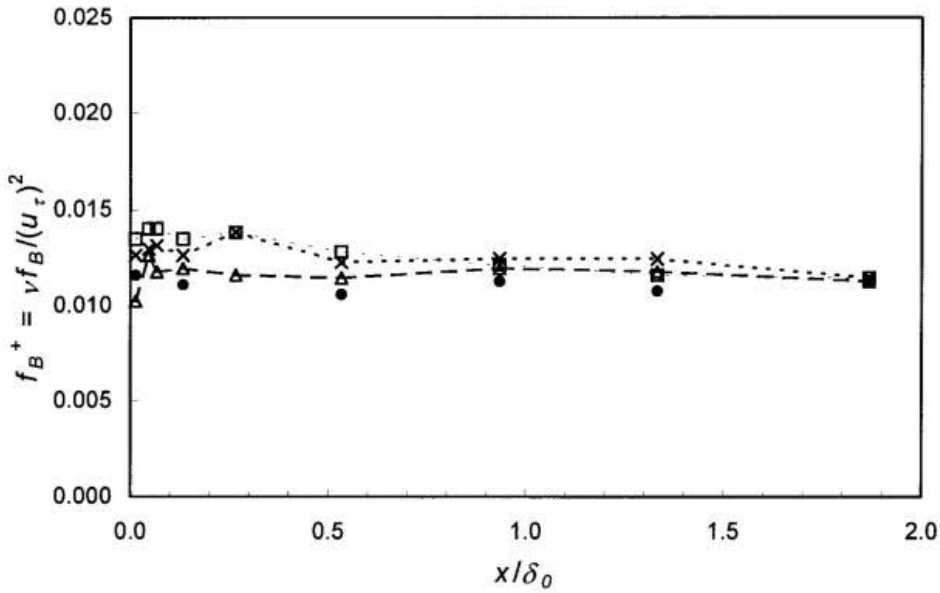

Fig. 5.3.3b Distribution of bursting frequency ($f_B^+ = \nu f_B/(u_\tau)^2$) downstream of the different sized SC-grooves at $R_\theta = 1000$. Δ, $d = 5$mm; ×, $d = 10$mm; □, $d = 20$mm; •, smooth-wall.

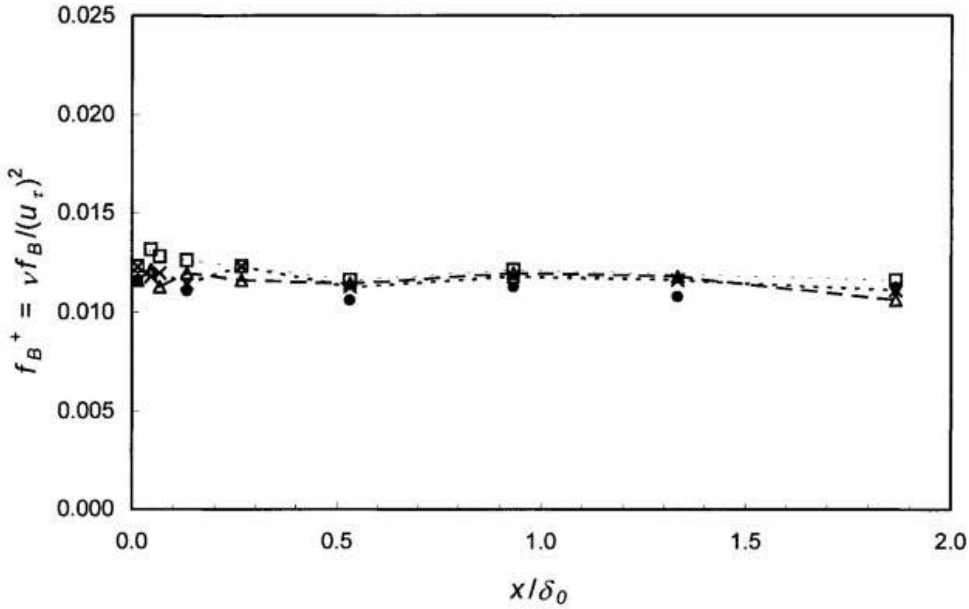

Fig. 5.3.3c Distribution of bursting frequency ($f_B^+ = \nu f_B/(u_\tau)^2$) downstream of the different sized TR-grooves at $R_\theta = 1000$. Δ, $d = 5$mm; ×, $d = 10$mm; □, $d = 20$mm; •, smooth-wall.

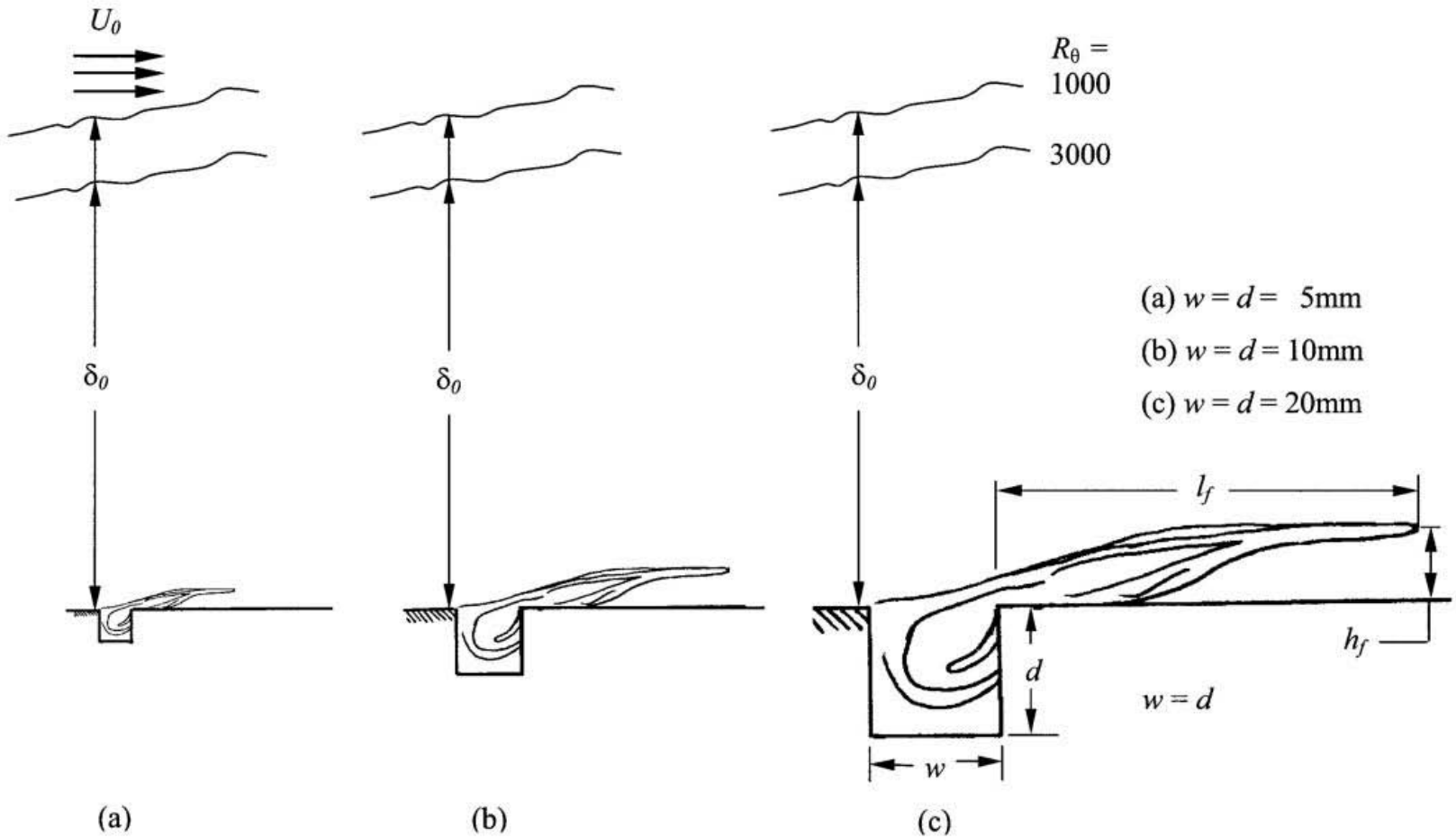

Fig. 5.4.1 (a) Schematic diagram of fluid ejection from the groove (reproduced from Ching et al., 1995b). Notations are added, which were absent in the original picture. Groove sizes are scaled relative to the boundary layer thickness (δ_0) at two R_θ values. (b) and (c) Enlarged version of (a) by 2× and 4×, respectively.

Chapter 6

Results and Discussion: Effect of Different Shapes of Grooves

In this chapter, the effects of the three different shaped grooves on the turbulent boundary layer are examined. In sections 6.1 and 6.2, results from the different shaped grooves are presented, while in section 6.3, the results are discussed and summarized. Only the results for the largest groove size (20mm) are presented, because the effect of the three different shapes is most prominent for this groove size. For the smaller groove sizes (5 and 10mm), on the other hand, the differences in the results from the three different shapes are small, and in general, it is difficult to draw any definitive conclusions from them. The skin friction coefficient (C_f), mean velocity (U) and the growth of the internal layer (d_i) for the three different shapes are presented and discussed. The streamwise and wall-normal turbulence intensities (u' and v'), Reynolds stress ($\langle -uv \rangle$),

turbulence energy spectra ($E(k_1)$), sweep and ejection events and bursting frequency are also discussed.

6.1 Mean Measurements

The distribution of $(C_f - C_{f,0})/C_{f,0}$ at $R_\theta = 1000$ and 3000 downstream of the three different shaped grooves is shown in Figs. 6.1.1a and 6.1.1b. The SQ-groove yields the largest increase in $((C_f - C_{f,0})/C_{f,0})_{max}$, while the TR-groove yields the smallest increase. The maximum and minimum in $(C_f - C_{f,0})/C_{f,0}$ downstream of the three different shaped grooves are summarized in Table 6.1. At the higher R_θ, the peak values in $(C_f - C_{f,0})/C_{f,0}$ occur immediately downstream of the groove, while they occur at $x/\delta_0 \approx 0.047$, 0.067 and 0.4, respectively, for the TR-, SC- and SQ-grooves at the lower R_θ. The maximum increase in C_f for the TR-, SC- and SQ-grooves at $R_\theta = 3000$ are approximately 27, 32 and 46 percent, compared to 20, 22 and 24 percent at $R_\theta = 1000$. The increase in C_f is followed by a decrease in C_f below the smooth-wall value at either R_θ for all shapes. For instance, a maximum reduction in C_f up to approximately 11 percent is observed for the SQ-groove at the higher R_θ, while this reduction is approximately 8 and 6 percent for the SC- and TR-grooves, respectively.

Table 6.1. Effect of d/δ_0 and d^+ on $((C_f - C_{f,0})/C_{f,0})_{max}$ and $((C_f - C_{f,0})/C_{f,0})_{min}$

Experiments of and groove shape	R_θ	d/δ_0	$d^+ = u_\tau d/\nu$	$((C_f - C_{f,0})/C_{f,0})_{max}$ (%)	$((C_f - C_{f,0})/C_{f,0})_{min}$ (%)
Pearson et al. (1997), square	1320	0.170*	100	200	-50
Elavarasan et al. (1996), square	1300	0.125	100	100	-50
Present study:					
- square	1000	0.267	128	24	-4
- semicircular base				22	-11
- Triangular				20	-6
Present study:					
- square	3000	0.333	296	46	-11
- semicircular base				32	-8
- Triangular				27	-6

* Based on δ at 50 mm upstream of the groove leading edge.

Mean velocity profiles downstream of the three different shaped grooves normalized using outer variables (U_0 and δ) are compared in Figs. 6.1.2a and 6.1.2b. At the lower R_θ, the effect of all three grooves on U/U_0 is not significant (Fig. 6.1.2a), with only the SQ-groove having a small increase (approximately 8 percent) in the U/U_0 profile in the inner region at the first downstream measurement location. As x increases, the effect of the three different shaped grooves on U/U_0 cannot be differentiated, and by x/δ_0 = 1.867, the profiles have relaxed back to the smooth-wall profile. The effect of the grooves on U/U_0 is more discernible at the higher R_θ (Fig. 6.1.2b). At the first

downstream location, there is an increase in U/U_0 for all three groove shapes in the region $y/\delta \leq 0.01$, while there is a decrease in U/U_0 in the buffer region. The local increase in U/U_0 is up to approximately 20 percent for the SQ- and TR-grooves and approximately 15 percent for the SC-groove at $x/\delta_0 = 0.013$ in the region $y/\delta \leq 0.01$. There is, however, no apparent effect of the groove shape on the U/U_0 profiles at $x/\delta_0 \geq 0.047$. The increase in U/U_0 in the inner region is no longer discernible at $x/\delta_0 = 0.133$. The decrease in U/U_0 in the buffer region, however, persists to $x/\delta_0 = 0.267$.

The mean velocity profiles at $R_\theta = 1000$ normalized using inner variables (u_τ and ν) are shown in Fig. 6.1.3a. The log-law lines of the form $U^+ = (1/0.41)\ ln(y^+) + 4.9$ for the smooth-wall profiles are also shown in the figure for comparison. The maximum downward shift of the grooved-wall U^+ profiles from the smooth-wall profile occurs at different streamwise locations for the different shaped grooves. The largest downward shift of the U^+ profiles occurs at $x/\delta_0 = 0.267$, 0.067 and 0.047 for the SQ-, SC- and TR-grooves, respectively. The profiles for the different shaped grooves collapse at $x/\delta_0 = 0.933$ with a slight upward shift. By $x/\delta_0 = 1.867$, the U^+ profiles have relaxed back to the corresponding smooth-wall profiles. At $R_\theta = 3000$, the effect of the grooves on U^+ is more significant (Fig. 6.1.3b). The largest downward shift occurs at $x/\delta_0 = 0.013$ for the SQ-groove, with the smallest shift for the TR-groove. The largest upward shift in U^+ profiles occurs at $x/\delta_0 = 1.867$, with the SQ-groove having the most significant effect. The effect of the TR-groove on the upward and downward shifts in U^+ is the weakest among the three shaped grooves in this instance.

The growth of the internal layer (d_i) as a response of the turbulent boundary layer to the presence of the grooves is shown in Fig. 6.1.4. At $R_\theta = 1000$, the groove shape does not play an important role in the rate of growth and the height of d_i. At $R_\theta = 3000$, however, the height of d_i for the SQ-groove is larger than that for the SC- and TR-grooves beyond $x/\delta_0 = 0.2$. For example, by $x/\delta_0 = 1.0$, d_i for the SQ-groove is approximately 5 percent larger than that for the SC- and TR-grooves. At this R_θ, the initial rates of growth of d_i for all three grooves are similar.

6.2 Turbulence measurements

The streamwise turbulence intensity (u'/U_0) profiles downstream of the three different shaped grooves are presented in Figs. 6.2.1a and 6.2.1b. At $R_\theta = 1000$, there is an increase in u'/U_0 downstream of all three grooves in the region $y/\delta < 0.04$ (Fig. 6.2.1a). The TR-groove displays a small increase in the maximum value of u'/U_0 ($(u'/U_0)_{max}$) over the corresponding smooth-wall value of approximately 13 percent. The corresponding increase in $(u'/U_0)_{max}$ for the SQ- and SC-grooves is less than 8 percent over $(u'/U_0)_{max,sw}$. The relaxation of u'/U_0 to the smooth-wall value takes longer than that for U/U_0 at this R_θ. A small increase in u'/U_0 due to the presence of the grooves is still discernible in the region $y/\delta < 0.02$ even at $x/\delta_0 = 1.867$.

At $R_\theta = 3000$, an increase in u'/U_0 is discernible in the range $0.004 \leq y/\delta \leq 0.06$ at $x/\delta_0 = 0.013$ (Fig. 6.2.1b), with the maximum increase being for the SQ-groove. For

example, at $y/\delta \approx 0.005$, the increase in u'/U_0 for the SQ-, SC- and TR-grooves are 30, 15 and 15 percent. The maximum in u'/U_0, however, is not greater than the peak value of the smooth-wall case, with the profile showing a relatively flat peak over the region $0.01 \leq y/\delta \leq 0.04$. It is not known if the u'/U_0 is higher at locations smaller than $x/\delta_0 = 0.013$. For all three groove shapes, the increase in u'/U_0 in the region $0.02 \leq y/\delta \leq 0.06$ propagates outwards in the layer as x/δ_0 increases (Fig. 6.2.2). For example, at $x/\delta_0 = 0.013$, there is an increase in u'/U_0 in the region $0.02 \leq y/\delta \leq 0.06$, and as x/δ_0 further increases, the range of y/δ where u'/U_0 is increased moves outwards. This seems to be consistent with the mean velocity profiles, which show a decrease in this region (Fig. 6.1.2b). The outer edge of the outward propagation of u'/U_0 is related to the internal layer (d_i) growth at the same R_θ. In the region $x/\delta_0 \leq 0.4$, the outward propagation of u'/U_0 is comparable with the d_i. For example, by $x/\delta_0 = 0.35$, the outward propagation and d_i reach the same thickness of approximately $0.09\delta_0$. The outward propagation rate is similar for all three groove shapes. By $x/\delta_0 = 1.867$, the u'/U_0 profiles for all three shapes have relaxed back to the smooth-wall values within the layer.

There is a less pronounced effect on the u'^+ profiles due to the SC- and TR-grooves compared to the effect of the SQ-groove (Fig. 6.2.3a). At $x/\delta_0 = 0.013$, a downward shift in u'^+ in the region $y^+ < 5$ for the SQ-groove from the corresponding smooth-wall value is observed, which is absent for the SC- and TR-grooves. As x/δ_0 increases, the downward shift in u'^+ profiles for the SQ-groove is more pronounced. At $x/\delta_0 = 0.267$, there is a considerable downward shift in u'^+ for the SQ-groove compared to

the profiles for the SC- and TR-grooves. At $x/\delta_0 = 0.933$, the u'^+ profiles for the three different shaped grooves collapse better than the profiles at other x-locations. Figure 6.2.3b shows the distribution of u'^+ profiles downstream of the three different shaped grooves at $R_\theta = 3000$. In general, there is no significant difference in the u'^+ profiles, except at $x/\delta_0 = 1.867$. At this location, the u'^+ profile for the SQ-groove is higher than that for the SC- and TR-grooves. The corresponding u'/U_0 profiles (Fig. 6.2.1b) for the three different shaped grooves collapse well at this x-location. Hence, the upward shift in the u'^+ profile for the SQ-groove is primarily due to the lower C_f for the SQ-groove at this x-location.

The wall-normal turbulence intensity profiles (v'/U_0) for the different shaped grooves at $R_\theta = 1000$ are shown in Fig. 6.2.4. There is a significant increase in v'/U_0 in the region $y/\delta < 0.06$ for all three groove shapes, especially at $x/\delta_0 = 0.013$. The effect of the SQ-groove on v'/U_0 is the most intense compared to the SC- and TR-grooves. The v'/U_0 is increased by up to approximately 50 percent for the SQ-groove at this x-location, compared to approximately 25 percent for both the SC- and TR-grooves. As x increases, the differences between the three different shapes become less distinguishable.

The Reynolds stress distribution ($\langle -uv \rangle/(U_0)^2$) downstream of the three different shaped grooves at $R_\theta = 1000$ is presented in Fig. 6.2.5. With the scatter in the data, it is difficult to distinguish any effect of the different shaped grooves on $\langle -uv \rangle/(U_0)^2$. As the downstream distance increases, the $\langle -uv \rangle/(U_0)^2$ in the region $y/\delta < 0.1$, however, increases above the corresponding smooth-wall values. At $x/\delta_0 = 1.867$, the $\langle -uv \rangle/(U_0)^2$ has still not

relaxed to the smooth-wall value for all three groove shapes, where an increase in $\langle -uv \rangle/(U_0)^2$ up to approximately 40 percent over the corresponding smooth-wall value in the region $y/\delta < 0.1$ is discernible.

Representative turbulence energy spectra of u' and v' are shown in Figs. 6.2.6a to 6.2.6c. At both R_θ, $E_1(k_1)/(u')^2$ for the different groove shapes collapse over the entire wave number (k_1) range. At the lower R_θ, the spectra over the grooved-walls are not distinguishable from the smooth-wall spectrum. At the higher R_θ, the grooves seem to enhance the role of the smaller energy containing eddies to the turbulent transport, which is reflected by an increase in the energy spectra at $k_1 > 1000\text{m}^{-1}$ over the corresponding smooth-wall spectrum. At $R_\theta = 1000$, the effect of the groove shape on $E_2(k_1)/(v')^2$ is not discernible (Fig. 6.2.6c). The redistribution of $E_2(k_1)/(v')^2$ within the whole k_1 range is consistent with the results for v'/U_0.

The distributions of q_2^+ and q_4^+ across the layer for the three different shaped grooves at $x/\delta_0 = 0.013$ are shown in Figs. 6.2.7a and 6.2.7b. A small decrease in q_2^+ and q_4^+ due to the presence of the TR-groove compared to the smooth-wall value is observed in the region $50 < y^+ < 200$ ($0.1 < y/\delta < 0.4$), but this groove causes an increase in q_2^+ and q_4^+ in the region closer to the wall (say $y^+ < 30$ or $y/\delta < 0.06$). The effects of the SQ- and SC-grooves on q_2^+ and q_4^+, on the contrary, are to increase these two events in the region $y^+ < 60$ ($y/\delta < 0.12$). The maximum increase in q_2^+ in the region $y^+ < 60$ is approximately 25, 15 and 10 percent for the SQ-, SC- and TR-grooves, respectively, and the corresponding increase in q_4^+ is approximately 30, 20 and 10 percent. In the region $y^+ >$

250 ($y/\delta > 0.5$), q_2^+ and q_4^+ are similar for both the smooth- and grooved-walls. The effect of the SQ-groove on q_1^+ and q_3^+ is the most pronounced, followed by the SC- and TR-grooves (Figs. 6.2.7c and 6.2.7d). The effect of the grooves on q_1^+ is more significant than on q_3^+ and penetrates farther away from the wall. For example, the increase (in negative value) in q_1^+ due to the presence of the SQ- and SC-grooves is clearly seen up to $y^+ \approx 50$ or $y/\delta \approx 0.1$, while the increase (in negative value) in q_3^+ due to the presence of the grooves is limited up to $y^+ \approx 25$ or $y/\delta \approx 0.05$. The maximum increase in q_1^+ in the region $y^+ < 30$ is approximately 300, 200 and 150 percent for the SQ-, SC- and TR-grooves, respectively, and the corresponding increase in q_3^+ is approximately 250, 200 and 150 percent. In general, q_1^+, q_2^+, q_3^+ and q_4^+ are affected the most by the SQ-groove, followed by the SC- and TR-grooves.

The f_B^+ obtained at $y/\delta \approx 0.03$ ($y^+ \approx 14$) downstream of the different shaped grooves is presented in Fig. 6.2.8. The average values of f_B^+ over the SQ-, SC- and TR-grooves are approximately 20, 16 and 9 percent higher than the f_B^+ over the smooth-wall. For the SQ-groove, f_B^+ shows a significant peak at $x/\delta_0 \approx 0.3$, which is absent for the SC- and TR-grooves. The maximum increase in f_B^+ is the most pronounced for the SQ-groove, followed by the SC-groove and TR-groove. The location of the maximum value of f_B^+ for the SQ-groove occurs farther downstream of the groove compared to the SC- and TR-grooves. The distribution of f_B^+ approximately resembles the C_f distribution (Fig. 6.1.1a), which is consistent with the observation that the turbulent bursting process in the near-wall region is related to the wall shear stress.

6.3 Discussion and Summary

The effect of the SQ-groove on the turbulent boundary layer is much more significant compared to the SC- and TR-grooves. The most obvious effect of the different shaped grooves on the turbulent boundary layer can be seen from the distribution of C_f downstream of the different grooves, especially at the higher R_θ (Fig. 6.1.1b). For instance, the largest increase in C_f is for the SQ-groove, followed by the SC- and TR-grooves. The higher increase in C_f for the SQ-groove is associated with an increase in the turbulence intensities (u'/U_0 and v'/U_0). The presence of the SQ-groove also causes a significant increase in the Reynolds stress ($\langle -uv \rangle/(U_0)^2$) and the near-wall bursting frequency (f_B^+).

The likely flow patterns inside the different shaped grooves (SQ-, SC- and TR-grooves) are shown schematically in Fig. 6.3.1. For the SQ-groove, in addition to the primary eddy with a typical diameter D_h, two smaller eddies are formed at the bottom corners of the groove (Ghia et al., 1982; Benjamin and Denny, 1979). These secondary eddies are probably absent in the SC-groove due to the rounded bottom corners. For the TR-groove, a secondary eddy at the apex of the groove is formed (Taneda, 1979; Moffat, 1964), the size of which is probably larger than that inside the SQ-groove. These vortical motions are periodically "pumped" out of the groove by the passage of the near-wall quasi-streamwise vortices over the groove (Townes and Sabersky, 1966; Ching et al., 1995b). The mass and momentum of the ejected fluid will have an effect on the wall shear stress immediately downstream of the groove. In this instance, the mass of fluid

ejected from the SQ- and SC-grooves would be similar, while it would be less for the TR-groove.

Haugen and Dhanak (1966) showed that the flow streamlines originating at the upstream shoulder of a square groove are slightly deflected downward as they move over the groove. Their analysis, however, did not resolve the flow streamlines around the downstream shoulder of the groove. The flow streamline pattern in the vicinity of the groove is constructed qualitatively in Fig. 6.3.2a. The downstream shoulder of the groove can impose significant disturbances to the flow streamlines close to it. It can be conjectured that if there is no flow separation at the downstream shoulder, a local favorable pressure gradient ($\partial p/\partial x$) is established as the streamlines come closer as the flow moves from point 1 to 2 in Fig. 6.3.2a. This $\partial p/\partial x$ is isolated in the near-wall region around the downstream shoulder of the groove and is probably small. The localized small favorable $\partial p/\partial x$ would result in an increase in C_f just downstream of the groove. The above conjecture about the pressure gradient ($\partial p/\partial x$) in the vicinity of the downstream shoulder of the SQ-groove should also be valid for the SC- and TR-grooves. The flow streamlines over the SC-groove are most probably similar to that for the SQ-groove, since the downstream wall of both grooves is at right angles to the main flow direction. The flow streamlines over the TR-groove, however, could be different since the downstream wall in this case is at a smaller angle to the main flow direction. A schematic of the streamlines over the TR-groove is shown in Fig. 6.3.2b. The favorable $\partial p/\partial x$ immediately downstream of the TR-groove is likely to be less than that for the SQ- or SC-groove due to the smaller deflection of the flow streamlines around the downstream shoulder. Both

the size and momentum of the ejected fluid and the local $\partial p/\partial x$ must play a role in the change in turbulent characteristics just downstream of the groove. These parameters are the smallest for the TR-groove, and are reflected in the results which indicate that the TR-groove has the smallest effect on the turbulent boundary layer.

In summary, the SQ-groove has the most significant effect on the turbulent characteristics at a given R_θ, with the effects being more significant at the higher R_θ. The main conclusions can be summarized as follows:

(1) The C_f is most affected by the SQ-groove and least affected by the TR-groove. The maximum increase of C_f over the smooth-wall value is approximately 24, 22 and 20 percent, respectively, for the SQ-, SC- and TR-grooves at the lower R_θ, and 46, 32 and 27 percent at the higher R_θ (Figs. 6.1.1a and b).

(2) At the lower R_θ, only the SQ-groove has a discernible effect on U/U_0 at the location closet to the groove. At the higher R_θ, there is an increase (up to approximately 20 percent) in U/U_0 due to the presence of the groove over the corresponding smooth-wall value in the near-wall region immediately downstream of the groove. As x increases, the effect of the groove on U/U_0 propagates outwards in the layer, and the differences due to the different shaped grooves are not distinguishable (Figs. 6.1.2a and b).

(3) At the higher R_θ, the internal layer for the SQ-groove grows more rapidly than that for the SC- and TR-grooves. At the lower R_θ, however, the d_i grows in a similar manner for all three groove shapes. At the higher R_θ , the height of the internal layer

for the SQ-groove is approximately 5 percent larger than for the SC- and TR-grooves by $x/\delta_0 = 1.0$ (Fig. 6.1.4).

(4) There are significant effects in u'/U_0 in the near-wall region immediately downstream of the groove at either R_θ. At the higher R_θ, the increase in u'/U_0 is more pronounced for the SQ-groove than that for the SC- and TR-grooves, although the $(u'/U_0)_{max}$ for all three groove shapes is not greater than $(u'/U_0)_{max,sw}$. At the lower R_θ, however, the effect of the TR-groove seems to be the most pronounced compared to the effects of the SQ- and SC-grooves. For the TR-groove, an increase in $(u'/U_0)_{max}$ up to approximately 13 percent just downstream of the groove at $R_\theta = 1000$ is observed, while the increase is less than 8 percent for the SQ- and SC-grooves. The increase in $(u'/U_0)_{max}$ over the TR-groove at the lower R_θ is rather unexpected as the other parameters are affected the most by the SQ-groove (Figs. 6.2.1a and b).

(5) The effect of the SQ-groove on v'/U_0 is more significant than that of the SC- and TR-grooves. The increase in v'/U_0 for the SQ-groove over the smooth-wall value immediately downstream of the groove is approximately 50 percent, compared to approximately 25 percent increases for the SC- and TR-grooves (Fig. 6.2.4).

(6) There is no apparent effect of the groove shape on the Reynolds stress ($\langle -uv \rangle/(U_0)^2$). There is, however, an increase in $\langle -uv \rangle/(U_0)^2$ for all three groove shapes in the region $y/\delta \leq 0.1$ (Fig. 6.2.5).

(7) The difference in the $E_1(k_1)/(u')^2$ and $E_2(k_1)/(v')^2$ over the three different groove shapes are not discernible. The presence of the groove, however, changes the turbulent energy spectra compared to the corresponding smooth-wall spectrum. For

R_θ = 3000, the $E_1(k_1)/(u')^2$ is increased at the higher k_1 and decrease at the lower k_1. This is also the case for the $E_2(k_1)/(v')^2$ at R_θ = 1000. The $E_1(k_1)/(u')^2$ for R_θ = 1000, on the other hand, are almost the same with the spectrum on the smooth-wall over the entire k_1 range (Figs. 6.2.6a to c).

(8) At R_θ = 1000, q_1^+, q_2^+, q_3^+ and q_4^+ are increased due to the presence of the SQ- and SC-grooves. The effect of the TR-groove, on the other hand, is to reduce q_2^+ and q_4^+ in the region $50 < y^+ < 200$ (or $0.1 < y/\delta < 0.4$) and to increase q_1^+ and q_3^+ in the region $y^+ < 30$ (or $y/\delta < 0.06$) (Figs. 6.2.7a to d). At R_θ = 1000, the average bursting frequency (f_B^+) immediately downstream of the SQ-, SC- and TR-grooves are approximately 20, 16 and 9 percent higher than that over the corresponding smooth-wall (Fig. 6.2.8).

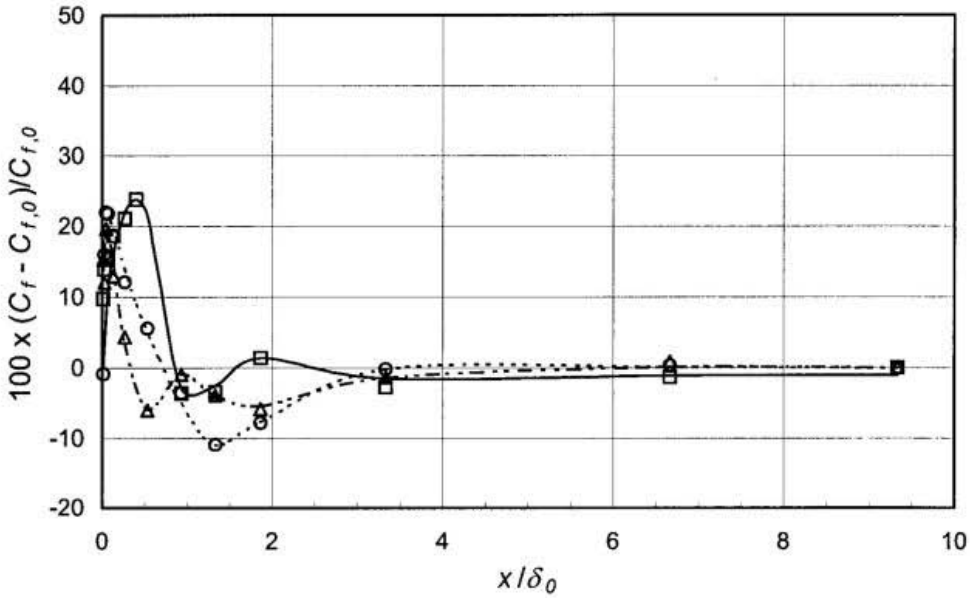

Fig. 6.1.1a Skin friction distribution downstream of three different shaped grooves with d = 20mm at R_θ = 1000: Δ, TR-groove; ○, SC-groove; □, SQ-groove.

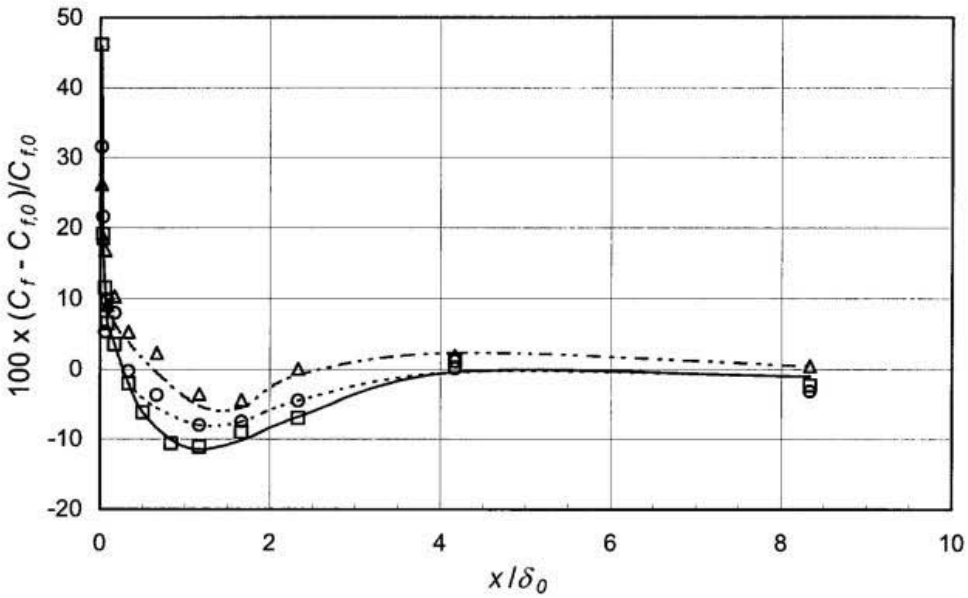

Fig. 6.1.1b Skin friction distribution downstream of three different shaped grooves with d = 20mm at R_θ = 3000: Δ, TR-groove; ○, SC-groove; □, SQ-groove.

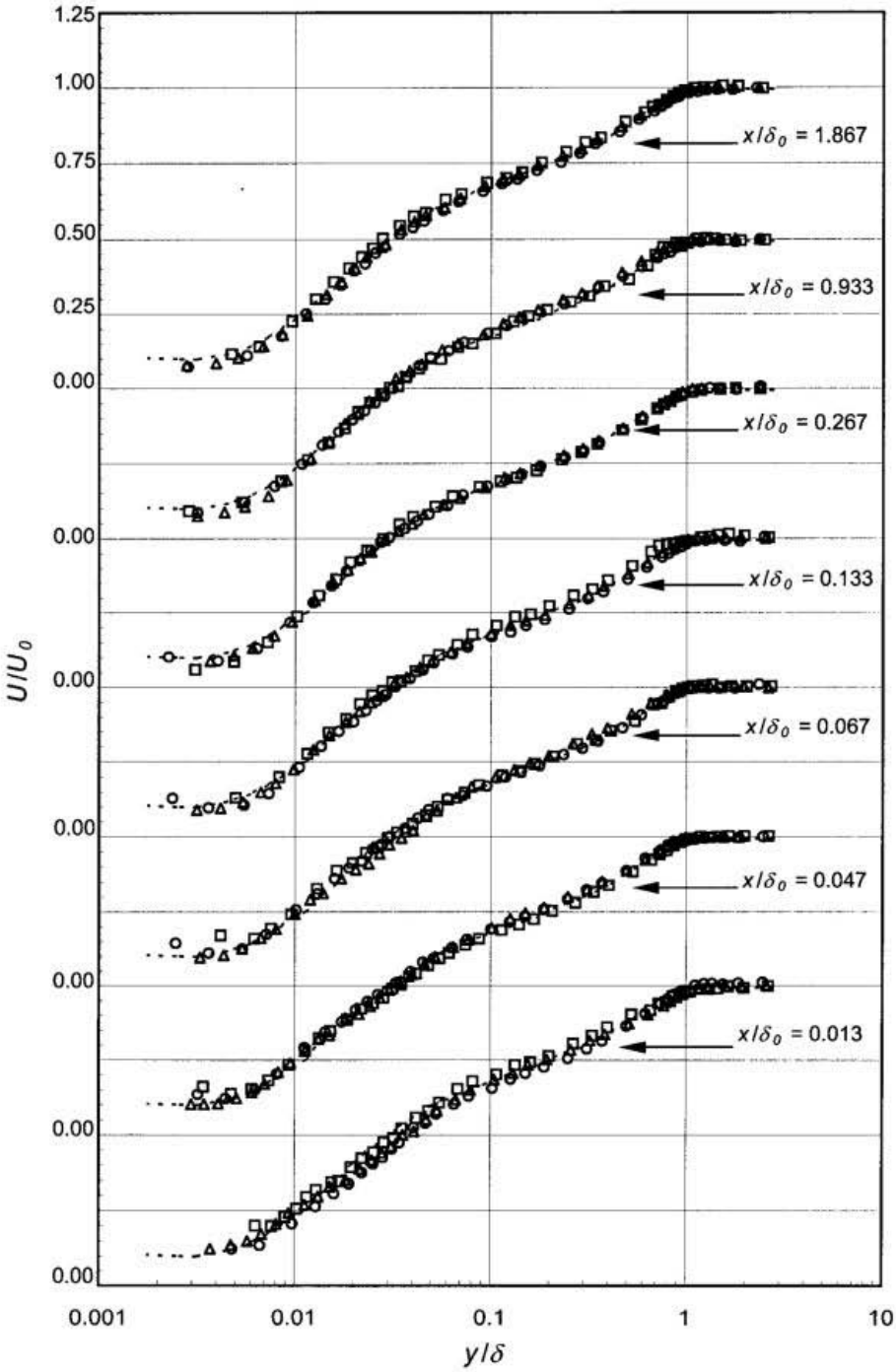

Fig. 6.1.2a Streamwise mean velocity profiles downstream of three different shaped transverse grooves for d = 20mm at R_θ = 1000. △, TR-groove; ○, SC-groove; □, SQ-groove; ------, smooth-wall.

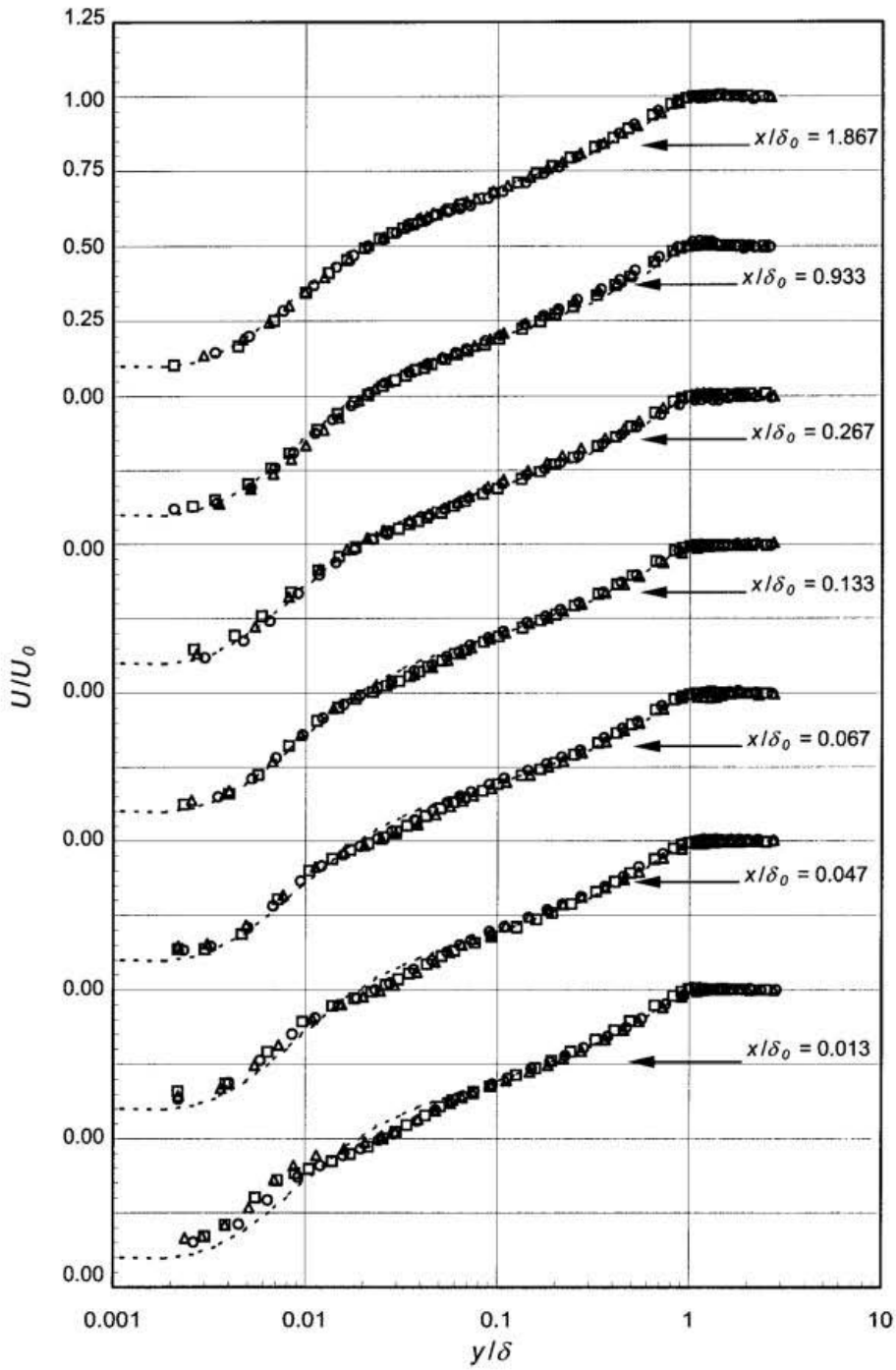

Fig. 6.1.2b Streamwise mean velocity profiles downstream of three different shaped transverse grooves for $d = 20$mm at $R_\theta = 3000$. △, TR-groove; ○, SC-groove; □, SQ-groove; ------, smooth-wall.

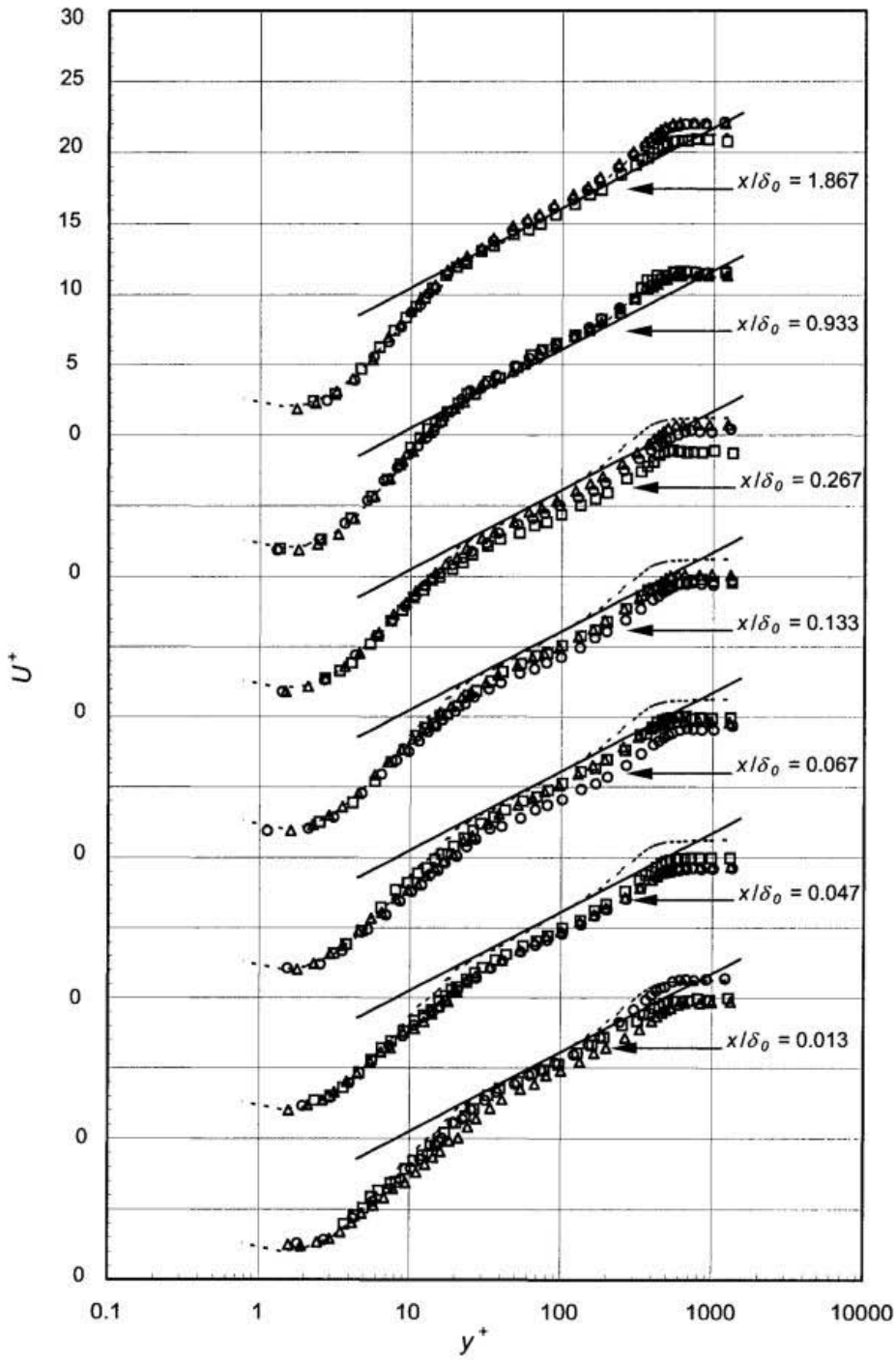

Fig. 6.1.3a Streamwise mean velocity profiles downstream of three different shaped transverse grooves at $R_\theta = 1000$. △, TR-groove; ○, SC-groove; □, SQ-groove; -------, smooth-wall. ——, Log-line: $U^+ = (1/0.41)\, ln\, y^+ + 4.9$.

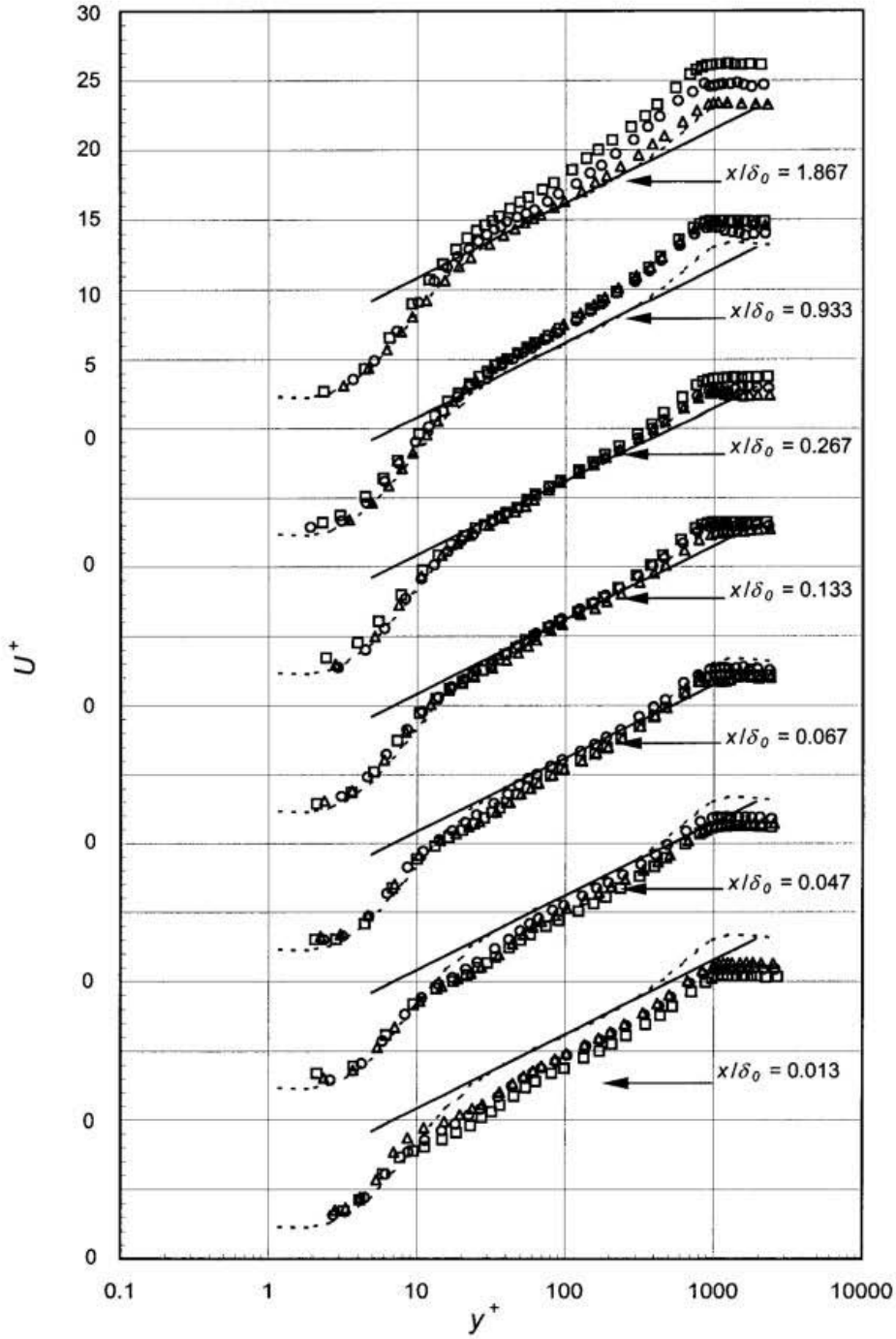

Fig. 6.1.3b Streamwise mean velocity profiles downstream of three different shaped transverse grooves at $R_\theta = 3000$. △, TR-groove; ○, SC-groove; □, SQ-groove; -------, smooth-wall. ———, Log-line: $U^+ = (1/0.43)\ ln\ y^+ + 5.5$.

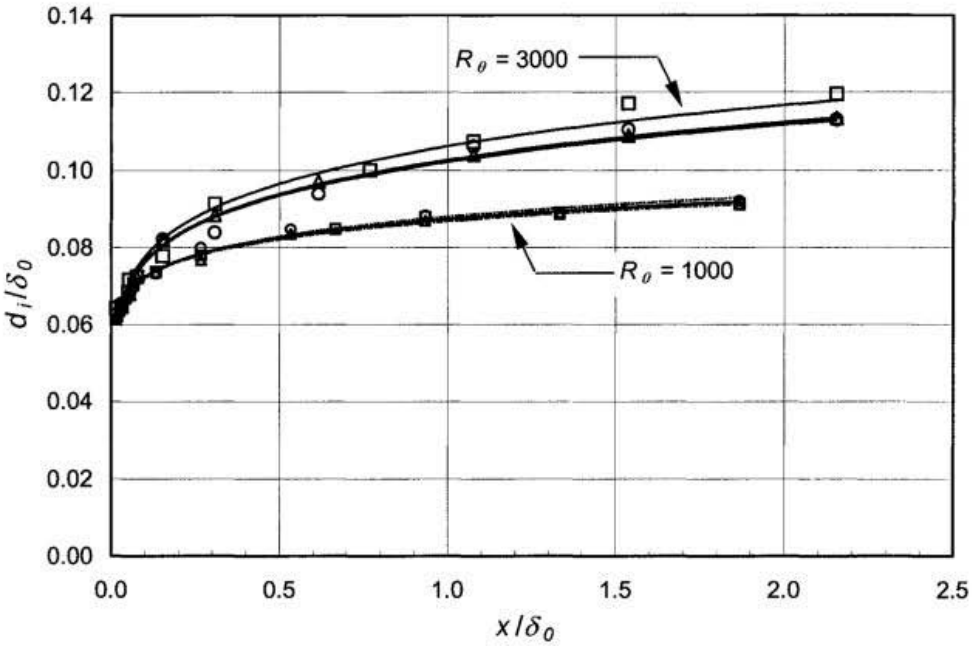

Fig. 6.1.4 Internal layer growth downstream of three different shaped transverse grooves. d = 20mm; R_θ = 1000 and 3000. △, TR-groove; ○, SC-groove; □, SQ-groove.

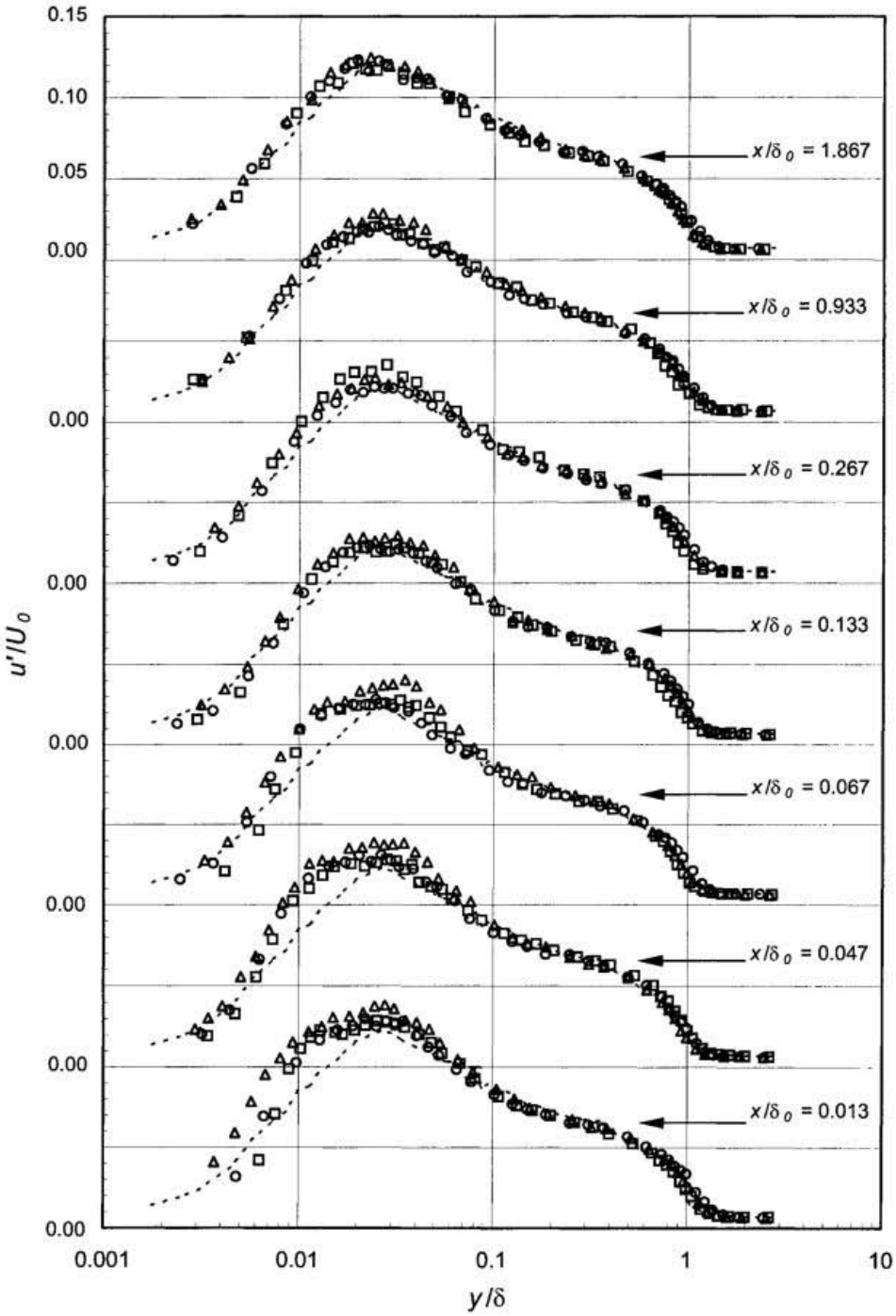

Fig. 6.2.1a Streamwise turbulence intensity profiles downstream of three different shaped grooves, $R_\theta = 1000$. △, TR-groove; ○, SC-groove; □, SQ-groove; ------, smooth-wall.

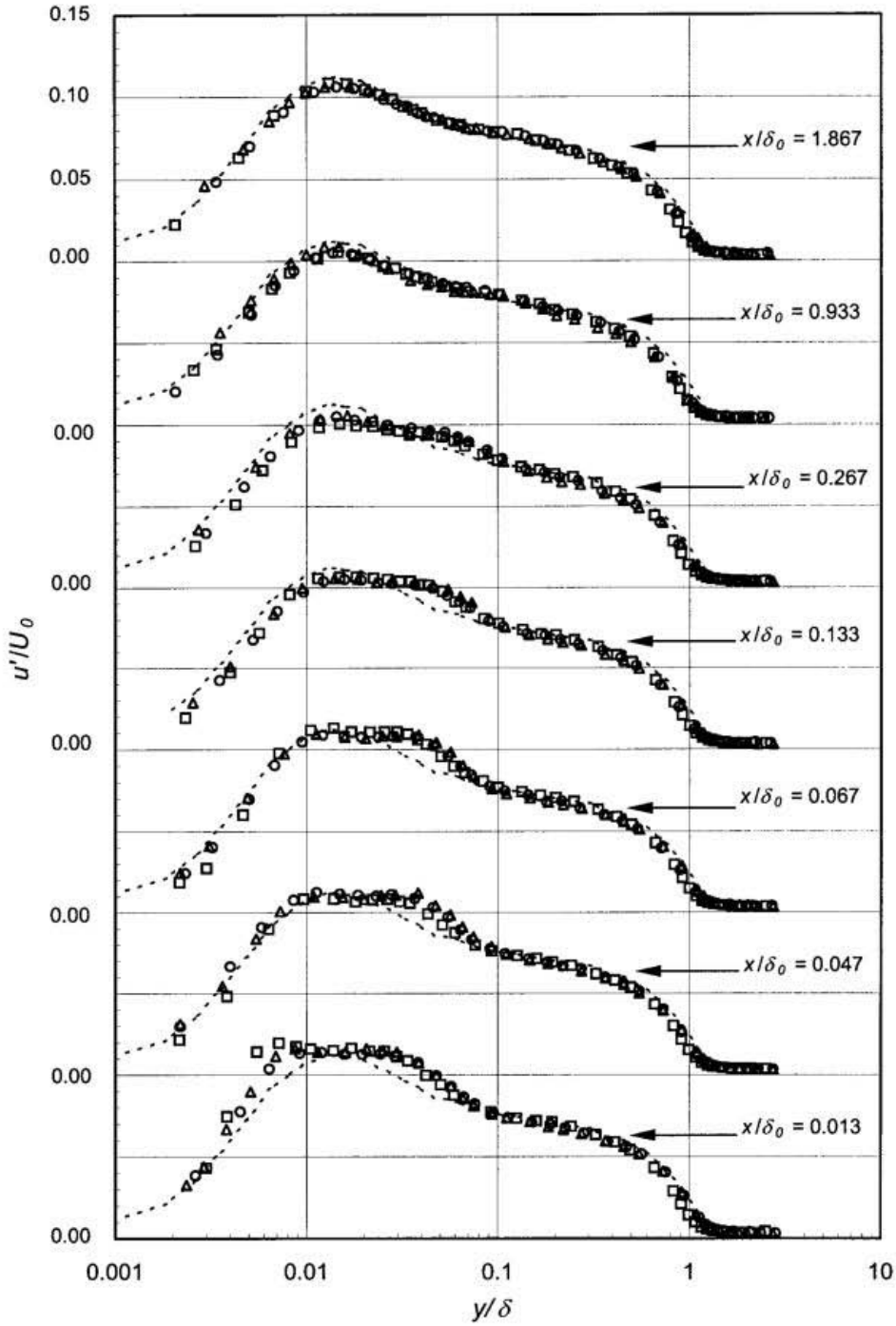

Fig. 6.2.1b Streamwise turbulence intensity profiles downstream of three different shaped grooves, $R_\theta = 3000$. △, TR-groove; ○, SC- groove; □, SQ-groove; ------, smooth-wall.

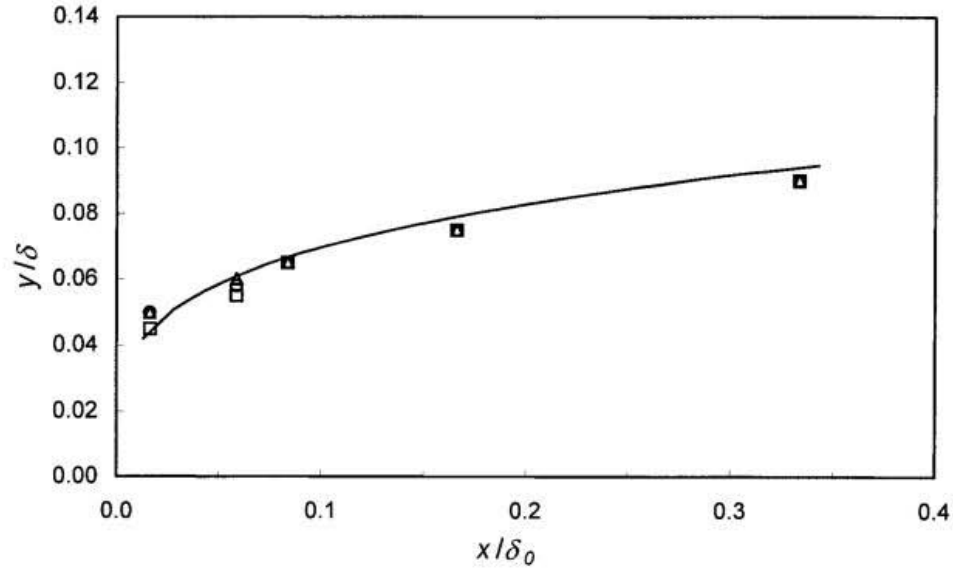

Fig. 6.2.2 Outer boundary where u'/U_0 is affected by the 20mm groove for three different shapes. $R_\theta = 3000$. □, SQ-groove; ○, SC-groove; Δ, TR-groove.

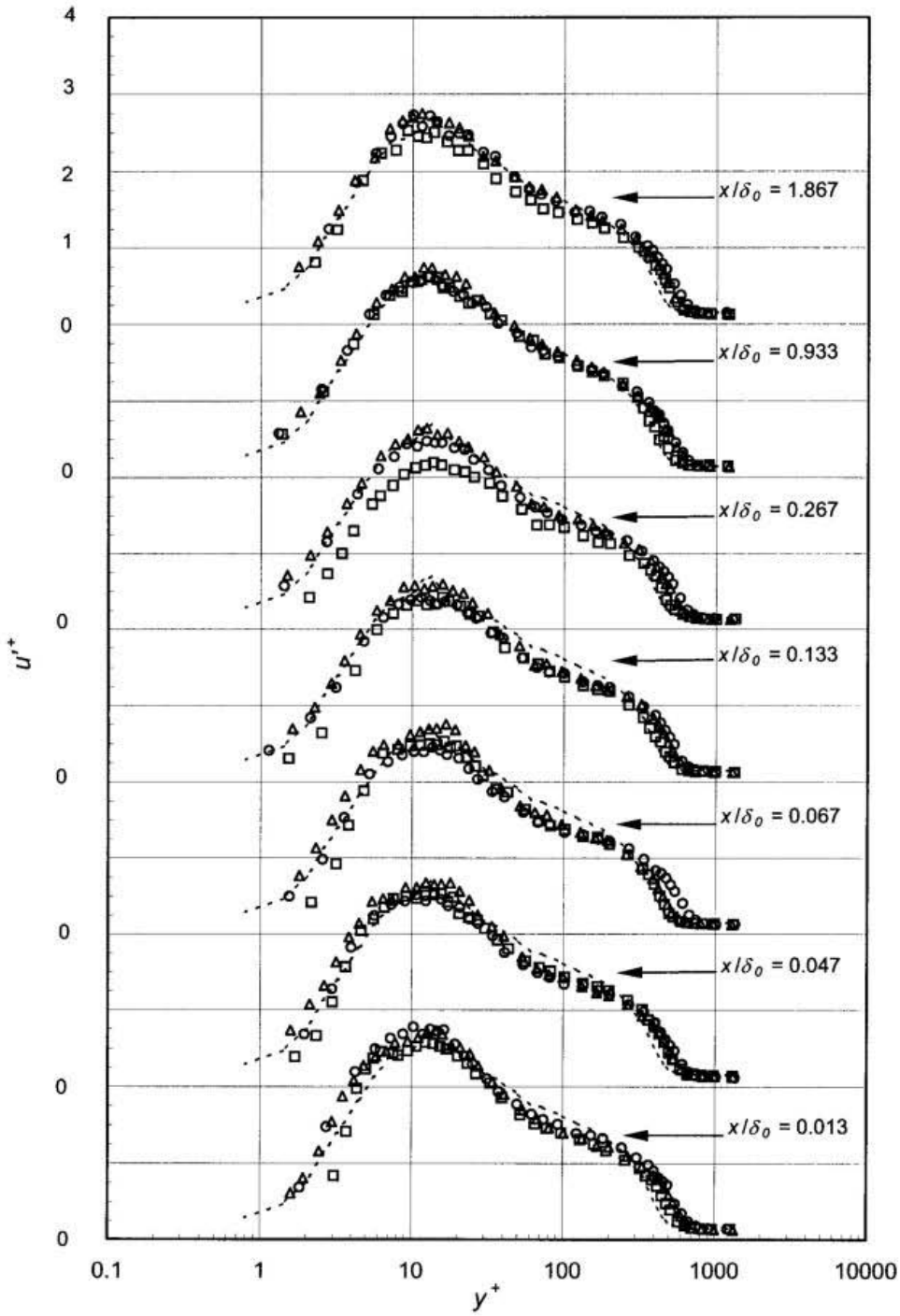

Fig. 6.2.3a Streamwise turbulence intensity profiles downstream of three different shaped grooves, R_θ = 1000. △, TR-groove; ○, SC-groove; □, SQ-groove; -------, smooth-wall.

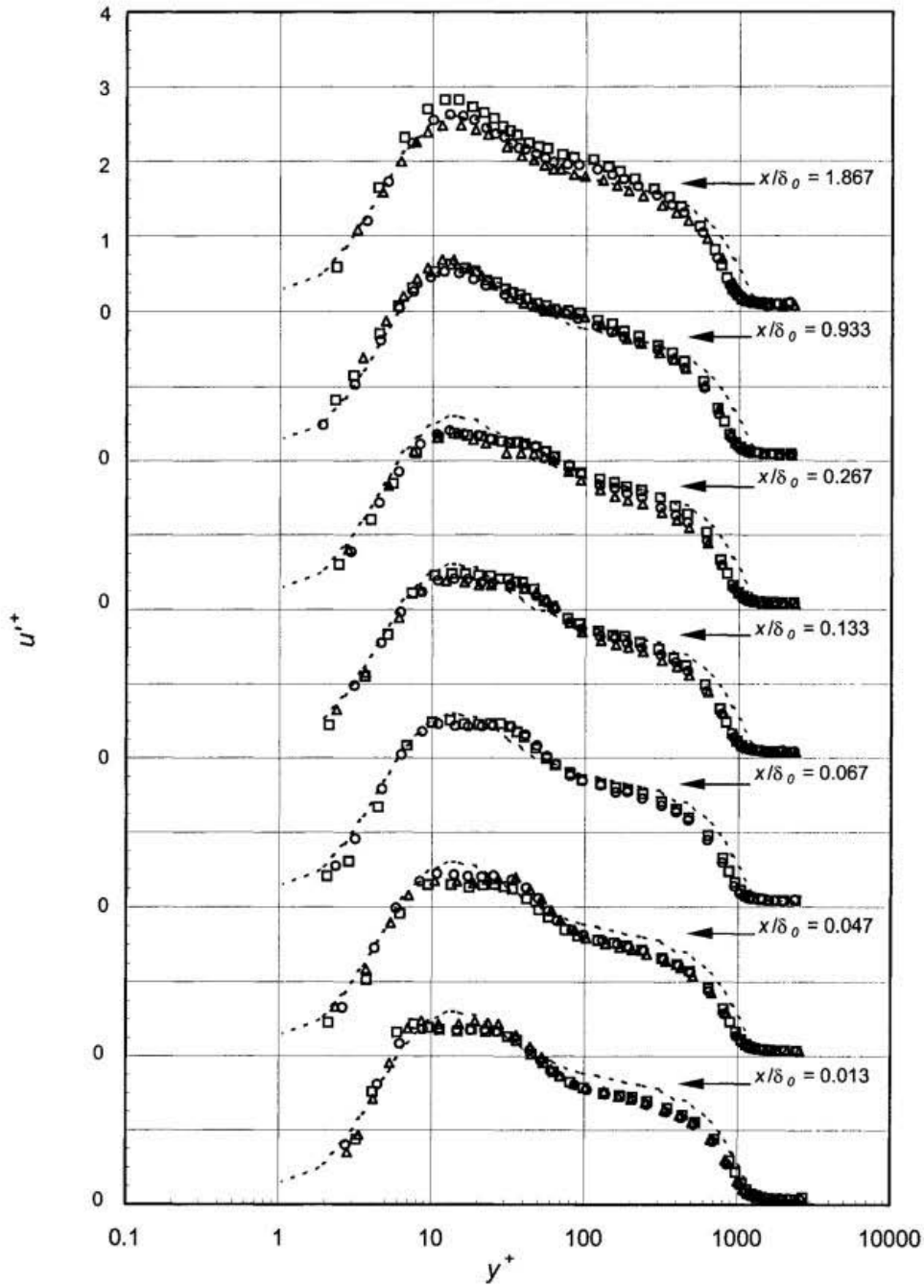

Fig. 6.2.3b Streamwise turbulence intensity profiles downstream of three different shaped grooves, R_θ = 3000. △, TR-groove; ○, SC-groove; □, SQ-groove; -------, smooth-wall.

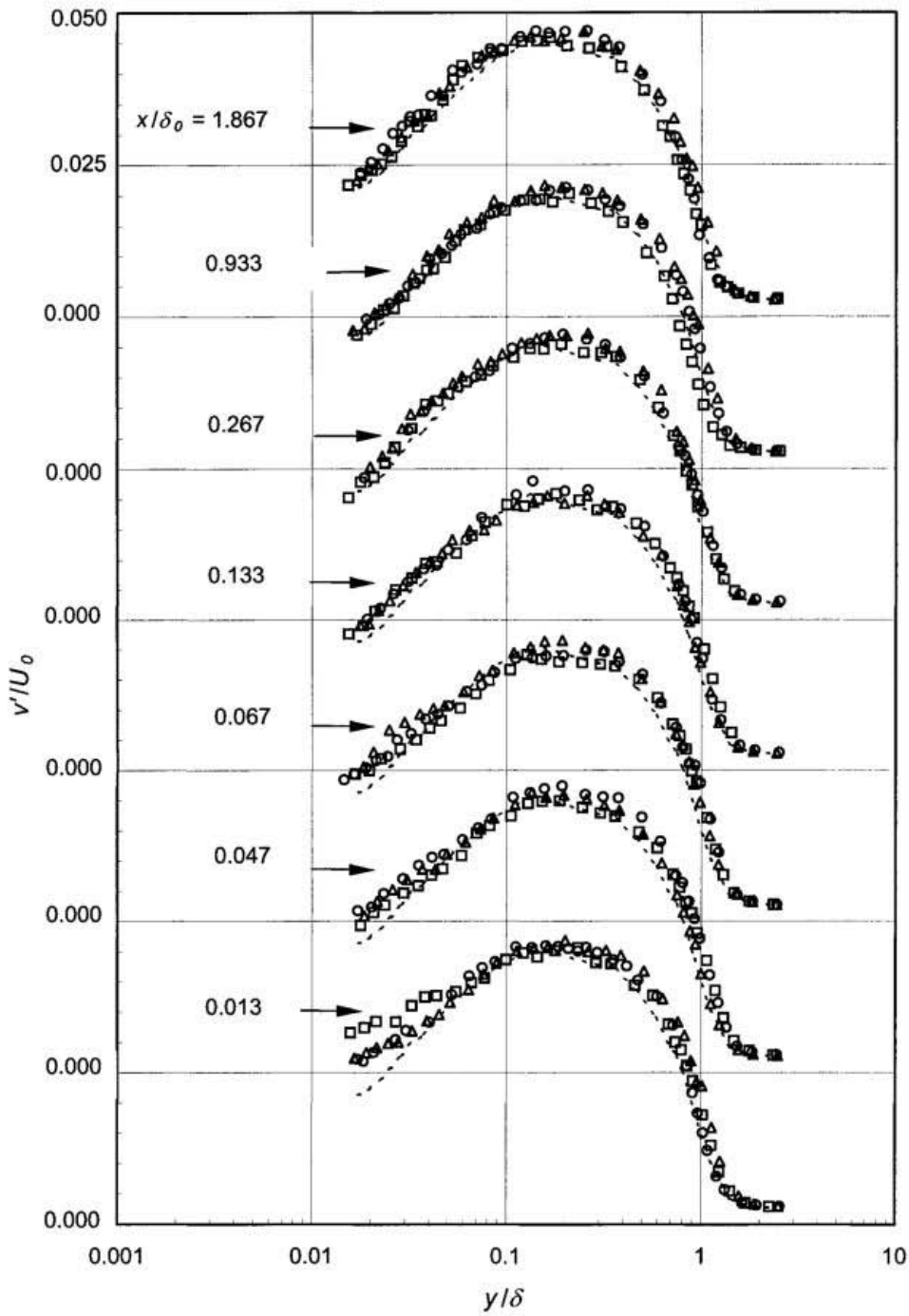

Fig. 6.2.4 Wall-normal turbulence intensity profiles downstream of different shaped transverse grooves, R_θ = 1000. △, TR-groove; ○, SC-groove; □, SQ-groove; ------, smooth-wall.

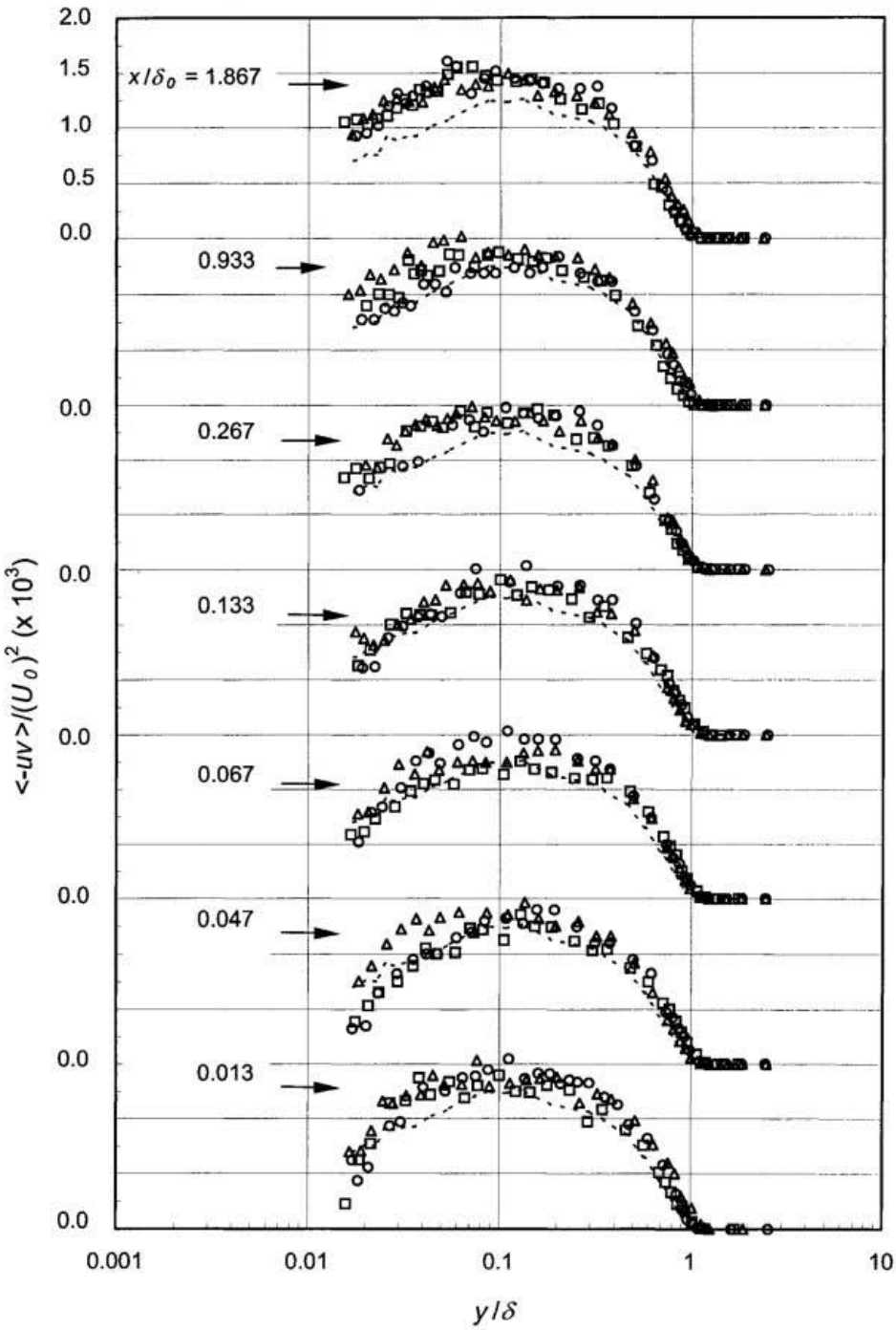

Fig. 6.2.5 Reynolds stress profiles downstream of three different shaped transverse grooves. R_θ = 1000. △, TR-groove; ○, SC-groove; □, SQ-groove; -------, smooth-wall.

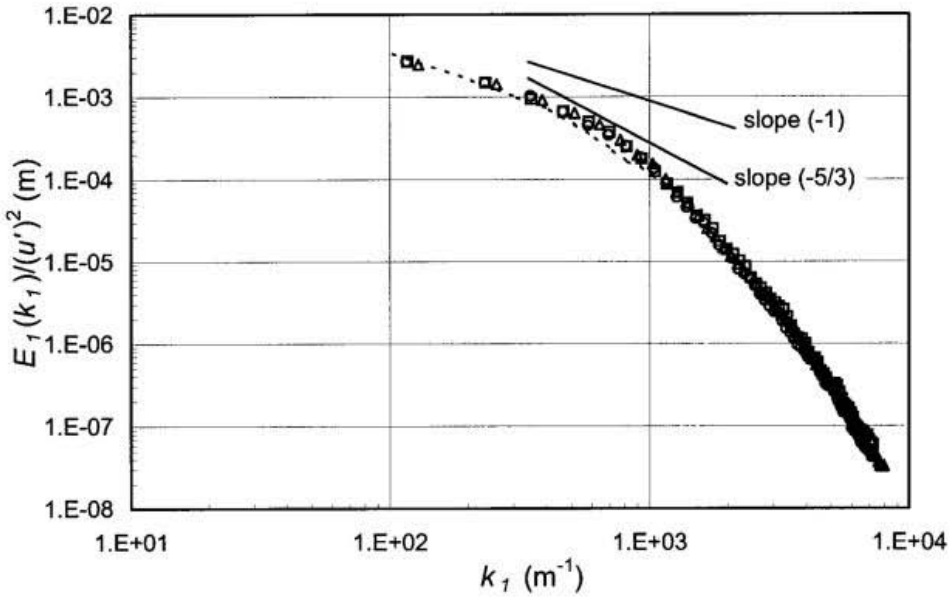

Fig. 6.2.6a Spectra of u' at a location where u'/U_0 is maximum ($y/\delta \approx 0.03$) and $x/\delta_0 =$ 0.013 for three different shaped grooves: Δ, TR-groove; ○, SC-groove; □, SQ-groove; ....., smooth-wall. $R_\theta = 1000$.

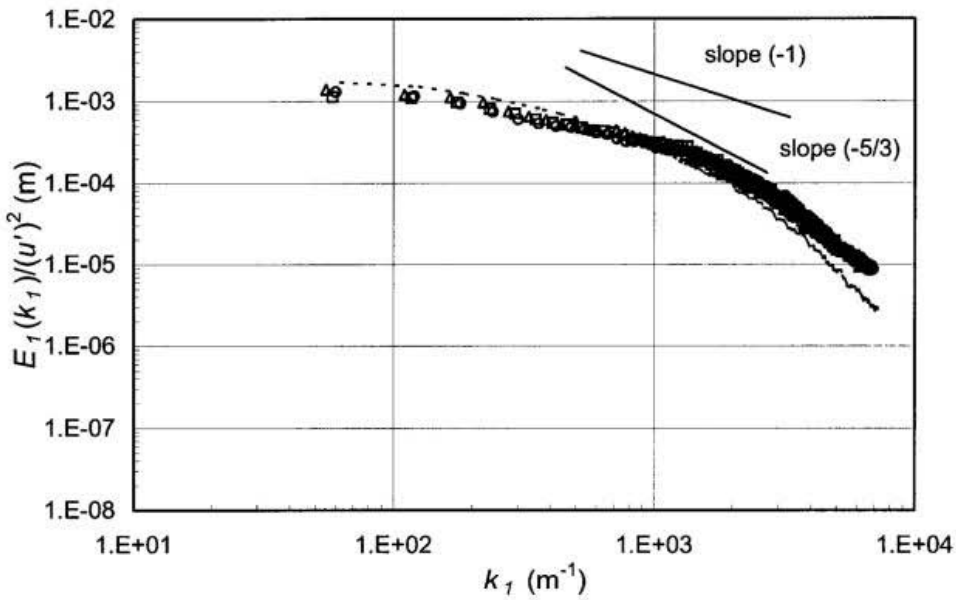

Fig. 6.2.6b Spectra of u' at a location where u'/U_0 is maximum ($y/\delta \approx 0.03$) and $x/\delta_0 =$ 0.013 for three different shaped grooves: Δ, TR-groove; ○, SC-groove; □, SQ-groove; ....., smooth-wall. $R_\theta = 3000$.

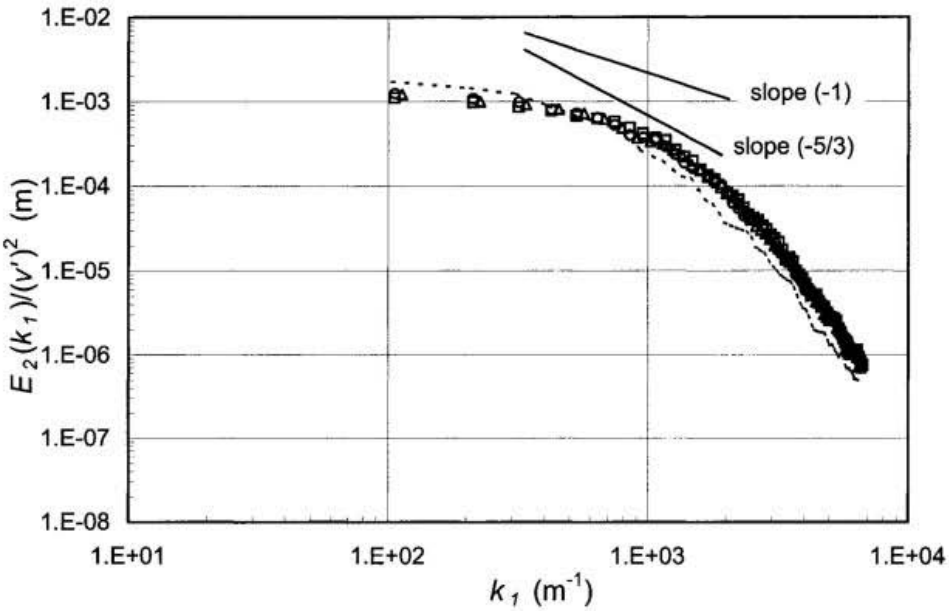

Fig. 6.2.6c Spectra of v' at a location where u'/U_0 is maximum ($y/\delta \approx 0.03$) and $x/\delta_0 =$ 0.013 for three different shaped grooves at $R_\theta = 1000$: △, TR-groove; ○, SC-groove; □, SQ-groove; ....., smooth-wall.

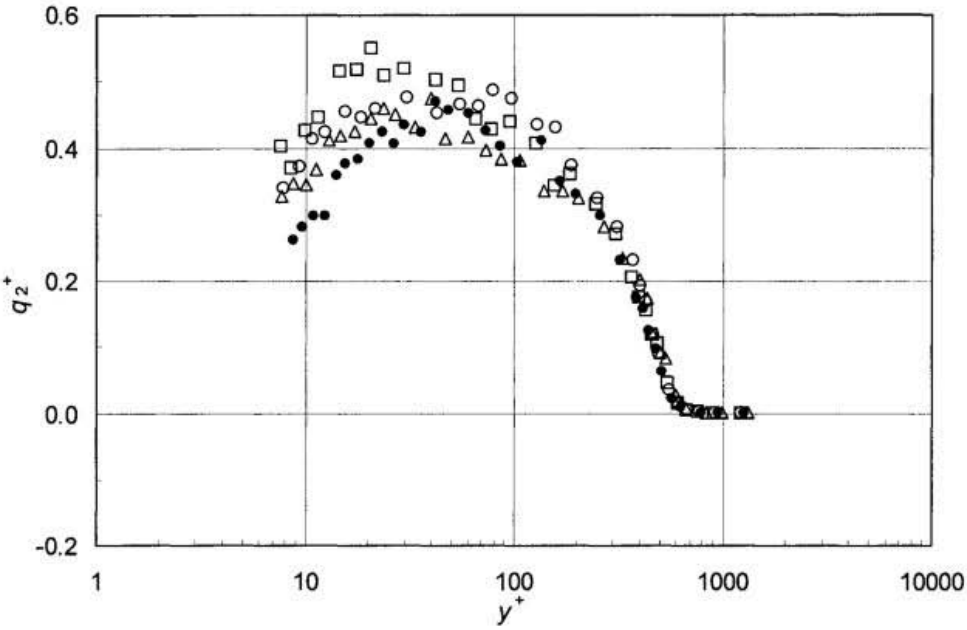

Fig. 6.2.7a Contribution of the second quadrant (q_2^+) to the Reynolds stress downstream of the different shaped grooves for d = 20mm at R_θ = 1000. △, TR-groove; ○, SC-groove; □, SQ-groove; •, smooth-wall. x/δ_0 = 0.013.

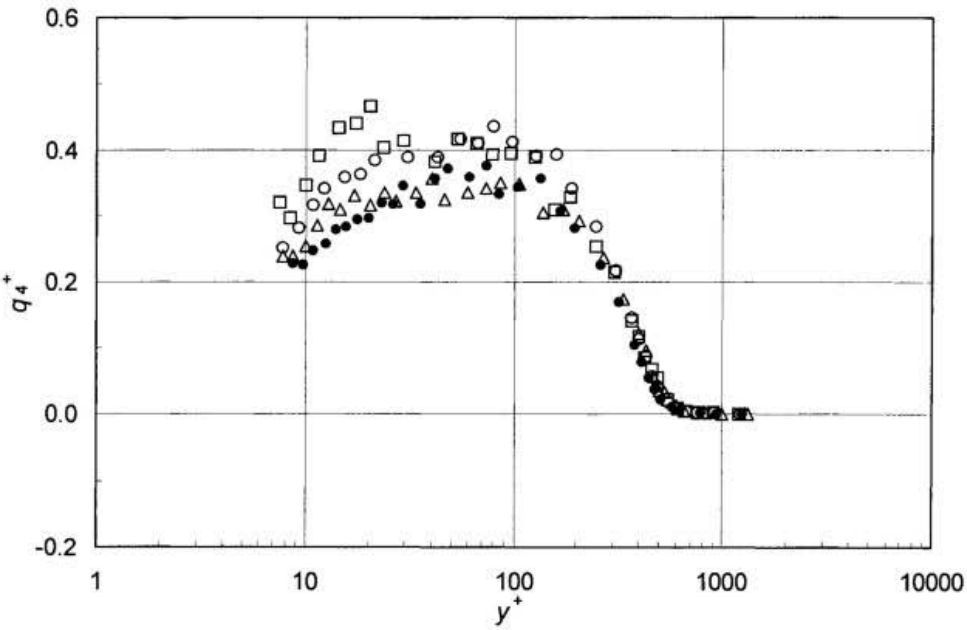

Fig. 6.2.7b Contribution of the fourth quadrant (q_4^+) to the Reynolds stress downstream of the different shaped grooves for d = 20mm at R_θ = 1000. △, TR-groove; ○, SC-groove; □, SQ-groove; •, smooth-wall. x/δ_0 = 0.013.

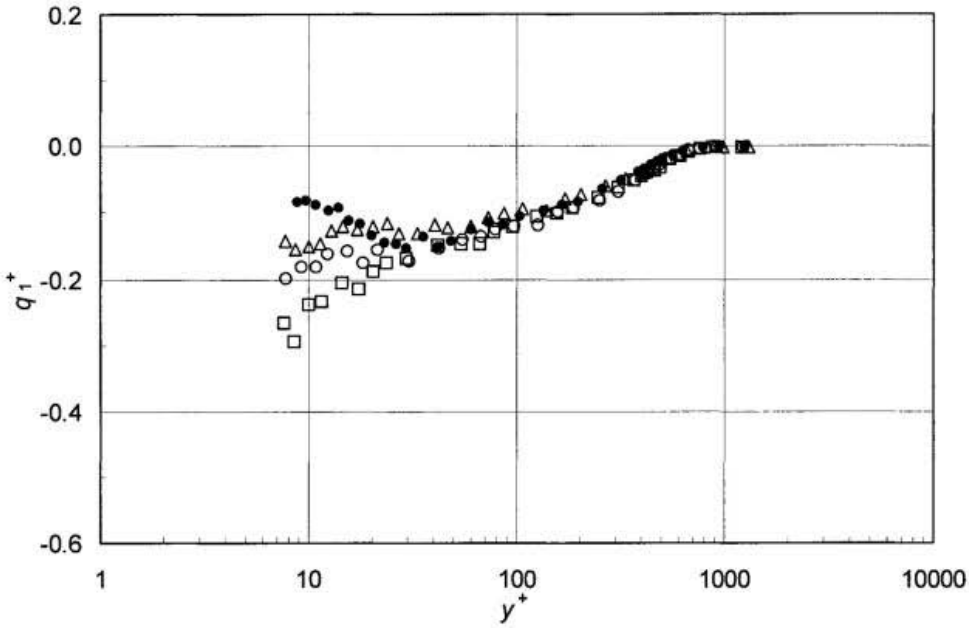

Fig. 6.2.7c Contribution of the first quadrant (q_1^+) to the Reynolds stress downstream of the different shaped grooves for d = 20mm at R_θ = 1000. △, TR-groove; ○, SC-groove; □, SQ-groove; •, smooth-wall. x/δ_0 = 0.013.

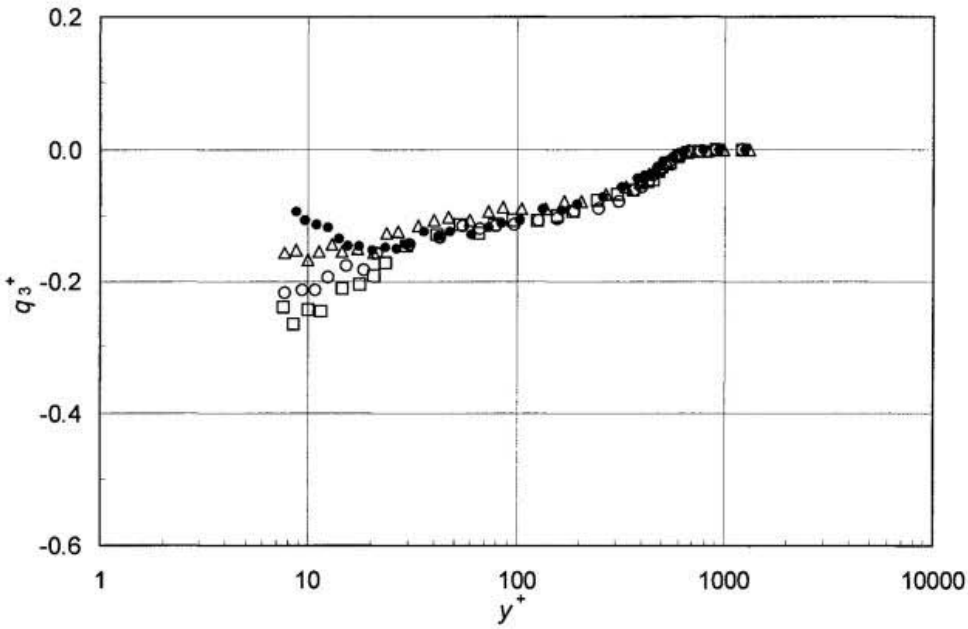

Fig. 6.2.7d Contribution of the third quadrant (q_3^+) to the Reynolds stress downstream of the different shaped grooves for d = 20mm at R_θ = 1000. △, TR-groove; ○, SC-groove; □, SQ-groove; •, smooth-wall. x/δ_0 = 0.013.

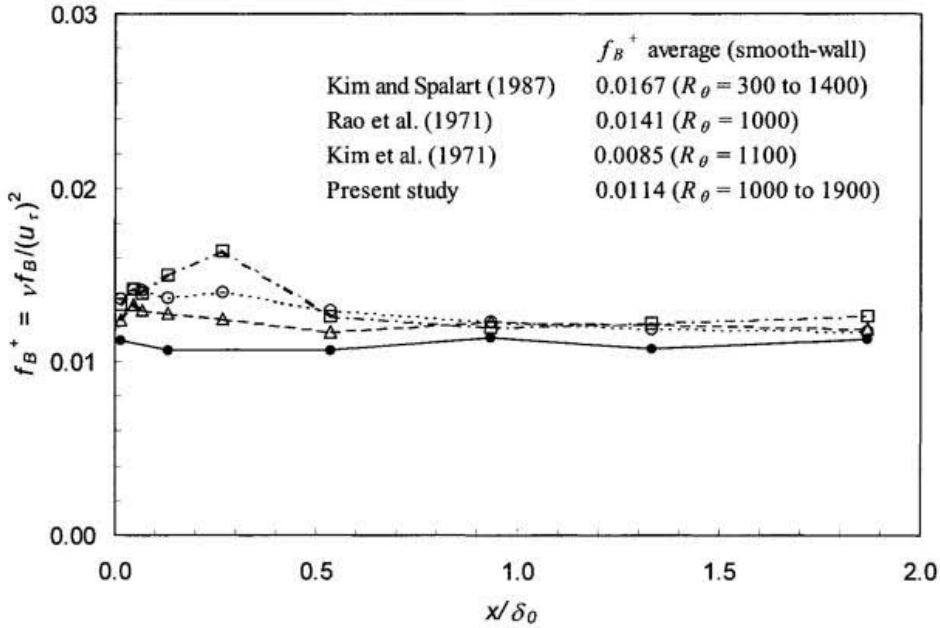

Fig. 6.2.8 Distribution of bursting frequency (f_B^+) downstream of three different shaped grooves at R_θ = 1000, $y/\delta \approx 0.03$, $y^+ \approx 14$. Δ, TR-groove; ○, SC-groove; □, SQ-groove; •, smooth-wall. Comparison of the average value of f_B^+ with the previous studies on the smooth-wall turbulent boundary layer is also shown in the figure.

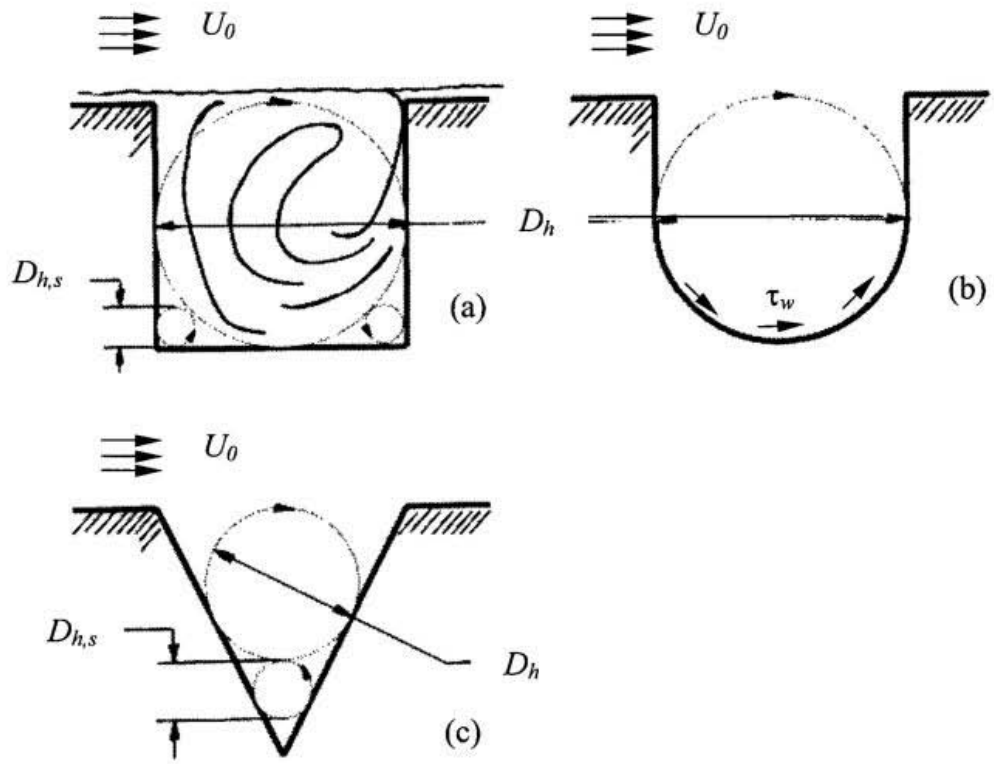

Fig. 6.3.1 Schematic diagram of vortical motions (eddies) inside the grooves showing the idealized primary and secondary eddies (large and small circles, respectively).
(a) SQ-groove, free-line drawing is adopted from Townes and Sabersky (1966);
(b) SC-groove;
(c) TR-groove;

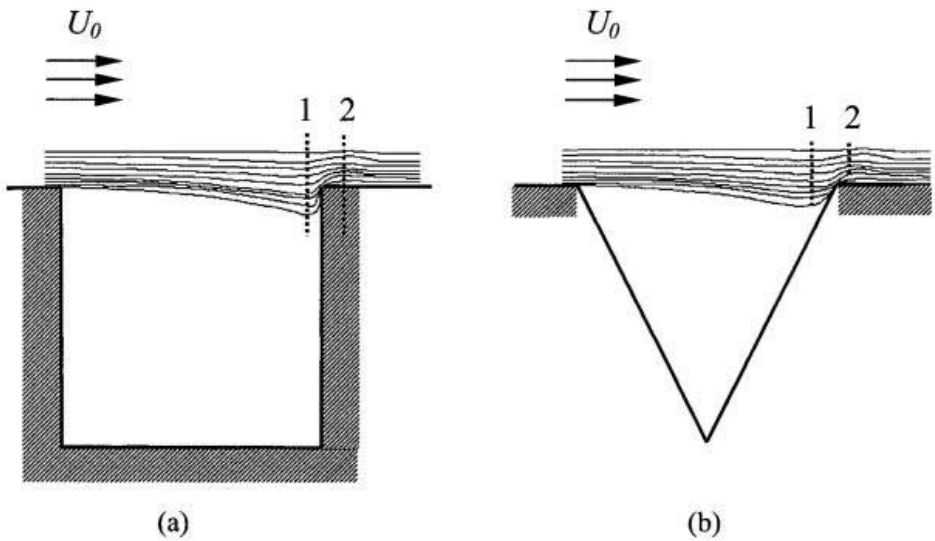

Fig. 6.3.2 Schematic diagram of flow streamlines over a transverse groove.
(a) SQ-groove; (b) TR-groove.

Chapter 7

Concluding Remarks

The response of a turbulent boundary layer under zero pressure gradient to different shaped transverse grooves (square, semicircular base and triangular) has been studied experimentally. Experiments were performed at freestream velocities of 2.0 and 5.5m/s, corresponding to R_θ of 1000 and 3000, based on the momentum thickness just upstream of the groove. Three groove sizes of 5, 10 and 20mm for each shape, with a depth to width (d/w) ratio of unity were used in the study. The groove sizes in terms of the boundary layer thickness just upstream of the grooves (δ_0) are $0.067\delta_0$, $0.133\delta_0$ and $0.267\delta_0$, respectively, for d = 5, 10 and 20mm, at U_0 = 2.0m/s. Corresponding smooth-wall experiments were also performed to obtain a baseline data set for comparison with the turbulent boundary layer over the grooved-walls (the smooth-wall with a single transverse groove). The turbulence characteristics downstream of the groove were measured using hot-wire anemometry. Streamwise mean velocity (U) measurements were

obtained in the laminar sublayer, which allowed an estimate of wall shear stress (τ_w) from the mean velocity gradient at the wall $(dU/dy)_{y=0}$).

7.1 Conclusions

The smooth-wall turbulent boundary layer results compare well with the results from previous studies (Klebanoff, 1955; Purtell et al., 1981; Spalart, 1988; DeGraff and Eaton, 2000). Four different wall shear stress (τ_w) measurement techniques were evaluated. The τ_w was estimated from the power-law, the log-law, $(dU/dy)_{y=0}$ and Preston tube measurements. While the Preston tube, the power-law and the log-law techniques can be used to estimate τ_w on the smooth-wall accurately, these techniques are not appropriate just downstream of the groove, since the boundary layer is not in equilibrium. The τ_w estimated from $(dU/dy)_{y=0}$ is considered more appropriate in this instance.

In general, the mean and turbulence quantities are most affected by the 20mm groove at either R_θ. For example, the maximum increase in C_f for the SQ-groove is approximately 46 percent with d = 20mm, while it is only 26 and 10 percent with d = 10 and 5mm, respectively, at R_θ = 3000. The SQ-groove has the most pronounced effect on the turbulent boundary layer compared to the effects of the SC- and TR-grooves. For instance, the maximum increase in C_f for the SQ-groove is about 46 percent for d = 20mm at the higher R_θ, compared to 32 and 27 percent for the SC- and TR-grooves. Also, the maximum increase in v'/U_0 for the SQ-groove over the corresponding smooth wall value is approximately 50 percent compared to only 25 percent for the SC- and TR-groove cases. The distribution of the bursting frequency (f_B) downstream of the groove is similar to the distribution of C_f.

The relaxation distances of u'/U_0 and v'/U_0 downstream of the groove take longer than that of U/U_0. In general, U/U_0 has relaxed back to the smooth-wall profiles within one δ_0 at either R_θ. At $R_\theta = 1000$, u'/U_0 and v'/U_0 have not relaxed by $x/\delta_0 = 2.0$, while at the higher R_θ, u'/U_0 profiles have relaxed back to the smooth-wall profile by $x/\delta_0 \approx 2.0$. The relaxation of $\langle -uv \rangle/(U_0)^2$ takes much longer, and has not completely relaxed by $2\delta_0$ for all groove shapes and sizes. These results are consistent with the suggestion that the first order moments adjust faster than the second order moments in a turbulent boundary layer after a perturbation (Smits and Wood, 1985). Webster et al. (1996) found that U/U_0 relaxed back to the smooth-wall profiles at approximately $17\delta_0$ downstream of the step change, while u'/U_0, v'/U_0 and $\langle -uv \rangle/(U_0)^2$ had not relaxed back at this location.

Overall, the effect of the groove on the turbulent characteristics at $R_\theta = 3000$ is more significant than that at $R_\theta = 1000$. At the two different R_θ, the ratio of groove depth (d) to the boundary layer thickness (δ_0) is not significantly different. For example, for $d =$ 20mm, $d/\delta_0 = 0.27$ and 0.33 at $R_\theta = 1000$ and $= 3000$, respectively. In terms of inner variables (u_τ and ν, $d^+ = u_\tau d/\nu$), however, d^+ differs significantly for the two R_θ, where $d^+ = 128$ and 296 at $R_\theta = 1000$ and $= 3000$, respectively. It is more appropriate to characterize the groove size in terms of the wall units in this instance.

7.2 Contributions

Contributions of this study to the existing literature can be summarized as follows.

1. A direct comparison of the turbulent boundary layer characteristics downstream of three different shaped grooves has been obtained. While there have been several

experimental studies on turbulent boundary layers perturbed by a SQ-groove, there have been limited studies using SC- and TR-grooves. This is the first study where a systematic comparison between different groove shapes and sizes on a turbulent boundary layer have been obtained.

2. A new Preston tube calibration equation, which is less sensitive to the tube diameter, has been obtained empirically. The maximum difference in the wall shear stress measurements from the different tubes is significantly reduced with the new calibration equation. The scatter in the data is reduced by approximately 40 and 70 percent compared to Patel's and Bechert's calibrations, respectively.
3. The Reynolds stress producing events, including the ejection and sweep events, the wall-ward and out-ward interactions and the bursting frequency, are obtained for the turbulent boundary layer perturbed by the different shaped grooves. While these events have been largely available in literature for the smooth-wall case, they have not been studied in the case of grooved-walls.

7.3 Recommendations

Although several aspects of turbulence have been obtained and analyzed in the present experimental study, the following recommendations are made for further studies.

1. Experimental studies using miniature X- or triple-wires are recommended. This would provide more detailed information on v', w', $\langle -uv \rangle$, $\langle -uw \rangle$ and $\langle -vw \rangle$ in the near-wall region and lead to an improved understanding of the turbulent characteristics in the vicinity of the groove.

2. Measurements of the pressure drag on the groove walls should be made to investigate the effect of the groove on the total drag, in addition to the skin friction drag.
3. Flow visualization studies with the different shaped grooves will be especially useful to understand the interaction between the motions inside the groove and the outer layer.

References

Andreopoulus, J. and Bradshaw, P. (1981), Measurements of turbulence structure in the boundary layer on a rough surface, *Boundary Layer Meteorol.*, Vol. 20, pp. 201-213.

Andreopoulus, J. and Wood, D. H. (1982), The response of a turbulent boundary layer to a short length of surface roughness, *J. Fluid Mech.*, Vol. 118, pp. 143-164.

Antonia, R. A. and Luxton, R. E. (1971a), The response of a turbulent boundary layer to an upstanding step change in surface roughness, *J. Basic Engineering*, Vol. 93, pp. 22-34.

Antonia, R. A. and Luxton, R. E. (1971b), The response of a turbulent boundary layer to a step change in surface roughness: Part 1, Smooth to rough, *J. Fluid Mech.*, Vol. 48, part 4, pp. 721-761.

Antonia, R. A. (1994), The effect of different types surfaces conditions on a turbulent boundary layer, *First International Conference on Flow Interaction*, Hong Kong.

Antonia, R. A. and Kim, J. (1994), Low-Reynolds number effects on near-wall turbulence, *J. Fluid Mech.*, Vol. 276, pp. 61-80.

Antonia, R. A., Zhu, Y., and Sokolov, M. (1995), Effect of concentrated wall suction on a turbulent boundary layer, *Phys. Fluids*, Vol. 7(10), pp. 2465-2474.

Antonia, R. A. and Djenidi, L. (1997), Reynolds stress producing motions in smooth and rough wall boundary layers, in *Self-Sustaining Mechanisms of Wall Turbulence* (Ed.: R. L. Panton), Computational Mechanics Publications, Southampton, UK; Boston, USA, pp. 181-199.

Azad, R. S. and Burhanuddin, S. (1983), Measurements of some features of turbulence in wall-proximity, *Experiments in Fluids*, Vol. 1, pp. 149-160.

Bacher, E. V. and Smith, C. R. (1986), Turbulent boundary layer modification by surface riblets, *AIAA Journal*, Vol. 24, no. 8, pp.1382-1385.

Bandyopadhyay, P. R. (1986), Drag reducing outer-layer devices in rough-wall turbulent boundary layers, *Experiments in Fluids*, Vol. 4, pp. 247-256.

Bandyopadhyay, P. R., and Watson, R. D. (1988), Structure of rough-wall turbulent boundary layer, *Phys. Fluids*, Vol. 31(7), pp. 1877-1883.

Barenblatt, G. I. (1993), Scaling laws for fully developed shear flows. Part 1. Basic hypotheses and analysis, *J. Fluid Mech.*, Vol. 248, pp. 521-529.

Bechert, D. W. (1995), Calibration of Preston tube, *AIAA Journal*, Vol. 34(1), pp. 205-206.

Bechert, D. W., Bruse, M., Hage, W., Van Der Hoven, J. G. T., and Hoppe, G. (1997), Experiments on drag-reducing surfaces and their optimization with an adjustable geometry, *J. Fluid Mech.*, Vol. 338, pp. 59 - 87.

Benjamin, A. S. and Denny, V. E. (1979), On the convergence of numerical solutions for 2-D flows in a cavity at large Re, *J. Computational Phys.* Vol. 33, pp. 340-358.

Bhatia, J. C., Durst, F., and Jovanovic, J. (1982), Corrections of hot-wire anemometer measurements near walls, *J. Fluids Mech.*, Vol. 122, pp. 411-431.

Bisset, D. K. and Antonia, R. A. (1991), Technical Note - Mean velociy and Reynolds shear stress in a turbulent boundary layer at low Reynolds numbers, *Aeronautical Journal*, Vol. 95, pp. 244-247.

Blackwelder, R. F. and Kaplan, R. E. (1976), On the wall structure of the turbulent boundary layer, *J. Fluid Mech.*, Vol. 76, part 1, pp. 89-112.

Blackwelder, R. F. and Eckelmann H. (1979), Streamwise vortices associated with the bursting phenomenon, *J. Fluid Mech.*, Vol. 94, part 3, pp. 577 – 594.

Blackwelder, R. F. and Haritonidis, J. H. (1983), Scaling of the bursting frequency in turbulent boundary layers, *J. Fluid Mech.*, Vol. 132, pp. 87-103.

Bogard, D. G. and Tiederman, W. G. (1986), Burst detection with single-point velocity measurements, *J. Fluid Mech.*, Vol. 162, pp. 389-413.

Bradshaw, P. (1971), *An Introduction to Turbulence and Its Measurement*, 1st edition, Pergamon Press, Oxford.

Brodkey, R. S., Wallace, J. M., and Eckelmann, H. (1974), Some properties of truncated turbulence signals in bounded shear flows, *J. Fluid Mech.*, Vol. 63, part 2, pp. 209-224.

Browne, L. W. B, Antonia, R. A., and Chua, L. P. (1989) Calibration of X-probes for turbulent flow measurements, *Experiments in Fluids*, Vol. 7, pp. 201 – 208.

Bruun, H. H., Nabhani, N., Al-Kayiem, H. H., Fardad, A. A., Khan, M. A., and Hogarth, E. (1990a), Calibration and analysis of X hot-wire probe signals, *Meas. Sci. Technol.*, Vol. 1, pp. 782-785.

Bruun, H. H., Nabhani, N., Fardad, A. A., and Al-Kayiem, H. H. (1990b), Velocity components measurements by X hot-wire anemometry, *Meas. Sci. Technol.*, Vol. 1, pp. 1314-1321.

Cantwell, B. J. (1981), Organized motion in turbulent flow, *Ann. Rev. Fluid Mech.*, Vol. 13, pp. 457-515.

Carpenter, P. (1997), The right sort of roughness, *Nature*, Vol. 388, pp. 713-714.

Cary, A. M., Weinstein, L. M. and Bushnell, D. M. (1980), Drag reduction characteristics of small amplitude rigid surface waves, in *Progress in Astronautics and Aeronautics*, (Ed.: G. R. Haugh), Vol. 72, pp. 143-167.

Cebeci, T. and Smith, A. M. O. (1974), *Analysis of Turbulent Boundary Layers*, 1st edition, Academic Press, New York.

Chen, C. -H. P. and Blackwelder R. F. (1978), Large-scale motion in a turbulent boundary layer: a study using temperature contamination, *J. Fluid Mech.*, Vol. **89**, pp. 1-31.

Ching, C. Y., Djenidi, L., and Antonia, R. A. (1995a), Low-Reynolds-number effects in a turbulent boundary layer, *Experiments in Fluids*, Vol. 19, pp. 61-68.

Ching, C. Y., Elavarasan, R., and Antonia, R.A. (1995b), Visualization of near wall region in a turbulent boundary layer over a *d*-type roughness, *Seventh International Symposium on Flow Visualization*, Seattle.

Ching, C. Y. and Parsons, B. L. (1999), Drag characteristics of a turbulent boundary layer over a flat plate with transverse square grooves, *Experiments in Fluids*, Vol. 26, pp. 273-275.

Choi, K. -S. and Clayton, B. R. (1998), The mechanism of turbulent drag reduction with wall oscillation, *Proceedings of the International Symposium on Seawater Drag Reduction*, Newport, Rhode Island, July 22-23, pp. 229-235.

Choi, K. -S. and Fujisawa, N. (1993), Possibility of drag reduction using *d*-type roughness, *Applied Scientific Research*, Vol. 50, pp. 315-324.

Choi, H., Moin, P. and Kim, J. (1993), Direct numerical simulation of turbulent flow over riblets, *J. Fluid Mech.*, Vol. 255, pp. 503-539.

Choi, K. -S. (1996), Turbulent drag reduction strategies, in *Emerging Techniques in Drag Reduction* (Eds.: K. -S. Choi, K. K. Prasad, and T. V. Truong), Mecahnical Engineering Publications Ltd., London, pp. 77-98.

Choi, K. -S. (2002), Near-wall structure of turbulent boundary layer with spanwise-wall oscillation, *Phys. Fluids*, Vol. 14(7), pp. 2530-2542.

Clauser, F. H. (1956), The turbulent boundary layer, *Advances in Applied Mechanics*, Vol. 4, pp. 1-51.

Coleman, H. W. and Steele Jr., G. W. (1989), *Experimentation and Uncertainty Analysis for Engineers*, John Wiley & Sons, New York.

Coles, D. (1956), The law of the wake in the turbulent boundary layer, *J. Fluid Mech.*, Vol. 1, pp.191-226.

Comte-Bellot, G., Sabot, J., and Saleh, I. (1978), Detection of intermittent events maintaining Reynolds stress, *Proc. Dynamic Flow Conference 1978 on Dynamic Measurements in Unsteady Flows*, Sep. 11-14, Marseille, France; Johns Hopkins University, Baltimore, USA, Sep. 18-21, pp. 213-229.

Coustols, E. and Savill, A. M. (1991), Turbulent skin friction drag reduction by active and passive means. Special Course on Skin Friction Drag Reduction, *AGARD Report*, Vol.786, pp. 8.1-8.80.

Cui, J., Patel, V. C., and Lin, C. -L. (2000), Large-eddy simulation of turbulent flow over rough surfaces. IIHR Tech Rep No. 413. The Univ Iowa, Iowa City, Iowa: 1-207.

Dean, R. B. (1976), A single formula for the complete velocity profile in a turbulent boundary layer, *J. Fluids Engineering*, Vol. 98, pp. 723-727.

DeGraaff, D. B. and Eaton, J. K. (2000), Reynolds-number scaling of the flat-plate turbulent boundary layer, *J. Fluid Mech.*, Vol. 422, pp. 113-135.

Djenidi, L. and Antonia, R. A. (1993), LDA measurements in low Reynolds number turbulent boundary layer, *Experiments in Fluids*, Vol. 14, pp. 280-288.

Djenidi, L., Anselmet, F., and Antonia, R. A. (1994), LDA measurements in turbulent boundary layer over a *d*-type rough wall, *Experiments in Fluids*, Vol. 16, pp. 323-329.

Djenidi, L., Dubief, Y., and Antonia, R. A. (1997), Advantages of using a power law in a low R_θ turbulent boundary layer, *Experiments in Fluids*, Vol. 22, pp. 348-350.

Djenidi, L., Elavarasan, R., and Antonia, R. A. (1999), The turbulent boundary layer over transverse square cavities, *J. Fluid Mech.*, Vol. 395, pp. 271-294.

Durst, F., Zanoun, E. S., and Pashtrapanska, M. (2001), In situ calibration of hot wires close to highly heat-conducting walls, *Experiments in Fluids*, Vol. 31, pp. 103-110.

Durst, F., Shi, J. -M., and Breuer, M. (2002), Numerical prediction of hot-wire corrections near walls, *J. Fluids Engineering*, Vol. 124, pp. 241-250.

Elavarasan, R., Ching, C. Y., and Antonia, R. A. (1996), Turbulent boundary layer over a smooth wall with widely separated transverse square cavities, *Applied Scientific Research*, Vol. 55, pp. 227-243.

Elsner, J. W., Domagala, P., and Elsner, W. (1993), Effect of finite spatial resolution of hot-wire anemometry on measurements of turbulence energy dissipation, *Meas. Sci. Technol.*, Vol. 4, pp. 517-523.

Falco, R. E. (1980a), Combined simultaneous flow visualization/hot-wire anemometry for the study of turbulent flows, *J. Fluids Engineering*, Vol. 102, pp. 174-182.

Falco, R. E. (1980b), The production of turbulence near a wall, *AIAA Paper*, 80-1356.

Falco, R. E. (1991), A coherent structure model of the turbulent boundary layer and its ability to predict Reynolds number dependence, *Phil Trans. R. Soc. London, A*, Vol. 336, pp. 103-129.

Fernholz, H. H. and Finley, P. J. (1996), The incompressible zero-pressure gradient turbulent boundary layer: An assessment of the data, *Prog. Aerospace Sci.*, Vol. 32, pp. 245-311.

Fisher, M., Jovanović, J., and Durst, F. (2001), Reynolds number effects in the near-wall region of turbulent channel flows, *Phys. Fluids*, Vol. 13(6), pp. 1755-1767.

Fox, R. W. and McDonald, A. T. (1994), *Introduction to Fluid Mechanics*, 4th edition, SI Version, John Wiley and Sons, Inc., New York.

Gad-el-Hak, M. and Bandyopadhyay, P. R. (1994), Reynolds number effects in wall-bounded turbulent flows, *App. Mech. Rev.*, Vol. 47(8), pp. 307-365.

Gad-el-Hak, M. (1996), Modern development in flow control, *App. Mech. Rev.*, Vol. 49(7), pp. 365-379.

George, W. K. and Castillo, L. (1997), Zero-pressure-gradient turbulent boundary layer, *App. Mech. Rev.*, Vol. 50(11), part 1, pp. 689-729.

Ghia, U., Ghia, K. N., and Shin, C. T. (1982), High-Re solutions for incompressible flow using the Navier-Stokes equations and a multigrid method, *J. Computational Phys.* Vol. 48, pp. 387-411.

Goldstein, D., Handler, R., and Sirovich, L. (1995), Direct numerical simulation of turbulent flow over a modelled riblet covered surface, *J. Fluid Mech.*, Vol. 302, pp. 333 - 376.

Grass, A. J. (1971), Structural features of turbulent flow over smooth and rough boundaries, *J. Fluid Mech.*, Vol. 50, part 2, pp. 233-255.

Grass, A. J., Stuart, R. J., and Mansour, T. M. (1991), Vortical structures and coherent motion in turbulent flow over smooth and rough boundaries, *Phil Trans. R. Soc. London, A*, Vol. 336, pp. 35-65.

Grek, G. R., Kozlov, V. V., Titarenko, S. V., and Klingmann, B. G. B. (1995), The influence of riblets on a boundary layer with embedded streamwise vortices, *Phys. Fluids*, Vol. 7(10), pp. 2504-2506.

Hanratty, T. J. and Campbell, J. A. (1983), Measurement of wall shear stress, in *Fluid Mechanics Measurements* (Ed.: R. J. Goldstein), New York, Hemisphere, pp. 559-615.

Haugen, R. L. and Dhanak, A. M. (1966), Momentum transfer in turbulent separated flow past a rectangular cavity, *J. App. Mech.*, Vol. 33, pp. 641-646.

Head, M. R. and Ram, V. (1971), Simplified presentation of Preston tube calibration, *Aeronautical Quarterly*, Vol. 22, pp. 295-300.

Head, M. R. and Bandyopadhyay, P. (1981), New aspects of turbulent boundary layer structure, *J. Fluid Mech.*, Vol. 107, pp. 297-338.

Hinze, J. O. (1975), *Turbulence*, 2nd edition, McGraw-Hill, New York.

Ho, C. -M. and Tai, Y. -C. (1998), Micro-electro-mechanical-syatems (MEMS) and fluid flows, *Ann. Rev. Fluid Mech.*, Vol. 30, pp. 579-612.

Janke, G. (1987), Hot wire in wall proximity, *Advances in Turbulence*, (Eds. G. Comte-Bellot and J. Mathieu), pp. 488-498, Springer, Berlin.

Jeong, J., Hussain, F., Schoppa, W., and Kim, J. (1997), Coherent structures near the wall in a turbulent channel flow, *J. Fluid Mech.*, Vol. 332, pp. 185-214.

Joslin, R. D. (1997), Discussion of DNS: Past, present, and future, *First International Conference on DNS and LES*, Ruston, Lousiana, August.

Kim, H. T., Kline, S. J., and Reynolds, W. C. (1971), The production of turbulence near a smooth wall in a turbulent boundary layer, *J. Fluid Mech.*, Vol. 50, part 1, pp. 133-160.

Kim, J. and Spalart, P. R. (1987), Scaling of the bursting frequency in turbulent boundary layers at low Reynolds numbers, *Phys. Fluids*, Vol. 30(11), pp. 3326-3328.

Kim, J. (1998), Active control of turbulent boundary layers, *Addendum to the Proceedings of the International Symposium on Seawater Drag Reduction*, Newport, Rhode Island, July 22-23, pp. 16.

Klebanoff, P. S. and Diehl, Z. W. (1952), Some features of artificially thickened fully developed turbulent boundary layers with zero pressure gradient, *NACA Report*, no. 1110.

Klebanoff, P. S. (1955), Characteristics of turbulence in a boundary layer with zero pressure gradient, *NACA Report*, no. 1247.

Kline, S. J., Reynolds, W. C., Schraub, F. A., and Rustandler, P. W. (1967), The structure of turbulent boundary layers, *J. Fluid Mech.*, Vol. 30, pp. 741-773.

Kodama, Y., Kakugawa, A., Takahashi, T., and Kawashima, H. (2000), Experimental study on microbubbles and their applicability to ships for skin friction reduction, *Int. J. Heat and Fluid Flow*, Vol. 21, pp. 582-588.

Krishnamoorthy, L. V., Wood, D. H., Antonia, R. A., and Chambers, A. J. (1985), Effect of wire diameter and overheat ratio near a conducting wall, *Experiments in Fluids*, Vol. 3, pp. 121-127.

Lange, C. F., Durst, F., and Breuer, M. (1999), Wall effects of heat losses from hot-wires, *Int. J. Heat and Fluid Flow*, Vol. 20, pp. 34-47.

Lattore, R. and Babenko, V. V. (1998), Role of bubble injection technique drag reduction, *Proceedings of the International Symposium on Seawater Drag Reduction*, Newport, Rhode Island, July 22-23, pp. 319 – 325.

Lee, C. and Kim, J. (2002), Control of viscous sublayer for drag reduction, *Phys. Fluids*, Vol. 14(7), pp. 2523-2529.

Lee, S. -J. and Lee, S. -H. (2001), Flow field analysis of a turbulent boundary layer over a riblet surface, *Experiments in Fluids*, Vol. 30, pp. 153-166.

Liakopoulos, A. (1983), Explicit representations of the complete velocity profile in a turbulent boundary layer, *AIAA Journal*, Vol. 22(6), pp. 844-846.

Lu, S. S. and Willmarth, W. W. (1973), Measurements of the structure of the Reynolds stress in a turbulent boundary layer, *J. Fluid Mech.*, Vol. 60, part 3, pp. 481-511.

Ligrani, P. M. and Bradshaw, P. (1987), Subminiature hot-wire sensors: development and use, *J. Phys. E: Sci. Instrum.*, Vol. 20, pp. 323-332.

Luchik, T. S. and Tiederman, W. G. (1987), Timescale and structure of ejections and bursts in turbulent channel flows, *J. Fluid Mech.*, Vol. 174, pp. 529-552.

Marec, J. P. (2000), Drag reduction: A major task for research, *CEAS/DragNet European Drag Reduction Conference 2000*, Postdam, Germany, June 19-21, pp. 17-27.

Matsumoto, A. (1994), Some features of turbulent boundary layers over grooved rough walls, *Transc. of The Japan Soc. for Aeronautical and Space Sci.*, Vol. 37(115), pp. 27-41.

McAllister, J. E., Pierce, F. J., and Tennant, M. H. (1982), Preston tube calibrations and direct force floating element measurements in two-dimensional turbulent boundary layer, *J. Fluids Engineering*, Vol. 104, pp. 156-161

Metzger, M. M. and Klewicki, J. C. (2001), A comparative study of near-wall turbulence in high and low Reynolds number boundary layers, *Phys. Fluids*, Vol. 13(3), pp. 692-701.

Mochizuki, S. and Nieuwstadt, F. T. M. (1996), Reynolds-number dependence of the maximum in the streamwise velocity fluctuations in wall turbulence, *Experiments in Fluids*, Vol. 21, pp. 218-226

Mochizuki, S. and Osaka, H. (1998), Drag reduction with submerged ribs and its mechanism in a turbulent boundary layer over *d*-type roughness, *Proc. of the Int. Symp. On Seawater Drag Reduction*, Newport, Rhode Island, July 22-23, pp. 121-126.

Modi, V. J. (1997), Moving surface boundary-layer control: A review, *J. Fluids and Structures*, Vol. 11, pp. 627 – 663.

Moffat, H. K. (1964), Viscous and resistive eddies near a sharp corner, *J. Fluid Mech.*, Vol. 18, part 1, pp. 1 - 18.

Moffat, R. J. (1982), Contributions to the theory of single-sample uncertainty analysis, *J. Fluids Engineering*, Vol. 104, pp. 250-260.

Moin, P. and Bewley, T. (1994), Feedback control of turbulence, *App. Mech. Rev.*, Vol. 47, pp. S3-S13.

Moin, P. and Mahesh, K. (1998), Direct numerical simulation: A tool in turbulence research, *Ann. Rev. Fluid Mech.*, Vol. 30, pp. 539 - 578.

Monin, A. S. and Yaglom, A. M. (1971), *Statistical Fluid Mechanics: Mechanics of Turbulence*, Vol. 1, The MIT Press, Cambridge, Massachusetts.

Munson, B. R., Young, D. F., and Okiishi, T. H. (1990), *Fundamentals of Fluid Mechanics*, 1st edition, John Wiley & Sons, New York.

Na, Y., Hanratty, T. J., and Liu, Z. C. (2001), The use of DNS to define stress producing events for turbulent flow over a smooth wall, *Applied Scientific Research*, Vol. 66, pp. 495-512.

Nikuradse, J. (1933), Laws of flows in rough pipes, *NACA TM*, no. 1292.

Osaka, H. and Mochizuki, S. (1988), Coherent structure of a *d*-type rough wall boundary layer, in *Transport Phenomena, Turbulent Flows: Theory, Experiments and Numerical Simulations* (Eds.: H. Hirata and N. Kasagi), Hemisphere, New York, pp. 199-211.

Österlund, J. M., Johansson, A. V., and Nagib, H. M. (2000), Comment on "A note on the intermediate region in turbulent boundary layers", *Phys. Fluids*, Vol. 12(9), pp. 2360-2363.

Park, J. and Choi, H. (1999), Effects of uniform blowing or suction from a spanwise slot on a turbulent boundary layer flow, *Phys. Fluids*, Vol. 11(10), pp. 3095-3105.

Patel, V. C. (1965), Calibration of the Preston tube and limitations on its use in pressure gradients, *J. Fluid Mech.*, Vol. 23, part 1, pp. 185-208.

Pearson, B. R., Elavarasan, R., and Antonia, R. A. (1997), The response of a turbulent boundary layer to a square groove, *J. Fluids Engineering*, Vol. 119, pp. 466-469.

Pearson, B. R., Elavarasan, R., and Antonia, R. A. (1998), Effect of a short roughness strip on a turbulent boundary layer, *Applied Scientific Research*, Vol. 59, pp. 61-75.

Perry, A. E., Schofield, W. H., and Joubert, P. N. (1969), Rough wall turbulent boundary layers, *J. Fluid Mech.*, Vol. 37, part 2, pp. 383-413.

Perry, A. E. and Abbel, C. J. (1975), Scaling laws for pipe-flow turbulence, *J. Fluid Mech.*, Vol. 67, part 2, pp. 257 – 271.

Piomelli, U. and Belaras, E. (2002), Wall-layer models for large-eddy simulations, *Ann. Rev. Fluid Mech.*, Vol. 34, pp. 349-374.

Pollard, A. (1996), Riblets and other methods of controlling near-wall turbulence, in *Emerging Techniques in Drag Reduction* (Eds.: K. -S. Choi, K. K. Prasad, and T. V. Truong), Mechanical Engineering Publication Ltd., London, pp. 45-76.

Potter, M. C. and Wiggert, D. C. (1997), *Mechanics of Fluids*, 2nd edition, Prentice-Hall, Upper Saddle River, NJ.

Preston, J. H. (1954), The determination of turbulent skin friction by means of Pitot tubes, *J. of the Royal Aeronautical Society*, Vol. 14, pp. 109-121.

Purtell, L. P., Klebanoff, P. S., and Buckley, F. T. (1981), Turbulent boundary layer at low Reynolds number, *Phys. Fluids*, Vol. 24(5), pp. 802-811.

Rao, K. N., Narasimha, R., and Narayanan, M. A. B. (1971), The 'bursting' phenomenon in a turbulent boundary layer, *J. Fluid Mech.*, Vol. 48, part 2, pp. 339-352.

Reynolds, A. J. (1974), *Turbulent Flows in Engineering*, 1st edition, John Wiley & Sons, London.

Roach, P. E. and Brierley, D. H. (1990), The influence of a turbulent free-stream on zero pressure gradient transitional boundary layer development. Part 1: Test cases T3A and T3B, in *Numerical Simulation of Unsteady Flows and Transition to Turbulence* (Eds.: O. Pironneau, W. Rodi, I. L. Ryhming, A. M. Savill, and T. V. Truong), Cambridge Univ. Press, pp. 318-347.

Robinson, S. K. (1991), Coherent motions in the turbulent boundary layer, *Ann. Rev. Fluid Mech.*, Vol. 23, pp. 601-639.

Rogallo, R. S. and Moin, P. (1984), Numerical simulation of turbulent flows, *Ann. Rev. Fluid Mech.*, Vol. 16, pp. 99-137.

Schetz, J. A. (1993), *Boundary Layer Analysis*, 1st edition, Prentice-Hall Inc., New Jersey.

Schlichting, H. (1979), *Boundary Layer Theory*, 7th edition, McGraw-Hill Book Company, New York.

Shah, D. A. and Antonia, R. A. (1989), Scaling of the "bursting" period in turbulent boundary layer and duct flows, *Phys. Fluids A*, Vol. 1(2), pp. 318-325.

Sill, B. L. (1986), Velocity profiles in the turbulent boundary layers, in *Advancements in Aerodynamics, Fluid Mechanics, and Hydraulics*, (Eds: R. E. A. Arndt, H. G. Stefan, C. Farell, and S. M. Peterson), ASCE, New York, pp. 9-18.

Sirovich, L. and Karlsson, S. (1997), Turbulent drag reduction by passive mechanism, *Nature*, Vol. 388, pp. 753-755.

Smith, C. R. and Schwartz, S. P. (1983), Observation of streamwise rotation in the near-wall region of a turbulent boundary layer, *Phys. Fluids*, Vol. 26(3), pp. 641-652.

Smith, D. S and Walker, J. H. (1958), Skin friction measurements in incompressible flow, *NACA TN*, no. 4231.

Smith, C. R. and Walker, J. D. A. (1997), Sustaining mechanisms of turbulent boundary layers: The role of vortex development and interactions, in *Self Sustaining Mechanisms of Wall Turbulence* (Ed.: R. L. Panton), Computational Mechanics Publications, Southampton, pp. 13-47.

Smits, A. J. and Wood, D. H. (1985), The response of turbulent boundary layers to sudden perturbations, *Ann. Rev. Fluid Mech.*, Vol. 17, pp. 321-358.

Sowdon, A. (1998), Investigation into the use of a flat plate as a drag reduction device, *72th General Meeting of Ship Research Institute*, Japan.

Spalart, P. R. (1988), Direct Simulation of a Turbulent Boundary Layer up to $R_\theta = 1410$, *J. Fluid Mech.*, Vol. 187, pp. 61-98.

Sutardi and Ching, C. Y. (1999), Development of a turbulent boundary layer downstream of transverse square cavity, *Proc. 17th Canadian Congress of Applied Mech., CANCAM99*, (Eds. S. Ziada and D. S. Weaver), Hamilton, Ontario, Canada, May 30-June 3, pp. 193-194.

Taneda, S. (1979), Visualization of separating Stokes flows, *J. Phys. Soc. Japan*, Vol. 46(6), pp. 1935-1942.

Tani, I., Iuchi, M., and Komoda, H. (1961), Experimental investigation of flow separation associated with a step or groove, *Aero. Res. Inst.*, Univ. Tokyo, 363.

Tani, I. (1968), Review of some experimental results on the response of a turbulent boundary layer to sudden perturbations, *Proc. of 1968 AFORS IFP Stanford Conference on Computation of Turbulent Boundary Layers*, Vol. 1, pp. 483-494, Stanford Univ., CA.

Tani, I., Munakata, H., Matsumoto, A., and Abe, K. (1987), Turbulence management by groove roughness, in *Turbulence Management and Relaminarisation*, (Eds.: H. W. Liepmann and R. Narasimha), IUTAM Symposium, Bangalore, India, pp. 161-172.

Tantirige, S. C. (1989), A flow visualization investigation of the turbulent boundary layer over regularly rough surfaces, *Ph.D. Thesis*, University of Toronto

Tantirige, S. C., Iribarne, A. P., Ojha, M., and Trass, O. (1994), The turbulent boundary layer over single V-shaped grooves, *Int. J. Heat Mass Transfer*, Vol. 37, no. 15, pp. 2261 – 2271.

Timin, T, Esmail, M. N, and Trass, O. (1983), Momentum exchange between turbulent flow sublayers and rough surfaces, *Proc. 9th Canadian Congress of Applied Mech., CANCAM83*, University of Saskatchewan, Sakatoon, Canada, May 30-June 03, pp. 583-584.

Townes, H. W. and Sabersky, R. H. (1966), Experiments on the flow over a rough surface, *Int. J. Heat Mass Transfer*, Vol. 9, pp. 729-738.

TSI-Incorporated (1998), Model 8360/8382/8383/8388 VelociCalc® plus air velocity meter, *Operation and Service Manual.*

Tullis, S. and Pollard, A. (1994), The time dependent flow over V- and U-groove riblets of different sizes, *Phys. Fluids*, Vol. 6(3), pp. 1310-1314.

Wallace, J. M., Eckelmann, H., and Brodkey, R. S. (1972), The wall region in turbulent shear flow, *J. Fluid Mech.*, Vol. 54, part. 1, pp. 39-48.

Walsh, M. J. (1980), Drag Characteristics of V-Groove and Transverse Curvature Riblets, in *Progress in Astronautics and Aeronautics*, (Ed.: G. R. Haugh), Vol. 72, pp. 168-184.

Walsh, M. J. (1990), Viscous drag reduction in boundary layers, in *Progress in Astronautics and Aeronautics,* (Eds.: D. M. Bushnell and J. N. Hefner), Vol. 123, pp. 203-261.

Webster, D. R., Degraaff, D. B., and Eaton, J. K. (1996), Turbulence characteristics of a boundary layer over a two-dimensional bump, *J. Fluid Mech.*, Vol. 320, pp. 53-69.

White, F. M. (1986), *Fluid Mechanics*, 2nd edition, McGraw-Hill, Inc., New York.

Willmarth, W. W. and Lu, S. S. (1972), Structure of the Reynolds stress near the wall, *J. Fluid Mech.*, Vol. 55, part. 1, pp. 65-92.

Wills, J. A. B. (1962), The correction of hot-wire readings for proximity to a solid boundary, *J. Fluid Mech.*, Vol. 12, pp. 388-396.

Wu, X., Squires, K. D., and Lund, T. S. (1995), Large eddy simulation of a spatially-developing boundary layer, *Proceedings of the 1995 ACM/IEEE Supercomputing Conference*, San Diego, California, USA.

Yavuzkurt, S. (1984), A guide to uncertainty analysis of hot-wire data, *J. Fluids Engineering*, Vol. 106, pp. 181-186.

Zagarola, M. V. and Smits, A. J. (1997), Scaling of the mean velocity profile for turbulent pipe flow, *Phys. Rev. Letters*, Vol. 78(2), pp. 239-242.

Zhu, Y. and Antonia, R. A. (1995), Effects of Wire separation on X-probe measurements in a turbulent flow, *J. Fluid Mech.*, Vol. 287, pp. 199-223.

Appendix A

Hot-wire Calibration and Program Listings

A.1 Calibration of a Single-Normal (SN) Hot-Wire and an X-Wire

A.2 Program Listings

A.1 Calibration of a Single-normal (SN) Hot-wire and an X-Wire

A third order polynomial is employed for the functional relationship between the hot-wire signal (Volts) and the velocity, U. (Eq. 3.1). A typical calibration curve for a single-normal hot-wire is shown in Fig. A.1. The instantaneous velocity can then be obtained directly from the anemometer output using the calibration curve. The data reduction is performed using MATLAB® and the corresponding mean, fluctuating, and rms-values are simultaneously calculated.

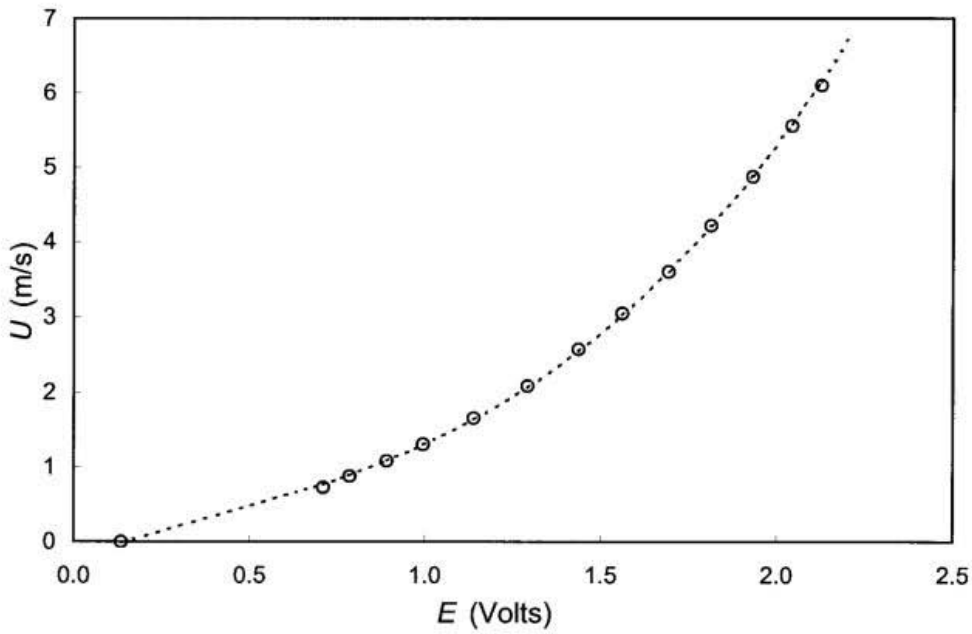

Fig. A.1 Typical calibration curve of a SN-wire. ○, data; - - - -, third order polynomial fit.

The calibration procedure of an X-wire consists of two steps. First, a velocity (U)-voltage (E) calibration curve of the two wires in the un-yawed position is obtained,

similar to that for a SN-wire. Typical *U-E* calibration curves for the two sensors of the X-wire is shown in Fig. A.2.

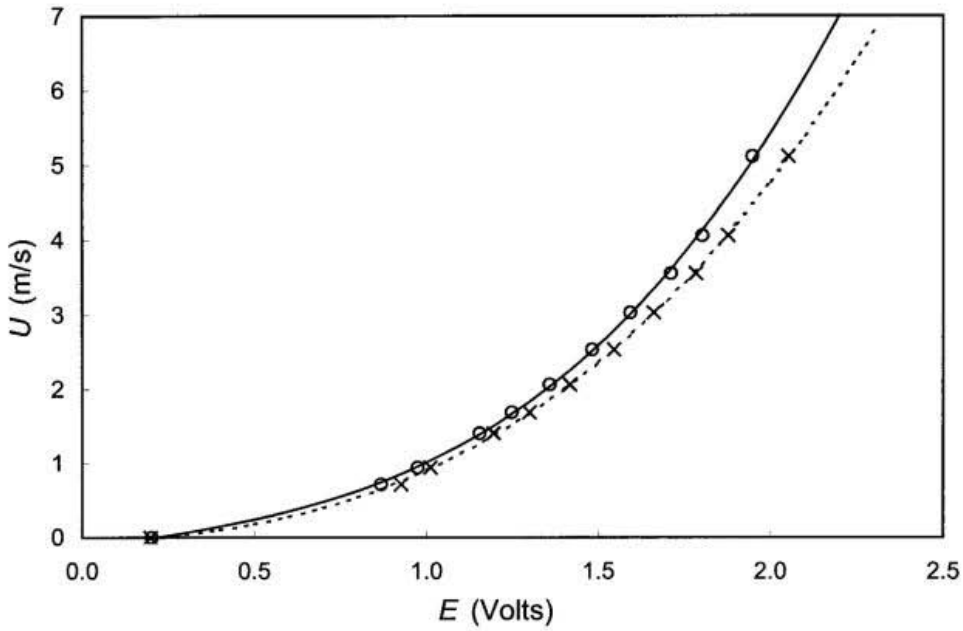

Fig. A.2 Typical calibration curves of the X-wire. ○, wire-1; ×, wire-2; ——, ------, third order polynomial lines.

An instantaneous velocity $\vec{S}$ can be resolved into its components (by assuming that the *z*-component of $\vec{S}$ is very small compared to the two other components) as

$$\vec{S}(t) = \tilde{u}(t)\ \hat{i} + \tilde{v}(t)\ \hat{j}, \tag{A.1}$$

where

$$\tilde{u}(t) = U + u(t) = \left|\vec{S}(t)\right| \cos\beta(t), \tag{A.2}$$

and

$$\tilde{v}(t) = V + v(t) = \left|\vec{S}(t)\right| \sin\beta(t). \tag{A.3}$$

Secondly, a yaw-calibration is performed simultaneously for the two wires. Consider a configuration of the X-wire as shown in Figs. A.3. The $\tilde{u}(t)$ and $\tilde{v}(t)$ components can be calculated if the instantaneous angle β, and the velocity magnitude $|\vec{S}|$ can be determined. The concepts of effective angle and effective cooling of an inclined wire are used to estimate β and $|\vec{S}|$ (Bradshaw, 1971).

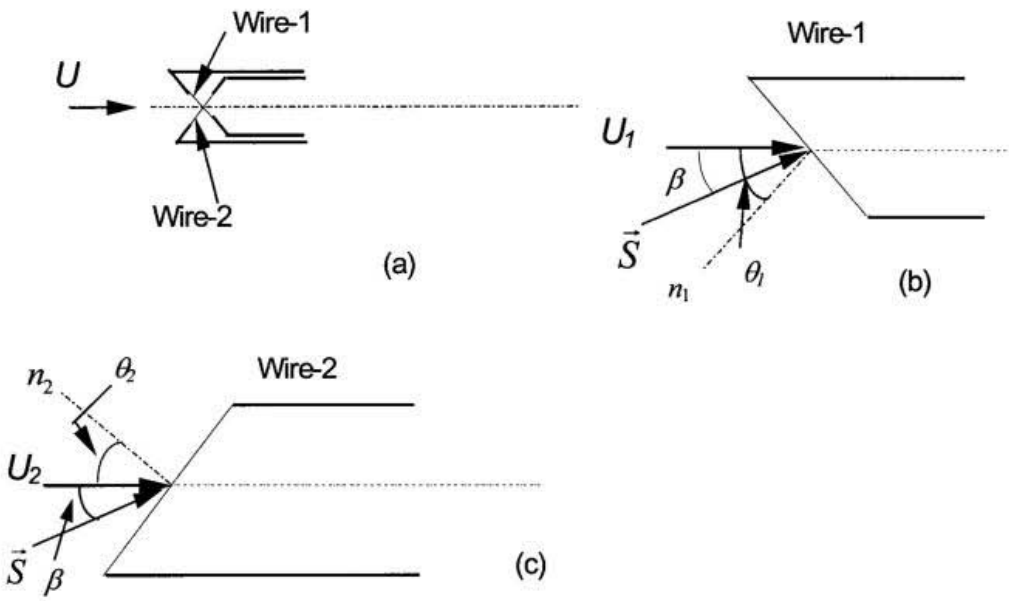

Fig. A.3 Wires of an X-wire. $\vec{S}$ is the instantaneous velocity vector that makes an angle of β with the main flow direction.

Consider an instantaneous velocity vector, $\vec{S}$, hitting a slanted hot-wire as shown in Fig. A.4, where $\vec{S}$ is in plane with the wire. If the output voltage from the anemometer due to the incoming velocity vector $\vec{S}$ is E_0, then an effective cooling velocity, V_{eff},

defined as the velocity which, if it were normal to the wire, will produce exactly the same voltage E_0. Hence, V_{eff} can be expressed as

$$V_{eff} = \left|\vec{S}\right| f(\theta). \tag{A.4}$$

Using a cosine cooling law (Bradshaw; 1971), Eq. (A.4) has the form of

$$V_{eff} = \left|\vec{S}\right| \cos(\theta_{eff}). \tag{A.5}$$

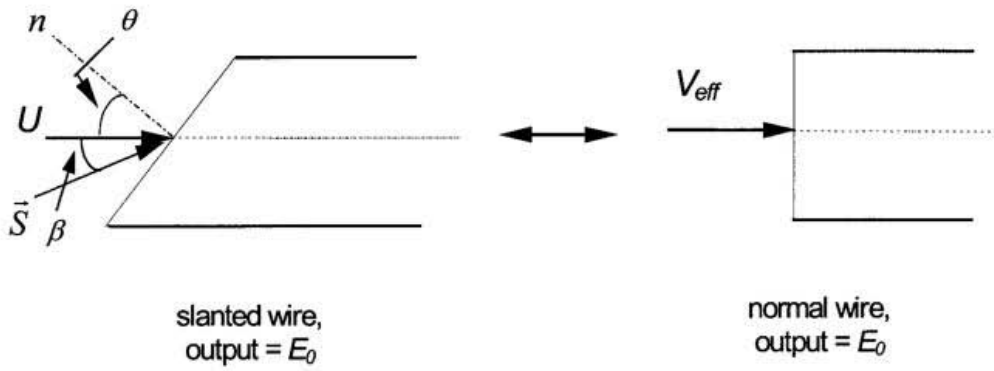

Fig. A.4 Slanted and normal wires with their output voltages.

Now, suppose the inclined hot-wire (the solid line in Fig. A.5) is placed in a free stream velocity U_1, and the corresponding anemometer output voltage is E_1. When the wire is yawed by an angle θ_{yaw} in a counter clockwise direction, as shown by a dashed line, let the output voltage of the anemometer be E_2. The voltage E_2 corresponds to a velocity of U_2 if the wire was in the un-yawed position (from the appropriate calibration curve, see Fig. A.2). Since the anemometer output of the wire is the same when the wire

is in the yawed position with velocity U_1 and if the wire is in the un-yawed position with velocity U_2, we can formulate

$$V_{eff} = U_2 \cos(\theta_{eff}) = U_1 \cos(\theta_{eff} + \theta_{yaw}). \tag{A.6}$$

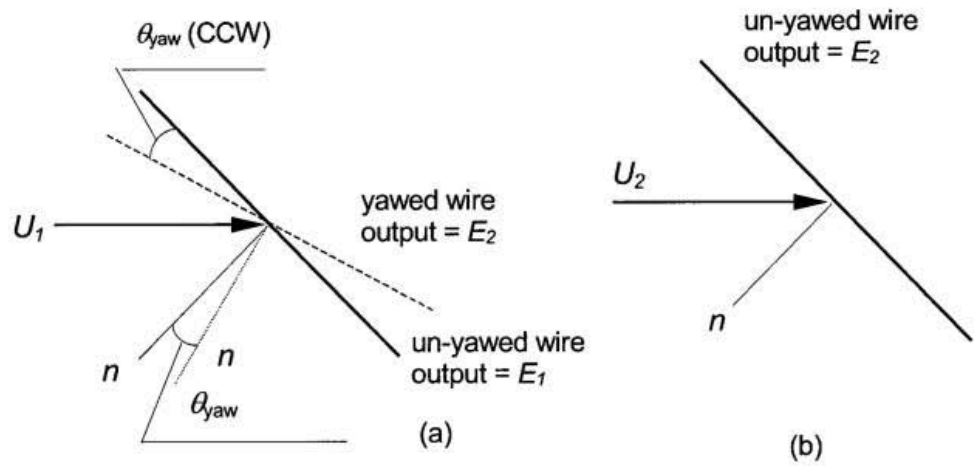

Fig. A.5 Yawed and un-yawed wires with their output voltages.

Furthermore, the effective angle, θ_{eff}, can be expressed as

$$\theta_{eff} = \tan^{-1}\left[\frac{\cos(\theta_{yaw}) - \frac{U_2}{U_1}}{\sin(\theta_{yaw})}\right]. \tag{A.7}$$

$U_2 \cos(\theta_{eff})$ in Eq. (A.6) is called *the effective cooling velocity* at an effective angle θ_{eff}. U_1 and U_2 are obtained from the *U-E* calibration curve, and for a given θ_{yaw}, the effective angle can be calculated. A complete yaw calibration was performed by yawing the wire from –25° to +25° in steps of 5°. At each yaw position, θ_{eff} was calculated, and an average value of θ_{eff} can be determined.

With reference to Fig. A.3, the cosine law states that

$$U_1 \cos(\theta_1) = S \cos(\theta_1 - \beta), \tag{A.8}$$

and

$$U_2 \cos(\theta_2) = S \cos(\theta_2 + \beta), \tag{A.9}$$

where θ_1 and θ_2 are the effective angles of wire-1 and wire-2, respectively. Since θ_1 and θ_2 are known, and U_1 and U_2 can be obtained from the calibration curve, the instantaneous velocity magnitude (S) and velocity vector angle (β), can be obtained by simultaneously solving Eqs. (A.8) and (A.9) (Bruun et al., 1990a, b; Browne et al. 1989), i.e.:

$$\beta = \tan^{-1}\left\{\frac{\left[\frac{U_1}{U_2} - 1\right]}{\tan(\theta_1) + \frac{U_1}{U_2}\tan(\theta_2)}\right\}. \tag{A.10}$$

Finally, S can be calculated from following equations:

$$S = \frac{U_1 \cos\theta_1}{\cos(\theta_1 - \beta)}, \tag{A.11a}$$

or

$$S = \frac{U_2 \cos\theta_2}{\cos(\theta_2 + \beta)}. \tag{A.11b}$$

Once S and β are determined, $\tilde{u}(t)$ and $\tilde{v}(t)$ can be calculated with Eqs. (A.2) and (A.3), respectively. The data reduction was performed using MATLAB®, and program listings are presented in Appendix A.2.

A.2. Program Listings

MATLAB Code 1: Program listing to obtain the calibration curve for a SN-wire.

```
************************************************************
clear

% filename: calibs1.m

% generate sequence of file names
file = ['cal_01.dat';
        'cal_02.dat';
        'cal_03.dat';
        'cal_04.dat';
        'cal_05.dat';
        'cal_06.dat';
        'cal_07.dat';
        'cal_08.dat';
        'cal_09.dat';
        'cal_10.dat';
        'cal_11.dat';
        'cal_12.dat';
        'cal_13.dat';
        'cal_14.dat';
        'cal_15.dat';];

for n=1:size(file,1);
   fid = fopen(file(n,1:size(file,2)),'r');
   data = fscanf(fid, '%i %i', [2, inf]);
   hwire(n) = mean(data(1,1:size(data,2)));
   pitot(n) = mean(data(2,1:size(data,2)));
   fclose(fid);
   clear data;
end

press  = 30.25;                          % in-Hg
temp   = 22;                             % C
 press = press*3386.38815789;
 temp  = temp + 273.15;
   rho = press / (287.0314 * temp);      % air density
   pitot_vel = (2 * 248.84 * ((pitot-
pitot(1))*(0.1/(4095))) / rho).^.5;

ps_0831 = polyfit(hwire, pitot_vel,3);  % Third order pol.

************************************************************
```

MATLAB Code 2: Program listing to calculate mean velocity and turbulence intensity from a SN-wire data.

```
************************************************************
clear

% MEAN AND RMS CALCULATION +++

load ps_0831              % Third order polynomial constants

% generate sequence of file names, velocity at a certain
% distance off the wall

file = ['s400_0.dat';
        's300_0.dat';
        's200_0.dat';
        's150_0.dat';
        's100_0.dat';
        's090_0.dat';
        's080_0.dat';
        's070_0.dat';
        's060_0.dat';
        's055_0.dat';
        's050_0.dat';
        's045_0.dat';
        's040_0.dat';
        's035_0.dat';
        's030_0.dat';
        's027_5.dat';
        's025_0.dat';
        's022_5.dat';
        's020_0.dat';
        's019_0.dat';
        's018_0.dat';
        's017_0.dat';
        's016_0.dat';
        's015_0.dat';
        's014_0.dat';
        's013_0.dat';
        's012_0.dat';
        's011_0.dat';
        's010_0.dat';
        's009_0.dat';
        's008_0.dat';
        's007_0.dat';
        's006_0.dat';
        's005_0.dat';
```

```
        's004_0.dat';
        's003_5.dat';
        's003_0.dat';
        's002_5.dat';
        's002_0.dat';
        's001_5.dat';
        's001_0.dat';
        's000_9.dat';
        's000_8.dat';
        's000_7.dat';
        's000_6.dat';
        's000_5.dat';
        's000_4.dat';
        's000_3.dat';
        's000_2.dat';
        's000_1.dat';
        's000_0.dat';];

for n=1:size(file,1);                          % file incrementer
    fid      = fopen(file(n,1:size(file,2)),'r');
    data     = fscanf(fid, '%i %i', [1, inf]);
    ndata_1  = data(1,:);
    u1       = polyval(ps_0831,ndata_1);

% Filtering:
            [z,wn] = buttord(1950/2000,2000/2000,1,50);
            [b,a]  = butter(z,wn);
            u1f    = filter(b,a,u1);
            u      = u1f(100:39900);

    u_mean(n)= mean(u(1,1:size(u,2)));
    u_prime  = u-u_mean(n);
    clear data ndata_1;
    fclose(fid);

    u_rms(n)  = 0;
       for m  = 1:size(u,2);
          u_rms(n) = u_rms(n)+(u_prime(m))^2;
       end;
    u_rms(n) = (u_rms(n)/size(u,2))^0.5;
    fclose(fid);

    clear u;                                   % make some room
end;                                           % repeat for every file

clear n m fid file fsaved;                     % tidy up
************************************************************
```

MATLAB Code 3: Program listing to obtain the calibration curve for an X-wire.

```
************************************************************
clear

% filename: xcalib29.m

% generate sequence of file names
file = ['xcal_00.dat';
        'xcal_01.dat';
        'xcal_02.dat';
        'xcal_03.dat';
        'xcal_04.dat';
        'xcal_05.dat';
        'xcal_06.dat';
        'xcal_07.dat';
        'xcal_08.dat';
        'xcal_09.dat';
        'xcal_10.dat';
        'xcal_11.dat';
        'xcal_12.dat';
        'xcal_13.dat';];

press   = 30.12;                                    % in-Hg
temp    = 25.50;                                    % C

for n = 1:size(file,1);
    fid  = fopen(file(n,1:size(file,2)),'r');
    data = fscanf(fid, '%i %i', [2, inf]);
    hwire1(n) = mean(data(1,1:size(data,2)));
    hwire2(n) = mean(data(2,1:size(data,2)));
    fclose(fid);
    clear data;
end

 press = press*3386.38815789;
 temp  = temp + 273.15;
   rho = press / (287.0314 * temp);          % air density
    pitot_vel = (2 * 248.84 * ((pitot-
   pitot(1))*(0.1/(4095))) / rho).^.5;

px0917_1  = polyfit(hwire1,pitot_vel,3);
px0917_2  = polyfit(hwire2,pitot_vel,3);

************************************************************
```

MATLAB Code 4: Program listing to obtain the effective angle for an X-wire.

```
************************************************************
clear
% Filename: tetaef.m
% generate sequence of file names
 load px0917_1
 load px0917_2

   file = ['x_03.dat';
           'x_04.dat';
           'x_05.dat';
           'x_06.dat';
           'x_07.dat';
           'x_08.dat';
           'x_09.dat';
           'x_10.dat';
           'x_11.dat';
           'x_12.dat';
          'x_13.dat';];

yaw     = [-25 -20 -15 -10 -5 0 5 10 15 20 25];

for n   = 1:size(file,1);
    fid    = fopen(file(n,1:size(file,2)),'r');
    data   = fscanf(fid,'%i %i', [2, inf]);
    hw1(n) = mean(data(1,1:size(data,2)));
    hw2(n) = mean(data(2,1:size(data,2)));
    fclose(fid);
    clear data;          % make some room
end                      % repeat for every file
for n = 1:size(file,1);
    vel_1(n) = polyval(px0917_1,hw1(n));
    vel_2(n) = polyval(px0917_2,hw2(n));
end

for n = 1:size(file,1);
   efang_1(n) = atan((cos(yaw(n)*pi/180)-
                (vel_1(n)/2.0347))/sin(yaw(n)*pi/180));
   efang_2(n) = atan((cos(-yaw(n)*pi/180)-
                (vel_2(n)/2.0345))/sin(-yaw(n)*pi/180));
  tetaef_1(n) = efang_1(n)*180/pi;
  tetaef_2(n) = efang_2(n)*180/pi;
end                              %repeat for every file
  av_eff_1 = mean(tetaef_1)
  av_eff_2 = mean(tetaef_2)
************************************************************
```

MATLAB Code 5: Program listing to calculate mean velocity and turbulence intensities from an X-wire data.

```
************************************************************
clear

% MEAN AND RMS CALCULATION +++

  load px0917_1;  % Third order polynomial constants for
                  % wire 1
  load px0917_2;  % Third order polynomial constants for
                  % wire 2

% generate sequence of file names, velocity at a certain
% distance from the wall

file = [  'x400_0.dat';
          'x300_0.dat';
          'x200_0.dat';
          'x150_0.dat';
          'x100_0.dat';
          'x090_0.dat';
          'x080_0.dat';
          'x070_0.dat';
          'x060_0.dat';
          'x055_0.dat';
          'x050_0.dat';
          'x045_0.dat';
          'x040_0.dat';
          'x035_0.dat';
          'x030_0.dat';
          'x027_5.dat';
          'x025_0.dat';
          'x022_5.dat';
          'x020_0.dat';
          'x018_0.dat';
          'x017_0.dat';
          'x016_0.dat';
          'x015_0.dat';
          'x014_0.dat';
          'x013_0.dat';
          'x012_0.dat';
          'x011_0.dat';
          'x010_0.dat';
          'x009_0.dat';
```

```
            'x008_0.dat';
            'x007_0.dat';
            'x006_0.dat';
            'x005_0.dat';
            'x004_0.dat';
            'x003_5.dat';
            'x003_0.dat';
            'x002_5.dat';
            'x002_0.dat';
            'x001_5.dat';
            'x001_0.dat';
            'x000_9.dat';];

tteta_1 = 47.1539;              % teta 1 effective in degrees
tteta_2 = 44.2203;              % teta 2 effective in degrees
teta1   = tteta_1*pi/180;       % teta 1 effective in radiant
teta2   = tteta_2*pi/180;       % teta 2 effective in radiant

tanteta1 = tan(teta1);
tanteta2 = tan(teta2);
costeta1 = cos(teta1);

for n       = 1:size(file,1);            %file incrementer
    fid     = fopen(file(n,1:size(file,2)),'r');
    data    = fscanf(fid, '%i %i', [2, inf]);
    ndata_1 = data(1,:);
    ndata_2 = data(2,:);
    u1_1    = polyval(px0917_1,ndata_1);   % wire 1
    u2_1    = polyval(px0917_2,ndata_2);   % wire 2

% Filtering:

            [z,wn] = buttord(4950/5000,5000/5000,1,50);
            [b,a]  = butter(z,wn);
            u1f    = filter(b,a,u1_1);
            u2f    = filter(b,a,u2_1);
            u1     = u1f(100:49900);
            u2     = u2f(100:49900);

% end of filtering

    for q = 1:size(u1,2);
      u(q) = (costeta1*u1(q))/(cos(teta1-atan((u1(q)/u2(q)-
             1)/(tanteta2*u1(q)/u2(q)+tanteta1))))*cos(atan
             ((u1(q)/u2(q)-1)/(tanteta2*u1(q)/u2(q)+
             tanteta1)));     % x-component of velocity
```

```
      v(q) = (costeta1*u1(q))/(cos(teta1-atan((u1(q)/u2(q)-
             1)/(tanteta2*u1(q)/u2(q)+tanteta1))))*sin(atan
             ((u1(q)/u2(q)-1)/(tanteta2*u1(q)/ u2(q)+
             tanteta1)));   % y-component of velocity
    end;

    u_mean(n) = mean(u(1,1:size(u,2)));
    v_mean(n) = mean(v(1,1:size(v,2)));
    u_prime   = u-u_mean(n);
    v_prime   = v-v_mean(n);
    clear data ndata_1 ndata_2;
    fclose(fid);


      for m = 1:size(u,1);
       uv_prime(m) = u_prime(m)*v_prime(m);
      end;

    u_rms(n)    = std(u);
    v_rms(n)    = std(v);
    uv_mean(n) = mean(uv_prime);

    fclose(fid);
    clear u1 u2 beta s u_prime v_prime uv_prime u v;
                % make some room
end;            % repeat for every file

clear n m fid file xsaved q pitot_vel press rho temp;
                % tidy up

************************************************************
```

Appendix B

Wall shear stress estimation

B.1 Log-law (Clauser-chart) technique

B.2 Power-law technique

B.3 Slope of U at the wall

B.1 Log-law (Clauser-chart) technique

Clauser (1956) suggested following relationship for U/U_0

$$\frac{U}{U_0} = \frac{u_\tau}{U_0} g\left[\left(\frac{u_\tau}{U_0}\right)\left(\frac{U_0 y}{\nu}\right)\right]. \tag{B.1}$$

The friction velocity (u_τ) was determined by plotting U/U_0 versus $U_0 y/\nu$ on semi-logarithmic axes. A typical plot of the Clauser-chart for the present smooth-wall data at $R_\theta = 2470$ is shown in Fig. B.1. The u_τ is determined by obtaining a best fit to the data, and the most appropriate value for u_τ in this case is 0.2195 m/s ($C_f = 0.003106$). The straight lines on Fig. B.1 have the form of

$$\frac{U}{U_0} = \frac{u_\tau}{U_0}\left[\frac{1}{\kappa}\ln\left(\frac{U_0 y}{\nu}\frac{u_\tau}{U_0}\right) + B\right]. \tag{B.2}$$

Equation (B.2) can be expressed as

$$\frac{U}{u_\tau} = \frac{1}{\kappa}\ln\left(\frac{u_\tau y}{\nu}\right) + B. \tag{B.3}$$

The velocity profile in Fig. B.1 is re-plotted in Fig. B.2 according to Eq. (B.3) using u_τ obtained from the best fit to the data. The figure shows that the log-law describes the velocity well in the region $20 \le y^+ \le 300$ in this case. At low R_θ, the use of the log-law to estimate wall shear stress is tenuous, since the log-region at low R_θ is very narrow, or even non existent (Spalart,1988; Ching et al.,1995a). In the present study, however, the

u_τ obtained from the log-law technique compares favorably with that obtained from the power-law technique at low R_θ.

Various values of von Kármán constant (κ) and y-intercept (B) for turbulent boundary layer and pipe flows have been proposed by several investigators (Table B.1), and Fig. B.3 shows a plot between κ versus B. A simple linear regression is shown in the figure together with ±8% error lines.

Table B.1. Various proposed values of κ and B.

κ	B	Proposed/used by	Flow type
0.417	5.89	Nikuradze (1933)	Pipe flow
0.410	4.90	Clauser (1956)	-
0.400	5.10	Coles (1965)	-
0.400	5.10	Monin and Yaglom (1971)	-
0.400-0.410	4.90-5.50	Cebeci and Smith (1974)	Boundary layer flow
0.385 ± 10%	-	Reynolds (1974)	-
0.410	5.00	Dean (1976)	Boundary layer flow
0.410	5.17	Dean (1976)	duct/pipe flows
0.400	5.50	Schlichting (1979)	Pipe flow
0.394	5.56	Schlichting (1979)	Boundary layer flow
0.410	5.00	Azad and Burhanuddin (1983)	Boundary layer flow
0.410	5.00	Liakopoulus (1983)	Boundary layer flow
0.400	5.00-5.50	Sill (1986)	-
0.410	5.00	White (1986)	-
0.400	5.00	Munson et. al (1990)	Pipe flow
0.410	5.00	Bisset and Antonia (1991)	-
0.420	5.45	Choi and Fujisawa (1993)	Boundary layer flow
0.400	5.00	Fox and McDonald (1994)	Pipe flow
0.436	6.13	Zagarolla and Smits (1997)	Pipe flow
0.410	4.90	Potter and Wiggert (1997)	Boundary layer flow
0.440	6.13	Sutardi and Ching (1999)	Boundary layer flow
0.380	4.10	Österlund et. al (2000)	Boundary layer flow
0.400	5.50	Fischer, Jovanovic and Durst (2001)	-

B.2 Power-law technique

Figure B.4 shows the power-law approximation together with the present data at the lower R_θ (R_θ = 830 and 1250) and at the higher R_θ (R_θ = 3100 and 4200). The DNS data from Spalart (1988) at R_θ = 1410 are also shown in the figure for comparison. At the lower R_θ, there is good agreement between the experimental data and the power-law in the region $30 \leq y^+ \leq 500$. The mean velocity data (normalized by u_τ obtained from the power-law approximation) are also in good agreement with the DNS data down to $y^+ \approx 2$. At $y^+ \leq 2$, the heat conduction from the sensor to the wall becomes significant, and resulting an increase in the anemometer output voltage. This is reflected as a spurious increase in velocity as the wall is approached. At the higher R_θ, on the contrary, the power-law fit in the overlap region is poor.

B.3 Slope of U at the wall

There are two steps to determine τ_w based on the slope of U at the wall technique. First, the velocity data is plotted and a least squares straight line is obtained for the data close to the wall as shown in Fig. B.5. From this, a first approximation for u_τ can be calculated. From the calculated u_τ, the U and y values are converted into normalized values, U^+ and y^+, respectively, and a new linear fit is applied to the data in the region $y^+ \leq 5.0$ (Fig. B.6). The new value of u_τ is considered valid only if the new linear fit describes the data well in the region $y^+ \leq 5.0$.

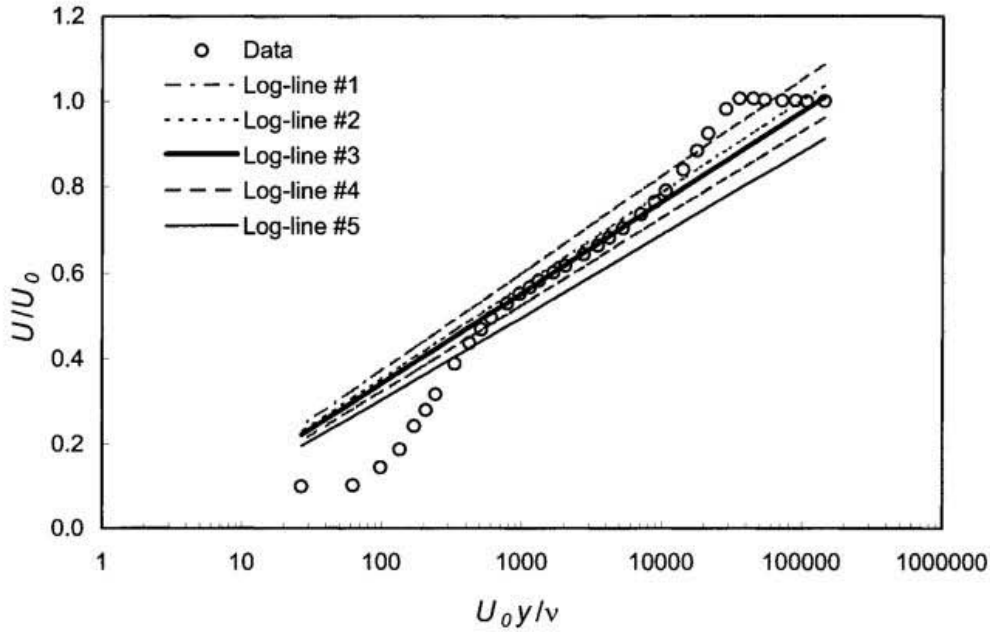

Fig. B.1 Typical of the Clauser-chart for determination of u_τ.
Log-line #1 is the uppermost line, while log-line #5 is the lowermost line.
Log-line #1, $u_\tau = 0.2350$; Log-line #2, $u_\tau = 0.2250$; Log-line #3, $u_\tau = 0.2195$;
Log-line #4, $u_\tau = 0.2100$; Log-line #5, $u_\tau = 0.2000$; u_τ is in m/s.

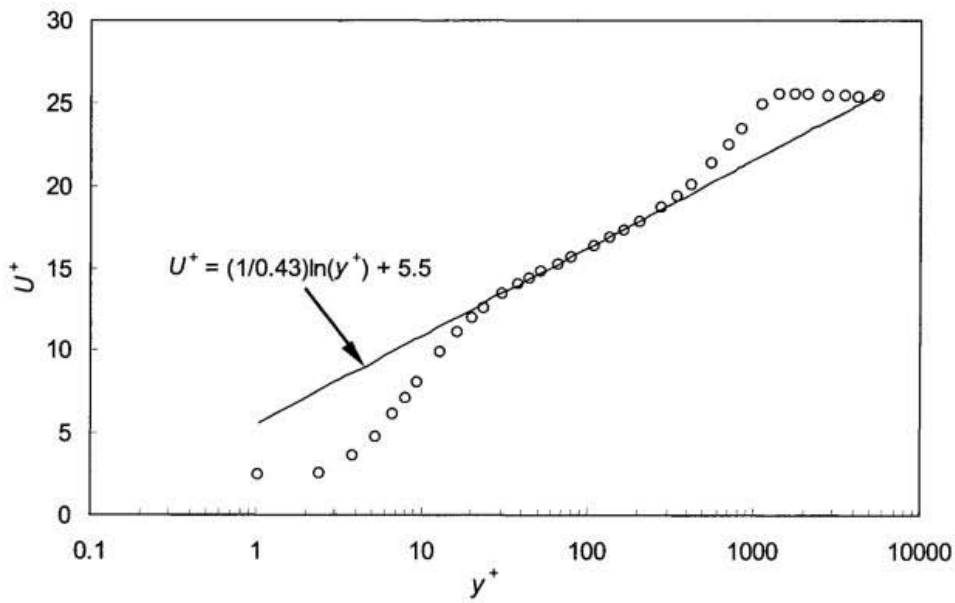

Fig. B.2 Clauser-chart technique for determining u_τ presented in a $U^+ - y^+$ plane.
○, smooth-wall data at $R_\theta = 2470$; ——, Log-line: $U^+ = (1/0.43)\ ln\ (y^+) + 5.5$.

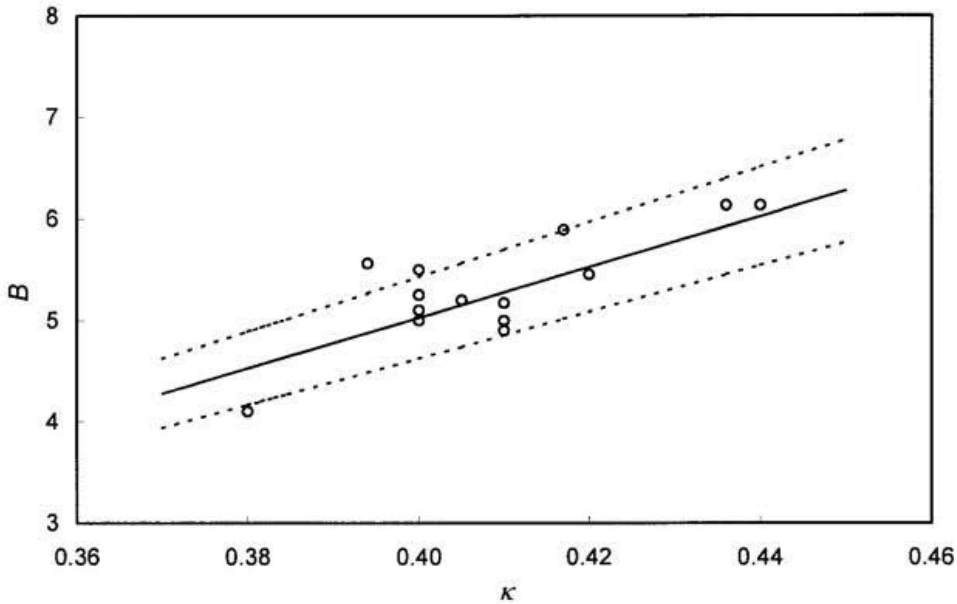

Fig. B.3 Plot of the y-intercept (B) versus von Kármán constant (κ) from various sources in Table B.1. ———, linear regression line: $B = 24.9\kappa - 4.93$; - - - -, ±8% variation.

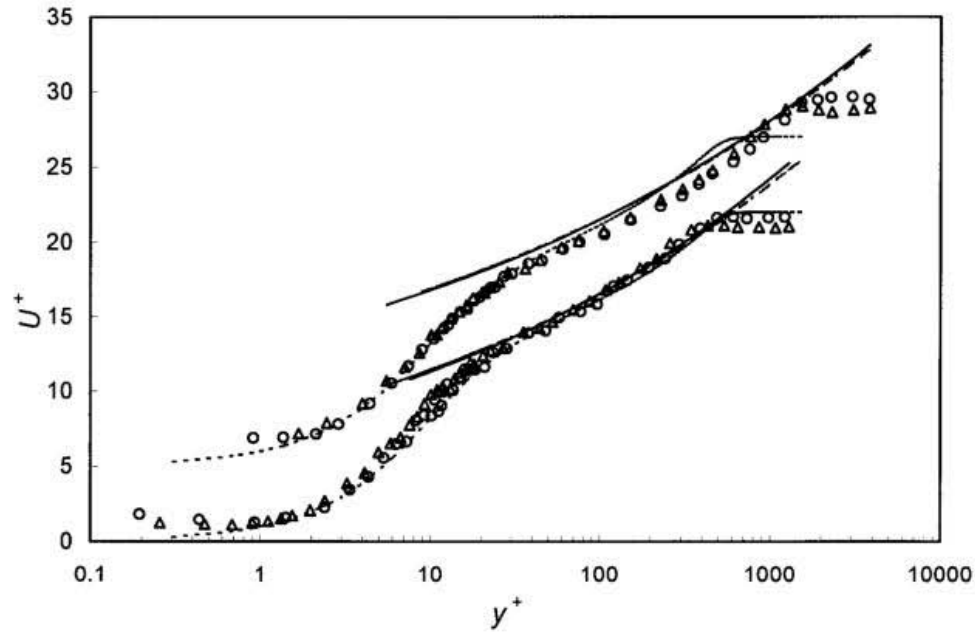

Fig. B.4 Mean velocity distribution. (i) lower plot: Δ, $R_\theta = 830$; ○, $R_\theta = 1250$; (ii) upper plot: Δ, $R_\theta = 3100$; ○, $R_\theta = 4200$; ———, ·-·-·-·-·-, Power-law approximation; - - - - -, DNS at $R_\theta = 1410$ (Spalart, 1988).

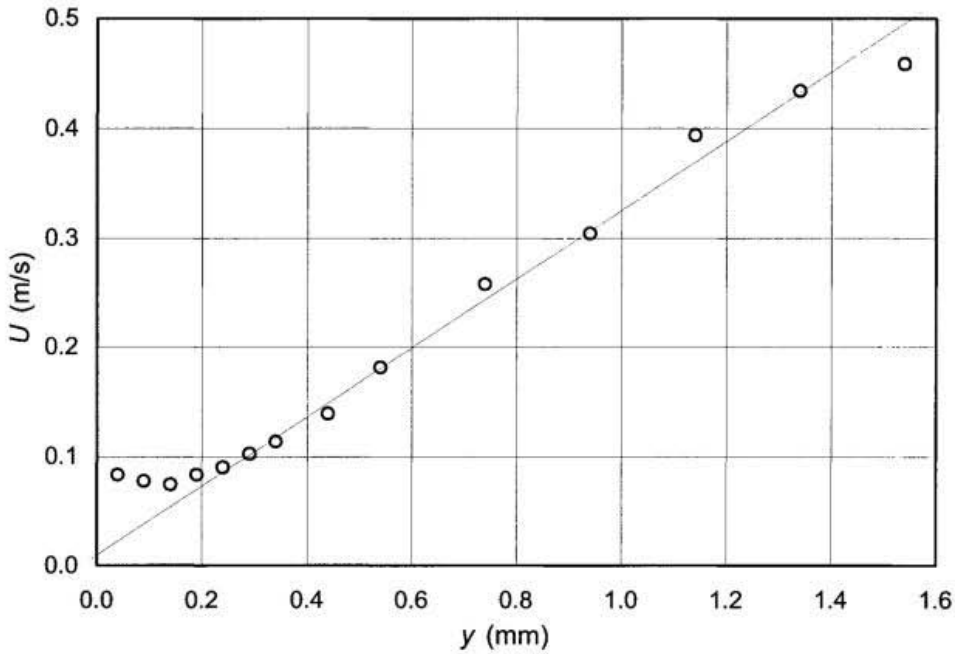

Fig. B.5 Mean velocity in the near-wall region. ○, current data, $U_0 = 1.40$ m/s.

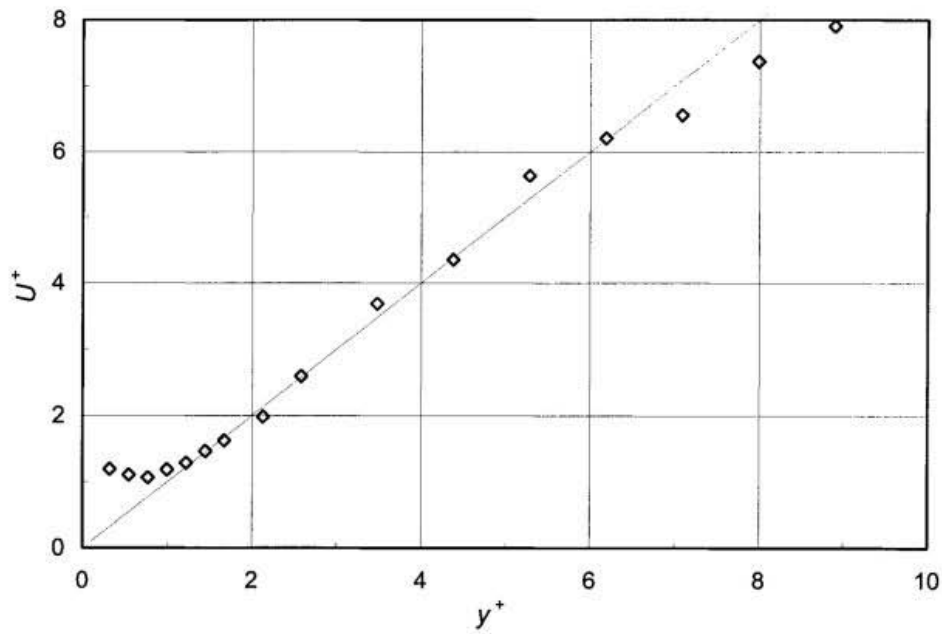

Fig. B.6 Normalized mean velocity in the near-wall region. ○, current data, $U_0 = 1.40$ m/s; ——, $U^+ = y^+$.

Appendix C

Experimental Uncertainties

C.1 Uncertainties in mean velocity (U) and turbulence intensity (u') in the streamwise direction

C.2 Uncertainties in the wall-normal turbulence intensity (v') and Reynolds stress ($\langle -uv \rangle$)

C.3 Uncertainty in δ.

C.4 Uncertainty analysis of u_τ and C_f

C.5 Uncertainty in the estimation of the probe distance from the wall

C.6 Summary

C.1 Uncertainties in mean velocity (U) and turbulence intensity (u') in the streamwise direction

The streamwise mean velocity U is obtained using a calibrated single-nornal (SN) hot-wire. The hot-wire was calibrated using an 8360-M-GB VelociCalc®Plus TSI air velocity meter, hereafter is referred to as the 'TSI instrument'.

Total uncertainty in U, denoted by ΔU_T, is a combination of the uncertainty of the 'TSI instrument' reading (ΔU_R) and the uncertainty of the calibration (ΔU_C), and is expressed as

$$\Delta U_T = \{(\Delta U_R)^2 + (\Delta U_C)^2\}^{0.5}. \tag{C.1}$$

Eq. C.1, can also be written as

$$(\Delta U_T)/U = (\alpha^2 + \beta^2)^{0.5}, \tag{C.2}$$

where α is a function of the 'TSI instrument' mean velocity (U) and β is expressed in following equation

$$\beta = \left[\frac{1}{n}\sum_{i=1}^{n}\left(\frac{\Delta U_d}{U}\right)_i^2\right]^{0.5}. \tag{C.3}$$

In Eq. (C.3), ΔU_d represents deviations of measured U from the calibration curve. For instance, α is obtained from the best fit of the measured 'TSI instrument' uncertainty data and is shown in Fig. C.1. From the calibration data, β can be calculated and is found that $\beta = 0.01615$. The total uncertainty in U can then be obtained from following expression

(Eq. C.4), and the result is also shown in Fig. C.1 (upper curve).

$$\frac{\Delta U_T}{U}(\%) = \left[\left(0.004425U^{-2.704} + 0.005579\right)^2 + 0.01615^2\right]^{1/2} \times 100. \qquad \text{(C.4)}$$

The uncertainty in the fluctuating velocity (u') is the same as the uncertainty in U (Yavuzkurt, 1984).

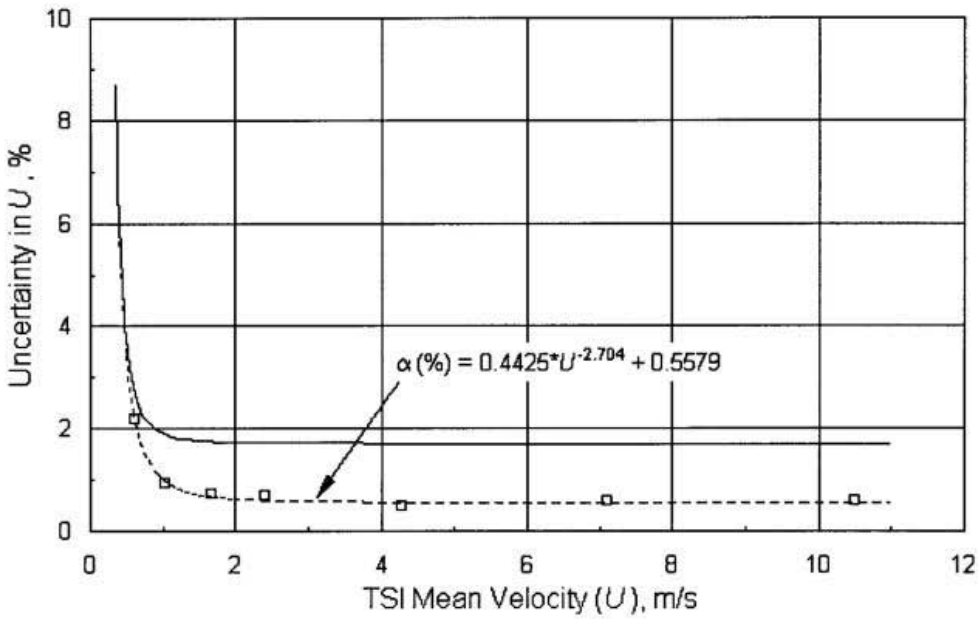

Fig. C.1 Uncertainty in U obtained from hot-wire calibrated using the 'TSI instrument'.
□, uncertainty of U measured by the 'TSI instrument'; - - - -, fit to the data;
——, total uncertainty in U.

C.2 Uncertainties in wall-normal turbulence intensity (v') and Reynolds stress ($\langle -uv \rangle$)

The uncertainty in v' is calculated from a rough estimation described briefly as follows, based on the experimental results on the smooth-wall turbulent boundary

layer using X-wire probe. As many as 30 smooth-wall v'-profiles are used to estimate the experimental uncertainty in v'. Figure C.2 shows the 'calculated' v' in the inner region ($y/\delta \approx 0.02$), and Fig. C.3 is the corresponding frequency distribution of v' as shown in Fig. C.2. The mean value of v' at this y-location is 0.048 m/s with an uncertainty ± 9.8 percent based on 95 percent confidence interval level. The uncertainty of v' in the outer region ($y/\delta \approx 1.0$) was estimated in the same way and the results are 0.00577m/s in mean and ± 7.0 percent in the relative v'-uncertainty. All of these estimations are based on the assumption that the v' data are normally distributed about the mean.

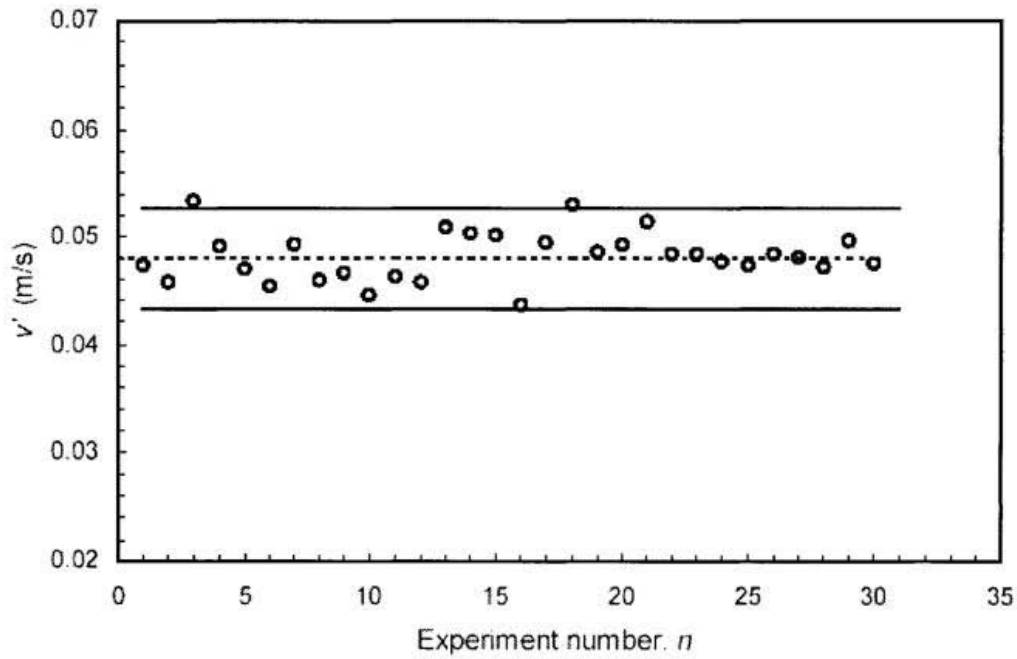

Fig. C.2 v' distribution at $y/\delta = 0.02$, for a smooth-wall flat plate turbulent boundary layer.

The uncertainty in $\langle -uv \rangle$ is calculated in the same way as the estimation in the uncertainty in v'. The values of the uncertainty in $\langle -uv \rangle$ are approximately 14.6

percent and 10.4 percent, respectively, in the inner and outer regions relative to the local value of $\langle -uv \rangle$.

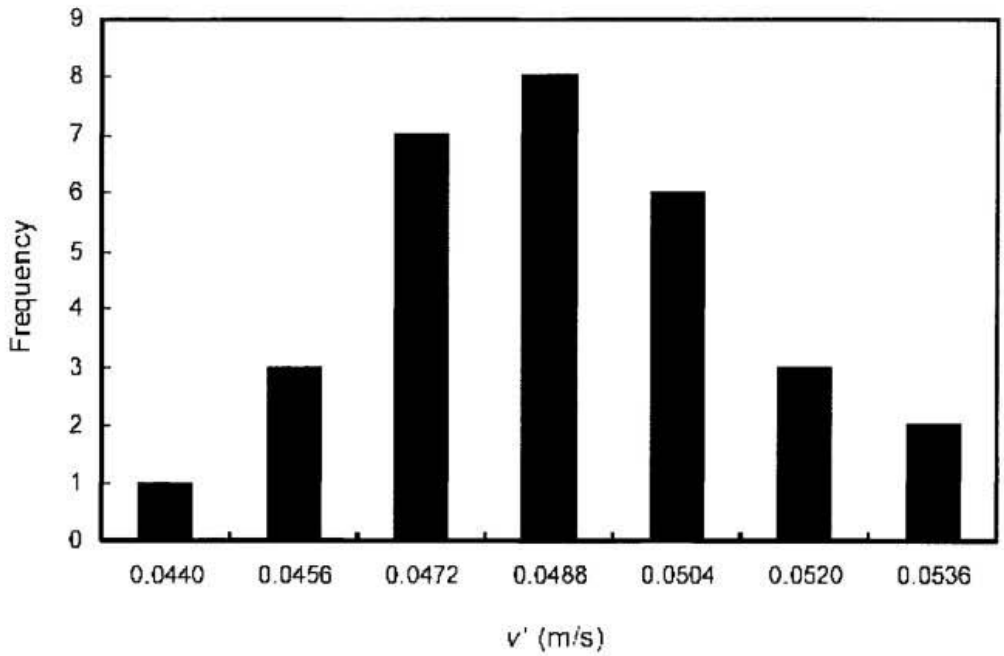

Fig. C.3 Histogram of v' distribution at $y/\delta = 0.02$, for a smooth-wall flat plate turbulent boundary layer. $v' = 0.048$m/s $\pm$ 9.8 percent (95 percent confidence interval level).

C.3 Uncertainty in δ.

The uncertainty of the boundary layer thickness (δ) is estimated to be approximately 0.6 percent and 0.3 percent at $R_\theta = 1000$ and 3000, respectively.

C.4 Uncertainty analysis of u_τ and C_f

C.4.1 Power-law technique

The skin friction coefficient (C_f) can be expressed in terms of fluid properties and flow variables as

$$C_f = \frac{\tau_w}{\frac{1}{2}\rho U_0^2}, \tag{C.5}$$

or

$$C_f = 2\left(\frac{u_\tau}{U_0}\right)^2, \tag{C.6}$$

where τ_w is wall shear stress, ρ is fluid density, and u_τ is friction velocity. Based on the power-law approximation of mean velocity profile in a turbulent boundary layer, Ching et al. (1995a) showed that

$$\frac{u_\tau}{U_0} = \left\{\frac{1}{\exp(3/2\alpha)}\left(\frac{\exp(3/2\alpha)}{C}\right)^{1/(1+\alpha)}\right\}, \tag{C.7}$$

where α and C are calculated with following equations

$$\alpha = \frac{3}{2\ln R_\delta}, \tag{C.8}$$

$$C = \frac{1}{\sqrt{3}}\ln R_\delta + \frac{5}{2}. \tag{C.9}$$

Combining Eqs. (C.7), (C.8), and (C.9) yields

$$u_\tau = \frac{\nu}{\delta}\left(\frac{U_0\delta/\nu}{\frac{1}{\sqrt{3}}\ln(U_0\delta/\nu)+\frac{5}{2}}\right)^{2+\frac{2}{\frac{3}{\ln(U_0\delta/\nu)}}}. \tag{C.10}$$

It is seen that $u_\tau = u_\tau(U_0, \delta, \nu)$, and the uncertainty in u_τ can be expressed as

$$\Delta u_\tau = \left\{ \left(\frac{\partial u_\tau}{\partial U_0} \Delta U_0 \right)^2 + \left(\frac{\partial u_\tau}{\partial \delta} \Delta \delta \right)^2 + \left(\frac{\partial u_\tau}{\partial \nu} \Delta \nu \right)^2 \right\}^{1/2} . \tag{C.11}$$

Assuming the uncertainty in ν is negligible, Eq. (C.11) can be written as

$$\Delta u_\tau = \left\{ \left(\frac{\partial u_\tau}{\partial U_0} \Delta U_0 \right)^2 + \left(\frac{\partial u_\tau}{\partial \delta} \Delta \delta \right)^2 \right\}^{1/2} . \tag{C.12}$$

Differentiating Eq. (C.10) with respect to U_0 and δ yields

$$\frac{\partial u_\tau}{\partial U_0} = \frac{1}{GR} \left(\frac{R}{B} \right)^{2/G} \left[\frac{6 \ln(R/B)}{G \ln(R^2)} + 2 - \frac{1.1548}{B} \right], \tag{C.13}$$

and

$$\frac{\partial u_\tau}{\partial \delta} = \frac{\nu}{\delta^2} \left(\frac{R}{B} \right)^{2/G} \left[\frac{6 ln(R/B)}{G^2 ln(R^2)} - 1 + \frac{2}{G} \left(1 - \frac{0.5774}{B} \right) \right], \tag{C.14}$$

where

$$R = U_0 \delta / \nu \quad ; \qquad B = 0.5774 ln(R) + 2.5; \qquad G = 2 + 3/ln(R). \tag{C.15}$$

Using Eq. (C.5) and following Moffat's (1982) argument, one can express the uncertainty in C_f as

$$\Delta C_f = \left\{ \left(\frac{\partial C_f}{\partial u_\tau} \Delta u_\tau \right)^2 + \left(\frac{\partial C_f}{\partial U_0} \Delta U_0 \right)^2 \right\}^{1/2}, \tag{C.16}$$

which can be simplified as

$$\Delta C_f = \frac{4u_\tau}{U_0^2} \left\{ (\Delta u_\tau)^2 + \left(\frac{u_\tau}{U_0} \Delta U_0 \right)^2 \right\}^{1/2}. \tag{C.17}$$

C.4.2 Log-law (Clauser-chart) technique

The friction velocity (u_τ) can be obtained from the log-law technique using the following equation:

$$\frac{U}{u_\tau} = \frac{1}{\kappa} ln\left(\frac{u_\tau y}{\nu} \right) + B. \tag{C.18}$$

It is not easy, however, to estimate the uncertainty of u_τ from the above expression. The uncertainty in u_τ in this case is approximated using the combination of the uncertainties in U and the uncertainty in the curve-fit for the log-region. This is illustrated using the experimental data shown in Fig. C.4.

The uncertainty in U for the range of interest is approximately 1.7 percent, which relates to a velocity range of 2.9 to 4.4 m/s. The uncertainty for determining the log-law curve-fit is obtained using Eq. (C.3), and the value is about 0.9 percent. Therefore, the total uncertainty of u_τ obtained using the log-law technique is approximately:

$$\Delta(u_\tau)/(u_\tau) = \{(1.7\%)^2 + (0.9\%)^2\}^{0.5} = 1.92\%.$$

A typical value of u_τ obtained using the log-law technique is 0.2310 m/s, and hence:

$$\Delta u_\tau = (0.0192)(0.2310 \text{ m/s}) = 0.004435 \text{ m/s}.$$

Inserting the values of u_τ = 0.2310 m/s, Δu_τ = 0.004435 m/s, U_0 = 5.50 m/s, and ΔU_0 = 0.094 m/s, ΔC_f calculated from Eq. (C.16) is 0.00018. Using a typical value of C_f = 0.003554 from the log-law technique, we have the uncertainty in C_f as 5.1 percent.

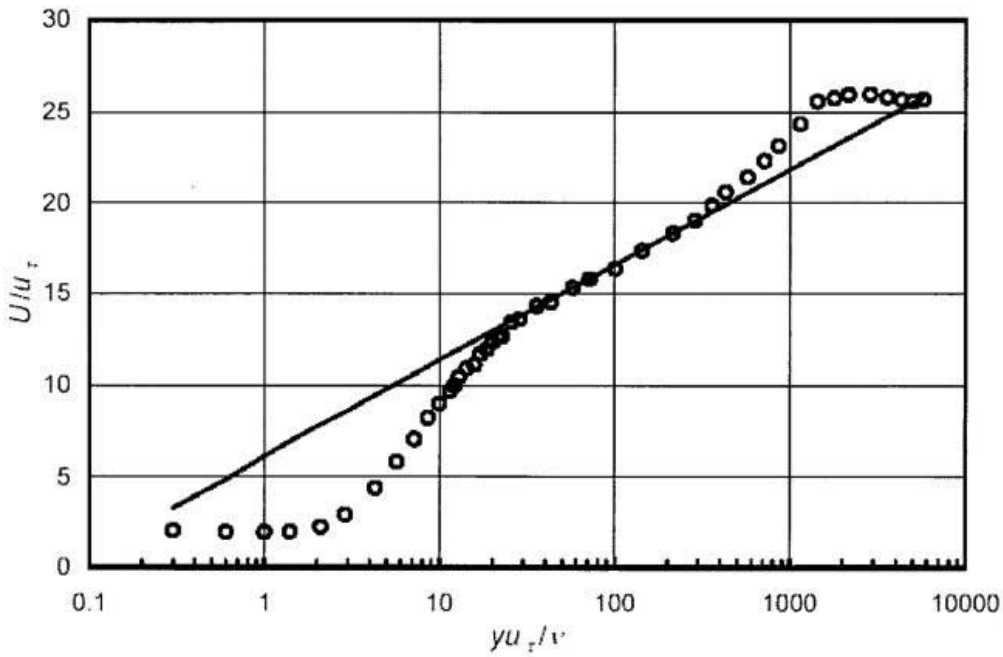

Fig. C.4 Estimation of u_τ using log-law technique. ○, experimental data; ———, log-law fit.

C.4.3 Preston tube measurements

The uncertainty analysis of using Bechert's (1995), Patel's (1965) and the present calibration equations to determine wall shear stress will be presented in the following paragraphs.

a) Bechert calibration equation

Bechert's equation can be expressed as

$$\frac{\tau_w d^2}{\rho\nu^2} = \left\{28.44\left(\frac{\Delta p d^2}{\rho\nu^2}\right)^2 + 0.00000661\left(\frac{\Delta p d^2}{\rho\nu^2}\right)^{3.5}\right\}^{1/4}. \qquad \text{(C.19)}$$

In terms of the friction velocity (u_τ), Eq. (C.19) can be expressed as

$$u_\tau = \sqrt{\frac{\tau_w}{\rho}} = \frac{\nu}{d}\left\{28.44\left(\frac{\Delta p d^2}{\rho\nu^2}\right)^2 + 0.00000661\left(\frac{\Delta p d^2}{\rho\nu^2}\right)^{3.5}\right\}^{1/8}. \qquad \text{(C.20)}$$

Equation (C.20) shows that $u_\tau = u_\tau\ (\Delta p, d, \rho, \nu)$, where Δp is the differential pressure between total and static pressures at the wall, d is the outside tube diameter, ρ and ν are the density and kinematic viscosity of air, respectively. By assuming that air behaves as a perfect gas, where $\rho = P_a/RT_a$, Eq. (C.20) can be rewritten as:

$$u_\tau = \frac{\nu}{d}\left\{28.44\left(\frac{\Delta p d^2 RT_a}{P_a\nu^2}\right)^2 + 0.00000661\left(\frac{\Delta p d^2 RT_a}{P_a\nu^2}\right)^{3.5}\right\}^{1/8}, \qquad \text{(C.21)}$$

or $u_\tau = u_\tau(\Delta p, d, R, P_a, T_a, \nu)$, where R is the gas constant for air, T_a and P_a are ambient air temperature and atmospheric pressure, respectively, at the test condition. For the uncertainty analysis purposes, let us replace Δp with P to avoid confusion of using Δ, hence P and Δp can be used interchangeably.

If the variation in ν is assumed to be very small, and R is a constant, according to Moffat (1982), the uncertainty Δu_τ can be expressed as

$$\Delta u_\tau = \left\{ \left(\frac{\partial u_\tau}{\partial d} \Delta d \right)^2 + \left(\frac{\partial u_\tau}{\partial P} \Delta P \right)^2 + \left(\frac{\partial u_\tau}{\partial T_a} \Delta T_a \right)^2 + \left(\frac{\partial u_\tau}{\partial P_a} \Delta P_a \right)^2 \right\}^{0.5} . \quad \text{(C.22)}$$

Partial derivatives in Eq. (C.22) can be obtained by differentiating Eq. (C.21) with respect to d, P, T_a, and P_a, respectively, and the results are as follow.

$$\frac{\partial u_\tau}{\partial d} = \frac{\nu}{d^2} \left(28.44(P^+)^2 + 0.00000661(P^+)^{3.5}\right)^{1/8} \left[\frac{14.23(P^+)^2 + 0.00000579(P^+)^{3.5}}{28.44(P^+)^2 + 0.00000661(P^+)^{3.5}} - 1 \right], \quad \text{....(C.23)}$$

$$\frac{\partial u_\tau}{\partial P} = \frac{\nu}{8dP} \left[\frac{56.88(P^+)^2 + 0.00002314(P^+)^{3.5}}{\{28.44(P^+)^2 + 0.00000661(P^+)^{3.5}\}^{7/8}} \right], \quad \text{(C.24)}$$

$$\frac{\partial u_\tau}{\partial T_a} = \frac{\nu}{8dT_a} \left[\frac{56.88(P^+)^2 + 0.00002314(P^+)^{3.5}}{\{28.44(P^+)^2 + 0.00000661(P^+)^{3.5}\}^{7/8}} \right], \quad \text{(C.25)}$$

$$\frac{\partial u_\tau}{\partial P_a} = -\frac{\nu}{8dP_a} \left[\frac{56.88(P^+)^2 + 0.00002314(P^+)^{3.5}}{\{28.44(P^+)^2 + 0.00000661(P^+)^{3.5}\}^{7/8}} \right], \quad \text{(C.26)}$$

where $P^+ = \dfrac{Pd^2RT_a}{P_a\nu^2}$.

b) Patel calibration equation

Patel calibration equation in the intermediate Reynolds number range is expressed in Eq. C.27.

$$y^* = 0.8287 - 0.1381x^* + 0.1437x^{*2} - 0.0060x^{*3}, \qquad \text{(C.27)}$$

valid for $1.5 < y^* < 3.5$ and $5.6 < u_\tau d/2\nu < 55$, where $x^* \equiv \log_{10}\left(\frac{Pd^2}{4\rho\nu^2}\right)$ and $y^* \equiv \log_{10}\left(\frac{\tau_w d^2}{4\rho\nu^2}\right)$. The uncertainty in y^*, according to Moffat (1982), can be expressed as

$$\Delta y^* = \left\{\left(\frac{\partial y^*}{\partial x^*}\Delta x^*\right)^2\right\}^{0.5},$$

or

$$\Delta y^* = (-0.1381 + 0.2874x^* - 0.018x^{*2})\Delta x^*. \qquad \text{(C.28)}$$

The uncertainty in x^* has the form of

$$\Delta x^* = \left\{\left(\frac{\partial x^*}{\partial d}\Delta d\right)^2 + \left(\frac{\partial x^*}{\partial P}\Delta P\right)^2 + \left(\frac{\partial x^*}{\partial T_a}\Delta T_a\right)^2 + \left(\frac{\partial x^*}{\partial P_a}\Delta P_a\right)^2\right\}^{0.5}, \qquad \text{(C.29)}$$

where

$$\frac{\partial x^*}{\partial d} = \frac{2}{\ln(10)d}; \qquad \frac{\partial x^*}{\partial P} = \frac{1}{\ln(10)P};$$

$$\frac{\partial x^*}{\partial T_a} = \frac{1}{\ln(10)T_a}; \qquad \frac{\partial x^*}{\partial P_a} = -\frac{1}{\ln(10)P_a};$$

The friction velocity (u_τ) can be expressed in term of y^*, and has the form of

$$u_\tau = 2\frac{\nu}{d}10^{(y^*/2)}. \tag{C.30}$$

Hence, the uncertainty in u_τ is

$$\Delta u_\tau = \left\{\left(\frac{\partial u_\tau}{\partial d}\Delta d\right)^2 + \left(\frac{\partial u_\tau}{\partial y^*}\Delta y^*\right)^2\right\}^{0.5}, \tag{C.31}$$

where

$$\frac{\partial u_\tau}{\partial d} = -2\frac{\nu}{d^2}10^{(y^*/2)}, \text{ and } \frac{\partial u_\tau}{\partial y^*} = \frac{\nu}{d}10^{(y^*/2)}\ln(10). \tag{C.32}$$

c) Present Calibration Equation

The present calibration equation has the form of

$$log_{10}(x_1)/(R_{e,d})^{0.135} = 0.767\ ln(log_{10}(x_2)) + 0.0097, \tag{C.33}$$

where: $x_1 \equiv \tau_w d^{\,2}/(\rho\nu^2)$ and $x_2 \equiv \Delta p d^{\,2}/(\rho\nu^2)$. Expressing new parameters $y^{**} \equiv log_{10}(x_1)/(R_{e,d})^{0.135}$ and $x^{**} \equiv log_{10}(x_2)$, leads to

$$y^{**} = 0.767\ ln(x^{**}) + 0.0097. \tag{C.34}$$

Hence, the uncertainty in y^{**} can be expressed as

$$\Delta y^{**} = \left\{\left(\frac{\partial y^{**}}{\partial x^{**}}\Delta x^{**}\right)^2\right\}^{0.5},$$

or

$$\Delta y^{**} = (0.767/x^{**})\Delta x^{**}. \tag{C.35}$$

The uncertainty in x^{**} is

$$\Delta x^{**} = \left\{ \left(\frac{\partial x^{**}}{\partial d} \Delta d \right)^2 + \left(\frac{\partial x^{**}}{\partial P} \Delta P \right)^2 + \left(\frac{\partial x^{**}}{\partial T_a} \Delta T_a \right)^2 + \left(\frac{\partial x^{**}}{\partial P_a} \Delta P_a \right)^2 \right\}^{0.5}, \tag{C.36}$$

where

$$\frac{\partial x^{**}}{\partial d} = \frac{2}{\ln(10) d}; \qquad \frac{\partial x^{**}}{\partial P} = \frac{1}{\ln(10) P};$$

$$\frac{\partial x^{**}}{\partial T_a} = \frac{1}{\ln(10) T_a}; \qquad \frac{\partial x^{**}}{\partial P_a} = -\frac{1}{\ln(10) P_a};$$

The friction velocity (u_τ) can be expressed in term of y^{**} and has the form of

$$u_\tau = \frac{\nu}{d} 10^n, \tag{C.37}$$

where $n \equiv \dfrac{y^{**}(U_0 d)^{0.135}}{2\nu^{0.135}}$

The uncertainty in u_τ is then:

$$\Delta u_\tau = \left\{ \left(\frac{\partial u_\tau}{\partial d} \Delta d \right)^2 + \left(\frac{\partial u_\tau}{\partial y^{**}} \Delta y^{**} \right)^2 + \left(\frac{\partial u_\tau}{\partial U_0} \Delta U_0 \right)^2 \right\}^{0.5}, \tag{C.38}$$

where

$$\frac{\partial u_\tau}{\partial d} = \left\{ -\frac{\nu}{d^2} + 0.1554 \frac{\nu^{1.135}}{d(U_0 d)^{0.865}} y^{**} U_0 \right\} 10^n,$$

$$\frac{\partial u_\tau}{\partial y^{**}} = 1.1513 \frac{\nu^{0.865}(U_0 d)^{0.135}}{d} 10^n, \text{ and}$$

$$\frac{\partial u_\tau}{\partial U_0} = 0.1554 \frac{y^{**}\nu^{0.865}}{(U_0 d)^{0.865}} 10^n. \tag{C.39}$$

C.4.4 Slope of Mean Velocity (U) at the Wall

The wall shear stress (τ_w) is calculated from the mean velocity gradient at the wall, i.e.

$$\tau_w = \mu \frac{\partial U}{\partial y} \Big|_{y=0}. \tag{C.40}$$

The uncertainty of τ_w is the combination of the uncertainty of U at the near-wall region and the uncertainty of y at the same region. Inserting Eq. C.5 into Eq. C.17 yields

$$\frac{\Delta C_f}{C_f} = \left\{ \left(\frac{\Delta \tau_w}{\tau_w} \right)^2 + \left(\frac{2\Delta U_0}{U_0} \right)^2 \right\}^{1/2}. \tag{C.41}$$

The uncertainty in τ_w and C_f will be treated based on the measured mean velocity (U) at $y^+ = U^+ = 3.5$. Equation C.40 can also be written as

$$\tau_w = \mu \frac{U}{y} \Big|_{near-wall}, \tag{C.42}$$

which has the uncertainty of $\Delta\tau_w$. Hence,

$$\frac{\Delta\tau_w}{\tau_w} = \left\{ \left(\frac{\Delta U_T}{U} \right)^2 + \left(\frac{\Delta y}{y} \right)^2 \right\}^{1/2} . \qquad \text{(C.43)}$$

In Eq. C.43, the relative uncertainty in U (denoted as $\Delta U_T/U$) can be obtained from Fig. C.1 for a given U, and the relative uncertainty in y at the near-wall region (denoted as $\Delta y/y$) is 6.3 percent and 14.9 percent, respectively, at U_0 = 2.0m/s and 5.5m/s. A brief description on how the $\Delta y/y$ is estimated is presented in Appendix C.5.

The results of the uncertainty in C_f calculated from Eqs. C.17 and C.41 using typical present experimental conditions are presented in Table C.1.

C.5 Uncertainty in the estimation of the probe distance from the wall

The uncertainty in the probe distance from the wall at the wall-region is different from the uncertainty at a distance remote from the wall. At the wall region, the reference value to determine the uncertainty of the probe distance from the wall is one wall unit (ν/u_τ), while at a distance remote from the wall, the linear displacement of 5mm is used as the reference value. One wall unit at R_θ = 1000 is approximately 0.158mm, while at R_θ = 3000, $\nu/u_\tau \approx$ 0.0671mm. Assuming that the uncertainty of the linear displacement of the probe is the same value as the minimum linear division of the traversing mechanism, for this instance is 0.01mm, then the uncertainty of the probe distance from the wall at the wall region is 6.3 percent and 14.9 percent, respectively, at R_θ = 1000 and 3000. In the outer region, the probe is moved in the wall-normal direction at a step of 5mm. With the absolute uncertainty of 0.01mm at both R_θ, the relative uncertainty in the wall distance measurement becomes approximately 0.2 percent in the outer region.

C.6 Summary

Some important results of the experimental uncertainties are summarized in Table C.1.

Table C.1 Experimental uncertainties

Flow variable	Uncertainty (%)	
	$R_\theta = 1000$	$R_\theta = 3000$
Mean velocity (U): - Outer region	1.7	1.7
- Wall-region	8.7	2.1
Streamwise turbulence intensity (u'):		
- Outer region	1.7	1.7
- Wall-region	8.7	2.1
Wall-normal turbulence intensity (v'):		
- Outer region	7.0	n/a[¶]
- Wall-region	9.8	n/a[¶]
Reynolds stress ($\langle -uv \rangle$)		
- Outer region	10.4	n/a[¶]
- Wall-region	14.6	n/a[¶]
Boundary layer thickness (δ)	0.6	0.3
Wall-distance (y)		
- Outer region	0.2	0.2
- Wall-region	6.3	14.9
Skin friction coefficient (C_f): - $(dU/dy)_{y=0}$	11.2	15.4
- power-law	5.8	-
- Log-law	-	5.1
- Preston tube	-	2.9 (B)
		3.2 (P)
		3.3 (S)

[¶] No X-wire measurements were taken at $R_\theta = 3000$.

P: Patel's equation; B: Bechert's equation; S: Present equation.